UNSTEADY FLOW OVER BLUFF BODIES

Thesis

Submitted by

BRIAN JEFFREY ARMSTRONG, B.Sc.

For the degree of

DOCTOR OF PHILOSOPHY

Department of Physics,

University of Edinburgh

SEPTEMBER, 1985.

To my parents.

C O N T E N T S

C O N T E N T S (Contd.)

C O N T E N T S (Contd.)

LIST OF SYMBOLS

$\left.\begin{matrix} A \\ B \end{matrix}\right\}$ hot-wire calibration constants

C_{pb} Base pressure coefficient = $\frac{Pb - P_\infty}{\frac{1}{2}\rho\overline{U}^2}$; $C_P'(n)$ fluctuating pressure coefficient.

C_D Drag coefficient

C_{DT} Fluctuating drag coefficient

C_L Sectional fluctuating lift coefficient = sectional fluctuation lift/$\frac{1}{2}\rho\overline{U}^2$

C_M Added mass coefficient

D Diameter of bluff bodies

E Voltage

F(t) Force acting on a bluff body

L_F Formation length

L_X Longitudinal length scale

L_Z Lateral length scale

N Number of data points

Re Reynolds number = UD/ν

R_o Viscous core radius

S_t Strouhal number = $nD/\overline{U}$;

S hot wire sensitivity

$S_F(n)$ power spectral density of force

$_F(n)/\overline{F}^2$ reduced spectral density of force

Su(n) power spectral density of velocity

$Su(n)/\overline{U}^2$ reduced spectral density of velocity

T Sampling interval

T_D total time of data record

$\overline{U}$ mean free-stream velocity

U_c vortex convection speed

$\overline{U}_w$ mean velocity at outer wake of a cylinder

U_b separation velocity

LIST OF SYMBOLS (Contd.)

V^e	Effective cooling velocity
b	Vortex lateral spacing
f_c	Nyquist frequency
f(t)	Fluctuating force
ℓ	Longitudinal spacing of the vortices In Chapter 4 is the length of side of a flat plate.
n	Vortex shedding frequency, except Chapter 2 where it refers to the perturbation frequency, otherwise
n_o	The perturbation frequency
p	Pressure
p'(n)	Pressure fluctuation at frequency n
r	Radial distance
t	Time
u, v, and w	velocity components in x, y and z directions, respectively.
x	Streamwise direction
y	Vertical direction
z	Spanwise direction.
$\gamma^2(n)$	The coherence function
ε_r	Normalised standard error
ν	Kinematic viscosity
θ	Angle
Γ	Vortex strength
$\chi^2(n)$	Aerodynamic admittance
ω	Vorticity $\omega D/\overline{U}$ reduced vorticity

ABSTRACT

The thesis describes a study made of the effects on the flow around bluff bodies of a single frequency perturbation superimposed upon the mean flow.

The forces acting on square flat plates exposed to the perturbed flow were measured and compared with measurements made when the plates were exposed to a turbulent flow.

The effect of the perturbation on the vortex shedding from each of three bluff cylinders was examined. The bluff cylinders used were a circular cylinder, a flat plate and a D-section. The vortex shedding was found to lock-in to the perturbation such that the vortex shedding frequency was exactly half of the perturbation frequency. The range of lock-in was found to increase with increasing perturbation amplitude. The base pressure was reduced with lock-in. The mean and fluctuating pressure distributions around the surface of the circular cylinder were measured for both steady and perturbed flows.

A detailed examination of the turbulent wake of the circular cylinder was made. The underlying mean wake was reconstructed using a conditional sampling technique similar to that used by Davies (1976). Measurements of the strength and spacing of the vortices in the wake of the cylinder were made. The results were compared with a viscous vortex model of the wake. With lock-in the vortex strength was found to increase and the lateral separation of the vortices to decrease.

Approximate numerical solutions to the unsteady flow around a

rectangular obstacle were obtained using a distributed array processor. At low Reynolds numbers a closed wake was found to form behind the obstacle. At higher Reynolds numbers regular vortex shedding was found. An attempt was made to obtain solutions to the unsteady flow around the obstacle when the oncoming flow had a superimposed sinusoidal perturbation.

Apart from Chapter 4 which was done in collaboration with Mr. M.J. Drabble of Heriot-Watt University, I declare that the work presented in this thesis was done by myself.

Brian J Armstrong

ACKNOWLEDGEMENTS

I have to thank Dr. Francis Barnes whose patient and thoughtful supervision during the course of this work was tremendously helpful. I would also like to thank Dr. Ian Grant for providing much of the funding required for new experimental equipment.

I am grateful to Peter McInnes, the Computing Officer of the Physics Department, for installing and maintaining the PDP11/23 PLUS Microcomputer.

I should also thank Tom Montgomery for his advice on the design of experimental apparatus, and for machining many of the required parts. Thanks are also extended to the technicians of the workshops of the Physics Department and also to the technicians of the workshop in the Engineering Department of Heriot-Watt University.

I acknowledge that during the course of this work I was supported by an S.E.R.C. grant. Thanks are also extended to Professor Roger Cowley for the hospitality and use of the facilities of the Physics Department.

Finally, I would like to thank Mrs. Ray Chester for the speed and the accuracy with which she typed this thesis.

CHAPTER 1

INTRODUCTION

Fluid motion has long been of interest as evidenced by an extensive history of scientific studies on the subject. Many of the studies have been concerned with the nature of the flow around obstacles. In particular, the field of wind engineering has become increasingly important with the design and construction of increasingly longer bridges and taller buildings. The design of such slender structures requires a detailed and accurate knowledge of the wind forces that are likely to be experienced by the structure at its intended location. The need for such knowledge provides justification for attempting to gain a better understanding of the fundamental nature of the flow around bodies.

When exposed to a wind, bodies experience both steady and unsteady forces. The unsteady forces acting on a body may be divided into two categories. The first comprises those fluctuating forces acting on the body which may be directly related to the fluctuations of the velocity of the incoming flow. These forces normally arise from the fluctuating pressure on the upstream face of the body. The second of the categories comprises those fluctuating forces which are not directly related to the velocity fluctuations of the incoming flow, but arise from the unsteadiness of the wake behind the body. These forces arise mainly from the fluctuating pressure on the surface of the afterbody of the obstacle.

Experimental studies are normally made in the laboratory using a wind tunnel where the conditions of the flow around the body are

most easily controlled. To gain a more fundamental understanding of the nature of the flow around bodies the structural shape of the body used in wind tunnel experiments is usually very simple. At all but the lowest Reynolds numbers the flow around many bodies separates from the body over a large part of the body surface and these bodies are classified as being bluff. Associated with the separated flow are free shear layers in which there is a high concentration of vorticity. This vorticity is generated in the boundary layer on the surface of the obstacle. For two-dimensional bluff bodies two such shear layers are produced, one containing positive vorticity and the other containing negative vorticity. The mutual interaction of these free shear layers leads to the formation of local concentrations of vorticity in the wake of the body. These concentrations form an array of two staggered rows of oppositely signed vortices known as a vortex street.

The vortices are formed close to the rear of the body and are then said to be "shed" into the wake. The details of the process of anti-symmetric vortex formation are dependent on the shape of the afterbody of the bluff body. A physical description of the process of vortex shedding has been given by Gerrard (1966). Diagram 1.1 indicates the filament line pattern behind a circular cylinder, at one particular instant of the vortex shedding cycle, of Gerrard's vortex-formation model. As the vortex continues to grow fed by circulation from, in this case, the upper shear layer, it then becomes strong enough to draw the opposite shear layer across the wake. The arrows indicate some of the entrainment flows that take place. Path a) represents the largest of the three flows,

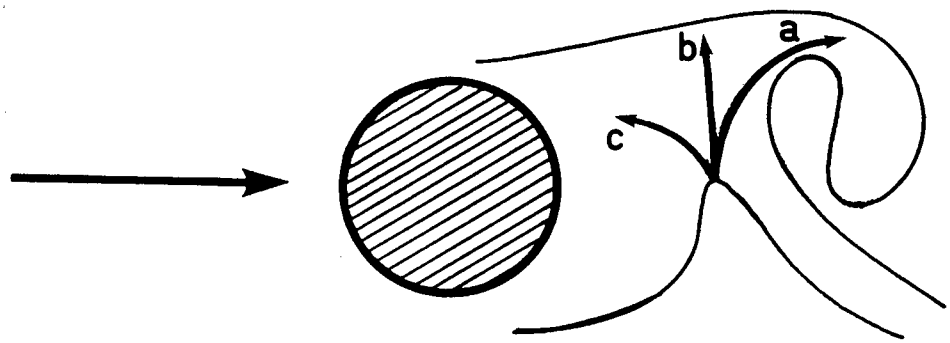

Diagram 1·1 The vortex formation model.

and as some of the fluid following this path contains vorticity of opposite sign to the growing vortex, there will be some cancellation of vorticity. Once the opposite shear layer has been drawn far enough across the wake, the supply of circulation to the growing vortex will be cut off, and the vortex is then said to be shed.

The process of vortex shedding has been observed over an enormous range of Reynolds numbers. At above a Reynolds number of about 40 a circular cylinder sheds vortices into its wake. In the laboratory this process has been observed to be maintained up to Reynolds numbers of about 10^6, but at some Reynolds numbers in this range, the vortex shedding is not very regular [Berger and Wille (1972)]. Several naturally occurring phenomena have shown the formation of vortices in bluff body wakes at much higher Reynolds numbers than are attainable in the laboratory with an incompressible fluid. For example, vortices were generated in the ocean current past a grounded oil tanker near Nantucket Island [Berger and Wille]. The vortices were made visible by oil leaking from the tanker, and the Reynolds number was estimated at 10^7. At the even higher Reynolds numbers of about 10^{11}, a pattern of vortices has been observed in satellite pictures of the cloud pattern downstream of the island of Guadalupe, off California [Berger and Wille].

Our knowledge of the interaction of the wake of a bluff body with oscillations of the body is incomplete. In an attempt to gain a better understanding of vortex induced structural vibration, many experiments have been carried out to investigate the effects of forced vibration on the mechanism of vortex shedding. If, for example, the body is vibrated transverse to the flow direction at a frequency close to the vortex shedding frequency, then the vortex shedding

may lock-in with the body vibration, such that vortices are shed at exactly the same frequency as the body vibration over a range of the free-stream velocity. Also, if the body is vibrated in-line with the flow direction at a frequency close to twice the vortex shedding frequency then lock-in may occur with the vortices being shed at exactly half of the body vibration frequency. In both cases of lock-in significant changes occur in the wake of the body. These changes may be observed in the values of the base pressure, the correlation length of the vortex shedding, the mean drag, the fluctuating lift and the spacings of the vortices in the wake of the body. Excellent reviews of the work concerned with the flow behaviour associated with oscillating bluff bodies have been written by Bearman (1984) and by Sarpkaya (1979).

The mechanism of vortex shedding may also be disturbed by perturbing the flow as well as by oscillating the body. For example, the effect of a transveresly oscillating flow was investigated by Pocha (1971) on the flow around a square-section cylinder. Also, some studies have been made where the flow oscillations were in-line with the mean flow [Chen and Ballengee (1971), and Hatfield and Morkovin (1973], but none appear to have been made where the occurrence of lock-in might have been possible.

Parallel to the experimental studies, a number of numerical studies have been made of the flow around bluff bodies. Many of the experimentally observed characteristics of the wakes of bluff bodies have been reproduced in the approximate solutions to the time-dependent governing flow equations. Most of the numerical work has been concerned with the two-dimensional flow around bluff bodies where the oncoming flow is steady and uniform. However, Clements (1975) has numerically modelled the flow around a blunt-based obstacle where the

oncoming mean flow had a superimposed oscillatory perturbation. Lock-in was found when the frequency of perturbation was close to twice, and close to four times, the frequency of vortex shedding.

The purpose of this thesis is to report on investigations of the effects on the flow around a bluff body of adding an oscillatory perturbation of single frequency to a constant mean flow. In Chapter 4, the relationship between the forces acting on square flat plates placed normal to the flow direction, and the flow, are investigated. Chapters 5 and 6 are concerned with the effects of the perturbation on the flow around a cylinder. A numerical study of the unsteady flow around a rectangular obstacle is described in Chapter 7, where an attempt is made to obtain approximate solutions for the unsteady flow when the oncoming mean flow has a superimposed sinusoidal perturbation.

Throughout this thesis the following terminology is used to describe the flow approaching the body:

steady flow	-	the approaching flow is uniform and has a constant velocity,
turbulent flow	-	the approaching flow is highly turbulent, the turbulence having been generated by a turbulence grid at the entrance to the working section of the tunnel,
oscillatory flow or perturbed flow	-	the approaching flow is unitorm with a mean velocity component and a superimposed oscillatory perturbation.

CHAPTER 2

EXPERIMENTAL APPARATUS

Two distinct investigations were carried out in the wind tunnel of the Physics Department of the University of Edinburgh.

The first investigation concerned the measurement of the aerodynamic forces acting on square flat plates placed normal to the flow direction. The forces were measured for three different flows; steady flow, turbulent flow, and oscillatory flow.

The second investigation was of the effects of an oscillatory flow on the vortex shedding from each of three bluff cylinders. The cylinders were a circular cylinder, a D-section and a flat plate. The flow over the circular cylinder was investigated further by examining the effect of the oscillatory flow on the turbulent wake of the cylinder.

The descriptions of the experimental arrangements for both investigations are given in this chapter.

(a) The Wind Tunnel

The wind tunnel is a closed-return low turbulence wind tunnel. Figure 2.1 shows the outline of the tunnel and the control room.

The working section is 3m long and is built on a 1.2m × 1.2m square frame. There is a gradual expansion of the working section to allow for the boundary layer growth on the walls of the working section, so that there is no pressure gradient along the working section. Perspex corner fillets are positioned in the working section which make its cross section octagonal and with a mean

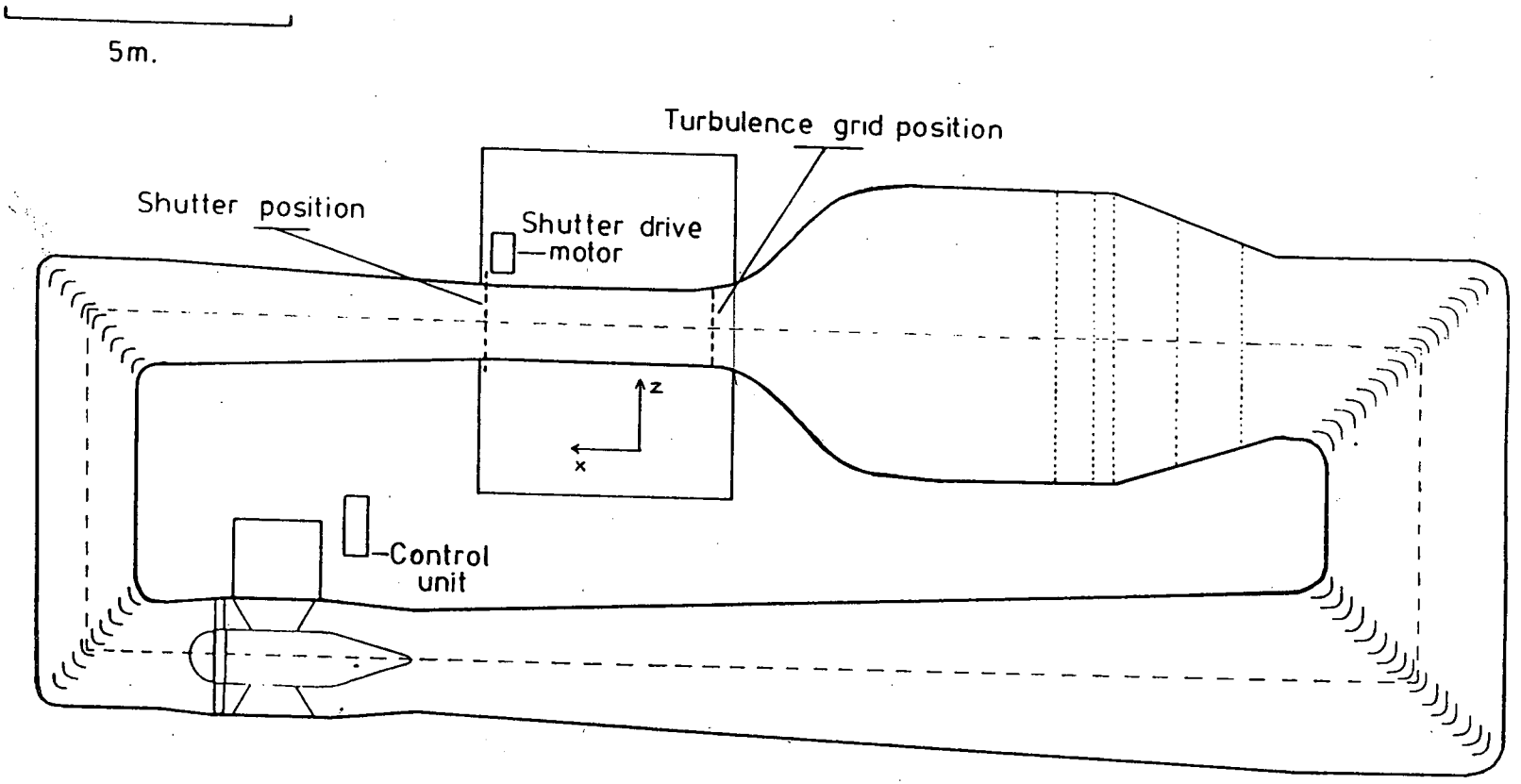

Figure 2·1. The layout of the wind tunnel.

cross-sectional area of $1.21m^2$. The perspex fillets are flexible, allowing fine adjustment of the mean pressure gradient. The section before the corner leading into the settling section has breather holes open to the atmosphere which ensure that the pressure in that section remains at atmospheric pressure when a flow is present in the tunnel. For a given flow, the flow velocity in the working section is much higher than the velocity in this "open" section and thus the pressure in the working section is lower than atmospheric pressure. The control room is therefore sealed from the atmosphere.

The settling section contains smoothing screens made of 38 mesh 36 swg phosphor-bronze wire having a blockage ratio of 0.506. The area ratio of the settling section to the working section is 15:1. At speeds of less than 10 ms^{-1} the free-stream turbulence level in the working section is less than 0.02%. [Barnes (1966)].

The wind tunnel fan has a diameter of 1.91m with 4 blades fixed to a 0.91m diameter spinner. An aluminium hemisphere of a diameter of 0.91m is fixed to the spinner immediately in front of the blades. Immediately behind the fan are seven straightner vanes, four of which are adjustable and three of which are fixed and cover the frame supporting the fan. The fan is driven by a 60 hp DC motor, situated outside the tunnel, via 3 rubber belts running along side one of the fan supports, inside a fixed straightner vane. The motor speed is controlled by a thyristor-diode three phase rectifier. When a wind speed is selected using the setting potentiometer the response timer provides an output which steadily increases towards the reference voltage on the

setting potentiometer. The response timer output ensures that the motor is smoothly accelerated up to the desired speed. The control amplifier gains the response timer output and feeds this signal to the firing unit, which controls the conduction period of the thyristors. A tachogenerator attached to the motor drive produces a voltage proportional to the speed of the motor. This voltage is fed back to the second stage of the control amplifier which differences the tachogenerator output and the reference voltage, thus reducing increases in motor speed as the motor approaches the correct speed. A current feedback loop to the second stage of the control amplifier prevents the control amplifier from cutting the current to the fan motor completely and also acts to stabilise the fan speed.

The control mechanism allows the very accurate maintenance of a stable and constant flow velocity in the working section. The manufacturers of the fan-motor controller quote the accuracy in the maintenance of the fan speed as 0.1% of the full speed. The tunnel has a maximum speed of 42 ms^{-1}. The velocity range used for the investigation of the vortex shedding from the bluff cylinders was 2.5 ms^{-1} to 4.5 ms^{-1}. The manufacturers' quotation would imply that at the lowest velocity in this range the mean velocity could be maintained to within $\pm 1.7\%$. In the investigation, however, it was found that the velocity could be controlled to within $\pm 1\%$ at the lowest velocity in the range and to within $\pm 0.7\%$ at the most commonly used velocity of 3.19 ms^{-1}. This error is, however, associated with the inaccuracy of the measurement of the velocity and not with any fluctuation of the mean velocity. In other words any fluctuation in the mean wind speed was less than the error associated with the measurement of the mean wind speed.

(b) The Shutter Mechanism

The flow perturbation was produced by a set of four shutters which were situated at the downstream end of the working section. The shutters comprised four pairs of rectangular mild steel plates which fitted into slots cut into four mild steel rods. The rods were positioned symmetrically about the centre line of the working section and set equal distances apart. The rods extended through the breather holes in the working section walls and were held in ball races at their ends. The ball races were fitted inside self-centering bearings which were attached to metal plates fixed to the control room wall. Rubber was inserted between the metal plates and the control room walls to reduce the transmission of vibrations. The four rods were provided with additional support at their centres by four ball races set into a vertical slender mild steel bar at the centre line of the working section. This bar also extended outside the working section walls and was fixed to supports extending from the control room wall. Thus, none of the shutter mechanism was in direct contact with the tunnel's working section.

The shutters were rotated in phase by a 1.5Kw variable DC motor using a belt drive system. The toothed belts were manufactured by Synchromesh and were made of nylon with flexible steel reinforcement. With no flow in the working section the shutter system ran smoothly with little vibration. The motor was controlled by a Shackleton System Drive Controller which operated in a fashion similar to the wind tunnel fan controller. The rotational frequency was measured by using a Hall-effect switch which detected the passing of a bar magnet attached to one of the rods. The period of 10 pulses produced

by the Hall-effect switch was measured using a Racal Dana 9902 Universal Counter Timer. Since the periodic blockage presented to the working section repeats itself for every half rotation of the rods, the frequency of the flow perturbation is exactly twice the frequency of rotation of the rods. A similar mechanism for producing a perturbation on the mean flow has been used previously by Morkovin, Loehrke and Fejer (1971) and by Miller and Fejer (1964).

The frequency of the perturbation produced by this mechanism was in the range of 0 - 20 Hz. The amplitude of the perturbation was found to depend on both the frequency of rotation and the mean velocity in the working section. At a constant frequency of rotation and constant mean velocity, the amplitude of the perturbation could be varied by using shutters of different widths. The four shutter widths were 0.19m, 0.21m, 0.23m and 0.24m. The four shutter sets will be denoted by shutters A, B, C and D respectively. The shutter sizes were chosen to give a reasonable range of perturbation amplitudes whilst at the same time allowing for the smooth running of the shutter mechanism.

(c) The Piezoelectric Balance

Most of the previous direct measurements of the forces acting on bluff bodies in an air flow have been made using strain-gauge balances. For example, Bearman (1969) used such a balance to measure the forces acting on square flat plates placed normal to the flow direction. The forces acting on the plates in a steady flow and in

a turbulent flow were measured. The flow velocities used in his investigation were up to 20 ms^{-1}. The purpose of the experiment described in Chapter 4 was to extend Bearman's investigation to the measurement of the fluctuating forces acting on square flat plates in an oscillatory flow. With the largest of the shutter sets used, the maximum mean velocity at which the shutter mechanism ran smoothly was 5 ms^{-1}. One would, therefore, expect that the value of the mean drag force acting on a plate of the same size as used by Bearman, would be approximately sixteen times less than that measured by Bearman. At such low flow velocities one would also expect that the magnitude of the fluctuating forces acting on the plate would be much less than those of Bearman's investigation. The experiment described in Chapter 4, therefore, required a very sensitive balance in order to make the measurements. For a given set of strain gauges a strain gauge balance only offers higher sensitivity at the expense of the natural frequency of the balance. However, the lowest natural frequency of the balance and attached plate, places a restriction on the frequency range over which the fluctuating forces may be measured and so a reduction in the natural frequency of the balance is to be avoided if at all possible.

A piezoelectric crystal produces a charge proportional to the stress placed on the crystal. It is very rigid and hence has a high natural frequency whilst also being very sensitive to the stress applied. Both the sensitivity and the natural frequency of the Kistler Instruments six component piezoelectric balance Type 9421 All were considered high enough to allow the possibility of measuring the forces acting on the flat plates in the oscillatory

flow. The balance itself has a natural frequency of around 1KHz.

The six component balance was mounted on a concrete block which rested on four rubber pads on the floor of the control room under the working section. An active cylinder was fixed to the balance top plate and extended into the working section. A sting was attached to the active cylinder and the sting and active cylinder were then protected from the flow by a shroud. The arrangement of the balance, the active cylinder, the sting and the shroud section is shown in Figure 2.2. The shroud section was nowhere in contact with the sting or the active cylinder. A flat plate was attached to the sting and some preliminary measurements were made. In this arrangement, however, the balance picked up too much noise through the rubber pads between the concrete block and the control room floor. Therefore a vibration-isolation mechanism similar to those used to isolate optical benches was installed. This system was used to support a large heavy metal plate to which a concrete block was firmly fixed. The balance frame was grouted into this new block and the experiment was set up in the same manner as used in the previous attempt. The signal to noise ratio was greatly improved when compared to that for the first arrangement. However, when the flow was oscillated the output signal from the balance contained too much noise. When the active cylinder and balance top, whose combined weight was 43.4 Kg, were removed, leaving only the measuring crystals, virtually no mechanical noise was picked up under the same conditions of oscillatory flow. The noise in the system was thus attributed to the very small oscillations of the balance top and active section relative to the concrete block. Owing to the

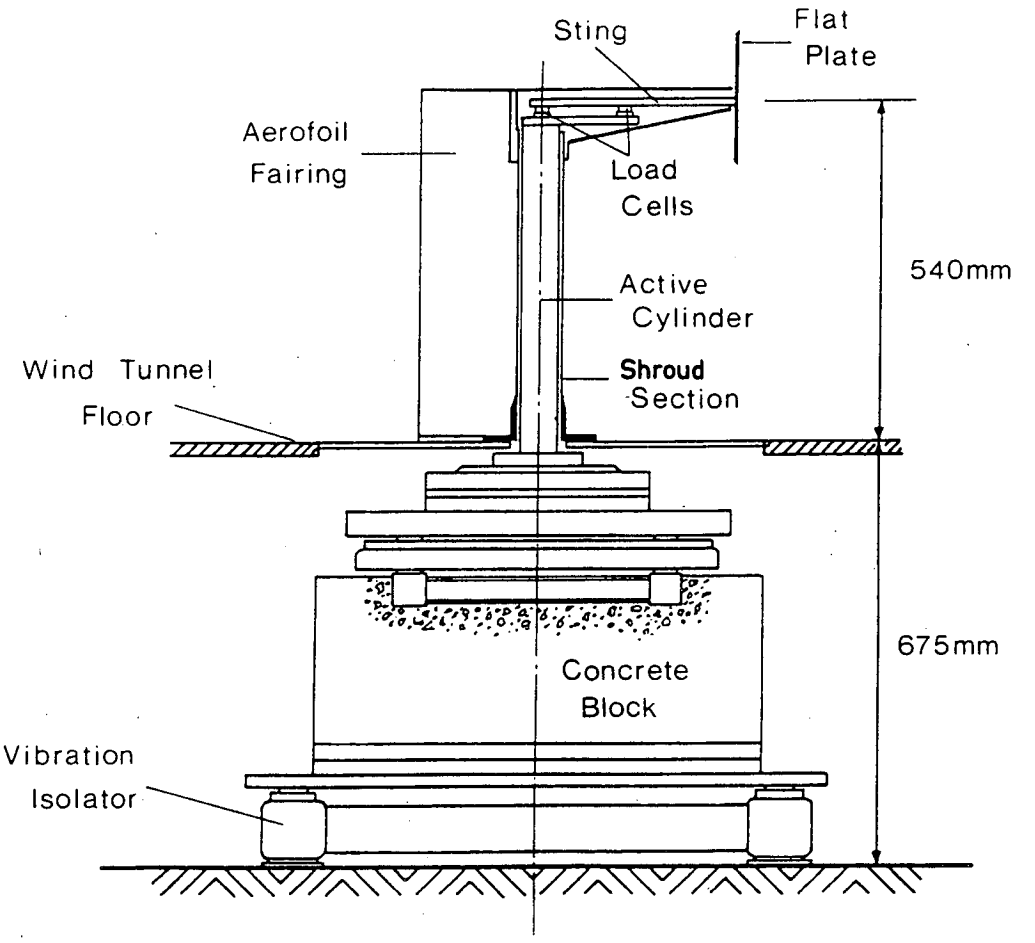

Figure 2·2. The piezoelectric balance arrangement.

large combined mass of the active cylinder and the balance top, these oscillations gave rise to measurable forces at the piezoelectric crystals. Therefore, it is desirable to have as small a mass as possible attached to the crystals so that the noise produced by a relative motion of the attached mass to the crystal's support, is kept to a minimum.

The reduction in the mass attached to the crystals was achieved by using two Kistler piezoelectric crystals (type 9251A) fixed 13 cm apart on a base plate which in turn was fixed to the top of the active cylinder. The crystals were used to support the sting to which the flat plates were fixed. With the 20 × 20 cm plate fixed to the end of the sting the mass attached to the crystals was 0.33 Kg. This arrangement can be seen in Figure 2.2. The active cylinder is, of course, nowhere in direct contact with the shroud or the working section. The cables connected to the crystals were fixed to the underside of the base plate, thus preventing forces acting on the crystals due to the vibration of the cables. The sting was shrouded from the flow by styrofoam. This styorfoam shroud was designed to give only a small clearance from the sting, and also to minimise its interference with the wake of the plate. The sting was 32 cm long and tapered from a width of 30 mm at the crystal nearest the plate, to 17 mm at the plate. The sting had sections milled out in order to reduce its mass without lowering its natural frequency to any great extent. The lowest natural frequency of the sting with the 20 cm × 20 cm plate attached was about 400 Hz, but the active cylinder had a natural frequency of about 90 Hz with the sting and plate attached. The frequency range of the measurements was therefore limited. In

the arrangement of Figure 2.2 the piezoelectric balance showed very high sensitivity to forces applied in the direction of the drag with excellent linearity and with a very good signal to noise ratio. The balance was very insensitive to forces applied in the y or z directions. The calibration procedure is described in Chapter 4.

(d) The Flat Plates

The purpose of the investigation of the forces acting on a flat plate placed normal to the flow direction was to relate the fluctuating forces acting on the plate to the upstream velocity fluctuations. A square shape was chosen because the vortex shedding from a plate of that shape is incoherent. Coherent vortex shedding had to be avoided because it produces forces which bear either little or no relation to the fluctuating velocities upstream of the plate. The choice of the sizes of the plates was governed by many factors. For a given flow velocity the magnitude of the drag force depends on the area of the plate. The reduced frequency parameter, $\frac{n\ell}{\overline{U}}$, where n is the frequency of the fluctuating force, ℓ is the length of side of the plate and $\overline{U}$ is the free-stream mean velocity, should be as high as possible as the most interesting results are expected at values of reduced frequency greater than 0.1. This factor requires the plate size to be as large as possible. However, the blockage of the plate in the tunnel working section must not be too large, and the ratio of the plate size to the distance of the plate from the active cylinder must not be too small. The plate sides were chosen to be 0.10m, 0.15m, 0.20m and 0.30m in length.

The sides of the plates were bevelled at 45° to ensure that separation took place as close as possible to the upstream edge of the plates. The plates were fixed firmly to the sting by 3 countersunk stainless steel screws. A small piece of smooth PVC tape was placed over the fixing screws to present to the flow as flat a surface as possible. The plate was 1.40m upstream of the shutters and 2.70m downstream of the turbulence grid.

(e) The Turbulent Grids

Many workers have used a square mesh grid to generate a highly turbulent flow field. At distances of more than 10 mesh lengths from the grid the turbulent flow field is closely homogeneous and isotropic. In this case, such a grid was used to generate a highly turbulent flow so that the relationship between the forces acting on a square plate, and the turbulent velocity fluctuations could be investigated. Three grids were constructed of wooden slats and were of biplanar design. They were made in two halves to allow them to be taken in and out of the tunnel via the working section access doors. The grids fitted tightly against the tunnel walls and it was, therefore, not necessary to screw them to the walls. The approximate position of a grid when placed in the working section can be seen in Figure 1.1. The grids will be referred to as grid A, B and C respectively. Grid A was constructed of 19mm × 19mm wooden slats spaced 120mm apart, grid B was constructed of 38mm × 19mm wooden slats spaced 182mm apart, and grid C was constructed of 76mm × 19mm wooden slats spaced 271mm apart.

(f) The Bluff Bodies

The main aim of the investigation of the flow around the bluff bodies was to examine the effect of the perturbation in oscillatory flow on the flow around the body. To investigate the lock-in regime the flow perturbation frequency must be near to twice the natural frequency of vortex shedding. Therefore, the criterion for the size of a bluff body was that, for flow velocities greater than 2 ms^{-1}, the frequency of vortex shedding should be less than half of the maximum perturbation frequency produced by the shutters. It was decided that the minimum flow velocity should be 2 ms^{-1} as below that velocity the errors in measuring the velocity with a pitot tube were unacceptably high. The highest perturbation frequency of large amplitude and low harmonic content was around 12 Hz. At flow velocities of around 3 ms^{-1} the size of a circular cylinder that sheds vortices at around 6 Hz is about 0.1m. A cylinder of this size has a blockage of approximately 10% of the working section cross sectional area. Whilst a 10% blockage was a little high it was none the less a reasonable compromise given the other criteria that had to be met, i.e. $\overline{U} \gtrsim 2ms^{-1}$, $n \sim 6$ Hz.

The flow over each of three bluff cylinders was investigated in both a steady flow and a perturbed flow. The cylinders were a circular cylinder, a D-section and a flat plate. Each cylinder was 1.1m long and was fitted with 0.5m diameter circular end plates. The circumferences of each end plate was bevelled at 45°. The design of the end plates was somewhat arbitrary. Therefore, for the circular cylinder, two other pairs of end plates were made, having diameters of 0.3m and 0.4m, so that an investigation of

the effect of the size of the end plates on the flow around the cylinder could be made. These effects are discussed in Chapter 5.

The circular cylinder was machined from an aluminium tube to a diameter of 101mm. The finish was smooth but not polished. The cylinder was tapped at 0.5D intervals along its length, with 0.75mm diameter holes. Each tapping was fitted with a small hypodermic needle such that the needle was not quite flush with the outer surface of the cylinder. The needles were sealed into the holes with plasticine to prevent any flow through the clearance between the needles and the tapping holes. The needles were connected to a Combist Instruments micromanometer using plastic tubing. The tubes were run out of the cylinder through holes in one of the end plates. The tubes fitted tightly in the end-plate holes and thus prevented any flow between the inside of the cylinder and the external flow. The D-section was tapped in a similar manner. However, the flat plate base pressures were measured using a long hypodermic needle attached to a plastic tube of 4mm outside diameter, which ran along the centre line of the rear face of the plate. The base pressure measurements of the flat plate showed good agreement with the base pressure measurements taken with a slender pitot tube aligned with the flow direction, and with the total head tapping placed at the centre line of the rear of the plate.

The flat plate was machined from aluminium with the long sides bevelled at 45°. The wider surface faced upstream and was 101mm in width. The thickness of the bar was 12mm.

The D-section comprised a semi-circle of PVC tubing and a flat aluminium plate. The semi-circle of PVC was obtained from a circular PVC tube of a diameter of 111mm by cutting the tube down a diameter along its length. The aluminium face plate of 111mm × 1.1mm was strengthened by a 12mm × 25mm mild steel bar which ran along the length of the inside of the D-section, on the centre line of the aluminium face plate.

Circular rods of diameter 25mm and 45mm in length were fixed to the centre of each end plate. Circular brackets, each having a hole of 25mm diameter, were fitted over these rods. The cylinder was positioned in the working section, 2.5m upstream of the shutter position, near the centre of the working section. The brackets were fixed to the walls of the working section and a small grub screw in each bracket prevented a rotational movement of the cylinder. For the circular cylinder a small rod was connected to the end plate rod through the tunnel wall. A steel bar was fixed to this rod and acted as a pointer which moves over a protractor fixed to the tunnel wall. The circular cylinder could be rotated in the working section and its angular position could be measured to ± 0.5°.

Approximately half way along the circular cylinder's length a 1.75mm hole was drilled. A 1.75mm outside diameter plastic tube was glued into this hole with the end of the tube just flush with the outer surface of the cylinder. The other end of this tube was fixed into a phosphor-bronze connector which was fitted to a Druck pressure Transducer. The internal diameter of the tube was 0.75mm and the total length of the tube between the transducer and the outer surface

of the cylinder was 2cm. The transducer was used to measure the fluctuating pressure at the surface of the cylinder in both steady and oscillatory flow. The calibration of the transducer is described in Chapter 5.

(g) Instrumentation

A pitot-static tube connected to a Combist Instruments micromanometer was used to measure the mean free-stream velocity. This pitot tube was positioned at the entrance to the working section. Mean and fluctuating velocities were measured by using Disa hot-wire probes (M55). The hot-wires were operated in a constant temperature mode by Disa 55 M01 bridges. The output signals of the bridges were fed through Disa 55D26 signal conditioners. DC voltages were measured using a Schlumberger Solartron A223 Digital Voltmeter. Fluctuating voltages were usually recorded on a 14 channel FM tape deck (EMI SE3000) for later analysis, but in some cases were transmitted to a PDP11/23 PLUS microcomputer where they were digitised directly using an AD01 A/D converter. The AD01 has programmable gains of 1, 2, 4 or 8 and has 8 differential input channels. The digitiser was accurate to $\pm \frac{1}{2}$ bit in 12 bits, at any gain, and could digitise at frequencies up to 10 KHz.

The PDP 11 was used to perform most of the data reduction. It ran under RSX 11M, a multi-user, multi-tasking, time-sharing operating system. It had a floating point processor with 0.5 Mbyte of Random Access Memory and two 10 Mbyte hard discs, one of which was used entirely for data storage purposes. An IEQ11/IEEE Bus Controller was installed which allowed computer control of any IEEE

device connected to the system. Two Hewlett-Packard HP-IB/IEEE Bus Extenders were used to communicate between the wind tunnel control room and the PDP 11.

A Bentham Instruments SMD 3B/IEEE stepping motor controller was connected to the IEEE bus. The controller drove the stepping motor according to instructions it received from the IEEE bus. The stepping motor linear traverse (Bentham Instruments T300X(250)) was used to traverse the hot-wire in steps of 5 μm. The stepping motor and linear traverser were mounted on a 6" diameter rotary turntable and the whole assembly of the hot-wire, the hot-wire support, the linear track and the stepping motor could be rotated in a vertical plane accurate to 0.1°. The rotary turntable and its support rested on the floor of the control room, on 3 levelling screws. The support and rotary table were heavy and transmitted very little vibration to the hot-wire. The probe support was nowhere in direct contact with the wind tunnel walls. The rotary mechanism was used for the calibration of the cross-wires and this calibration procedure is described in Chapter 3.

The PDP 11 was used for digitisation of the data and for data reduction. Data reduction included the Fourier analysis of the data, the computation of correlation coefficients and coherence functions, and performing least squares fits to calibration data. These methods are described in Chapter 3. The results of these analyses were communicated, via the Physics Department Vax 11/750, to either an ICL 2972 or ICL 2988 mainframe computer. The University mainframes and the Filestore system allowed storage of large amounts of data. Various plotter facilities and line printer outputs were available on the ICL machines.

An interactive graphics program which was written in IMP was used to draw the figures presented in this thesis. It has facilities for curve fitting and spline fitting of data. The program was made available to other members of the Fluid Dynamics group.

CHAPTER 3

METHODS OF DATA REDUCTION AND ACQUISITION

In this chapter the methods of experimental data reduction and acquisition are described. The following topics are discussed briefly in this chapter.

a) The Fourier Transform

b) Spectral Analysis

c) The Correlation functions

d) The Coherence function

e) Statistical Accuracy

f) The U-wire Calibration

g) The Cross-Wire Calibration

h) The Temperature Correction of Hot-Wire Data.

All the methods of data reduction presented in this chapter were implemented as programs or commands on the PDP 11, and were written in Fortran. The programs were written as to be of general use to other members of the Fluid Dynamics group.

(a) The Fourier Transform

The definition of a Fourier transform $H(f)$, of a continuous series, $h(t)$, is given by

$$H(f) = \int_{-\infty}^{\infty} h(t)\, e^{-i2\pi ft}\, dt \qquad (3.1)$$

which exists only when $\int_{-\infty}^{\infty} |h(t)|dt < \infty$ (3.2)

[Bracewell (1978)]

The inverse transform is given by

$$h(t) = \int_{-\infty}^{\infty} H(f)\, e^{i2\pi ft}\, df \quad . \tag{3.3}$$

Other definitions of the Fourier transform and its inverse are in common use but differ from (3.1) and (3.3) by constant factors only. The definition of the discrete Fourier transform pair is

$$H(n) = \frac{1}{N} \sum_{k=0}^{N-1} h(k)\, e^{\frac{-i2\pi nk}{N}} \tag{3.4}$$

and

$$h(k) = \sum_{n=0}^{N-1} H(n)\, e^{\frac{i2\pi nk}{N}} \tag{3.5}$$

where $H(n)$ represents the value of $H(f)$ at $f = \frac{n}{NT}$ and $h(k)$ represents the value of $h(t)$ at $t = kT$, where T is the sampling interval at which the values of $h(t)$ are known, and N is the number of samples taken. Other definitions of the discrete Fourier transform and its inverse exist but differ from (3.4) and (3.5) by constant factors only. There is no loss of information about $h(t)$, according to the sampling theorem, if $h(t)$ contains no frequencies above the Nyquist frequency, f_c, when $T \leq \frac{1}{2f_c}$ [Bracewell]. The transforms of (3.4) and (3.5) require that both $H(n)$ and $h(k)$ be periodic with period NT.

If two discrete series $x(k)$ and $y(k)$ are both real and are both to be Fourier transformed, the transforms may be performed simultaneously by constructing a complex series $z(k) = x(k) + iy(k)$.

By the linearity theorem [Brigham (1974)]

$$Z(n) = X(n) + iY(n)$$

$$= [X_r(n) + iX_i(n)] + i[Y_r(n) + iY_i(n)]$$

$$= [X_r(n) - Y_i(n)] + i[X_i(n) + Y_r(n)]$$

$$= A(n) + iB(n) \qquad (3.6)$$

where X, Y, Z, are the discrete Fourier transforms of x, y, and z respectively and subscripts r and i denote the real and imaginary parts. A(n) and B(n) are entirely real, whereas X(n) and Y(n) are complex.

If N samples of each series are known then

$$Z(n) = \frac{Z(n)}{2} + \frac{Z(n)}{2}$$

$$= [\frac{Z(n)}{2} + \frac{Z(-n)}{2}] + [\frac{Z(n)}{2} - \frac{Z(-n)}{2}]$$

$$= Z_e(n) + Z_o(n) \qquad (3.7)$$

where the subscripts e and o represent even part and odd part respectively. Noting that Z(n) = Z(N-n) as Z(n) has period N

$$Z(n) = [A(n) + A(-n)]/2 + [A(n) - A(-n)]/2$$

$$+ i[B(n) + B(-n)]/2 + i[B(n) - B(-n)]/2$$

$$= [A(n) + A(N-n)]/2 + [A(n) - A(N-n)]/2$$

$$+ i[B(n) + B(N-n)]/2 + i[B(n) - B(N-n)]/2$$

$$= A_e(n) + A_o(n) + iB_e(n) + iB_o(n) \; . \qquad (3.8)$$

But $X(n) = A_e(n) + iB_o(n)$

and $Y(n) = B_e(n) - iA_o(n)$ from the properties of

Fourier transforms [Brigham].

Thus

$$X_r(n) = [A(n) + A(N-n)]/2$$

$$X_i(n) = [B(n) - B(N-n)]/2$$

$$Y_r(n) = [B(n) + B(N-n)]/2$$

$$Y_i(n) = -[A(n) - A(N-n)]/2 \qquad (3.9)$$

Thus by using one Fourier transform, 2 real series may be transformed simultaneously provided that (3.9) is used to unpack the results. This method was used in the programs which ran on the PDP 11 and which required the Fourier transformation of data. A library set up in a Directory on the PDP 11 system disc contains a standard complex Fast Fourier Transform routine called FFTXIY, along with routines to unpack the results.

(b) Spectral Analysis

The power spectral density of a continuous series $x(t)$ is defined as

$$S(f) = |X(f)|^2 \qquad (3.10)$$

where $X(f)$ is the Fourier transform of $x(t)$.

For a discrete series the power spectral density estimate at $f = \frac{n}{NT}$ is given by

$$\hat{S}_{XX}(n) = X(n)X^*(n) \qquad (3.11)$$

where $X^*(n)$ is the complex conjugate of $X(n)$. Similarly, the cross-spectral density estimate at $f = \frac{n}{NT}$, of two discrete time series $x(k)$ and $y(k)$ is given by

$$\hat{S}_{XY}(n) = X(n)\bar{Y}^*(n) \quad . \tag{3.12}$$

$\hat{S}(n)$ is related to the actual power spectral density $S(n)$ by

$$S(n) = NT\,\hat{S}(n) \quad . \tag{3.13}$$

Taking eq. (3.10),

$$S(f) = X(f)X^*(f)$$

$$= \int_{-\infty}^{\infty} e^{-i2\pi ft}\, x(t)\, dt \int_{-\infty}^{\infty} x(s)\, e^{+i2\pi fs}\, ds$$

$$= \int_{-\infty}^{\infty}\int_{-\infty}^{\infty} e^{-i2\pi f(t-s)}\, x(t)x(s)\, dt\, ds.$$

Substituting $t - S = \tau$ this may be re-written as

$$S(f) = \int_{-\infty}^{\infty}\int_{-\infty}^{\infty} x(t+\tau)x(t)e^{-i2\pi f\tau}\, dt\, d\tau. \tag{3.14}$$

and since $R(\tau) = \int_{-\infty}^{\infty} x(t)x(t+\tau)dt$ where $R(\tau)$ is the auto-correlation function then

$$S(f) = \int_{-\infty}^{\infty} R(\tau)\, e^{-i2\pi f\tau}\, d\tau \, .$$

The auto-correlation function and the power spectral density function are a Fourier transform pair.

Therefore,

$$R(\tau) = \int_{-\infty}^{\infty} S(f) e^{i2\pi f\tau}\, df$$

$$\text{and} \quad R(0) = \int_{-\infty}^{\infty} S(f)\, df. \tag{3.15}$$

$R(0) = \int_{\infty}^{\infty} x(t)x(t)dt$, which is the variance in the signal. This relationship was used to check the power spectral density estimates computed using a program implemented as a command called FFT, on the PDP 11.

The data was pre-whitened before computing the power spectral density estimates by the removal of the mean and linear drift from the data and by tapering the data at the edges of each record of N points with a Bingham window. The taper is given by d(n) where

$$\begin{aligned} d(n) &= \tfrac{1}{2}\left(1 - \cos \frac{10\pi n}{N}\right) \quad \text{for} \quad 0 \leq n \leq \frac{N}{10} \\ &\qquad\qquad \text{and} \quad \frac{9N}{10} \leq n \leq N \\ &= 1 \qquad\qquad \text{for} \quad \frac{N}{10} < n < \frac{9N}{10}\,. \end{aligned} \tag{3.16}$$

This taper improves the boxcar spectral window by reducing the "leakage". Leakage arises from the truncation of the time domain by taking only N samples from an infinite series. The truncation of the time domain is equivalent to multiplying the infinite series by the boxcar function. The transformed data is thus convolved with the transform of the boxcar function, which is a sinc function. The sinc function has large side lobes which "leak" power and spread power between the spectral estimates of the spectrum. The Fourier transform of the Bingham window has much smaller side lobes, which reduces leakage at the expense of a slight reduction

in the resolution or bandwidth of the power spectrum [Newland (1975)].

(c) The Correlation Functions

The normalised discrete circular cross-correlation function may be computed as

$$R_{XY}(m) = \frac{\sum_{k=0}^{N-1} x(k)y(k+m)}{\sqrt{var(x)\ var(y)}} \qquad (3.17)$$

where $var(x) = \langle x^2 - \langle x \rangle^2 \rangle$, where $\langle x \rangle$ denotes the average or mean value of x, and there is a similar expression for $var(y)$, and where x and y are periodic over N terms such that $y(k+m) = y(k+m-N)$ for values of $k+m$ greater than N. The circular auto-correlation function is obtained from (3.17) by substituting x for y. The circular auto-correlation and cross-correlation functions may also be obtained from the power spectral density functions by a Fourier transformation. Great savings in computational time are possible by using FFT methods to compute the correlation functions rather than using a direct application of (3.17). The normalised discrete cross-correlation function may be computed as

$$\hat{R}_{XY}(m) = \frac{\sum_{k=0}^{N-1-m} x(k)\,y(k+m)}{\sqrt{var(x)\ var(y)}} \qquad (3.18)$$

$\hat{R}_{XY}(m)$ is biased as only $N-m$ terms are used in the summation. This function may also be computed using FFT's by the following method [Brigham].

First, N zeros are added to each series such that

$$\begin{aligned} x(k) &= 0 \quad ; \quad k = 0, 1, \ldots N-1 \\ x(k) &= x(N-k); \quad k = N, \ldots 2N-1 \\ y(k) &= y(k) \quad ; \quad k = 0, 1, \ldots N-1 \\ \text{and} \quad y(k) &= 0 \quad ; \quad k = N, \ldots 2N-1. \end{aligned} \tag{3.19}$$

The transforms of the new series $x(k)$ and $y(k)$ are computed simultaneously using the method described in section (a). The product

$W(m) = X(m)\, Y^*(m)$ is computed and finally

the inverse transform is found using the forward transform

$$\hat{R}(m) = \left(\sum_{k=0}^{2N-1} (2N \cdot W^*(m))\, e^{\frac{-i2\pi mk}{2N}} \right)^* \tag{3.20}$$

The origin of $\hat{R}(m)$ is then shifted to $m = N$ to compensate for the shifting of $x(k)$ in (3.18). If the series $x(k)$ and $y(k)$ are samples of an infinite series then these finite series may be thought of as the corresponding infinite series multiplied by the boxcar function. The boxcar function is also correlated when computing $\hat{R}(m)$ and thus biases the estimates of $\hat{R}(m)$. The function may be unbiased by using

$$R(m) = \frac{N}{N-m} \hat{R}(m) \quad \text{for} \quad 0 \leq m \leq N-1 \, . \tag{3.21}$$

The error in the estimate of the correlation function increases with increasing m as only $N-m$ terms are used to obtain $\hat{R}(m)$. To avoid large errors at large values of m, the program only printed out the first $\frac{N}{2}$ values of $\hat{R}(m)$. If required the unbiasing operation of (3.21) may not be performed giving the true finite correlation function.

The above method may be used to calculate the auto-correlation function by simply replacing y with x throughout. The forward transform was used in equation (3.20) to compute the inverse Fourier transform, thereby avoiding the necessity of writing an inverse FFT routine. The program which used this method to compute the correlation functions was implemented on the PDP 11 as a command called COR and was used to compute the length scales of the turbulence behind the turbulence grids. Correlation coefficients defined only at $\tau = 0$ were computed directly from the digitised data to save writing the data to the disc. By not writing the data to the disc very large amounts of data could be used to compute, for example, the correlation coefficients at $\tau = 0$ with ease, as large amounts of data storage space were not required.

(d) The Coherence Function

The discrete coherence function is defined as $\gamma^2_{XY}(n)$ where

$$\gamma^2_{XY}(n) = \frac{|S_{XY}(n)|^2}{S_{XX}(n)\ S_{YY}(n)} \qquad (3.22)$$

$\gamma^2_{XY}(n)$ must lie between 0, and 1. This function is useful as it indicates the degree of correlation between $x(k)$ and $y(k)$. A value of 1 indicates perfect correlation. When the value is less than 1 there are a number of possible causes. The signals may contain noise, the relationship between $x(k)$ and $y(k)$ may be non-linear, or $y(k)$ may depend on other variables in addition to $x(k)$. The phase difference between $x(k)$ and $y(k)$ at a frequency $f = \frac{n}{NT}$, is defined by

$$\theta(n) = \tan^{-1}\left[\frac{\text{im } S_{XY}(n)}{\text{Re } S_{XY}(n)}\right] \qquad (3.23)$$

where im and Re denote imaginary part and real part, respectively.

The value of $\theta(n)$ is only significant when $\gamma^2_{XY}(n)$ has a value of at least 0.2. A program has been written and implemented as a command called COH on the PDP 11 to compute the coherence function from data of $x(k)$ and $y(k)$. The program was used to compute the phase differences between signals of force and velocity or the phase difference between velocities at two measuring stations.

(e) Statistical Accuracy

Using an FFT method to analyse signals to obtain power spectral density estimates is equivalent to measuring the variance of a band passed signal for each frequency band Δn from the frequency of OH_z to f_c. It can be shown that for band passed filtration of a Gaussian random variable $x(t)$ the standard error ε is given by

$$\varepsilon_r = \frac{\text{s.d.}[S_{XX}(n)]}{S_{XX}(n)} \simeq \frac{1}{\sqrt{Be\ T_D}} \qquad (3.24)$$

[Bendat and Piersol (1966)]

where s.d. is the standard deviation, Be is the resolution bandwith of the FFT analysis and T_D is the total time over which data is available. The Fourier coefficients can be shown to be uncorrelated random variables with zero mean. If the Fourier coefficients are a and b then

$$S_{XX}(n) = a^2 + b^2 .$$

$S_{XX}(n)$ has a chi-square distribution with 2 degrees of freedom. The standard error is given by

$$\varepsilon_r = \left(\frac{2}{n_f}\right)^{\frac{1}{2}} \qquad \text{[Bendat and Piersol]} \qquad (3.26)$$

where n_f is the number of degrees of freedom. For one raw spectral estimate the standard error is equal to the raw estimate itself. The spectral estimates are, therefore, very inaccurate and unstable. If several records are taken, say r records, and an ensemble average is made over these records, then each spectral estimate has $2r$ degrees of freedom, thus reducing the standard error to

$$\varepsilon_r = \left(\frac{1}{r}\right)^{\frac{1}{2}} . \qquad (3.27)$$

This error may be further reduced by averaging over adjacent spectral estimates, say m points, thus giving each estimate $2mr$ degrees of freedom and the standard error is given by

$$\varepsilon_r = \left(\frac{1}{mr}\right)^{\frac{1}{2}} \qquad (3.28)$$

However the effective resolution is reduced by a factor of m, when m adjacent spectral estimates are averaged.

If peaks are to be accurately located in the spectrum then no adjacent point averaging was used and (3.27) applies. For the estimation of the spectra of the velocity fluctuations in turbulent flow adjacent point averaging was used, in addition to averaging over several records. These spectra were plotted on a log-log plot and were smoothed by taking m adjacent points for the estimate at the lowest frequency and then $(m+p)$ estimates for each pth consecutive plotted spectral estimate. This is purely a means by

which crowding of the points at higher frequencies on the log-log plot is avoided. As a consequence the estimates become progressively more accurate with increasing frequency.

For a continuous spectrum $S_{XX}(f)$ where the location of a sharp peak is required, it must be noted that the spectral estimate at the peak has a large bias error given by

$$S_{XX}(f) \simeq S_{XX}(f) + \frac{B_e^2 S''_{XX}(f)}{24} \quad . \qquad (3.29)$$

[Bendat & Piersol]

A description of the bias error is given in Bendat and Piersol.

At a peak $S''_{XX}(f)$ will, obviously, be very large. Normally, however, only the frequency at which the peak occurs is of interest when analysing "peaky" spectra.

The normalised standard error for circular correlation estimates is given by

$$\varepsilon_r = \frac{1}{\sqrt{B_e T_D}} \qquad \text{[Bendat \& Piersol]} \qquad (3.30)$$

For ordinary correlation estimates computed using (3.18) the error depends on the lag value. The error becomes larger as the lag increases and for the mth lag value of $\hat{R}(m)$ the error is given by

$$\varepsilon_r = \sqrt{\frac{1}{\frac{m-1}{B_e T_D}}} \quad . \qquad (3.31)$$

The cross spectral density function $S_{XY}(f)$ is a complex quantity and may be written as

$$S_{XY}(f) = C_{XY}(f) - iQ_{XY}(f) \qquad (3.32)$$

where $C_{XY}(f)$ is the co-spectral density

and $Q_{XY}(f)$ is the quad spectral density.

The coherence function estimate is given by

$$\gamma^2_{XY}(f) = \frac{|S_{XY}(f)|}{S_{XX}(f)\ S_{XY}(f)} \tag{3.33}$$

and the phase difference between $x(t)$ and $y(t)$ is given by

$$\theta_{XY}(f) = \tan^{-1}\left[\frac{Q_{XY}(f)}{C_{XY}(f)}\right] . \tag{3.34}$$

The bias errors for the estimates of $C_{XY}(f)$ and $Q_{XY}(f)$ are given by

$$\begin{aligned} \text{bias error } \{C_{XY}(f)\} &\simeq \frac{B_e^2\ Q''_{XY}(f)}{24} \\ \text{bias error } \{Q_{XY}(f)\} &\simeq \frac{B_e^2\ Q''_{XY}(f)}{24} \end{aligned} \tag{3.35}$$

For a peaky spectrum the bias errors will be high near a spectral peak. The confidence limits on the phase angle estimate, $\theta_{XY}(f)$, are given by

$$\sin\varepsilon = \left[\frac{\{1 - \gamma_{XY}(f)\}\{(1-p)^{-2/n} - 1\}}{\gamma_{XY}(f)}\right]^{\frac{1}{2}} \tag{3.36}$$

where $n = 2B_eT_D$ and p = prob. $\left|\dfrac{\hat{H}(f) - H(f)}{H(f)}\right| < \sin\varepsilon$ (3.37)

and $\left|\hat{\theta}_{XY}(f) - \theta_{XY}(f)\right| < \varepsilon$ (3.38)

[Bendat & Piersol]

where $\hat{H}(f) = \dfrac{\hat{S}_{XY}(f)}{\hat{S}_{XX}(f)}$; $\hat{H}(f)$ denotes the true value of $H(f)$.

For a coherence of 0.95 and a 99.5% confidence, 50 records give 100 degrees of freedom, giving $\sin\varepsilon = 0.07$ and consequently a phase error of $\pm 4.4^{\circ}$. This gives an error of $\pm$ 1.2% on the calculation of vortex convection speeds with $\pm$99.5% confidence. The vortex convection speed measurements are presented in Chapter 6.

(f) The U-wire Calibration

Throughout the investigations presented in this thesis the hot-wires were used in a constant temperature mode.

Problems arise in hot-wire calibrations due to the non-linear response of the wires to the velocities in the flow. The calibration is sensitive to temperature fluctuations and dust contamination. The wires are also subject to aero-elastic vibrations induced by the passing fluid and the possible vibrations of the probe supports. The bridges used to drive the hot-wires must be carefully adjusted to obtain the best response from the wires. Recently Perry (1982) has suggested the use of a dynamical shaker as a means of subjecting the hot-wire to a known velocity fluctuation at low frequencies. Using this method no assumptions involving cooling laws are made. Unfortunately such a mechanism was not available during the course of these experiments and so calibrations using a power law or cubic fit were used. These calibrations were performed carefully by carrying out a series of calibrations fitting the same calibration data to different laws and using extra points not included in the calibration data to check the fitted calibration curve. The usual power law was used whereby

$$E^2 = A + BU^n \tag{3.39}$$

where E is the output voltage, U is the known flow velocity and A and B are fitted by a least squares method. The value of n was varied by small amounts to investigate how the goodness of fit varied with n. Three values of n, 0.40, 0.45, and 0.50, were tried and the results of the calibration can be seen in Fig. 3.1. The

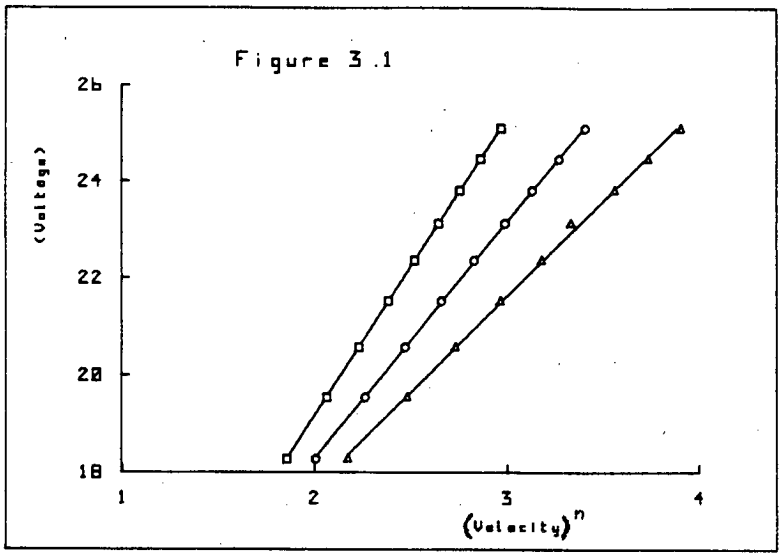

Figure 3.1. The hot-wire calibration data fitted to King's Law with various values of the exponent, n.
□ *n = 0.40 ;* ○ *n = 0.45 ;* △ *n = 0.50.*

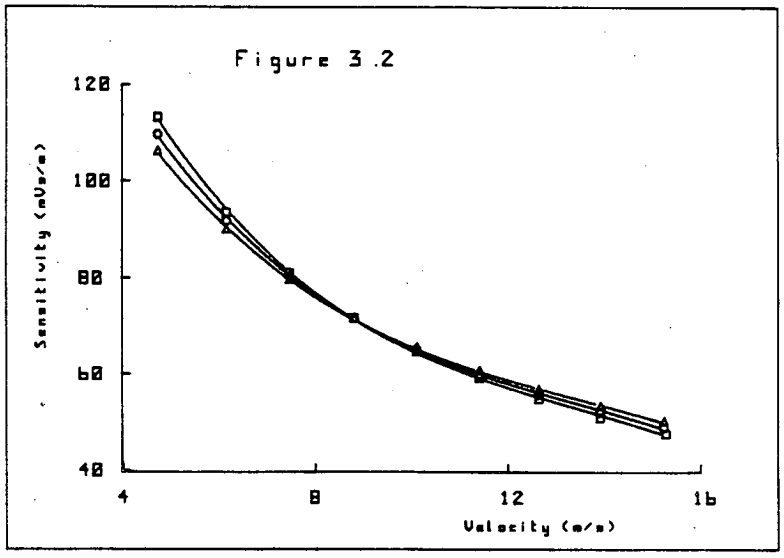

Figure 3.2. The sensitivity of the hot-wire to velocity fluctuations, computed from the calibrations of figure 3.1.
□ *n = 0.40 ;* ○ *n = 0.45 ;* △ *n = 0.50.*

corresponding sensitivity curves were calculating using

$$S = \frac{\partial E}{\partial U} = \frac{nB(\bar{U})^{n-1}}{2\bar{E}} \tag{3.40}$$

where $\bar{E}$ and $\bar{U}$ are the mean values of E and U respectively, and these are presented in Figure 3.2. The corresponding sensitivity curve computed from the cubic fit calibration followed, very closely, the sensitivity curve for the $n = 0.40$ power law calibration and is, therefore, not presented for the purposes of clarity.

As can be seen in Fig. 3.1 the data fits all three values of n, well. Using the extra points as checks the $n = 0.40$ power law was found more accurate for the whole velocity range. All values of n showed very close agreement over the central one third portion of the calibration range. This can be seen in Fig. 3.2, where all the sensitivities computed from the power law fits are in agreement at the central part of the calibration range and diverge towards the ends of the range. The worst disagreement found for each of the calibration sets is given in Table 3.1. The power law $n = 0.40$ is seen to be the best power law and the cubic fit appears to be the best fit overall. The cubic fit agrees well with the $n = 0.40$ calibration over the range of velocities investigated.

During these experiments a cubic fit to the calibration data was used most frequently but for some of the experiments a power law was used, when accuracy was not vital, as the power law fits were more easily obtained than the cubic fit. The range of velocities to be investigated were always within the central one third of the range of calibration velocities. If a wide range of velocities was

to be studied, then the calibration was divided into subranges, which overlapped. Computer software was used to select the appropriate calibration. In these experiments, however, the range of velocities was often small so that only one calibration was necessary.

(g) The Cross-Wire Calibration

The cooling velocity for a wire inclined to the flow may be written as

$$V^e(t) = |U(t)|f(\theta) \tag{3.41}$$

where $U(t)$ is the instantaneous flow velocity and $f(\theta)$ is the yaw function for the instantaneous yaw angle $\theta(t)$ between the normal of the wire and the flow direction. Figure 3.3 shows the coordinate system used to describe the cross-wires.

$$\begin{aligned} V_1^e(t) &= |U(t)|\ f(\alpha_1 + \psi) \\ V_2^e(t) &= |U(t)|\ f(\alpha_2 - \psi) \end{aligned} \tag{3.42}$$

where the V^e terms represent the effective cooling velocity.

Normally $f(\theta)$ is represented by

$$f(\theta) = \begin{cases} \cos^m \theta \\ (\cos^2\theta + k^2\sin\theta)^{\frac{1}{2}} & \text{[Perry]} \end{cases}$$

and in this analysis it is assumed that $f(\theta) = \cos^m\theta$, where $m = 1$. It is also assumed that $\alpha_1 = \alpha_2$. These assumptions are commonly used [Perry].

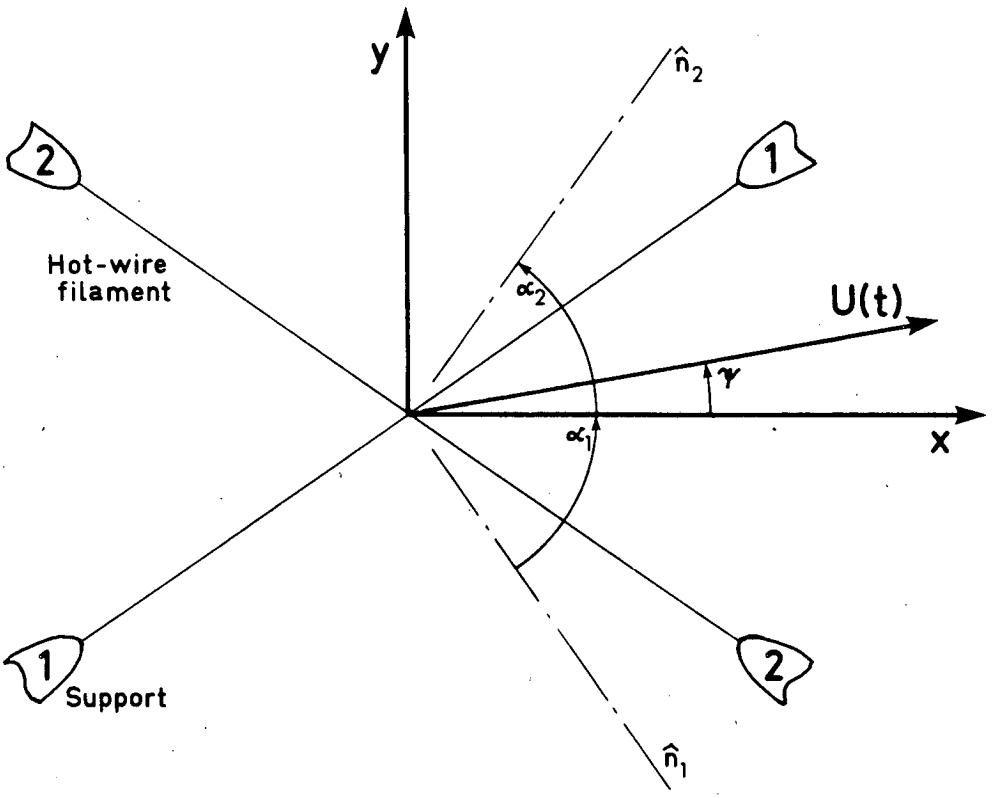

Figure 3·3. A diagram of the cross-wires.

TABLE 3.1 *Worst errors found for various hot-wire calibrations.*

Power law	n=0.40	n=0.45	n=0.50	Cubic
Calibration Point	0.24%	0.52%	0.77%	0.13%
Extra Point	0.21%	0.64%	3.4%	0.23%

$$V_1^e(t) = |U(t)|\cos(\alpha + \psi) = |U(t)|(\cos\alpha\cos\psi - \sin\alpha\sin\psi)$$

$$V_2^e(t) = |U(t)|\cos(\alpha - \psi) = |U(t)|(\cos\alpha\cos\psi + \sin\alpha\sin\psi) \qquad (3.43)$$

$$u(t) = |U(t)|\cos\psi$$

$$v(t) = |U(t)|\sin\psi$$

thus $$V_1^e(t) = \cos\alpha \cdot u(t) - \sin\alpha \cdot v(t)$$

$$V_2^e(t) = \cos\alpha \cdot u(t) + \sin\alpha \cdot v(t)$$

which reduces to

$$u(t) = \frac{V_1^e(t) + V_2^e(t)}{2\cos\alpha}$$

$$\text{and} \quad v(t) = \frac{V_2^e(t) - V_1^e(t)}{2\sin\alpha} \qquad (3.44)$$

Cross-wires are normally constructed with $\alpha = 45°$.

Suppose now that the wires are aligned to the x-axis and that the normal of wire 1 is at an angle of α_1 and that the normal of wire 2 is at an angle α_2 to the x direction. If, for wire 1, the voltage is measured at a constant flow velocity at this position and we label this voltage E_{R1}, we may write, assuming King's Law,

$$E_{R1}^2 = A_1 + B_1|U|^n(\cos^n \alpha_1) \; . \qquad (3.45)$$

Now suppose that the whole assembly is yawed through an angle ψ so that the normal of wire 1 is at an angle $(\alpha_1 + \psi)$ to the flow and the normal of wire 2 is at an angle of $(\alpha_2 - \psi)$ to the flow. Then

$$E_1^2 = A_1 + B_1|U|^n(\cos(\alpha_1 + \psi))^n$$

$$E_2^2 = A_2 + B_2|U|^n(\cos(\alpha_2 - \psi))^n \; .$$

$$\text{Thus} \qquad (E_1^2 - A_1)^{1/n} = (B_1)^{1/n}|U|\cos(\alpha_1 + \psi)$$

$$(E_{RI}^2 - A_1)^{1/n} = (B_1)^{1/n}|U|\cos\alpha_1 \qquad (3.46)$$

$$\text{and} \qquad \left[\frac{(E_1^2 - A_1)}{(E_{RI}^2 - A_1)}\right]^{1/n} = \frac{\cos\alpha_1 \cos\psi - \sin\alpha_1 \sin\psi}{\cos\alpha_1}$$

$$= \cos\psi - \tan\alpha_1 \sin\psi \ .$$

$$\text{Thus} \qquad W_1 = \tan\alpha_1 \sin\psi$$

$$\text{where} \qquad W_1 = -\left[\frac{(E_1^2 - A_1)}{(E_{RI}^2 - A_1)}\right]^{1/n} + \cos\psi. \qquad (3.47)$$

$$\text{Similarly} \qquad W_2 = \tan\alpha_2 \sin\psi$$

$$\text{where} \qquad W_2 = \left[\frac{(E_2^2 - A_2)}{(E_{R2}^2 - A_2)}\right]^{1/n} - \cos\psi. \qquad (3.48)$$

The problem remains, however, as to how to align the cross-wires such that the mean flow direction is exactly at ± 45° to each wire. The following procedure was adopted for aligning cross-wires to the flow.

1. The cross-wires were positioned in the wind tunnel on the stepping motor traverse. The traverse was mounted on a rotating turntable which could yaw the cross-wires accurate to 0.1°. The wires were calibrated in this position.

2. The wires were yawed through successive angles at a constant flow velocity, and readings of the voltages were taken at each yaw angle.

3. A plot was made of the data from the hot-wires using eqs. (3.47) and (3.48) where the W parameters were plotted against $\sin\psi$. The gradient of this plot is $\tan\alpha$, where α is the angle of the normal of the wire to the flow.

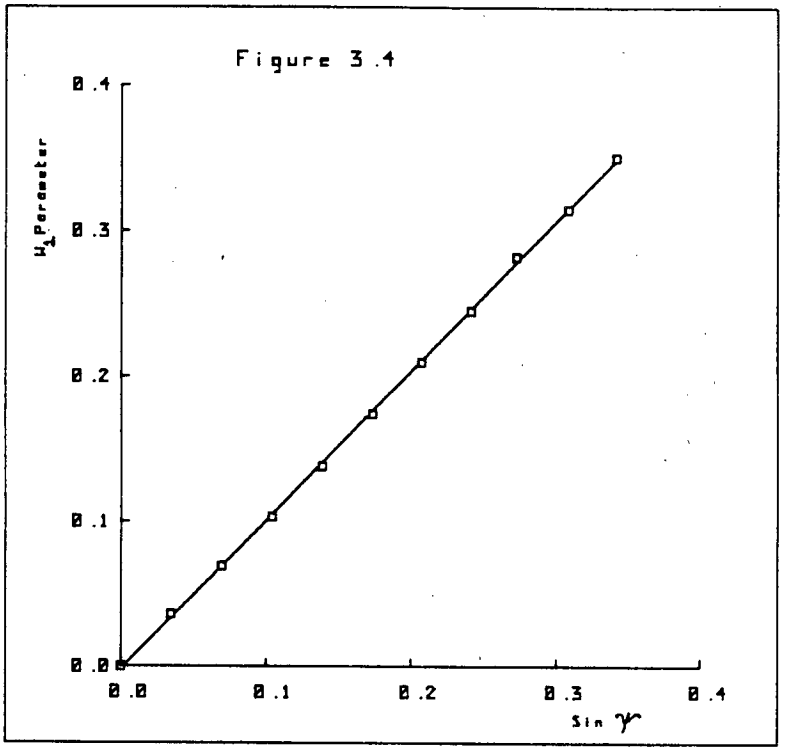

Figure 3.4. The W_1 parameter plotted against yaw angle for one of the hot-wires of a cross-wire pair.

4. The wires were then yawed through a correction angle from original calibration position and recalibrated at the new yaw angle. This new yaw angle was such that each wire was as close as possible to $\pm 45°$ to the flow direction.

A plot of W_1 against $\sin \psi$ for wire 1 can be seen in Fig.3.4. The tangent of this line gives $\alpha_1 = 45.4°$. The corresponding angle for the other wire was found to be $\alpha_2 = 44.0°$. The wires, in this case, were yawed through an angle of $0.3°$ so that the new α angles were $\alpha_1 = 45.7°$ and $\alpha_2 = 44.3°$. In the reduction of the cross-wire data, it was assumed that $\alpha_1 = \alpha_2 = 45°$. In most cases, the errors in the estimates of the magnitude of the u and v velocity components, determined from cross-wire measurements was less than 1% of $\overline{U}$.

(h) Temperature Correction of Hot Wire Data

Temperature variations in the flow have a serious effect on the calculation of velocity, if they are not taken into account. For example, when the turbulence grids were used in the tunnel, the ambient temperature rose about 2°C during a 10-15 minute run. This temperature dropped quickly when the run was completed and so the temperature never stabilised when the grids were being used. This required that compensation for temperature drift from the calibration temperature, be made. The uncorrected mean velocities may be up to $\pm$ 2% inaccurate for a temperature drift of $\pm 2°C$. If E_c is the corrected voltage and E_o is the measured voltage, then

$$E_c = E_o + \left.\frac{\partial E}{\partial \theta}\right|_U \Delta\theta \tag{3.49}$$

and $$S_c = S_o + \left.\frac{\partial S}{\partial \theta}\right|_U \Delta\theta \tag{3.50}$$

where S_c and S_o are the corrected and uncorrected sensitivities respectively and $\Delta\theta$ is the temperature difference from the calibration temperature, θ. Using a power law with $n = 0.45$ for a straight wire

$$\frac{1}{E}\left.\frac{\partial E}{\partial \theta}\right|_U = \frac{-C}{2\mu(R-1)} \qquad \text{[Perry]} \tag{3.51}$$

where $R = 1.8$ the overheat ratio

$C = -3.5 \times 10^{-3}\ K^{-1}$ for platinum wire

$\mu = 1 + C\theta$

and $$\frac{1}{S}\left.\frac{\partial S}{\partial \theta}\right|_U = \frac{-C}{\mu(R-1)} \; . \tag{3.52}$$

An approximation is used in that $C\theta$ is usually very small and thus $\mu \approx 1$ and

$$E_c = E_o\left(1 - \frac{C}{2(R-1)}\Delta\theta\right) \; . \tag{3.53}$$

For U-wires the voltages were corrected using (3.53) before converting into velocities and thus the correct sensitivity was used in computing the fluctuating velocities. For the cross-wires the output voltages were first corrected for the effect of temperature drift before the velocities were computed using the power law calibration.

It is interesting to note that the temperature drift was less than $\pm$ 1°C over several hours when the shutters were being operated

or when steady flow was used in the working section. In oscillatory flow the perturbation is small yet the flow behind the shutters must be highly turbulent. The production of turbulent energy behind the shutters must nevertheless be much less than that produced by the turbulence grids and, therefore, much less heat is produced in the dissipation of the turbulent energy. In oscillatory flow the value of $\overline{U}$ is much lower than the value of $\overline{U}$ used in turbulent flow and this may partly account for the lower rate of production of turbulent energy.

CHAPTER 4

FORCES ON FLAT PLATES

Introduction

It has long been realised that in the design of tall or slender structures some account must be taken of both the steady and unsteady wind loads acting on the structure. Traditionally structures were designed to withstand the highest mean wind speed recorded at or near the site of the structure. A more statistical approach was adopted when structures were designed to withstand a mean wind speed equal to the maximum instantaneous wind speed that was likely to occur only once in a specified period of time, say the design lifetime of the structure. Also, attempts were made to include the unsteadiness of the wind by estimating gust factors from which the additional transient forces could be estimated. Tall or slender structures may flex appreciably in response to the action of the unsteady wind loading which could cause damage to the structure if the response is large. Therefore, for flexible structures, the extreme response is the most important design criterion. The response may be estimated using a statistical approach based on the spectrum of the fluctuations of the forces acting on the structure. If the structure's response is assumed to be linearly related to the forces acting on the structure, then the response spectrum may be computed from the force spectrum by the use of the mechanical admittance function, the mechanical admittance function being the transfer function relating the response spectrum to the force

spectrum. If, in addition, the relationship is known between the velocity spectrum of the wind fluctuations and the resulting force spectrum acting on the structure in this wind, then the response spectrum may be computed from whatever wind spectrum may occur at the site of the structure. The extreme response of the structure may then be estimated from the response spectrum.

In order to investigate the relationship between the velocity fluctuations in a flow and the resulting force fluctuations, Wardlaw and Davenport (1964) measured the forces acting on flat plates in a turbulent wind. The spectrum of the fluctuating force acting on the plate and the spectrum of the velocity fluctuations in the wind were measured. The force spectrum was related to the velocity spectrum by a transfer function which Davenport called the aerodynamic admittance. Vickery (1965) made measurements of the aerodynamic admittance of various bluff bodies and proposed an empirical form of the admittance function which best fitted the measured admittances. Bearman (1969) carried out a very careful investigation of the forces acting on square flat plates in a turbulent wind and found that Vickery's empirical admittance function fitted his results reasonably well.

In turbulent flow the aerodynamic admittance has a value of near unity at low values of $n\ell/\overline{U}$, where n is the frequency of the fluctuation of the force or the velocity, ℓ is a typical dimension of the body and $\overline{U}$ is the mean wind speed. The admittance drops off rapidly at values of $n\ell/\overline{U} > 0.1$. A brief discussion of the form of the admittance in a turbulent flow is given in section (g). In a mean flow with a small oscillatory perturbation, where the flow velocity is invariant in space the admittance is expected to rise rapidly for $n\ell/\overline{U} > 0.1$. Davenport (1961) made measurements of the forces acting on two-dimensional bluff bodies which were oscillated in a steady water current.

If the fluid is incompressible, this is equivalent to a stationary body in a uniform flow with an oscillatory perturbation. He presented measurements of the fluctuating drag coefficient and the added mass coefficient at various values of $n\ell/\overline{U}$, but did not present the admittance values which could have been calculated from these results.

The purpose of this investigation was to measure the forces acting on square flat plates in an oscillatory flow. The forces acting on the plates in a turbulent flow field were first measured to allow a comparison with the results obtained previously by other workers. Some preliminary measurements of the turbulent and oscillatory flow fields are presented in sections (a) and (b) respectively. The unsteady force measurements in a turbulent flow are present in section (e), and in an oscillatory flow in section (f).

Throughout this chapter, the perturbation frequency is denoted by n and $n\ell/\overline{U}$ is referred to as the reduced frequency. Also the plates used in the investigation are referred to as the 10 × 10, 15 × 15, 20 × 20 and 30 × 30 plate, thereby omitting the units of cm.

(a) Preliminary Measurements in Turbulent Flow

The flow behind each of the grids A, B and C were examined in turn. The grids are described in Chapter 2, section (e).

At the plate position, 2.7m downstream of the grid position, the mean velocity and the rms intensity of the fluctuating velocity

were measured, using a U-wire probe. The voltage output of the wire was digitised and converted into velocity records using the methods described in Chapter 3, section (f). The mean velocity and the rms of the velocity fluctuations were computed from the velocity records. Measurements were made at 0.1m intervals, both vertically and across the working section from - 0.4m to +0.4m about the centre line of the working section. The mean velocity was found constant to within ±1%, ±2% and ±4% for grids A, B and C respectively. The rms intensity of the velocity fluctuations was found constant to within ± 2%, ±2% and ±4% for grids A, B and C respectively.

At various positions downstream of the grid position, along the wind tunnel centre line at the height of the sting, measurements were made of the scale, intensity and the u, v and w velocity spectra of the turbulent flow produced by each grid. The measurements of the spectra and the intensity were made using a cross-wire probe. The voltage outputs of the cross-wires were digitised and the digital voltage records were converted into velocity records using the method described in Chapter 3, section (g). The measurements of the scale of the turbulence were made using a U-wire and a Hewlett-Packard digital correlator, model (3721A). The longitudinal length scale of the turbulence was estimated as the area under the auto-correlation of the fluctuating u component. Figure 4.1 shows the u, v and w spectra of grid A at a distance of 3.76m downstream of the grid. The v and w component spectra can be seen to contain slightly less energy than the u component spectrum, and this result is in accord with those of other workers [Bearman (1972)]. The total energy contained in the v and w component

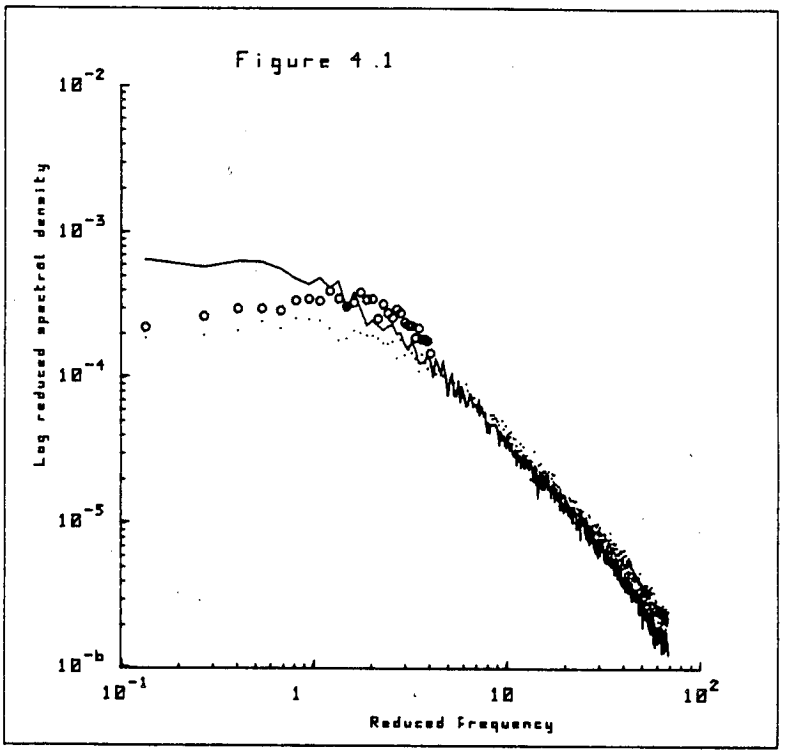

Figure 4.1. The spectra of the u, v, and w components of velocity fluctuations 3.76m downstream of grid A at $\bar{U}$ =7.2m/s.
—— u spectrum; · v spectrum; ○ w spectrum.

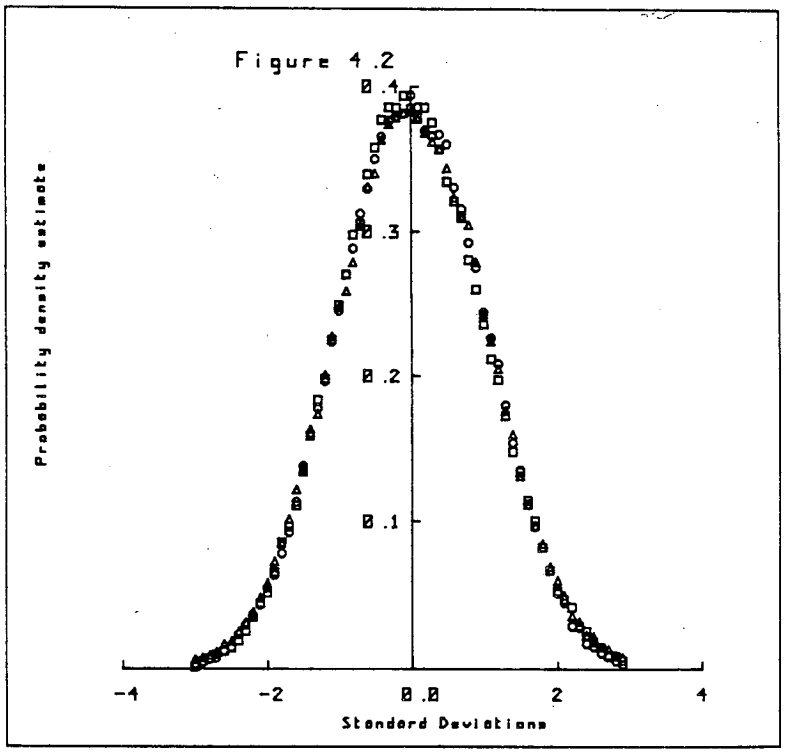

Figure 4.2. Probability density functions of the u, v, and w velocity component fluctuations 3.76m downstream of grid A at $\bar{U}$ =7.2m/s.
□ u component ; ○ v component ; △ w component.

fluctuations was generally about 20% less than the total energy in the u component fluctuations of the turbulent flow field behind each of the grids. The probability density function (pdf) for each of the u, v and w components can be seen in Figure 4.2. The functions were computed from digital records of the u, v and w components of velocity. 100K points were used to calculate each pdf. The mean and standard deviation of the velocity records were first computed and then data points were sorted according to their deviation from the mean. The pdf's show good collapse and are closely Gaussian as is expected for a turbulent flow [Batchelor (1953)].

The von-Kármán spectrum of the u component of the turbulence behind each grid at the plate position is shown in Figure 4.3, plotted as

$$\frac{S(n)\bar{U}}{2\pi L_X \overline{u^2}} = \hat{\theta}_u \quad \text{against} \quad \frac{2\pi n L_X}{\bar{U}} = \hat{n} \tag{4.1}$$

where each of the symbols used is defined in the list of symbols table. The spectra show good collapse into the theoretical von-Kármán spectrum, which has the form

$$\theta_u = (\frac{2}{\pi})[1 + 1.8\hat{n}^2]^{-5/6} \tag{4.2}$$

Due to the action of viscous dissipation the energy content of turbulence decays with time. For the initial period of decay of homogeneous turbulence, Batchelor (1953) has proposed the following relation

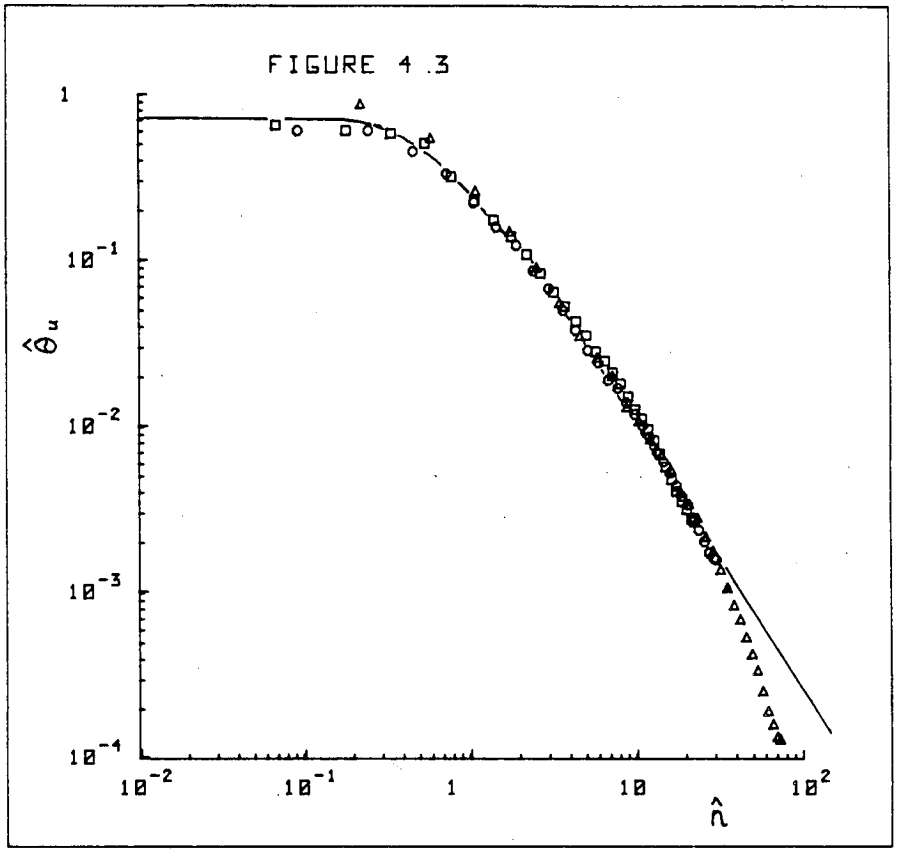

Figure 4.3. The von-Karman spectra of the u component fluctuations behind the turbulence grids at the model position with $\bar{U}$ =7.1m/s.
—— Theoretical ; □ grid A ; ○ grid B ; △ grid C.

$$\frac{\overline{U}^2}{\overline{u}^2} = B(^{x}/M - ^{x_o}/M) \qquad (4.3)$$

where M is the mesh size of the grid

x is the downstream distance from the grid

and x_o is the apparent origin at which it is assumed the decay of turbulent energy begins.

Figure 4.4 shows the variation of the turbulent energy with downstream distance plotted as $\frac{\overline{U}^2}{\overline{u}^2}$ against log $(^{x}/M - ^{x_o}/M)$. The gradient of each of the solid lines is 1. Figure 4.5 shows the variation of the rms intensity of the u component with downstream distance from the grid position.

As was mentioned earlier the longitudinal length scale was estimated as the area under the auto-correlation curve of the u component fluctuations. Assuming Taylor's hypothesis, it is given by

$$L_x = \overline{U} \int_0^\infty R_1(\tau)d\tau \qquad (4.4)$$

where $R_1(\tau) = \overline{u(x,y,z,t)u(x,y,z,t+\tau)}/\text{var}(u(x,y,z,t))$, where $u(x,y,z,t)$ is the fluctuating part of the u component of velocity at position (x,y,z) and at time t, and $\text{var}(u(x,y,z,t))$ represents the variance of $u(x,y,z,t)$.

The lateral length scale L_z may be estimated using the cross-correlation curve of the u component fluctuations as

$$L_z = \int_0^\infty R_2(Z)dZ \qquad (4.5)$$

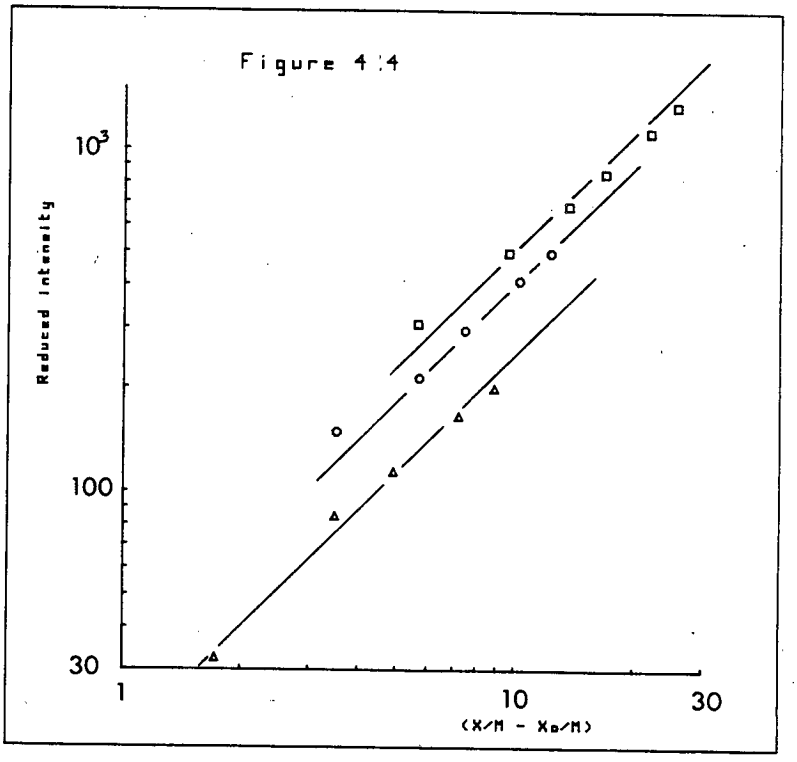

Figure 4.4. The decay of the u-component of turbulent energy with downstream distance from the turbulence grids.
□ *grid A ;* ○ *grid B ;* △ *grid C.*

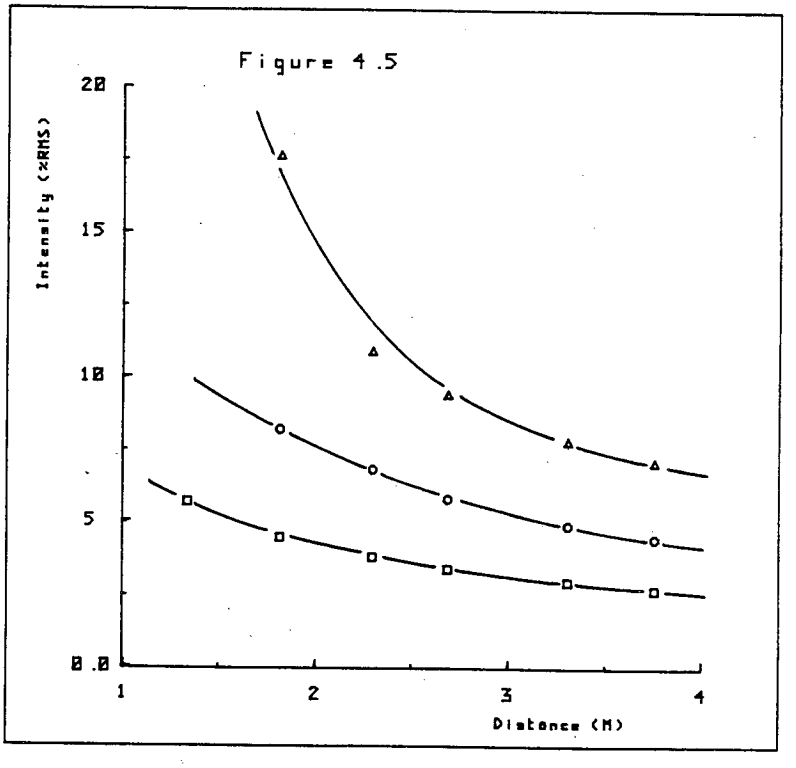

Figure 4.5. The variation of the rms intensity of the u-component of velocity fluctuations with downstream distance from the turbulence grids.
□ *grid A ;* ○ *grid B ;* △ *grid C.*

where $R_2(Z) = u(x,y,z,t)u(x,y,z+Z,t)/var(u(x,y,z,t))$.

Figure 4.6 shows the auto-correlation curves for each of the grids at the plate position. The Hewlett-Packard digital correlator was used to auto-correlate the voltage output of a U-wire held at the plate position. For turbulence where the rms intensity is less than 15% fluctuations in the output voltage of a U-wire are, to a very good approximation, linearly related to the velocity fluctuations in the flow, and, therefore it is possible to obtain the auto-correlation of the u fluctuations by auto-correlating the U-wire output voltage. The longitudinal length scale was estimated by using Simpons rule to compute the area under correlation curves. Figure 4.7 shows the variation of the longitudinal scale for each grid with downstream distance. The scale can be seen to gradually increase with downstream distance from the grid position, in accordance with the results of other workers [Bearman (1969)]. The gradual increase in the length scale of the turbulence is due to the preferential decay of the energy of the smaller scale motion. The measurements of the lateral scale were made by positioning one U-wire in a fixed position and traversing a second U-wire away from the fixed wire and in the z-direction. The PDP 11 was used to compute the cross-correlation coefficient between the U-wire output voltages, at several positions of lateral separation of the wires. The results showed that $L_Z = 0.5L_X$ to within ± 12%, in accordance with the prediction from the theory of homogeneous turbulence [Batchelor (1953)].

A brief investigation of the distortion of the turbulence approaching the plate was made. Measurements of the u-spectra of

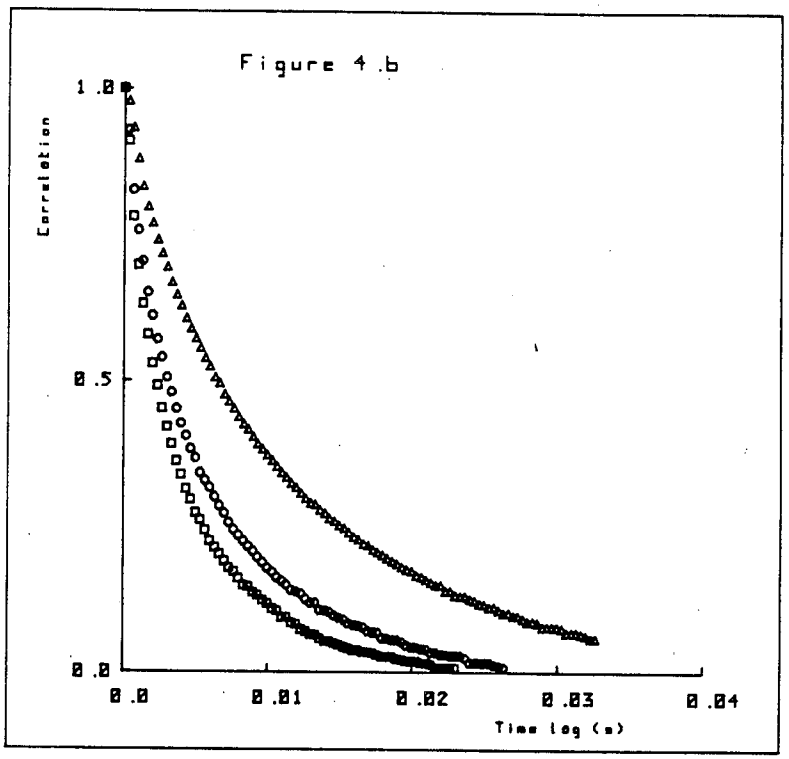

Figure 4.6. The auto-correlation of the u component of the turbulence behind the grids at the plate position.
□ *grid A,* $\bar{U}$ *= 12.82m/s ;* ○ *grid B,* $\bar{U}$ *= 12.71m/s ;* △ *grid C,* $\bar{U}$ *= 8.27m/s.*

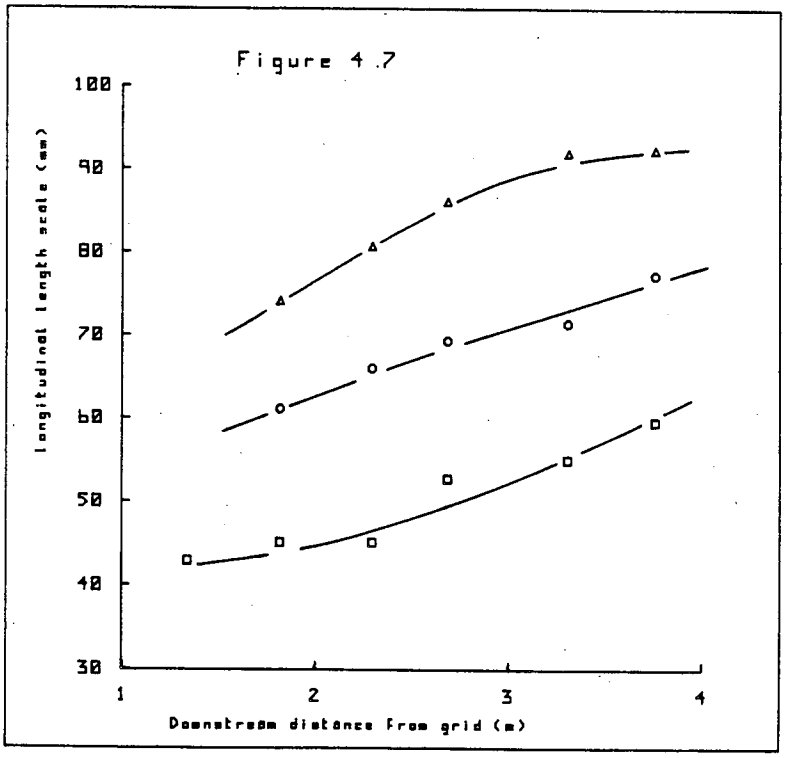

Figure 4.7. The variation of the longitudinal length scale of turbulence with downstream distance from the grids.
□ *grid A ;* ○ *grid B ;* △ *grid C.*

the turbulence were made with a U-wire at 4 positions approaching the 20×20 plate along the stagnation streamline. Figure 4.8 shows the spectra measured at each of the 4 positions, $\frac{1}{3}\ell$, $\frac{2}{3}\ell$, ℓ and 2ℓ upstream of the plate. The spectra appear to show a slight increase in the u component fluctuations near the plate at low values of the reduced frequency $n\ell/\bar{U}$. At high values of $n\ell/\bar{U}$ there appears to be a slight reduction in the energy of the u fluctuations as the plate is approached. The total energy of the u component fluctuations, however, remains very nearly constant as the plate is approached. These results may be compared to the predictions of Hunt's (1973) theory for the distortion of turbulence approaching a two-dimensional bluff body. The theory is applicable under the following conditions. Firstly, the mean flow must be irrotational and hence the analysis is not applicable to the wake or to the boundary layer on the body's surface. Secondly, $\sqrt{\overline{u^2}} << \bar{U}$, which implies that the stretching and twisting of the vortex filaments is due only to the mean flow and not to the influence of the vortex filaments themselves. Thirdly, the distortion of the turbulence must be rapid enough so that no energy is lost due to the action of viscous dissipation. This requirement reduces to

$$\frac{L_x}{\ell} >> \frac{\sqrt{\overline{u^2}}}{\bar{U}} \quad . \tag{4.6}$$

In this investigation all of these conditions are met. The theory predicts that as $L_x/\ell \to 0$ the magnitude of the u component fluctuations will be amplified as the plate is approached and as $L_x/\ell \to \infty$, the fluctuations will be reduced in amplitude as the plate is approached. The value of L_x/ℓ for the 20×20 plate used was only $\sim \frac{1}{3}$. At this

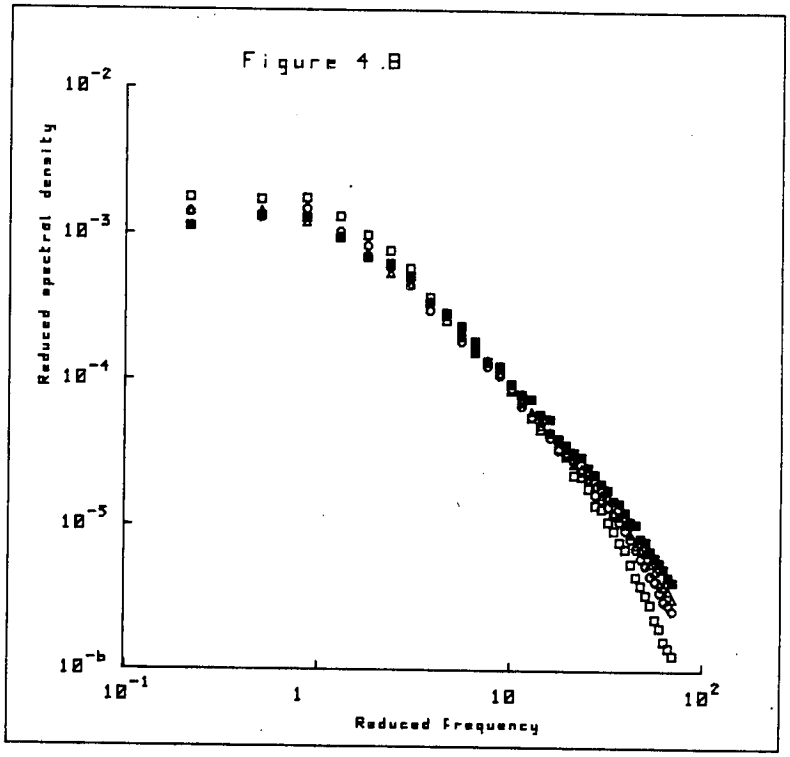

Figure 4.8. The distortion of the u-component of turbulence produced by grid B approaching the 20x20 plate along the stagnation streamline

□ *1/31 ahead ;* ○ *2/31 ahead ;* △ *1 ahead ;* ■ *21 ahead.*

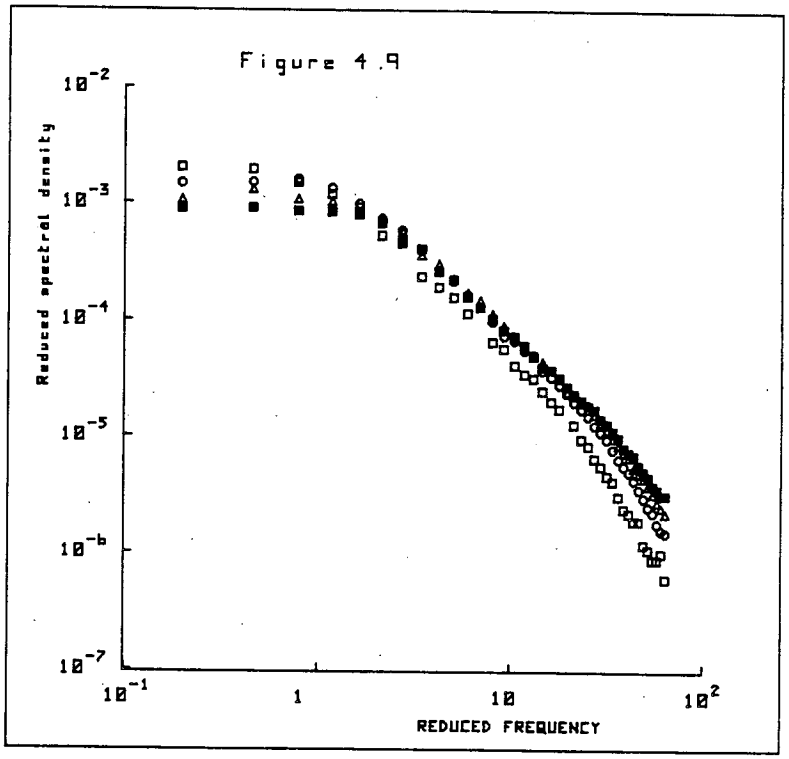

Figure 4.9. The distortion of the u-component of turbulence produced by grid B at a position of 0.065m upstream of the square plates.

□ *30x30 plate ;* ○ *20x20 plate ;* △ *15x15 plate ;* ■ *10x10 plate.*

value a combination of the effects of $L_x/\ell \to 0$ amd $L_x/\ell \to \infty$ may be possible. Bearman (1969) found in his investigation that with $L_x/\ell = 0.75$, the total energy of the u component fluctuations was reduced as the plate was approached. His spectra did not cross over at any value of $n\ell/\overline{U}$. The spectra of the u component fluctuations at positions closer to the plate showed lower energy content, at all values of $n\ell/\overline{U}$, than the spectra taken further away from the plate. The behaviour of the spectra in Bearman's investigation, wherein $L_x/\ell = 0.75$, were similar to that predicted by Hunt's theory for values of $L_n/\ell \to \infty$. In the present investigation $L_x/\ell = \frac{1}{3}$, and thus one might expect that perhaps a combination of the predictions of the theory as $L_x/\ell \to 0$ and as $L_x/\ell \to \infty$ might occur. It is thought that such a combination should occur when $L_x/\ell = O(1)$.

As a check on the results the investigation was repeated, but this time the plate size was changed and the U-wire held a fixed distance upstream of the plate and on the stagnation streamline. This eliminates any effects on the spectra due to the variation of the intensity of the turbulence with distance downstream of the grid. The value of L_x/ℓ, however, was changed dramatically by changing the plate size. Nevertheless the spectra plotted in Figure 4.9 show very similar behaviour to those presented in Figure 4.8. Again the total energy of the u fluctuations remains very nearly constant as the distortion is increased.

It would appear that in this investigation the total energy of the u component of the turbulence remains approximately constant as the distortion of the turbulence is increased. Hunt's

theory predicts that when $L_x/\ell >> 1$ the distortion of the turbulence will attenuate the u component fluctiations in a similar manner to the attenuation of the mean velocity. When $L_x/\ell << 1$ the distortion of the turbulence will result in the amplification of $\sqrt{u^2}$. However, in this investigation $L_x/\ell = 0(1)$ and there is amplification of the low wavenumbers and attenuation of the high wavenumbers.

These results are not in agreement with those of Bearman (1972), who investigated the distortion of turbulence approaching a two-dimensional bluff body with a filled-in wake. In his investigation the scale of the turbulence was in the range $1.2 \lesssim L_x/\ell \lesssim 2.38$. He found that as the turbulence approached the body there was an attenuation of the low wavenumbers and an amplification of the high wavenumbers. His results were in good agreement with the predictions of Hunt's theory. However, the conditions of his investigation much more closely satisfied the conditions under which Hunt's theory is applicable, than do the conditions of the present investigation. The body used in his investigation was two-dimensional and the effects of the unsteadiness of the wake were reduced to a minimum by the filled-in wake. In the present investigation, however, the body is three-dimensional and the wake was not filled-in. Also the condition of (4.6) may not have been adequately met and, therefore, the inertial forces of the turbulence may have had an effect on the motion of the fluid as it approached the plate. When (4.6) is not adequately met the turbulence may be said to have a finite intensity, rather than a negligibly low intensity. There is a need for a great deal more experimental work on the non-linear effects on a turbulence

of finite intensity as it approaches a body.

(b) Preliminary Measurements in Oscillatory Flow

The method for producing an oscillatory flow in the working section by using shutters is described in Chapter 2, section (b). As mentioned in that chapter, many workers have used this method to generate oscillatory flow. The periodic blockage presented to the flow by the shutters produces an oscillatory perturbation upon the mean flow. It was hoped that the perturbation so produced would be periodic with little harmonic content. It was also hoped that the flow perturbation would be well correlated within the working section and that the flow would behave as if the fluid were incompressible.

A fluid behaves incompressibly to a very good approximation, if $\omega\ell/a \ll 1$, where ω is the angular frequency of the perturbation, ℓ is a representative length of the flow, and a is the speed of sound in the fluid. Taking the largest plate as an example, the parameter $\omega\ell/a$ reaches a maximum value of 0.05 at a perturbation frequency of 20 Hz. Thus as far as the flow around the flat plates is concerned, the fluid behaves to a very good approximation as an incompressible fluid. For distances equal to the length of the working section, this parameter reaches a maximum value of around 0.5 and the fluid over such distances may no longer be thought of as an incompressible fluid. For distances comparable to the length of the tunnel the value of $\omega\ell/a$ is greater than 1. A brief discussion on how the

flow is thought to behave during the operation of the shutters is now given.

The effect of the rotation of the shutters is transmitted to the flow by acoustic radiation. The details of the acoustic radiation depends upon many factors. Among these factors are the dimensions of the tunnel, the variation of the cross-section of the tunnel throughout the length of the tunnel, the flexibility of the tunnel walls, and the frequency of rotation of the shutters.

Morkovin, Loehrke and Fejer (1971) discuss the acoustic resonances that occurred in the ITT oscillatory velocity wind tunnel. They found a resonance whose wavelength corresponded to the length of the wind tunnel side, and also a resonance whose wavelength corresponded to the length of the circuit of the wind tunnel. They also discuss the occurrence of Parker modes [Parker (1967)]. In the present investigation the length of the circuit of the wind tunnel is about 51m and hence a resonance might be expected at around 6 Hz. The length of the side of the wind tunnel is about 25m and, therefore, a resonance might also be expected at around 13 Hz. The resonances allow higher amplitudes of perturbation to be reached. Parker modes are very unlikely to occur in the present investigation as, below frequencies of 20 Hz, the size of the working section is too small to allow their existence.

Nevertheless, care must be taken to ensure that the perturbation produced by the shutters is uniform and closely periodic. Therefore, measurements were made to investigate the uniformity and frequency content of the perturbation in the working section. Spectra of the u component fluctuations were measured at a number

of perturbation frequencies and at a number of wind speeds, with a U-wire positioned near the centre line of the working section. These spectra were taken at a mean wind speed of 3.69 ms^{-1} and are plotted in Figure 4.10. The spectra show clearly that higher harmonics are always present. However, the estimated energy content of these harmonics is always at least one order of magnitude less than the fundamental. Some frequencies have low harmonic content and as far as possible the perturbation frequencies with the lowest harmonic content were used in this investigation. A small range of frequencies near 10 Hz was avoided as, within this frequency range, the flow perturbation contained a very high harmonic content and was far from sinusoidal. The shutter mechanism did not operate smoothly in this frequency range, which may account for the unusual form of the perturbation near 10 Hz. At $\sim$ 6 Hz, and near 12.5 Hz, the spectra show less than 3% harmonic content and the shutter mechanism operated very smoothly. These frequencies correspond to the expected resonances of the tunnel in which the wavelength of the acoustic radiation generated by the shutters was equal to the length of the circuit of the wind tunnel and equal to the length of the side of the wind tunnel.

Measurements were made of the rms of the velocity perturbation using a hot-wire and a Bruel & Kjaer rms meter. The hot-wire signal was low-pass filtered at 31.5 Hz. The mean voltage output of the wire was measured using an integrator. The rms perturbation was found to depend on both the frequency of the perturbation and the mean velocity in the working section for a given shutter set. At a constant mean wind speed the rms perturbation amplitude

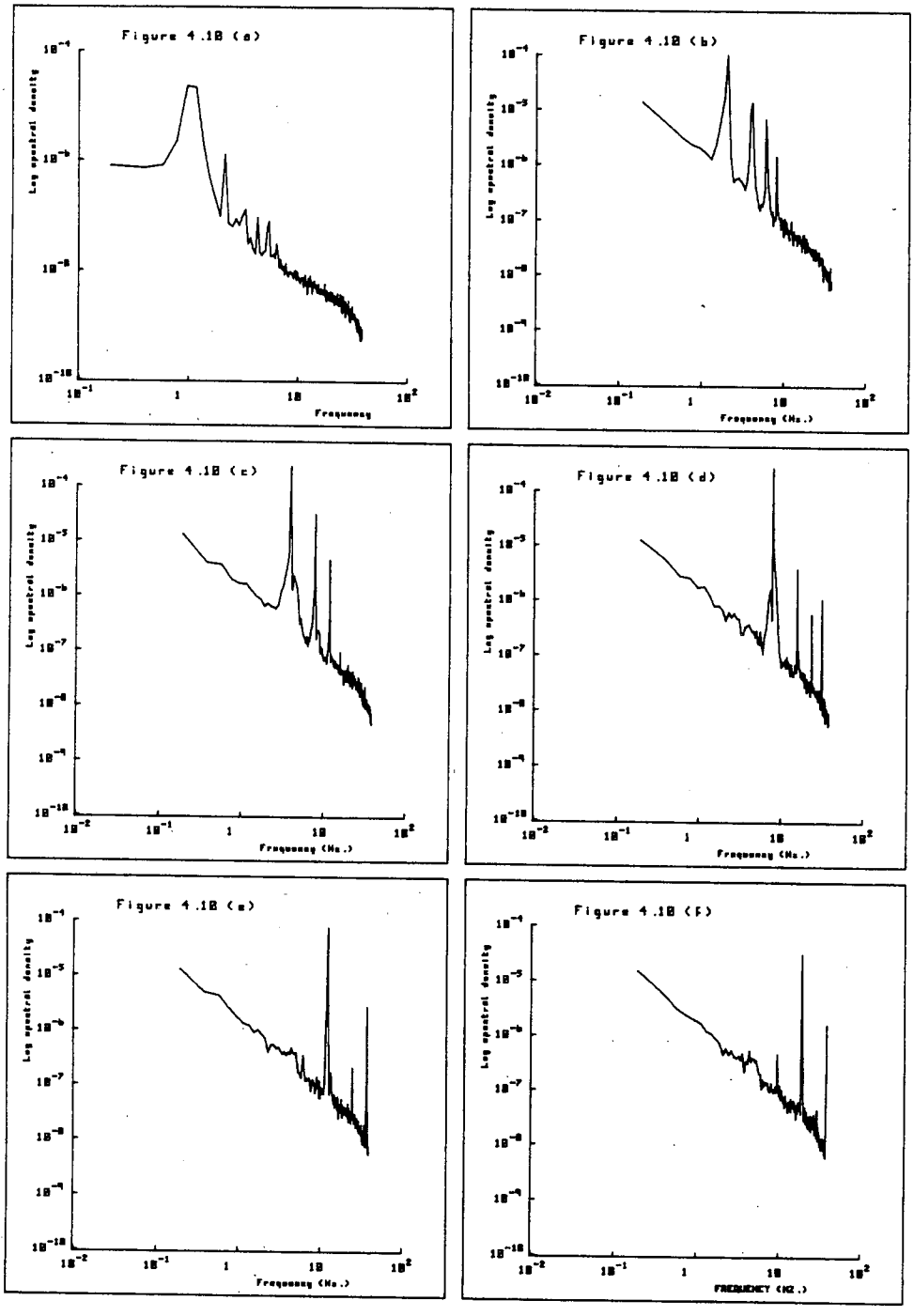

Figure 4.10. The spectra of the velocity fluctuations produced by shutters D at various perturbation frequencies. (a) 1Hz. (b) 2Hz. (c) 4Hz. (d) 8Hz. (e) 12.5 Hz. (f) 20Hz.

was measured at various frequencies for each of the shutters A, B, C and D. Figure 4.11(a) shows these measurements. The resonances at around 6 Hz and 12.5 Hz can clearly be seen. The resonances are the same for all the shutter sets and thus are a property of the tunnel. At a constant frequency of perturbation the amplitude was dependent on the mean velocity given by the empirical relation

$$u_{rms} = \alpha(f)\ \overline{U}^2 \qquad (4.7)$$

where $\alpha(f)$ is a frequency dependent constant for a given shutter set. Figure 4.11(b) shows the variation of the rms perturbation amplitude with mean velocity at three different frequencies.

Measurements were made of the uniformity of the perturbation amplitude and phase across the working action, at a distance of 2.5m upstream of the shutters and also down the length of the working section. Two hot-wires were used and the signals were low-pass filtered at 315 Hz before being digitised by the computer. Measurements were made at nine positions 0.1m apart across the working section, from -0.4m to +0.4m about the centre line of the tunnel. With a mean velocity of 3.19 ms^{-1} and a perturbation frequency of 12.36 Hz, the perturbation amplitude was constant to within ± 1%. With a reference wire at -0.4m the perturbation velocity was found to be in phase to within ± 2° across the working section. Along the axis of the working section, from the cylinder position to a position 1.8m downstream, the rms perturbation amplitude was constant to within ± 2%. With a reference wire at the cylinder position, the phase difference of the perturbation increased linearly with distance downstream, as is shown in Figure 4.12(a). The solid line

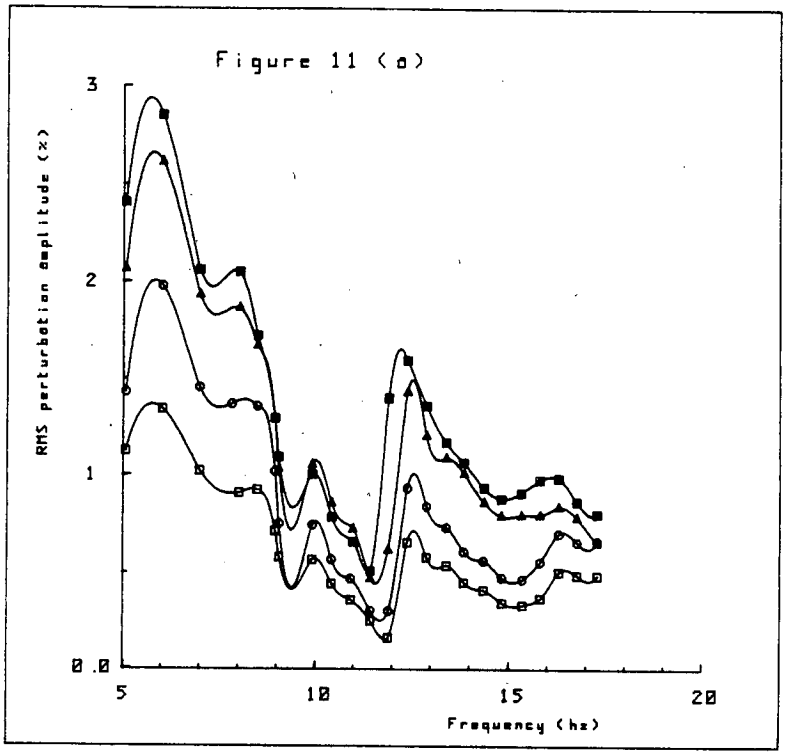

Figure 11(a). The variation of the rms perturbation amplitude with perturbation frequency for each shutter set at $\bar{U}$ =4.17m/s.
□ *shutters A ;* ○ *shutters B ;* △ *shutters C ;* ■ *shutters D.*

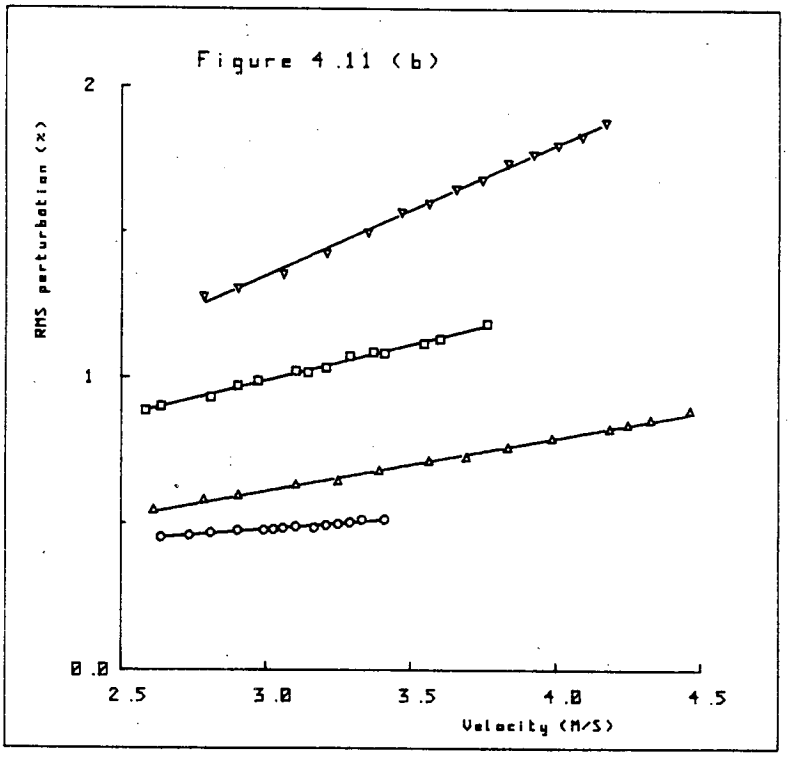

Figure 4.11(b). The variation of the rms perturbation amplitude with mean velocity at constant frequency.
○ *shutters A, n =12.36Hz. ;* ▽ *shutters C, n =8.0Hz.*
△ *shutters C, n =14.70Hz. ;* □ *shutters C, n =12.36Hz.*

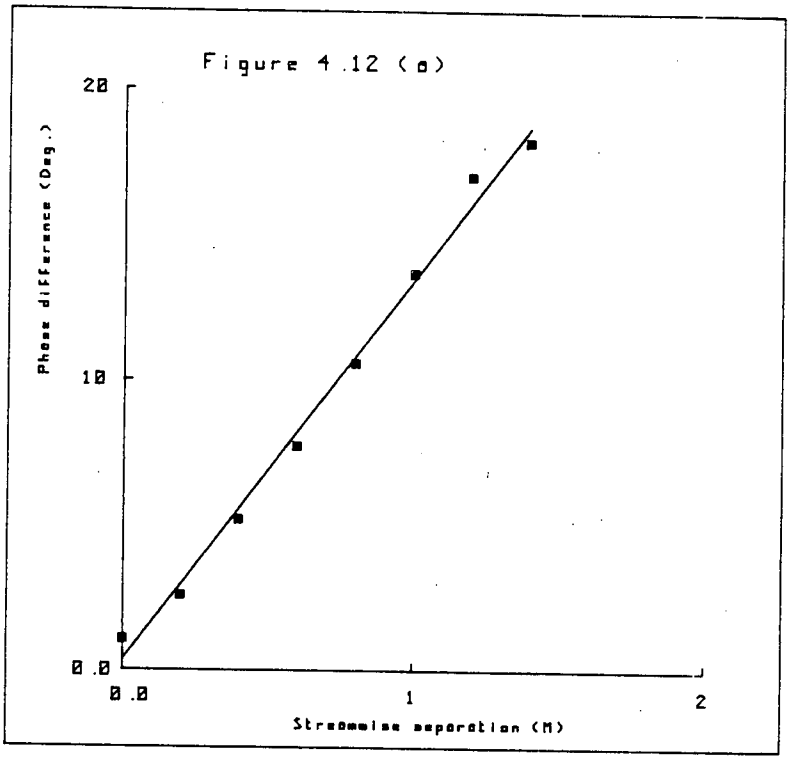

Figure 12(a). The phase difference of the perturbation velocity versus streamwise separation distance with n =12.36Hz. and $\bar{U}$ =3.19m/s.

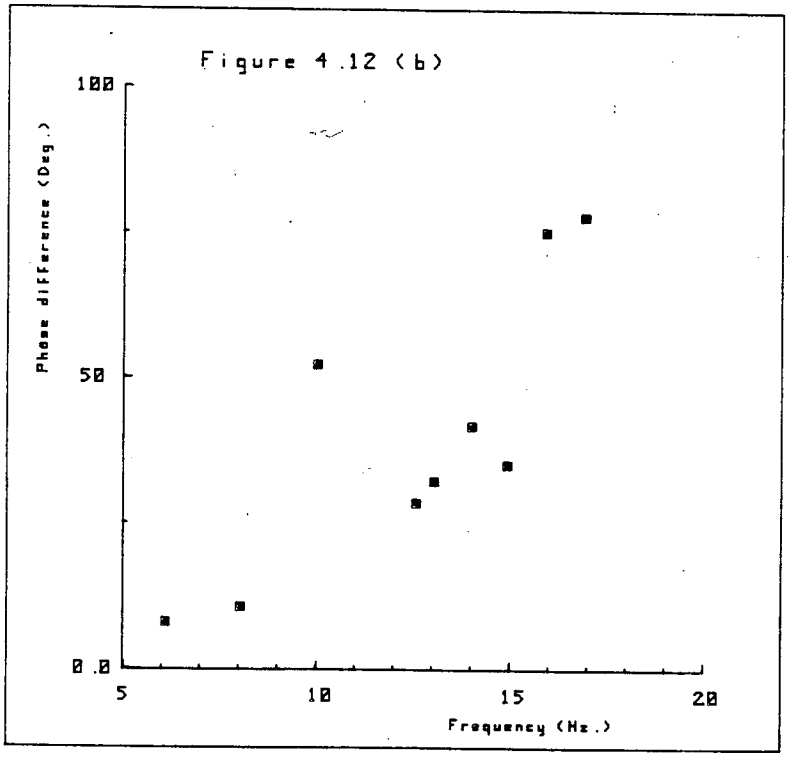

Figure 12(b). The phase difference of the perturbation velocity vesus the perturbation frequency for a fixed streamwise separation distance of 1.4m. at $\bar{U}$ = 3.19m/s.

is a least squares fit to the data. The wires were also positioned a constant distance of 1.4m apart in the downstream direction and the variation of the phase difference with perturbation frequency is as shown in Figure 4.12(b). Again the frequency of 10 Hz shows a rather odd effect and does not follow the general trend of the results.

To conclude, these preliminary measurements show that, apart from a small range of frequencies close to 10 Hz, the perturbation produced by the shutters is uniform and highly periodic with little harmonic content. At frequencies close to 6Hz and 12.5Hz, the perturbation amplitude is increased owing to acoustic resonance. At these frequencies the flow is uniform and closely sinusoidal, and, therefore, these frequencies were used in this investigation and a frequency close to 12.5 Hz was used in the investigations presented in Chapters 5 and 6.

(c) The Base Pressure Measurements

The base pressures of the plates attached to the sting were measured using a slender pitot tube. The tube was alligned with the flow direction and positioned with its total head tapping close to the rear of the plate and 2 cm vertically above the plate's centre. The pitot tube was held in this position by being fixed to the top of the aerofoil fairing [Figure 2.2]. A flexible plastic tube connected the total head tapping of the pitot tube to a Combist micromanometer. The other side of the Combist micromanometer was connected to the static pressure holes of the pitot tube that was

used to measure the free-stream velocity. The base pressures of each of the plates in steady, turbulent and oscillatory flows were measured. The measurements of the base pressures were made at several mean flow velocities and the base-pressure coefficient showed no significant Reynolds number dependence within the experimental accuracy of the measurements. The accuracy in the estimation of the base-pressure coefficients is approximately ± 2%. Measurements of the base-pressure coefficient made at a number of positions on the rear surface of the 20 × 20 plate showed that within experimental accuracy, the base pressure was uniform over the rear surface of the plate. The values of C_{Pb}, corrected using Maskell's method (1965), are presented in Table 4.1. A reasonable collapse of the results for the steady and oscillatory flows can be seen. The base-pressure coefficients in steady flow collapse to a value of approximately -0.375. Bearman (1969) found $C_{Pb} = -0.363$ in steady flow. The small difference between the value of C_{Pb} obtained in this investigation and the value of C_{Pb} obtained by Bearman is within experimental error. However, it must be remembered that in the present investigation the plates were supported by a sting, whereas in Bearman's investigation the base pressure measurements were made with the plates supported by wires attached to the corners of the plate. In the turbulent flow field the base-pressure coefficients are significantly lower than in the steady and oscillatory flows. This result, it is argued by Bearman, is due to the turbulent entrainment of fluid out of the wake, which reduces the wake pressure. It is argued that in turbulent flows

TABLE 4.1 *The mean base pressure coefficients in steady , turbulent and oscillatory flow*

Plate	Steady	Oscillatory	Turbulent
10x10	-0.375	-0.375	-0.438
15x15	-0.373	-0.379	-0.411
20x20	-0.379	-0.396	-0.416
30x30	-0.370	-0.370	-0.387

TABLE 4.2 *The mean drag coefficients in steady, turbulent and oscillatory flow*

Plate	Steady	Oscillatory	Turbulent
10x10	1.168	1.182	1.234
15x15	1.157	1.166	1.185
20x20	1.162	1.136	1.191
30x30	1.140	1.151	1.162

C_{Pb} is a function of the following variable

$$C_{Pb} = F\left(\frac{Lx^2}{\ell^2} \frac{\sqrt{\overline{u^2}}}{\overline{U}}\right) \quad . \tag{4.8}$$

The variable $\frac{Lx^2}{\ell^2} \frac{\sqrt{\overline{u^2}}}{\overline{U}}$ is called the turbulence parameter and the turbulent base-pressure coefficients are plotted against this parameter in Figure 4.13(a). The dashed line represents the results of Bearman. The values for the oscillatory flow base pressures show no significant differences from the steady flow values. This is most likely due to the small amplitude of the perturbation. Much larger amplitudes of perturbation would presumably be required to determine the effects, if any, of the perturbation on the base-pressure coefficient.

(d) The Steady Drag Measurements

The arrangement of the piezoelectric balance is shown in Figure 2.2. A description of the balance and its support is given in Chapter 2, section (c). The balance was calibrated using weights attached to the sting by a string running over a pulley. The weights were hung vertically and the pulley was positioned so that the string was aligned with the drag direction. A number of weights were used and the output voltage of the balance was noted for each. The calibration showed excellent linearity and a very high sensitivity, as can be seen in Figure 4.14. The sensitivity of the balance to forces applied in the drag direction was 0.837 V/N. The pulley arrangement was repositioned to apply a force in-line with the cross-

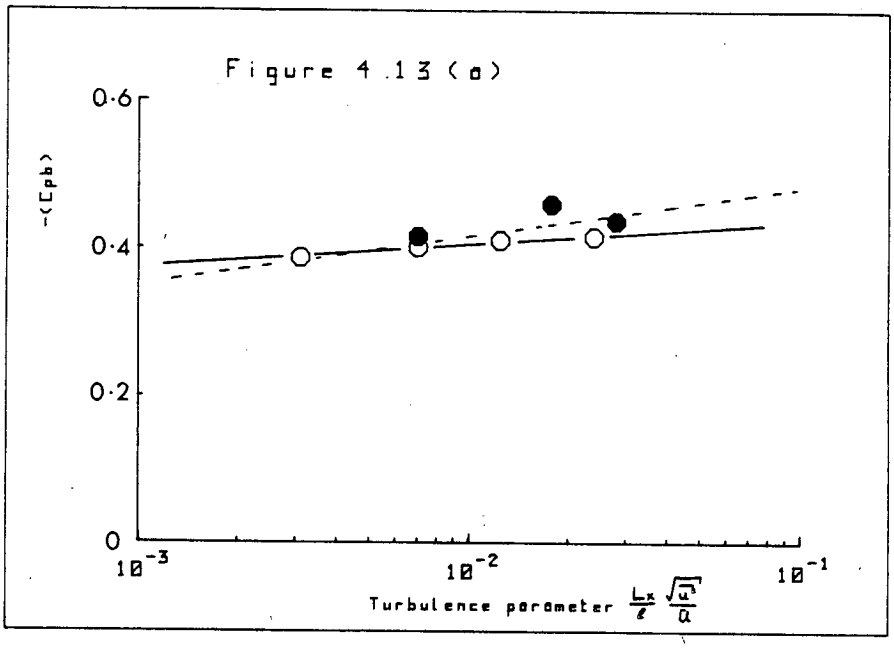

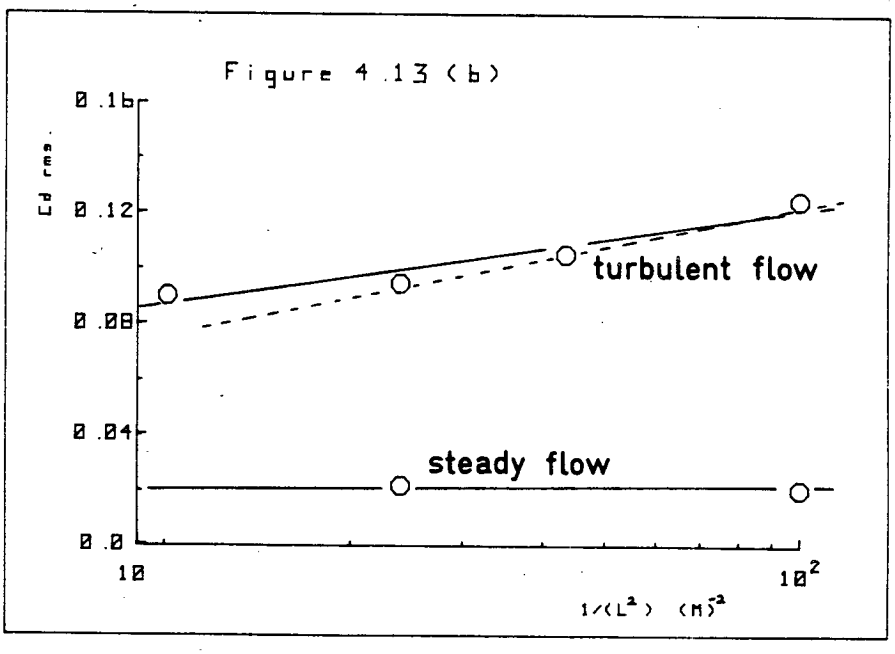

Figure 4.13(a). The variation of the base pressure coefficient with the turbulence parameter
○ plates behind grid B ; ● 20x20 plate behind each grid.

Figure 4.13(b). The variation of the fluctuating drag coefficient Cd.rms with the inverse area of the plate 1/l .

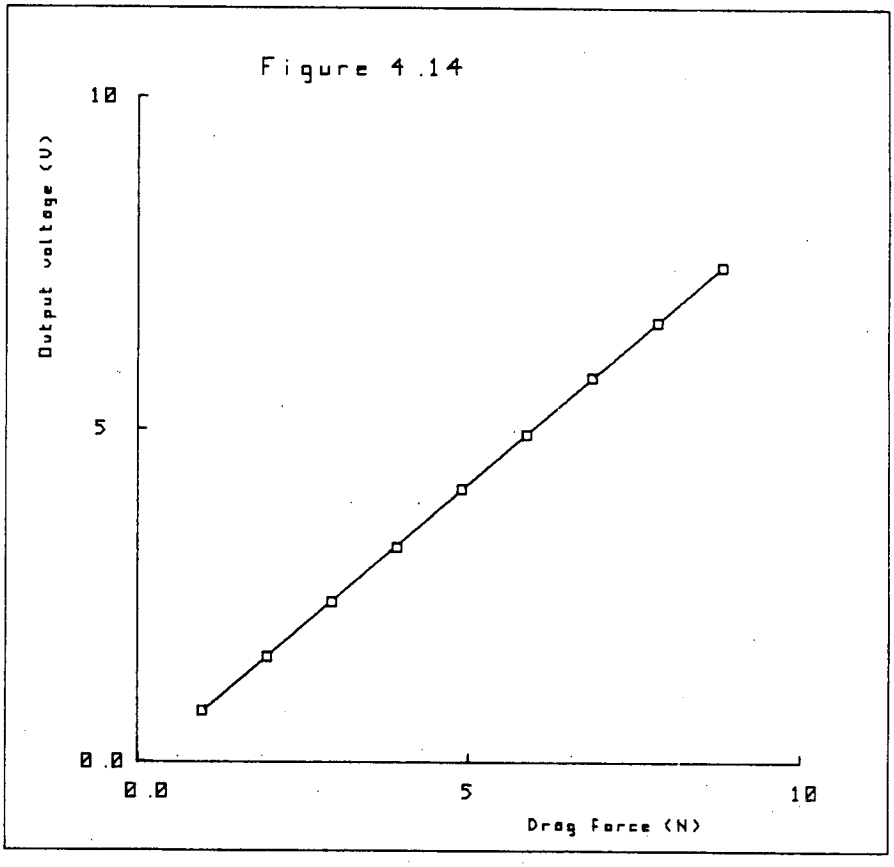

Figure 4.14. The voltage output from the piezo-electric balance versus the applied force in the drag direction.

force direction, which is horizontal and perpendicular to the direction of the drag. The output voltage of the balance, with different weights attached to the string, was recorded and the sensitivity of the balance to forces applied in this direction was less than 3% of the sensitivity of the balance to forces applied in the drag direction. The weights were then hung vertically from the end of the sting and the output voltage of the balance was noted. The sensitivity of the balance to this applied force was again less than 3% of the sensitivity to a force applied in the drag direction. The cross-talk of the balance is thus less than 3%. A plate was attached to the sting and the pulley arrangement was positioned to apply a force in the direction of the drag force at various positions on the plate surface. The string was fixed to the plate surface by a piece of PVC insulating tape. For a constant weight applied to the string the drag balance output voltage was constant to within ± 2%. This error was considered to be the limit of the accuracy of the measurement of a drag force on the plate.

Each of the plates were mounted in the sting in turn. In steady flow the tunnel velocity was increased in steps and the pitot reading and the mean voltage output of the balance were recorded once they had reached steady values. The drag coefficient was computed at each of the flow velocities used and showed no Reynolds number dependence over the range of velocities from 2.8 ms^{-1} to 10 ms^{-1}, to within ± 2%.

In the turbulent flow field a hot-wire was used to measure the flow velocity. At each mean flow velocity, the hot-wire voltage and the output voltage of the balance were digitised.

10K points of each voltage signal were digitised. The hot-wire voltage records were converted into velocity records from which the mean velocity was computed. The mean voltage of the balance output was computed and converted into a mean force. The drag coefficients computed in this way showed no variation with Reynolds number, over a range of mean velocities from around 3 ms^{-1} to 10 ms^{-1}, within the experimental accuracy. A similar procedure used for the measurement of C_D in an oscillatory flow. Again no Reynolds number dependence was found over a range of velocities from 3 ms^{-1} to 5 ms^{-1}, within the experimental accuracy. The smaller range of velocity was used as smooth operation of the shutter mechanism was not possible at flow velocities above 5 ms^{-1}.

The results of the measurements of C_D are presented in Table 4.2. The results were corrected for the effects of tunnel blockage by using Maskell's (1965) correction method. In steady and oscillatory flow the results show a good collapse in the value of C_D. The oscillatory flow drag coefficient is expected to show no change from the steady flow value, as the base pressure coefficients showed no changes between steady and oscillatory flows. The drag coefficients in turbulent flow, on the other hand, show an increase compared to the steady flow values but only for the smallest plate. This indicates that the base pressure contributes only partly to the overall drag, as a relative change in base pressure causes much smaller relative change in the drag coefficient. Bearman (1969) quotes that the base pressure contributes about 30% to the overall drag on the basis that a 30% change in base pressure coefficient causes only a 10% change in the drag coefficient. For the 10 × 10

plate in this investigation, the base pressure coefficient, in turbulent flow, decreased by about 17% from its steady flow value, whilst the corresponding increase in the drag coefficient was about 5.7%. The results would appear to substantiate Bearman's finding that the base pressure contributes about 30% to the overall drag.

(e) The Unsteady Drag Measurements in Turbulent and Steady Flow

The fluctuating drag acting on the four plates was measured in a steady flow and in a turbulent flow. The measurements in the turbulent flow were made with all the plates exposed to the flow behind grid B. Some measurements were made with the 20 × 20 plate behind grid B over a range of Reynolds numbers. At one particular Reynolds number the fluctuating drag on the 20 × 20 plate was measured in the turbulent flow fields of grids A, B and C. Spectra of the fluctuating drag were computed for each of the above measurements. The rms of the fluctuating drag was computed by taking the square root of the area under the drag spectrum. Figure 4.13(b) shows the values of C_{Drms} plotted against $1/\ell^2$. Clearly, the smallest plate has the largest fluctuating drag coefficient. The dashed line plotted in Figure 4.13(b) indicates the results obtained by Bearman (1969). The smallest plate is thought to have the largest fluctuating drag coefficient as the correlation of the energy containing eddies is greatest over the surface of the plates. As the plate size increases the correlation of the flow over the surface

is reduced and hence the fluctuating drag is reduced. In a steady flow the 10×10 and 20×20 plates only were used to measure $C_{D.rms}$ and the results plotted in Figure 4.13(b) show no change with $1/\ell^2$

It is interesting to compare the unsteady forces in turbulent and oscillatory flows before presenting the force spectra. Figures 4.15(a) - (d) show the velocity and drag force fluctuations measured in these flow fields. Comparing the turbulent velocity trace shown in Figure 4.15(a) with the trace of the resulting drag force shown in Figure 4.15(b), it can be seen that the high frequency content of the latter is much less than that of the former. One might therefore expect that the transfer function relating the spectra might be rather like a low-pass filter. On the other hand, Figures 4.15(c) and 4.15(d) show that there is a high correlation between the velocity and the drag force in an oscillatory flow.

Figure 4.16 shows the spectra of the fluctuating drag on the 10×10 and the 20×20 plate in a steady flow. The fluctuating drag acting on these plates arises from the unsteady pressure distribution acting on the rear face of the plate. The concept of aerodynamic admittance, requires that the fluctuating drag is strongly related to the fluctuations in the oncoming flow field. Thus, the drag spectra measured in a steady flow give an indication of the "noise" of the measurement. Figure 4.17 shows the drag spectra for each plate measured in the turbulent flow

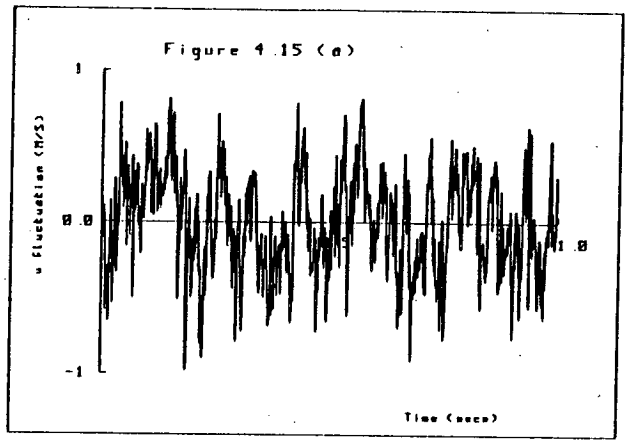

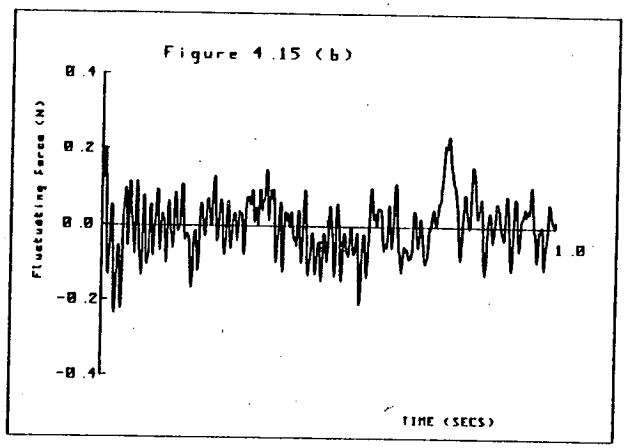

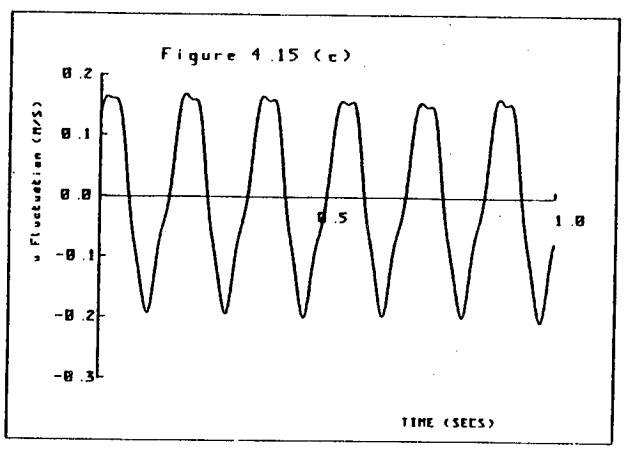

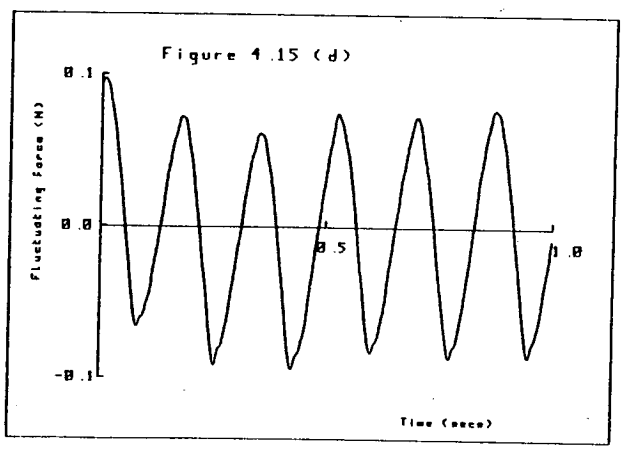

Figure 4.15. A comparison of the time histories in turbulent and oscillatory flows of the fluctuating forces and velocities.
(a) The velocity fluctuations behind grid B at $\bar{U}$ =3.69m/s.
(b) The force fluctuations acting on the 20x20 plate behind grid B at $\bar{U}$ = 3.69m/s.
(c) The velocity fluctuations in oscillatory flow at 5.9Hz.and $\bar{U}$ = 3.69m/s.
(d) The forces acting on the 20x20 plate in the oscillatory flow described in (c).

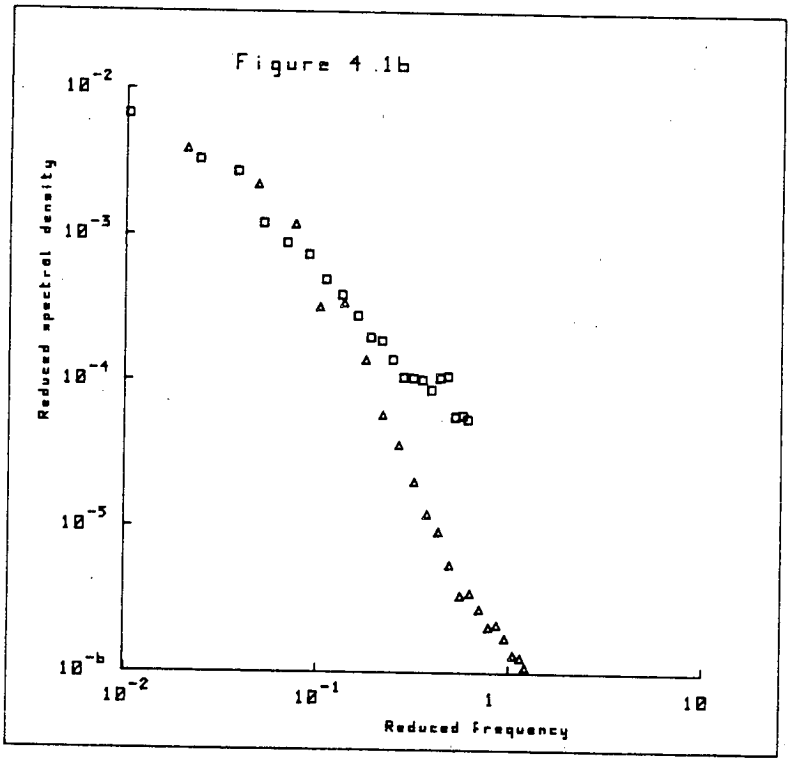

Figure 4.16. The spectra of the forces acting on the 10x10 and 20x20 plates in steady flow at U =7.1m/s.
□ *10x10 plate ;* △ *20x20 plate.*

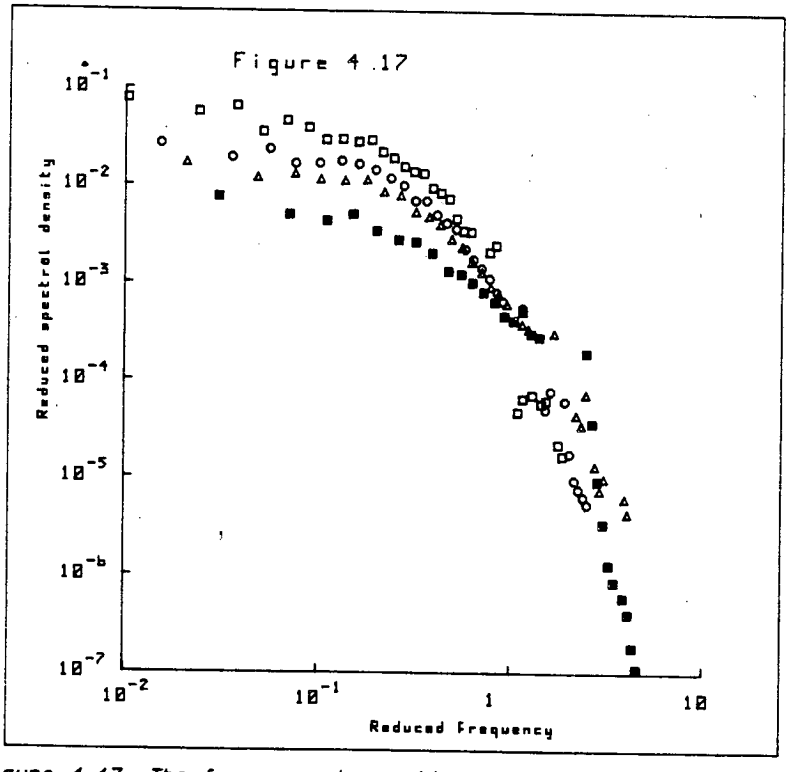

Figure 4.17. The force spectra acting on the plates in the turbulent flow behind grid B with U =7.1m/s.
□ *10x10 plate ;* ○ *15x15 plate ;* △ *20x20 plate ;* ■ *30x30 plate.*

field of grid B. For the 10×10 plate the magnitude of the drag spectrum at low $n\ell/\overline{U}$ is about 10 times greater in turbulent flow than in steady flow. For $n\ell/\overline{U} > 0.1$ it is 100 to 1000 times greater in the turbulent flow than in the steady flow. For the 20×20 plate the magnitude of the drag spectrum at low $n\ell/\overline{U}$ is about three times greater in turbulent flow than in steady flow, but for $n\ell/\overline{U} > 0.1$, it is again 100 to 1000 times greater in turbulent flow than in steady flow. The "signal to noise" ratio is thus dependent on the plate size and improves with decreasing plate size.

The spectra shown in Figure 4.17 show a good collapse at high values of $n\ell/\overline{U}$. Therefore at high values of $n\ell/\overline{U}$ it would appear that the fluctuating force acting on the plate is dependent upon only the plate size and not upon the nature of the approaching turbulence. Bearman (1969) suggests that at high $n\ell/\overline{U}$, the drag fluctuations may be related more to the unsteadiness of the pressure distribution on the rear face of the plate, than to the fluctuations of the velocity in the oncoming flow. This suggestion is substantiated by the result that the rate of fall off of the drag spectra in steady and turbulent flow, is the same. At low values of $n\ell/\overline{U}$, in turbulent flow, the energy content of the drag fluctuations increases with reducing plate size. This is due to the greater correlation of the flow over the surface of the smaller plates. A small peak in the force spectra was evident at around 40Hz, and was present in all the drag spectra. This peak was due to electronic noise, and thus the spectral estimates near this frequency are omitted. The electronic noise was associated with the charge

amplifiers used to convert the charge on the piezoelectric crystals into a voltage.

The spectra of the fluctuating drag forces acting on the 20 × 20 plate in the turbulent flow fields of grids A, B and C, are plotted in Figure 4.18. The collapse is poor and this may be attributed to the different intensities of the turbulence produced by the grids at the plate position. If it is accepted that at high $n\ell/\overline{U}$ the fluctuating drag is associated more with the unsteady wake fluctuations than the fluctuations in the oncoming flow, then the measurements of Figure 4.18 suggest that the magnitude of the wake fluctuation is dependent in some way upon the intensity of the turbulent flow around the plate.

Figure 4.19 shows the drag spectra measured with the 20 × 20 plate in the turbulent flow behind grid B at three mean wind velocities. The collapse of the spectra is excellent at all values of $n\ell/\overline{U}$, indicating that the drag spectra are not Reynolds number dependent in the range of Reynolds numbers between 5.6×10^4 and 1.4×10^5.

The aerodynamic admittance estimates were computed using the following relation

$$\chi^2(n) = \frac{1}{4} \frac{S_F(n)}{S_u(n)} \frac{\overline{U}^2}{\overline{F}^2} \qquad (4.9)$$

where $S_F(n)$ is the power spectral density of the fluctuating drag frequency n,

$S_u(n)$ is the power spectral density of the u component velocity fluctuations at frequency n.

$\overline{U}^2$ and $\overline{F}^2$ are the mean square values of the velocity and the drag respectively,

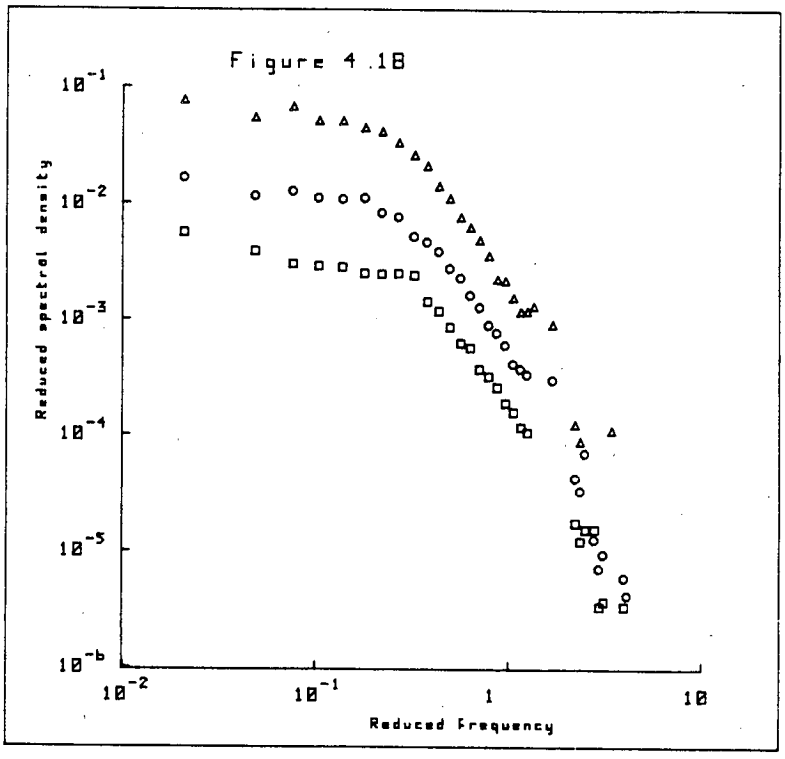

Figure 4.18. The force spectra acting on the 20x20 plate in the turbulent flow behind grids A, B, and C at $\bar{U}$ =7.1m/s.
□ *grid A ;* ○ *grid B ;* △ *grid C.*

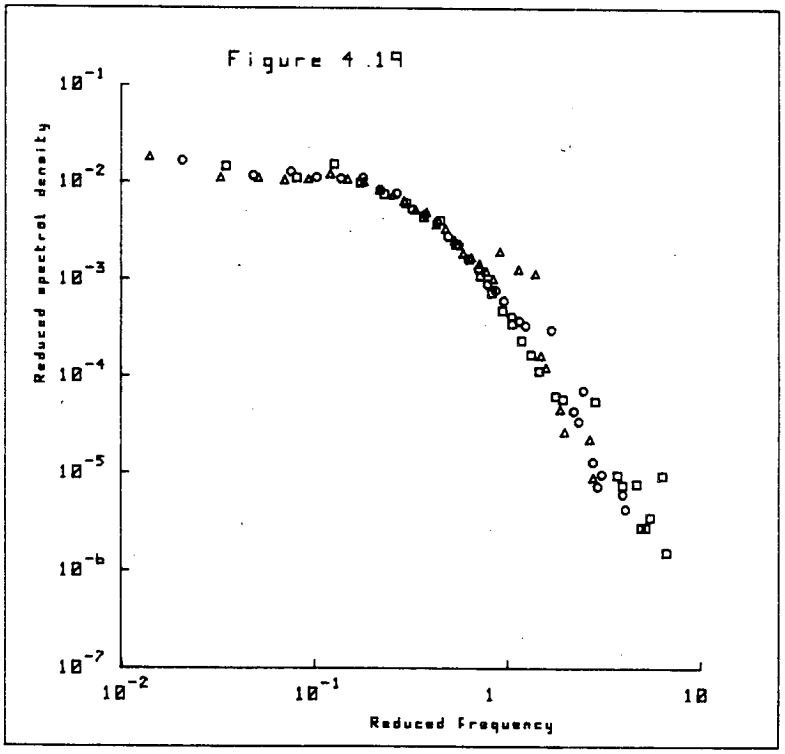

Figure 4.19. The force spectra acting on the 20x20 plate in the turbulent flow behind grid B at various mean velocities.
□ $\bar{U}$ = 4.2m/s ; ○ $\bar{U}$ = 7.1m/s ; △ $\bar{U}$ = 10.4m/s.

and $\chi^2(n)$ is the aerodynamic admittance function.

The theory of the aerodynamic admittance is presented in Appendix I. The aerodynamic admittances computed using equation (4.9), for the plates in the turbulent flow behind grid B, are plotted in Figure 4.20. The solid line is the empirical relation proposed by Vickery (1965) and is given by

$$\chi^2(n) = \{1 + (\frac{2n\ell}{\overline{U}})^{4/3}\}^{-2} \qquad (4.10)$$

The results presented in Figure 4.20 show reasonable collapse and follow the empirical relation suggested by Vickery. The results suggest that there is little, if any, dependence of the admittance values on the parameter $^{Lx}/_{\ell}$. For the results of Figure 4.20 the value of $^{Lx}/_{\ell}$ was in the range of 0.22 to 0.68. These results are in excellent agreement with those obtained by Bearman (1969).

The admittances calculated for the 20 × 20 plate exposed to the turbulent flow fields of grids A, B and C are plotted in Figure 4.21. The admittance results collapse well, although in the range of $^{n\ell}/_{\overline{U}}$ from 0.1 to 1.0, the admittance values obtained with grid C are slightly higher than those obtained with grids A and B. This result is unlikely to be significant, as the value of $^{Lx}/_{\ell}$ varied between 0.26 and 0.42, which is a smaller range than the range of $^{Lx}/_{\ell}$ that was used to obtain the results of Figure 4.20. It must be noted, however, that the results of Figures 4.20 and 4.21 perhaps indicate that, in the range of $^{n\ell}/_{\overline{U}}$ from 0.1 - 1, the aerodynamic admittance increases slightly with increasing $^{Lx}/_{\ell}$. This is also true of Bearman's results.

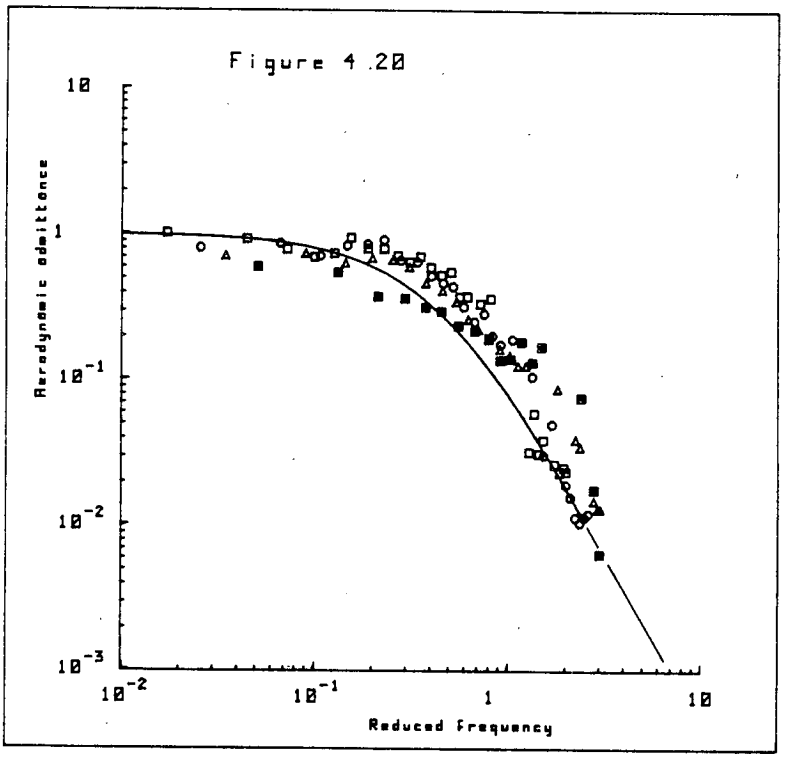

Figure 4.20. The aerodynamic admittance measurements for the flat plates in the turbulent flow behind grid B at $\bar{U}$ =7.1m/s.
—— Vickery's empirical relation ; □ 10x10 plate ; ○ 15x15 plate △ 20x20 plate ; ■ 30x30 plate.

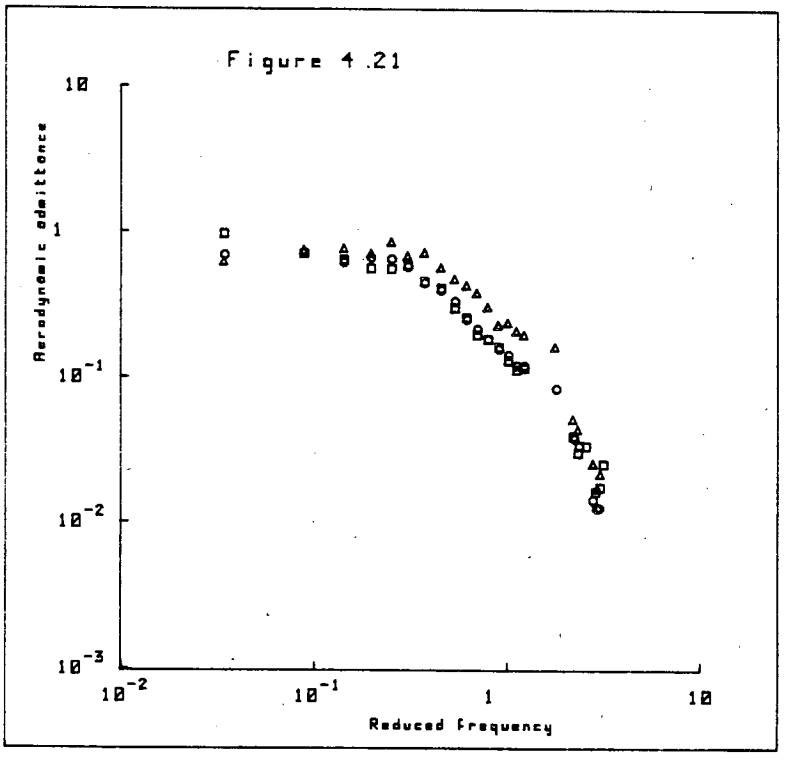

Figure 4.21. The aerodynamic admittance measurements for the 20x20 plate in the turbulent flow behind grids A, B, and C at $\bar{U}$ =7.1m/s.
□ grid A ; ○ grid B ; △ grid C.

Figure 4.22 shows the admittances calculated for the 20 × 20 plate behind grid B at the 3 values of mean velocity used. The admittance shows no significant dependence on the Reynolds number between the Reynolds numbers 5.6×10^4 and 1.4×10^5.

For the aerodynamic admittance to have any validity a high correlation must exist between the fluctuations of the drag and the fluctuations of the velocity in the oncoming flow. This was investigated by positioning a hot-wire at a number of distances upstream of the 20 × 20 plate and along the stagnation streamline. Grid B was used to produce the turbulent flow field. The output voltage of the piezoelectric balance and the hot-wire output voltage were fed into a Hewlett-Packard digital correlator. The correlator was used to compute the cross-correlation function of the fluctuating drag and the fluctuating velocity. For low intensities of turbulence of < 10 - 15% the fluctuating voltage output of the hot-wire may be assumed to be linearly related to the fluctuating velocity (see equation (3.40)). The cross-correlation functions are plotted in Figure 4.23. The peak of the correlation occurs approximately at a time lag corresponding to the time taken for the turbulence to convect from the measuring wire to the plate at the mean free-stream velocity. The lag at which the peak occurs obviously increases as the distance of the hot-wire from the plate increases. The peak value of the correlation is approximately 0.6 at the largest separation distance of 2D and this value may depend on the parameter Lx/ℓ. If $Lx >> \ell$, the distortion of the energy containing eddies will be small and, therefore, there will be a high correlation between the fluctuating force and the

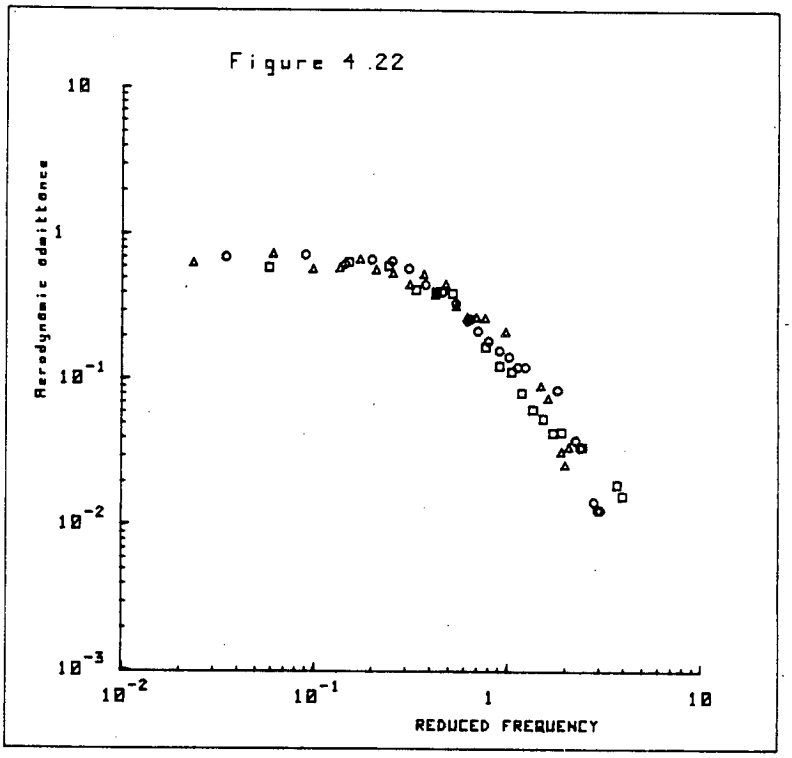

Figure 4.22. The aerodynamic admittance measurements for the 20x20 plate in the turbulent flow behind grid B at various mean velocities.
□ $\bar{U}$ = 4.2m/s ; ○ $\bar{U}$ = 7.1m/s ; △ $\bar{U}$ = 10.4m/s.

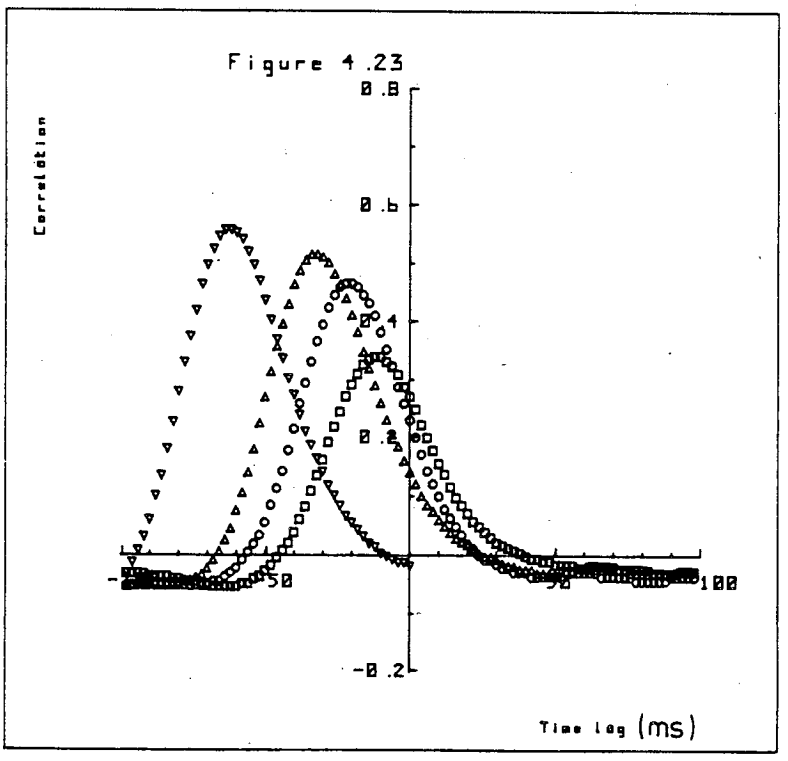

Figure 4.23. The correlation of the fluctuations of the force with the fluctuations of the velocities approaching the plate along the stagnation streamline.
□ *1/3l ahead ;* ○ *2/3l ahead ;* △ *1 ahead ;* ▽ *2l ahead.*

fluctuating velocity. For $Lx << \ell$ the turbulence will be highly distorted and the correlation between the fluctuating force and the fluctuating velocity will be small. For a separation distance of ℓ Bearman (1969) found the peak value in the cross-correlation of the force and the velocity to be about 0.65, with $^{Lx}/_{\ell} = 0.75$. In the present investigation for a separation distance of ℓ the peak value is about 0.56, but in this case $^{Lx}/_{\ell} \sim \frac{1}{3}$. These results substantiate the argument that the value of the peak of the cross-correlation of the fluctuating force and the fluctuating velocity at a given position unpstream of the plate, is dependent on the value of $^{Lx}/_{\ell}$, and that the value of the peak decreases as $^{Lx}/_{\ell}$ decreases. The peak value of the correlation function becomes smaller as the plate is approached owing to the increasing distortion of the turbulence by the plate.

(f) The Unsteady Measurements in Oscillatory Flow

Each of the plates were mounted on the sting in turn and exposed to the oscillatory flow produced by shutter set D. The mean velocity was 3.69 ms^{-1} and the perturbation frequencies ranged from 1 Hz to 20 Hz. At each frequency of perturbation the drag spectrum was measured. The corresponding velocity spectrum was computed from measurements taken at the plate position in the empty tunnel. The energy of the fluctuation at the perturbation frequency was estimated from the spectrum by integrating the power spectral density estimates over a small range of frequencies centred at the perturbation frequency. The range of frequencies

was approximately $n \pm 4\%$. At the perturbation frequency the aerodynamic admittance was computed using

$$\chi^2(n) = \frac{1}{4} \frac{E_F(n)}{E_u(n)} \frac{\overline{U}^2}{\overline{F}^2} , \qquad (4.11)$$

where $E_F(n)$ and $E_u(n)$ are the energies under the drag and velocity spectra over a small band of frequencies centred on the perturbation frequency.

Figure 4.24 shows the admittances in oscillatory flow computed using this method. The solid line represents the theoretical admittance for oscillatory flow and is given by

$$\chi^2(n) = 1 + \{(\frac{C_M}{C_{DT}})(\frac{2\pi n\ell}{\overline{U}})\}^2 , \qquad (4.12)$$

[Bearman, 1969]

where C_M is the added mass coefficient and C_{DT} is the fluctuating drag coefficient. The solid line represents a value of $C_M/C_{DT} = 0.5$. The line is not intended as a best fit to the data, but merely as a guide to the form of the admittance in oscillatory flow, at one particular value of C_M/C_{DT}. The admittances plotted in Figure 4.24 show a good collapse onto a single curve. The admittance results fall onto the plotted theoretical curve at values of $n\ell/\overline{U} > 1$ but the theoretical curve underestimates the aerodynamic admittance between $n\ell/\overline{U} = 0.1$ and $n\ell/\overline{U} = 1$. A higher value of C_M/C_{DT} would fit the results more closely at low $n\ell/\overline{U}$, but would overestimate the admittance at high values of $n\ell/\overline{U}$. This suggests that the ratio of C_M/C_{DT} is not independent of $n\ell/\overline{U}$.

A brief discussion of the behaviour of the aerodynamic admittance in turbulent and oscillatory flows is given in section (g) of this chapter.

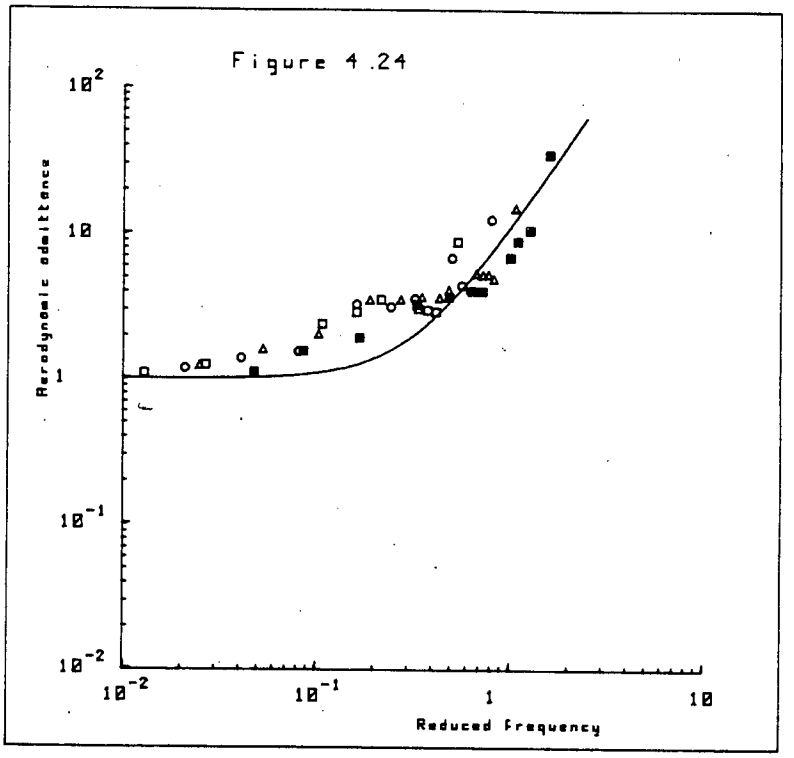

Figure 4.24. The aerodynamic admittance measurements for the flat plates in the oscillatory flow produced by shutters D at $\bar{U}$ = 3.69m/s.
□ 10x10 plate ; ○ 15x15 plate ; △ 20x20 plate ; ■ 30x30 plate ;
—— Theory Cm/Cd=0.5.

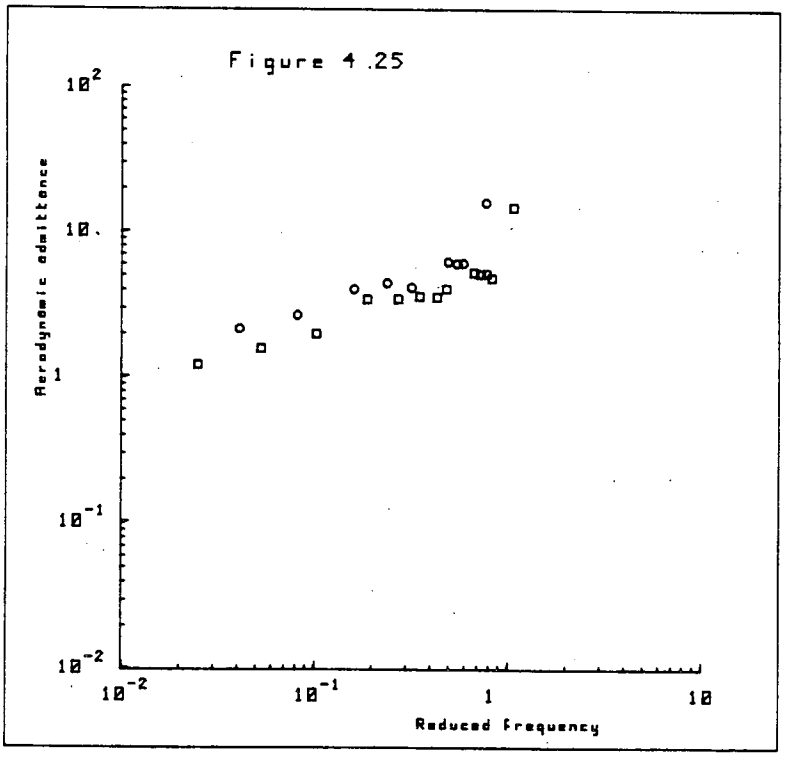

Figure 4.25. The aerodynamic admittance measurements in the oscillatory flow produced by shutters D at two mean flow velocities.
□ $\bar{U}$ = 3.69m/s ; ○ $\bar{U}$ = 5.04m/s

The 20 × 20 plate was attached to the sting and exposed to the oscillatory flow produced by shutter set D at a mean velocity of 5.04 m/s. Figure 4.25 shows the admittance results for the 20 × 20 plate in this flow field plotted with the admittance results for the 20 × 20 plate in the oscillatory flow generated by shutter set D at a mean velocity of 3.69 m/s. There is, perhaps, a difference in the results with the admittance values measured at the higher mean flow velocity being greater than the admittance values measured at the lower mean flow velocity, over the range of reduced frequencies included in the measurements. The velocity range over which the measurements were made was limited at the lower end of the range by the accuracy with which $\overline{U}$ could be measured and at the upper end of the range as the shutters operate smoothly only below $\overline{U} = 5\ ms^{-1}$. Therefore, it was not possible to investigate further any Reynolds number dependence of the admittance in oscillatory flow.

The amplitude of the perturbation at a constant mean velocity was, as mentioned earlier in section (b), dependent on the frequency of the perturbation. At a constant mean velocity the amplitude of the perturbation has large peaks at about 6 Hz and 12.5 Hz. The admittance results of Figure 4.24 give no indication that the aerodynamic admittance is dependent on the amplitude of the perturbation as all the results collapse reasonably well over the range of reduced frequencies investigated. One would not expect a reasonable collapse, if the admittance was dependent on the perturbation amplitude, as the peaks in the perturbation amplitude occur at definite frequencies, whilst the results are plotted against reduced frequency, $n\ell/\overline{U}$. To investigate the dependence of the admittance on the

perturbation amplitude more thoroughly measurements were made of the fluctuating drag on the 20 × 20 plate exposed to the oscillatory flow produced by shutters B at $\overline{U}$ = 3.69 m/s. The admittances computed from these measurements were compared to the admittances obtained with the 20 × 20 plate exposed to the oscillatory flow produced by shutters D with $\overline{U}$ = 3.69 m/s. The frequencies of perturbation used with shutters B were chosen to be close to the frequencies used with shutters D, so that the results are only slightly separated in reduced frequency. Figure 4.26 shows the admittances for the 20 × 20 plate obtained using the two shutter sets. The results show an excellent collapse indicating that, indeed the aerodynamic admittance is independent of the amplitude of the perturbation over the range of amplitudes investigated. For a constant perturbation amplitude, as the value of $^{n\ell}/\overline{U}$ increases so also does the inertial force acting on the plate, whereas the drag fluctuating force remains approximately constant, in magnitude. The inertial force arises from the acceleration of the flow and thus is 90° ahead in phase of the fluctuating velocity in a sinusoidally perturbed flow. As the contribution of the inertial force on the overall force increases with increasing $^{n\ell}/\overline{U}$, the phase of the fluctuating force compared to the fluctuating velocity should increase towards 90° (see equation A1.2).

Measurements were made of the phase difference between the fluctuating velocity and the fluctuating force acting on each of the plates in the oscillatory flow generated by shutters D at $\overline{U}$ = 3.69 m/s. For the phase measurements the fluctuating velocity was measured in the plane of the plate 0.4m above the centre of the plate. Figure

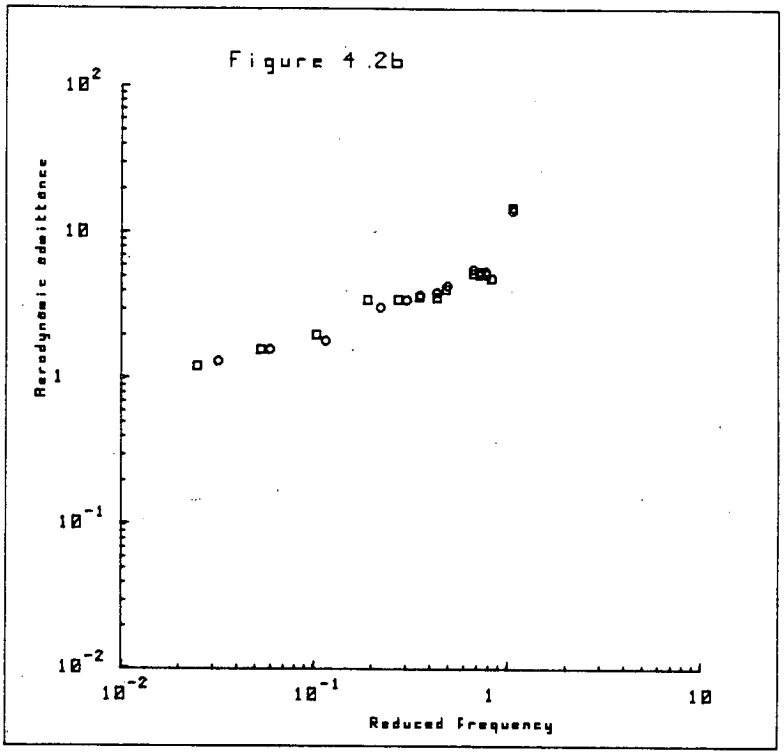

Figure 4.26. The aerodynamic admittance measurements in the oscillatory flow produced by shutters B and D at $\bar{U}$ = 3.69m/s.
□ shutters D ; ○ shutters B.

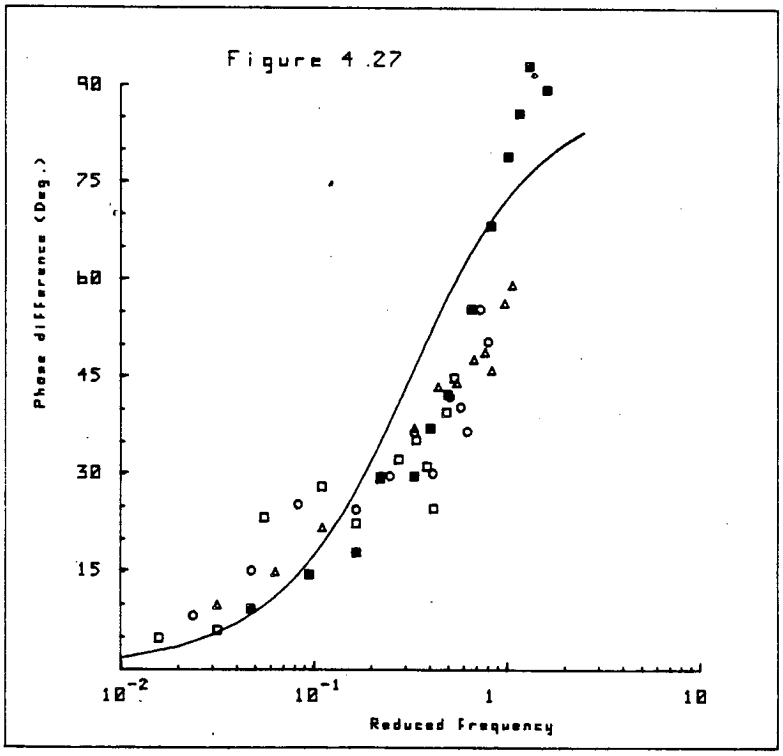

Figure 4.27. The phase difference between the fluctuating force acting on the plate and the fluctuating velocity in oscillatory flow at $\bar{U}$ = 3.69m/s.
□ 10x10 plate ; ○ 15x15 plate ; △ 20x20 plate ; ■ 30x30 plate.

4.27 shows the phase difference measurements plotted against $n\ell/\overline{U}$ for each of the plates. The solid line is computed from theory using $C_M/C_{DT} = 0.5$. Again the theoretical line is plotted only as a guide and not as a best fit to the results. The results follow the theoretical line and the collapse of the results is reasonably good. That the results do not all collapse onto the theoretical line over the whole range of $n\ell/\overline{U}$, is another indication that C_M/C_{DT} is not constant over the reduced frequency range.

From the theory presented in Appendix 1 the values of C_{DT} and C_M may be computed from the admittance values and phase values using the following relations.

$$\left(\frac{C_M}{C_{DT}}\right) = \alpha = \frac{\tan\theta(n)}{\left(\frac{2\pi n\ell}{\overline{U}}\right)} \tag{4.13}$$

and

$$\left(\frac{C_{DT}}{C_D}\right)^2 = \frac{\chi^2(n)}{\left[1 + \alpha^2 \left(\frac{2\pi n\ell}{\overline{U}}\right)^2\right]} \tag{4.14}$$

where $\theta(n)$ is the measured phase difference between the fluctuating velocity and the fluctuating drag, and $\chi^2(n)$ is the measured admittance, corresponding to the measured value of $\theta(n)$, at the perturbation frequency. The fluctuating drag coefficients and the added mass coefficients computed from the measurements using the above relations are presented in Figures 4.28 and 4.29 respectively. The fluctuating drag coefficient increases as $n\ell/\overline{U}$ increases, and its value for small values of $n\ell/\overline{U}$ is close to its steady flow value. The

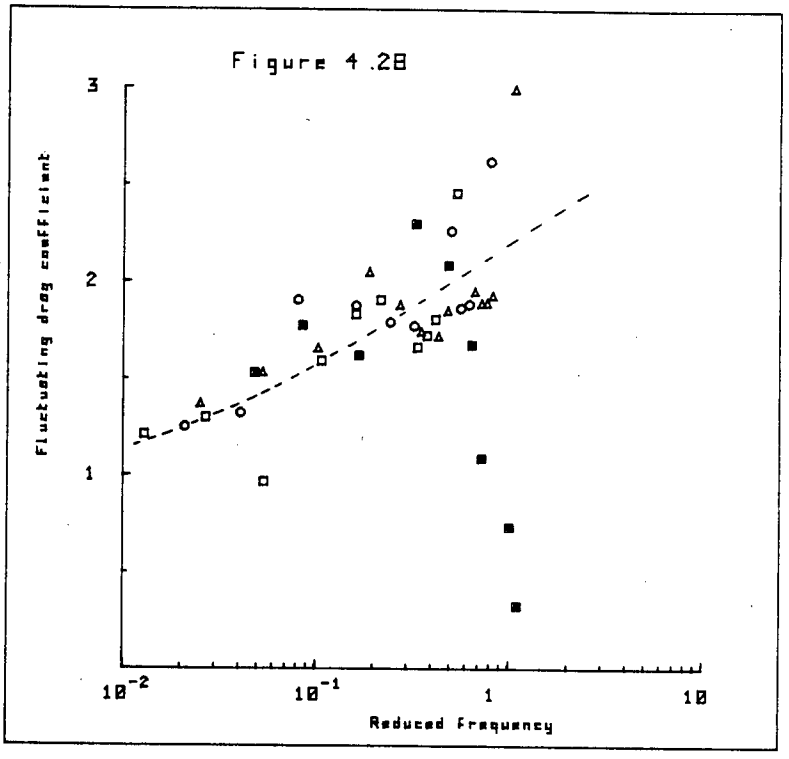

Figure 4.28. The fluctuating drag coefficients for the plates in the oscillatory flow generated by shutters D at $\bar{U}$ = 3.69m/s.
□ *10x10 plate ;* ○ *15x15 plate ;* △ *20x20 plate ;* ■ *30x30 plate.*

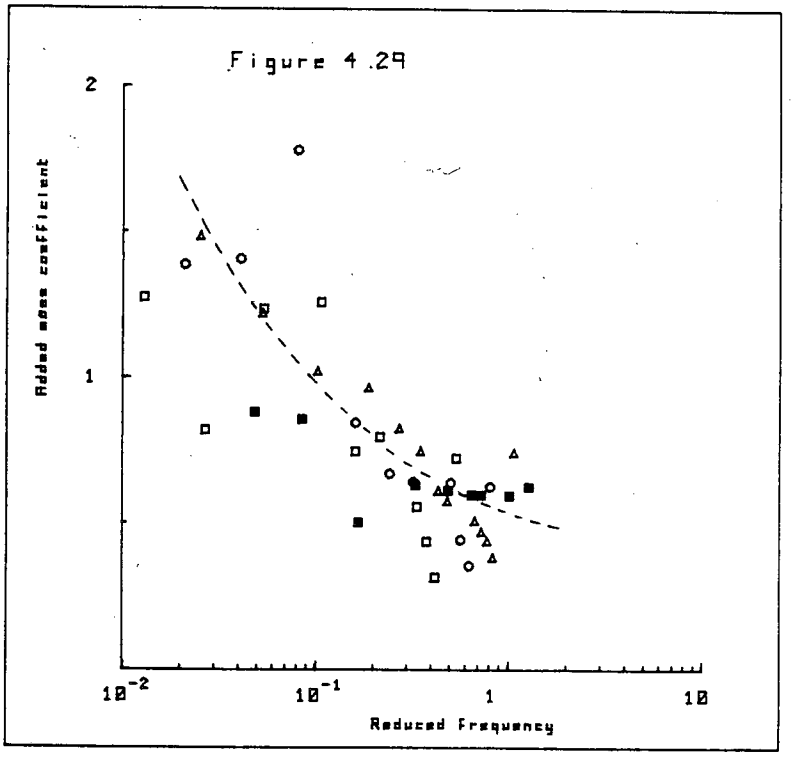

Figure 4.29. The added mass coefficients for the plates in the oscillatory flow generated by shutters D at $\bar{U}$ = 3.69m/s.
□ *10x10 plate ;* ○ *15x15 plate ;* △ *20x20 plate ;* ■ *30x30 plate.*

scatter of the data is admittedly large but the general behaviour is clear and is indicated by the dashed line. The 30 × 30 plate results, at the higher values of $n\ell/\overline{U}$, are very different from the other results. However, these results are perhaps unreliable. Errors in the measurement of θ, as θ approaches 90°, will cause very large changes in $\tan\theta$. Since α must be obtained first, before C_{DT} is calculated using (4.14), the value of C_{DT} at high $n\ell/\overline{U}$ may be very much in error. The results obtained using the 30 × 30 plate may also be less reliable than the other results owing to the plate's large blockage of about 7.4% in the tunnel. In addition, when the 30 × 30 plate is used the shroud cylinder is one plate length only behind the plate. Consequently, there could be interference effects taking place. The increase of C_{DT} with $n\ell/\overline{U}$ is in agreement with the behaviour of the fluctuating drag coefficients found in Davenport's (1961) investigation. Davenport investigated the fluctuating forces in a rectangular plate oscillating in a steady water current. The Reynolds range of his investigation was 5×10^3 to 5×10^4 and the plates had aspect ratios of 3 and 6. With such plates coherent vortex shedding into the wake would have occurred, giving rise to a small drag fluctuation at twice the frequency of vortex shedding. It is unlikely, however, that this fluctuating drag contribution would have had much effect on the results. In the present investigation, the vortex shedding would perhaps be in the form of vortex rings and a small fluctuating drag might occur at the frequency of shedding of these rings. In the present investigation there was no evidence of coherent vortex shedding from the flat plates.

The added mass coefficients plotted in Figure 4.29 show a large scatter. The dotted line is an indication of the variation of the added mass coefficient with reduced frequency. At high $n\ell/\overline{U}$ the value of C_M tends towards a value of around 0.6. The variation of C_M with reduced frequency is qualitatively similar to the variation found by Davenport for flat plates. The value of C_M in his investigation tended to about 1 at high $n\ell/\overline{U}$.

It is clear from the results of Figures 4.28 and 4.29 that the ratio of C_M/C_{DT} is not constant with reduced frequency. The ratio C_M/C_{DT} is about 1 at low $n\ell/\overline{U}$ and reduces to less than 0.5 at higher $n\ell/\overline{U}$. A satisfactory theory for the admittance would, therefore, have to include the variation of C_M and C_{DT} with $n\ell/\overline{U}$.

(g) Discussion

The aerodynamic admittance in oscillatory flow is computed theoretically by using A1.11 in Appendix 1. The admittance in this flow field has a value of unity at low $n\ell/\overline{U}$ and increases at higher $n\ell/\overline{U}$. The increase in the admittance is associated with the increasing contribution of the inertia force as $n\ell/\overline{U}$ increases. For a constant perturbation amplitude, the energy contribution of the inertia force fluctuations is proportional to the perturbation frequency squared. The volume taken for the displaced mass is ℓ^3 for a flat plate. Normally the volume is taken as the volume of fluid displaced by the body, and for a flat plate this would, theoretically, be equal to zero. However, the near wake may be thought of as a volume of fluid trapped close to the body and hence

the volume of the body may be taken as the volume of the near wake. For a square flat plate the appropriate volume is chosen to be ℓ^3. Obviously the value of ℓ^3 is rather arbitrary, but it is usual for the added mass coefficient to be calculated on the basis of this volume. Regardless of the choice of the volume, the product $C_M\ell^3$ must, of course, always have the correct value as its value is determined from measurements of the force.

The form of the admittance function in turbulent flow is considerably different from its form in oscillatory flow, especially at the values of $n\ell/\overline{U} > 0.1$. The measured admittance falls off from near unity at low $n\ell/\overline{U}$, as $n\ell/\overline{U}$ increases. The decrease in the admittance is a consequence of the decrease in the size of the eddies as $n\ell/\overline{U}$ increases, which in turn results in a decreasing correlation of the velocity fluctuations over the surface of the plate. It is thought that the decrease in correlation outweighs the increase in the inertia contribution as $n\ell/\overline{U}$ increases. At low values of $n\ell/\overline{U}$—the size of the eddies in the turbulent flow, associated with this reduced frequency are large compared to the size of the plate, and, therefore, the velocity fluctuations at low $n\ell/\overline{U}$ are well correlated over the surface of the plate. As $n\ell/\overline{U}$ increases the size of the associated eddies decreases and, for example, at $n\ell/\overline{U} \sim 10$ the eddy size is, to an order of magnitude, about one-tenth of the size of the plate. The fluctuating velocity associated with these smaller eddies is poorly correlated over the surface of the plate, and, therefore, one might expect the admittance value to decrease with increasing $n\ell/\overline{U}$. These arguments take no account of the distortion of the turbulence as it approaches the plate but are, nevertheless, illuminating.

Figure 4.30 shows the aerodynamic admittance measurements obtained in turbulent flow and in an oscillatory flow. This figure clearly shows the considerable difference in the form of the admittance in a turbulent flow to its form in oscillatory flow. At $n\ell/\overline{U} \sim 1$, the admittance values obtained in an oscillatory flow are 2-3 orders of magnitude greater than the admittance values obtained in a turbulent flow.

(h) Conclusions

The forces on flat plates in steady, turbulent and oscillatory flows have been measured. The mean drag coefficient and base pressure measurements show variations similar to those found by Bearman (1969), in steady and turbulent flows. The oscillatory flow drag coefficient and base-pressures show no significant differences from their corresponding values in a steady flow. The distortion of the turbulence approaching the flat plates is such that the energy of the u fluctuations is neither amplified nor attenuated.

The aerodynamic admittance measurements made in a turbulent flow agree with admittance measurements made by other workers. Vickery's empirical relation is found to fit the data reasonably well, but underestimates the admittance at values of $n\ell/\overline{U}$ around 1. These findings agree well with those of Bearman.

The aerodynamic admittance measurements made in an oscillatory flow follow the variation expected from the theoretical admittance function for oscillatory flow. However, the value of C_M/C_{DT} is found to vary with reduced frequency. A comparison of the admittances

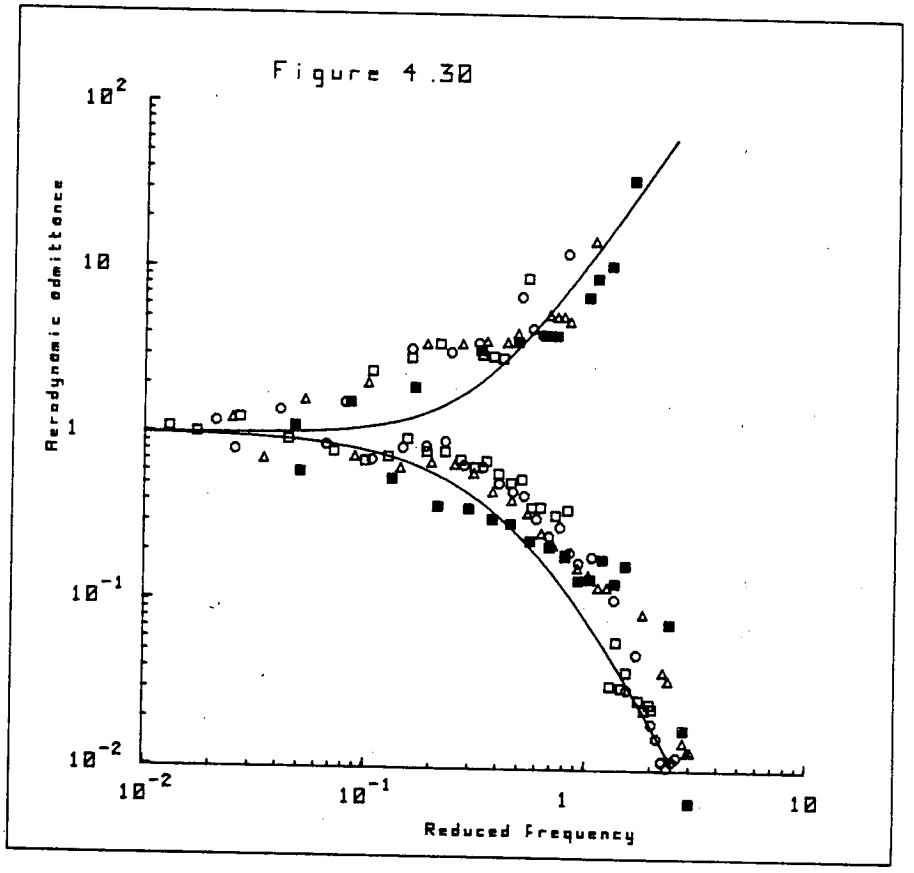

Figure 4.30. The comparison of the aerodynamic admittances in turbulent flow and in oscillatory flow.
——Vickery's empirical relation, and oscillatory flow theory with Cm/Cd=0.5.
□ 10x10 plate ; ○ 15x15 plate ; △ 20x20 plate ; ■ 30x30 plate.

obtained in both a turbulent and an oscillatory flow is shown in Figure 4.30. The admittance in oscillatory flow is about 3 orders of magnitude greater at $n\ell/\overline{U} \sim 1$, than the admittance in turbulent flow.

The variation of the fluctuating drag coefficient, and the added mass coefficient, with reduced frequency is similar to that found by Davenport, for flat plates oscillated in a steady flow. C_{DT} increases from its steady flow value, C_D, as $n\ell/\overline{U}$ increases. The value of C_M decreases as $n\ell/\overline{U}$ increases, to a value of around 0.6.

APPENDIX I

THE THEORETICAL AERODYNAMIC ADMITTANCE IN PERFECTLY CORRELATED FLOW

In a perfectly correlated flow the velocity at any instant is invariant in space. If the velocity at time t is given by

$$U(t) = \overline{U} + u(t) \tag{A1.1}$$

then the force acting on a flat plate in such a flow field is given by

$$F(t) = \tfrac{1}{2}\rho U^2(t) C_D \ell^2 + \rho \ell^3 C_M \dot{U}(t) \tag{A1.2}$$

$$= \tfrac{1}{2}\rho C_D \ell^2 (\overline{U}^2 + 2\overline{U}\, u(t) + u^2(t)) + \rho \ell^3 C_M \dot{u}(t) , \tag{A1.3}$$

where $\dot{U}(t) = \frac{\partial U(t)}{\partial t}$.

Equation (A1.2) is often referred to as Morrison's equation. If $F(t)$ is represented by a steady part $\overline{F}$ and a fluctuating part $f(t)$, then neglecting higher order terms than $u(t)$

$$\overline{F} = \tfrac{1}{2}\rho(\overline{U}^2 + \overline{u}^2) C_D \ell^2 \tag{A1.4}$$

$$\approx \tfrac{1}{2}\rho \overline{U}^2 C_D \ell^2 \quad \text{for} \quad |u| << |\overline{U}|$$

and $$f(t) = \rho \overline{U} C_{DT} \ell^2 u(t) + \rho \ell^3 C_M \dot{u}(t) , \tag{A1.5}$$

where C_{DT} is the fluctuating drag coefficient which is to be distinguished from the steady flow drag coefficient C_D.

To compute the spectrum of the force fluctuations it is first necessary to auto-correlate the fluctuating force.

$$\overline{f(t)f(t+\tau)} = \rho^2\bar{U}^2\ell^4C_{DT}^2\,\overline{u(t)u(t+\tau)} + \rho^2\ell^6\,C_M^2\,\overline{\dot{u}(t)\dot{u}(t+\tau)}$$

$$+ \rho^2\bar{U}\ell^5C_{DT}C_M\,\overline{\{u(t)\dot{u}(t+\tau) + \dot{u}(t)\,u(t+\tau)\}} \quad \text{(A1.6)}$$

The overbar denotes the average in time.

For a stationary time series

$$\overline{u(t)\,\dot{u}(t+\tau)} = -\overline{\dot{u}(t)\,u(t+\tau)} \quad \text{(A1.7)}$$

and $$\overline{\dot{u}(t)\,\dot{u}(t+\tau)} = -\frac{d^2}{d\tau^2}\,\overline{u(t)\,u(t+\tau)}$$

and thus

$$\overline{f(t)f(t+\tau)} = \rho^2\bar{U}^2\ell^4C_{DT}^2\,\overline{u(t)u(t+\tau)} - \rho^2\ell^6C_M^2\,\frac{d^2}{d\tau^2}\,\overline{u(t)u(t+\tau)} \quad . \quad \text{(A1.8)}$$

Taking the Fourier transform of both sides gives

$$S_F(n) = 2\int_{-\infty}^{\infty}\rho^2\bar{U}^2\ell^4C_{DT}^2\,\overline{u(t)u(t+\tau)}\,e^{-i\omega\tau}\,d\tau - 2\int_{-\infty}^{\infty}\rho^2\ell^6C_M^2\,\frac{d^2}{d\tau^2}\,\overline{u(t)u(t+\tau)}\,e^{-i\omega\tau}\,d\tau \quad \text{(A1.9)}$$

where $\omega = 2\pi n$.

Thus

$$\frac{S_F(n)}{\bar{F}^2} = \frac{4\,S_u(n)}{\bar{U}^2}\left[\left(\frac{C_{DT}}{C_D}\right)^2 + \left(\frac{C_M}{C_D}\right)^2\left(\frac{2\pi n\ell}{\bar{U}}\right)^2\right] \quad \text{(A1.10)}$$

and the aerodynamic admittance is given by

$$\chi^2(n) = \left[\left(\frac{C_{DT}}{C_D}\right)^2 + \left(\frac{C_M}{C_D}\right)^2\left(\frac{2\pi n\ell}{\bar{U}}\right)^2\right] \quad \text{(A1.11)}$$

In an ocsillatory flow given by

$$U(t) = \bar{U}(1 + p \cos \omega t) \qquad p << 1 \qquad \text{(A1.12)}$$

The fluctuating force acting on the plate is given by

$$f(t) \simeq \rho C_D \ell^2 \bar{U}^2 p \cos\omega t - \rho \ell^3 C_M \bar{U} p\omega \sin\omega t. \qquad \text{(A1.13)}$$

The phase of the fluctuating force compared to the phase of the fluctuating velocity is given by

$$\theta = \tan^{-1}\left[\frac{C_M}{C_{DT}} \frac{2\pi n\ell}{\bar{U}}\right] . \qquad \text{(A1.14)}$$

THEORY FOR THE ADMITTANCE IN TURBULENT FLOW

Vickery (1965) has suggested that the forces acting on a body in turbulent flow may be calculated by treating the body as a lattice like structure. The elements of the lattice are assumed to be very small and do not distort the turbulence. The eddy sizes of the turbulence are assumed to be much greater than the lattice size and the parameter $n\ell/\bar{U}$ is thus assumed to be very small. As a consequence of these assumptions the inertia force may be neglected. The drag force on an element dA of the lattice is given by

$$\delta f(t) = \rho \bar{U} C_D \, dA \, u(t) \qquad \text{(A1.15)}$$

and the expression for the auto-correlation of $f(t)$ is given by

$$\overline{f(t)f(t+\tau)} = \int_S \int_S \overline{\delta f(a,t)\delta f(b, t + \tau)} \, dS_a \, dS_b \qquad \text{(A1.16)}$$

where a and b are two points on the lattice surface S, and $f(t)$

is the total fluctuating load on the structure. To simplify the problem the mean velocity is assumed to be uniform over space, and the turbulence is assumed to be homogeneous. The correlation between two points in such a flow is dependent only on the distance between them. Equation (A1.16) reduces to

$$\overline{f(t)f(t+\tau)} = \rho^2\overline{U}^2C_D^2 \int_S \int_S \overline{u(a,t)\ u(b,\ t+\tau)}\ dS_a\ dS_b\ . \tag{A1.17}$$

Taking the Fourier transform of both sides yields

$$S_F(n) = 2C_D^2\rho^2\overline{U}^2 \int_S \int_S \int_{-\infty}^{\infty} \overline{u(a,t)\ u(b,t+\tau)}\ e^{-i\omega\tau}\ d\tau\ dS_a\ dS_b. \tag{A1.18}$$

In isotropic turbulence the imaginary part of the spectrum is zero and hence $S_u(a,b;n) = P_u(a,b;n)$.

Substituting this expression back into (A1.18) gives

$$S_F(n) = \rho^2C_D^2\overline{U}^2 \int_S \int_S P_u(a,b;n)dS_a\ dS_b \tag{A1.19}$$

$$\text{and}\quad \frac{S_F(n)}{\overline{F}^2} = \frac{4}{A^2\overline{U}^2} \int_S \int_S P_u(a,b;n)\ dS_a\ dS_b\ . \tag{A1.20}$$

Substituting for the admittance gives

$$\chi^2(n) = \frac{1}{A^2} \int_S \int_S \frac{P_u(a,b;n)}{S_u(n)}\ dS_a\ dS_b\ . \tag{A1.21}$$

For a flat plate of length ℓ this gives

$$\chi^2(n) = \frac{1}{\ell^4} \int_0^{\ell} \int_0^{\ell} \int_0^{\ell} \int_0^{\ell} \frac{P_u(r_{ab};n)}{S_u(n)} \, dx_2 \, dx_3 \, dx' \, dx' \qquad \text{(A1.22)}$$

where r_{ab} is the distance between the points a and b. This has been shown by Bearman (1969) to further reduce to

$$\chi^2(n) = \frac{4}{\ell^4} \int_0^{\ell} \int_0^{\ell} (\ell - x_3)(\ell - x_2) \frac{P_u(r_{ab};n)}{S_u(n)} \, dx_2 \, dx_3. \qquad \text{(A1.23)}$$

Vickery has measured the function $P_u(r_{ab};n)$ behind a turbulence grid and fitted the results with the empirical relation

$$P_u(r_{ab};n) = S_u(n) \, e^{-7.5(\theta/2\pi)} \cos 1.4\pi(\theta/2\pi)$$

$$\text{where } (\theta/2\pi) = \frac{r_{ab}}{2\pi L_x} \left[1 + \frac{2\pi n L_x}{\bar{U}} \right)^2 \Bigg]^{\frac{1}{2}} . \qquad \text{(A1.24)}$$

By substituting the expression for $P_u(r_{ab};n)$ in equation (A1.24) into equation (A1.23) the aerodynamic admittance may be computed. The evaluation of this integral is difficult and at low $n\ell/\bar{U}$ it yields values for the admittance of less than unity, depending on the parameter L_x/ℓ. The value of the admittance at low $n\ell/\bar{U}$ decreases as L_x/ℓ decreases. This prediction is not in accord with experimentally measured admittances. As $L_x/\ell \to \infty$ the theoretically predicted admittance function is the closest to the measured admittances. Vickery (1965) has suggested an empirical form of the admittance fitted to the measured admittances of various bluff bodies in turbulent flow, as

$$\bar{\chi}^2(n) = \frac{1}{\left[1 + \left(\frac{2n\sqrt{A}}{\bar{U}}\right)^{4/3}\right]^2} \qquad \text{(A1.25)}$$

where A is the frontal area of the body.

CHAPTER 5

UNSTEADY FLOW AROUND THE BLUFF CYLINDERS

INTRODUCTION

The two-dimensional flow around bluff cylinders whose axes are perpendicular to the flow direction has attracted considerable interest over the years. One of the major properties of such a flow is the periodic shedding of vortices into the wake. Much of the work concerning this property of the flow has been reviewed by Berger and Wille (1972). The vortex shedding gives rise to a fluctuating pressure distribution on the surface of the body such that fluctuating lift and drag forces act on the body. The frequency of the fluctuating lift is the same as the freuency of vortex shedding, whereas the fluctuating drag frequency is twice that of the vortex shedding. The magnitude of the fluctuating lift force is usually much greater than the magnitude of the fluctuating drag. Hence, if the body is flexible, or flexibly mounted, the usual response is for the body to oscillate transversely to the flow direction. If the vortex shedding frequency is close to the natural frequency of the body, the motion may become large enough to control the shedding process. The frequency of vortex shedding may then become synchronised with the oscillation. Substantial changes in the wake properties take place during lock-in and, for example, the correlation of the vortex shedding over the length of the body becomes much greater.

Lock-in may also occur if the body is forced to oscillate near the vortex shedding frequency, over a range of reduced

velocities, $\bar{U}/n_o D$, close to $\frac{1}{S}$, where n_o is the frequency of the forced oscillation, and $S = nD/\bar{U}$ where n is the frequency of vortex shedding. Koopman (1967) and Griffin and Ramberg (1976) have shown that the range of reduced velocities over which lock-in occurs depends on the amplitude of the oscillation. Bishop and Hassan (1964) have shown, for a circular cylinder, that when lock-in takes place there is a substantial increase not only in the oscillatory lift force but also in the mean drag. These increases can cause serious damage or even failure of bluff structures or structures with bluff components.

The work concerned with vortex shedding from oscillating bluff cylinders has been reviewed by Sarpkaya (1979) and Bearman (1984). In addition, McCroskey (1977), in a general review of unsteady fluid dynamics, included a section on the above topic. From the reviews it can be seen that most of the investigations have been concerned with circular cylinders having a transverse motion, either where the motion was induced by vortex shedding, or where the circular cylinder was forced to vibrate at a constant amplitude. However, bodies with other shapes have been used, for example, Bearman and Obasaju (1982) investigated the fluctuating pressure distribution on a square section cylinder forced to vibrate transversely to the flow direction. Also, Davies (1976) examined the detailed wake properties of a transversely oscillated D-section when the shedding was locked-in to the motion, and compared these wake properties to those of the stationary D-section in steady flow.

Whilst most of the investigations have concerned transverse motion, there have been some studies in which the cylinder vibration was in-line with the flow direction. An interesting example

of this type of flow has been described by Wooton, Warner and Cooper (1974), who investigated the behaviour of three full-scale piles attached to the jetty at Immingham. They found that the in-line vibration of the piles occurred not only when the shedding frequency was about half the natural frequency of the piles but also when it was about one third of the natural frequency. For the latter vibration, the vortices were shed symmetrically and it was only further downstream that the familiar arrangement of staggered vortices became apparent. King, Prosser and Johns (1973) found that model piles exhibited the same behaviour, but whilst lock-in occurred for the former vibration, it did not for the latter.

Lock-in may also occur if the body is forced to oscillate in-line with the flow direction, near twice the vortex shedding frequency, over a range of reduced velocities close to $\frac{1}{2S}$. Tanida, Okajima and Watanabe (1973) measured the lift and drag forces acting on, and the frequency of vortex shedding from, a circular cylinder which was given an in-line vibration of constant amplitude as it was towed through still water. For Reynolds numbers of 80 and 4000, lock-in was found in which the vortex shedding frequency remained at half the cylinder frequency over a range of cylinder frequencies. The range included the frequency which was twice that of vortex shedding from the cylinder when it was not vibrated. Griffin and Ramberg (1976) measured the variation of the threshold amplitude for lock-in with the cylinder frequency at a Reynolds number of 190, and also the characteristics of the two distinct vortex wake patterns which were found with lock-in.

Very few investigations have been carried out on the case of

a stationary body held in a uniform flow with a superimposed oscillatory perturbation. It was remarked in Chapter 4 that for incompressible fluids a body oscillating in-line with the flow direction in a steady flow, is equivalent to a body held stationary in a uniform flow with the appropriate superimposed oscillatory perturbation. A more complete discussion of this remark is given in section (c) of this chapter.

On the basis of this remark one would, therefore, expect lock-in to occur when the frequency of the perturbation was close to twice that of the vortex shedding. Some work has been done with a mean flow with a superimposed oscillatory perturbation. For example, Chen and Ballenjee (1971) measured the instantaneous frequency of vortex shedding from a stationary circular cylinder in an oscillatory flow, but only for perturbation frequencies very much less than the shedding frequency. However, it appears that the only experimental investigation of the possibility of lock-in for this type of flow has been by Hatfield and Morkovin (1973). They measured the fluctuating surface pressure on a circular cylinder at a position close to the separation point and concluded that no lock-in took place for a range of perturbation frequencies about the shedding frequency. However, the range of perturbation frequencies did not extend to twice the shedding frequency, where lock-in is expected.

Finally, some numerical work has been done by Clements (1975), who used a discrete vortex model to examine the formation of vortices behind a blunt based body. The free-stream was given an oscillatory perturbation, and lock-in was predicted by the model for frequency ranges about twice and four times the shedding frequency. Three

perturbation amplitudes were used and it was found that the frequency range range for lock-in increased as the amplitude increased. Also, an examination of the mean drag showed that a substantial increase occurred during lock-in.

The purpose of the investigation described in this chapter was to study the vortex shedding from a bluff cylinder in a uniform flow whose velocity has an oscillatory perturbation. Three bluff cylinders were used, namely a circular cylinder, a flat bar and a D-section. A description of these bluff cylinders is given in Chapter 2. Lock-in was found for each of the cylinders. The effect of the perturbation amplitude on the range of lock-in, the base pressure coefficient, the wake profiles and the correlation length was studied. For the circular cylinder, the mean and fluctuating pressure distribution around the surface, was investigated.

The results presented are expected to be relevant to the flow around a body which itself is downstream of a two-dimensional bluff body, and also to the flow about a marine structure subject to a steady current and waves.

Throughout this chapter and Chapters 6 and 7, n_o is used to refer to the perturbation frequency, and n is used to refer to the vortex shedding frequency. Also, $\overline{U}/n_o D$ is referred to as the reduced velocity and $n_o D/\overline{U}$ is referred to as the reduced frequency.

(a) STEADY FLOW MEASUREMENTS

The cylinders were mounted in turn at the cylinder position and measurements of the vortex shedding frequency in steady flow were made. The frequency of the shedding was determined from a Fourier analysis of the voltage output of a hot-wire positioned 30 cm downstream of the cylinder position and 20 cm below the centre line of the cylinder. Figure 5.1 shows the measurements of the Strouhal number plotted against Reynolds number. The area blockage ratio of the circular cylinder and the flat plate was 9.2% and that for the D-section was 10.0%. The results have not been corrected for the effects of blockage. The Strouhal number shows little variation with Reynolds number over the range of Reynolds numbers investigated. Figure 5.2 shows the base pressure coefficients for each of the sections plotted against Reynolds number. Again the results are not corrected for blockage effects and show that the base pressure coefficients vary only slightly over the range of Reynolds numbers investigated. The base pressure measurements are in agreement with those made by West and Apelt (1982) for a circular cylinder having approximately the same blockage and aspect ratios.

The measurements of the base pressure coefficient along the span of the cylinders is shown in Figure 5.3. The base pressure coefficients, C_{pb}, are uniform along the span of the cylinders These results indicate that the flow around the cylinders is reasonably two-dimensional.

Measurements were made of the correlation of the vortex

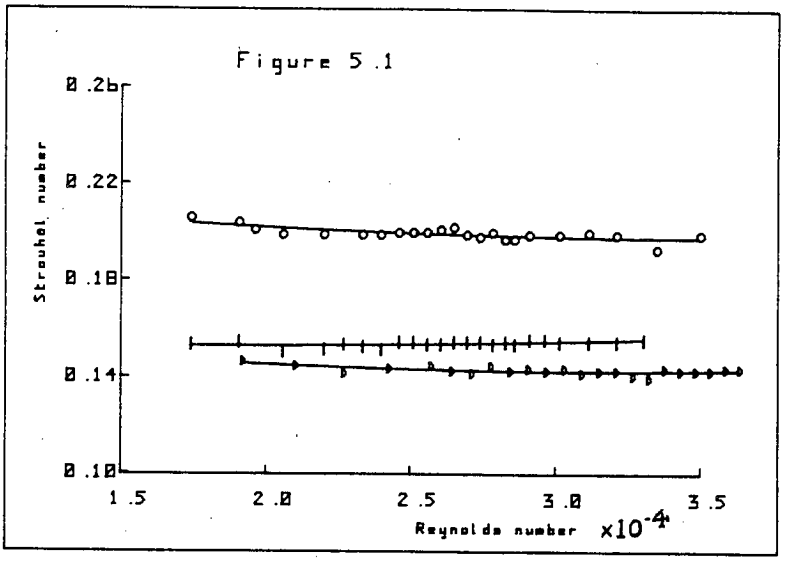

Figure 5.1. The variation of the Strouhal number with Reynolds number for the three bluff cylinders.
○ the circular cylinder ; | the flat plate ; D the D-section.

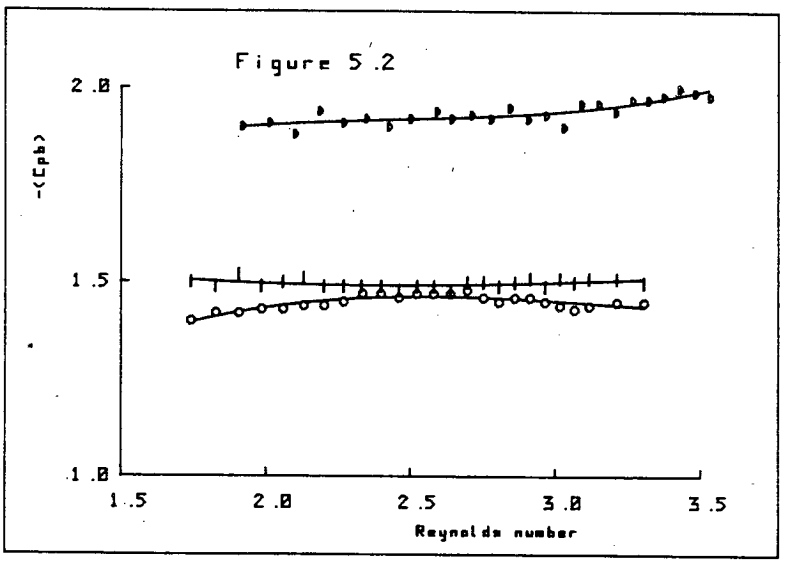

Figure 5.2. The variation of the base pressure coefficient with Reynolds number for the three bluff cylinders.
○ the circular cylinder ; | the flat plate ; D the D-section.

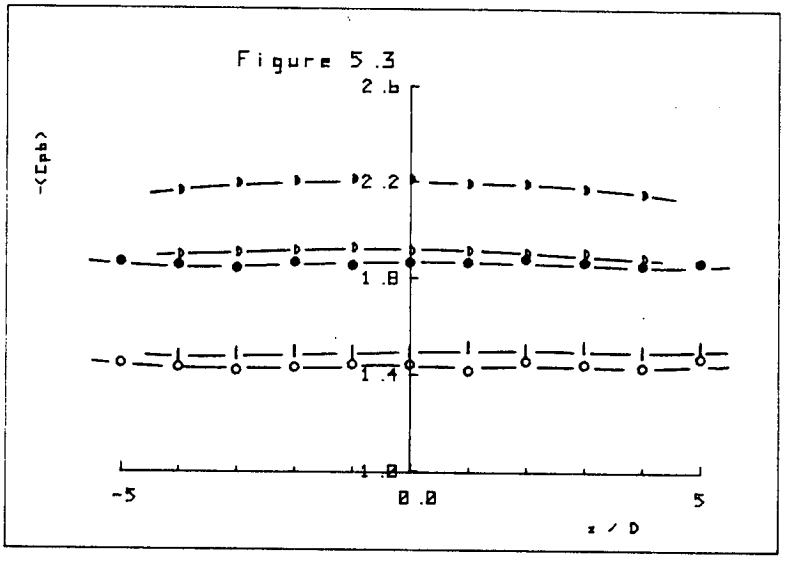

Figure 5.3. The spanwise variation of the base pressure coefficient.
○ *The circular cylinder, $\bar{U}$ = 3.19m/s, steady flow ;*
● *the circular cylinder, $\bar{U}$ = 3.19m/s, n_o=12.36Hz, shutters D ;*
| *the flat plate $\bar{U}$ = 3.19m/s, steady flow ;*
D *the D-section $\bar{U}$ = 3.19m/s, steady flow ;*
◗ *the D-section, $\bar{U}$ = 3.19m/s, n_o=9.24Hz, shutters D.*

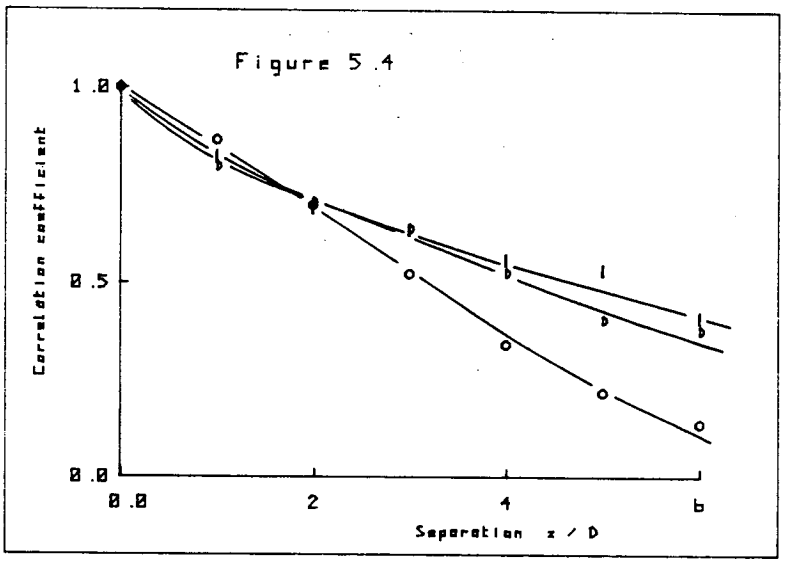

Figure 5.4. The correlation of the vortex shedding for the three bluff cylinders.
○ *the circular cylinder ;* | *the flat plate ;* D *the D-section.*

shedding along the span of each cylinder in steady flow. A hot-wire was fixed at a spanwise position of - 2.5D from the centre of the cylinder, 20 cm above the cylinder centre line and 30 cm downstream of the cylinder position. A second hot-wire was traversed in 1D steps in the spanwise direction from just adjacent to the first hot-wire to a position of +3D. The results are plotted in Figure 5.4. The correlation lengths of the vortex shedding are estimated as the area under the curves presented in Figure 5.4. The correlation lengths for the circular cylinder, the flat plate, and the D-section are 3D, 4.4D and 5D respectively. These results are in agreement with those of other workers [see Sarpkaya (1979) and Davies (1975)].

(b) THE PERTURBED FLOW MEASUREMENTS

i) The Frequency of Vortex Shedding

With the perturbation frequency held constant, measurements were made of the frequency of vortex shedding from a cylinder as the mean flow velocity was varied. The vortex shedding frequency was detected by a hot-wire placed downstream of the cylinder just outside its wake. A second hot-wire and a pitot-static tube were placed a distance of approximately 10D upstream of the cylinder position and 3D above the cylinder's centre line to measure the perturbation amplitude and the mean velocity of the flow respectively. The signal from the hot-wire was low-pass filtered at 31.5 Hz and the perturbation amplitude was measured using a Bruel and Kjaer rms meter. The measurements of the shedding frequency were obtained by Fourier analysis of the digitised

hot-wire signals and the error in each measurement was ± 0.4%. For the circular cylinder and the flat plate a perturbation frequency of 12.36 Hz was used, whilst a frequency of 9.24 Hz was used for the D-section. A typical time history of the hot-wire signals when the shedding was locked-in to the flow perturbation is shown in Figure 5.5. Figure 5.6 shows the ratio of the shedding frequency to perturbation frequency plotted against the reduced velocity for the case of the circular cylinder. The results for the perturbed flows generated by shutters A and C are shown. It can be seen that the shedding frequency is locked-in to the perturbation frequency such that over a range of reduced velocities the shedding frequency remains constant at exactly half the perturbation frequency. Similar results to those of Figure 5.6 were obtained for the flat bar and the D-section. The measurements were taken by increasing the mean wind speed in small successive steps. However, results of measurements obtained by decreasing the mean wind speed in successive steps showed no differences from those obtained by increasing the mean wind speed.

Lock-in was also observed when the perturbation frequency was varied and the flow velocity was held constant. However, this was not a particularly satisfactory method as the flow velocity had to be adjusted every time the perturbation frequency was changed. Also, as can be seen in Figure 4.11(a), the perturbation amplitude varies considerably with the perturbation frequency, at a constant mean velocity of the flow. Even with the method used, in which the preturbation frequency was held constant and the flow velocity varied, the perturbation amplitied varied. However, over the range of reduced velocities used the change in amplitude was small.

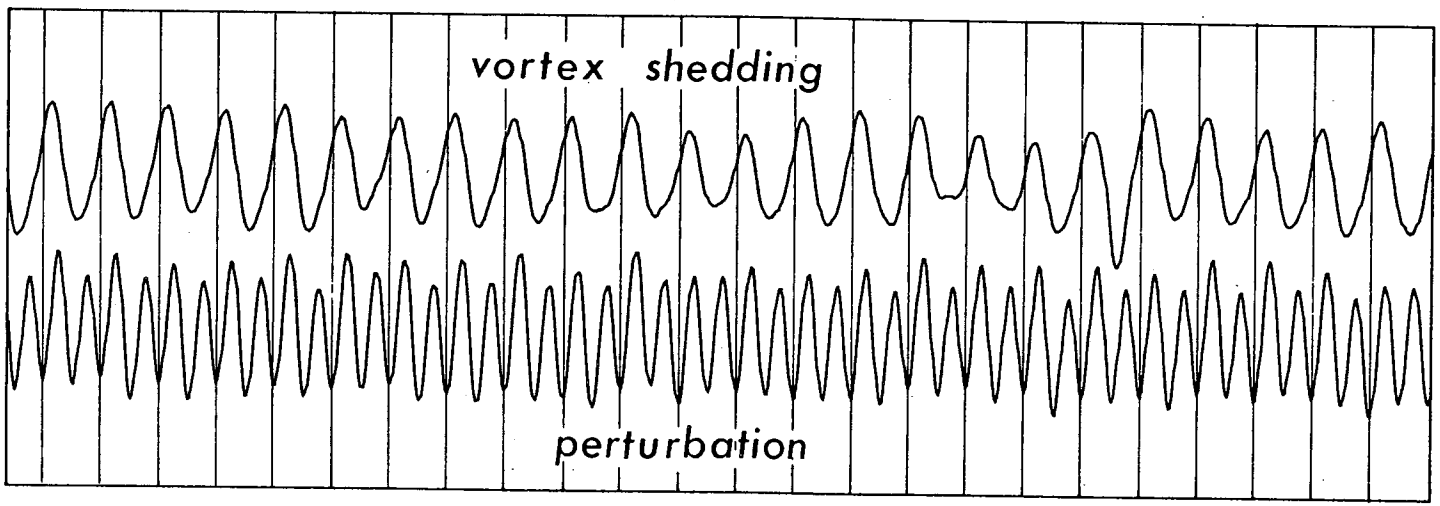

Figure 5.5. A time history of the flow perturbation and the vortex shedding sensor during lock-in.

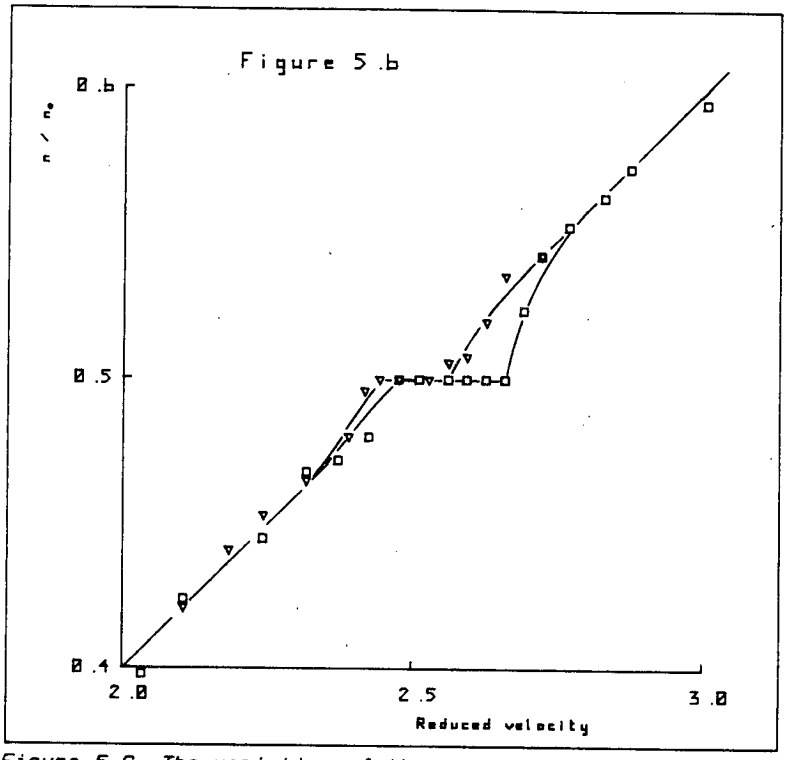

Figure 5.6. The variation of the vortex shedding frequency with reduced velocity for the circular cylinder.
▽ *shutters A, n_0=12.36hz.*
□ *shutters C, n_0=12.36Hz.*

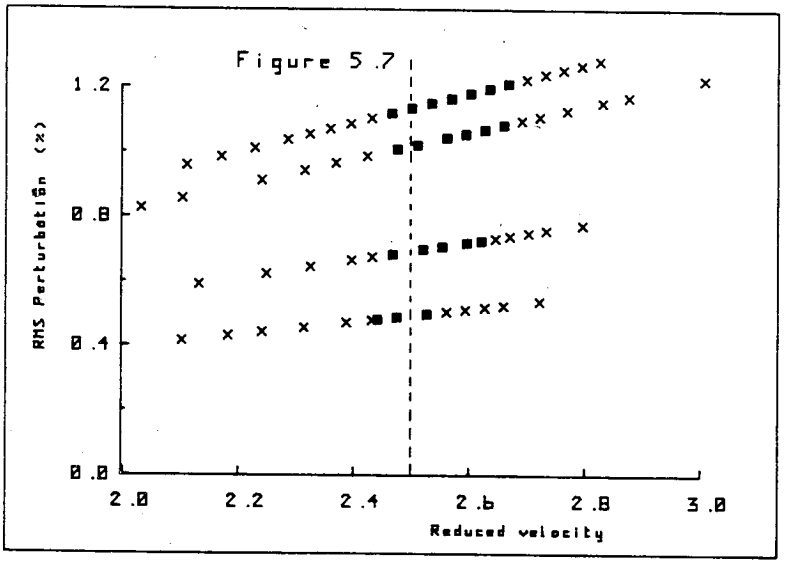

Figure 5.7. The variation of the range of lock-in with the perturbation amplitude fot the circular cylinder.
X *vortex shedding not locked-in ;* ■ *vortex shedding locked-in.*

The effect of changing the perturbation amplitude on the range of lock-in was investigated by using the four different sets of shutters A, B, C and D in turn. The criterion used to define lock-in was that the ratio of the vortex shedding frequency n, to the perturbation frequency n_o should be such that $0.495 \leq \frac{n}{n_o} \leq 0.505$. This criterion was based upon the accuracy with which $\frac{n}{n_o}$ was measured. n_o was measured to an accuracy of 0.1%. The Fourier analysis of the vortex shedding signal determined n to an accuracy of ± 0.4%. This was the accuracy associated with the resolution bandwidth of the Fourier analysis. However, the bandwidth of the vortex shedding signal was approximately the same as the resolution bandwidth of the Fourier analysis and, therefore, the error in n was greater than ± 0.4%. It was, therefore, decided that the above criterion should be used to determine whether or not lock-in had occurred. The effect of the perturbation amplitude in the range of lock-in for the circular cylinder, is shown in Figure 5.7. The results show that the range of reduced velocities for which there is lock-in, increases as the perturbation amplitude $u'/\overline{U}$ increases. The dotted line marked in Figure 5.7, and also in Figures 5.8 and 5.9, indicates the resonant point at which the perturbation frequency is exactly twice the vortex shedding frequency that would occur in a steady flow with the same mean free-stream velocity as the perturbed flow. The figure also shows the small increase in the perturbation amplitude as the flow velocity is increased for a given shutter size. The change in the perturbation amplitude between successive measurements was too small to be resolved by the Bruel and Kjaer rms meter. Therefore, the perturbation amplitude was

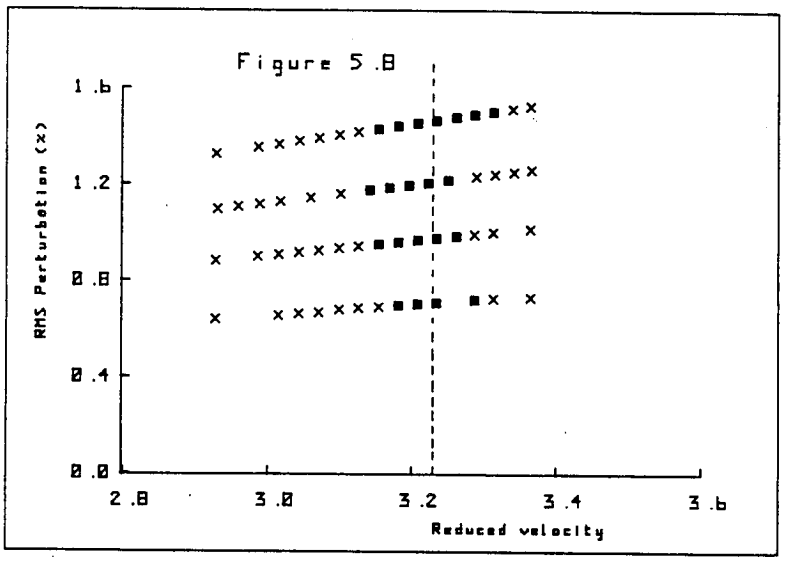

Figure 5.8. The variation of the range of lock-in with the perturbation amplitude for the flat plate.
X *vortex shedding not locked-in ;* ■ *vortex shedding locked-in.*

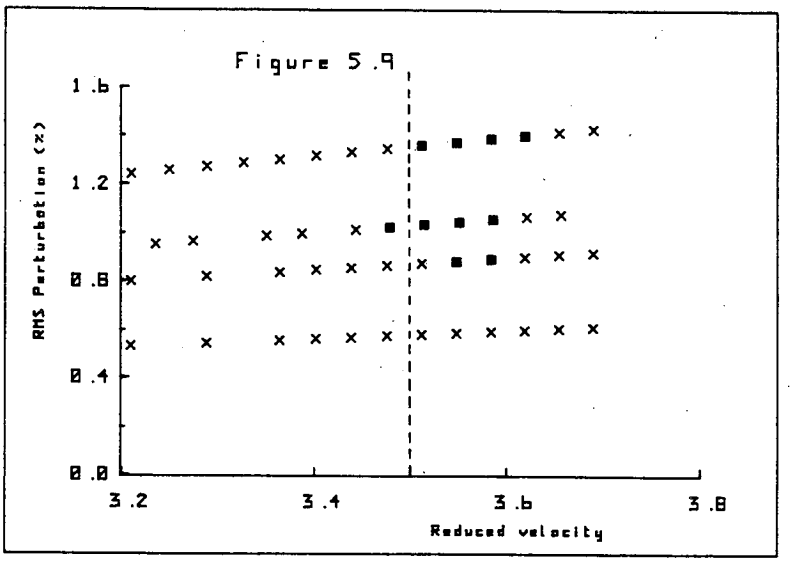

Figure 5.9. The variation of the range of lock-in with the perturbation amplitude for the D-section.
X *vortex shedding not locked-in ;* ■ *vortex shedding locked-in.*

measured at several widely separated velocities and the perturbation amplitude was interpolated at the velocities in between by assuming a linear increase in the amplitude of $u'/\bar{U}$ with the mean flow velocity.

Figures 5.8 and 5.9 show the variation of the lock-in range with the perturbation amplitude for the flat plate and the D-section respectively. The ranges are only about half the comparable ranges for the circular cylinder. Also, Figure 5.9 shows that no lock-in was observed at the smallest perturbation amplitude.

Bearman (1984) has pointed out that for cylinders undergoing forced vibration the position of the resonant point relative to the lock-in range is dependent on the shape of the cylinder. In the present case, the resonant point occurs when the reduced velocity has a value which is equal to $1/2S$. For the circular cylinder the Strouhol number is 0.200 and it can, therefore, be seen from Figure 5.7 that the resonant point lies within the lock-in ranges and close to their lower limits. This result may be compared with the finding by Bearman and Currie (1979) that, for the case of a circular cylinder in forced vibration, the resonant point was at the beginning of the lock-in range. Taneda et al., however, found that the lock-in range straddled the resonant point for a circular cylinder oscillating in-line or transverse to the flow direction.

For the flat plate and the D-section the values of the reduced velocities of the resonant points are 3.23 and 3.50 respectively. The resonant point for the flat plate lies well within the lock-in ranges, whilst that for the D-section lies at the beginnings of the ranges. Bearman and Obasaju (1982) found that for both a D-section

and a flat plate the lock-in range straddles the resonant point and therefore the present result for the D-section would seem to disagree with that found for a vibrating D-section. However, it should be noted that the error in the measurement of the free-stream velocity is ± 0.7% and that the lock-in range, even for the largest perturbation is less than 4% of the value of the reduced velocity at the resonant point. Therefore, no special significance should be put on the disagreement.

ii) Mean Pressure Measurements

Measurements were made of the mean base pressure through lock-in and the results for the circular cylinder are shown in Figure 5.10. The effect of the different perturbation amplitudes on the base pressure can be seen clearly with the base pressure reduction with lock-in becoming larger when the perturbation is increased. Figure 5.11, in which the ratio of the minimum value of the base pressure at lock-in to the value when there is no perturbation is plotted against the perturbation amplitude, illustrates this effect clearly. For a perturbation produced by shutters D the base pressure coefficient of the circular cylinder decreases from approximately -1.44 with no lock-in to -1.85 with lock-in.

The base pressure of a circular cylinder can be affected by the design of the end plates [Stansby (1974)]. The effect of the end plates on the base pressure was investigated for the case of the circular cylinder. Figure 5.12 shows the variation of the mean base pressure coefficient through lock-in. The end plate sizes were 0.3m,

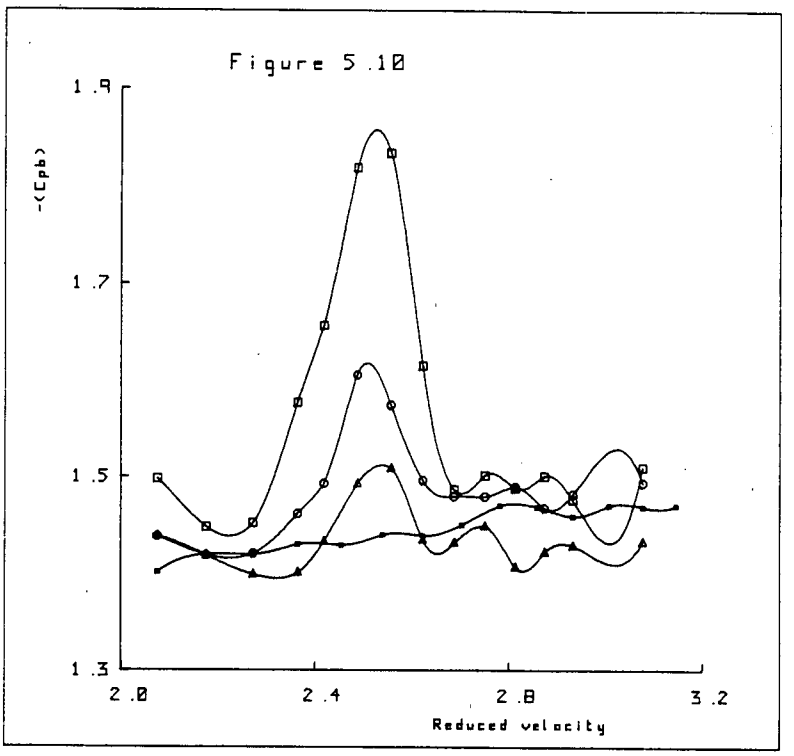

Figure 5.10. The variation of the base pressure coefficient with reduced velocity for the circular cylinder with n_o = 12-36Hz. ■ steady flow ; △ shutters A ; ○ shutters B ; □ shutters D.

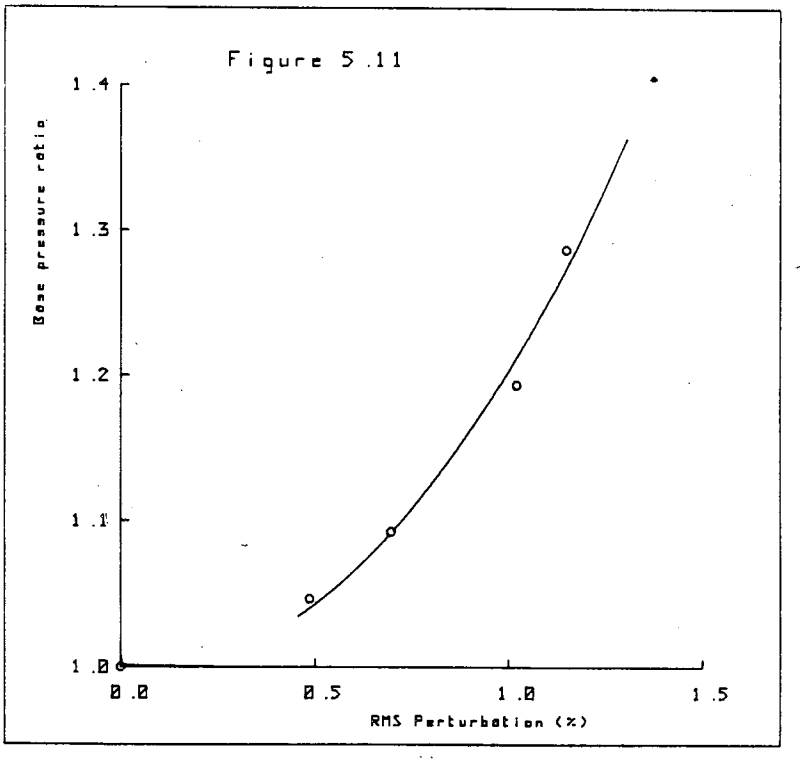

Figure 5.11. The ratio of the minimum base pressure coefficient in lock-in to the steady flow base pressure coefficient versus the perturbation amplitude.

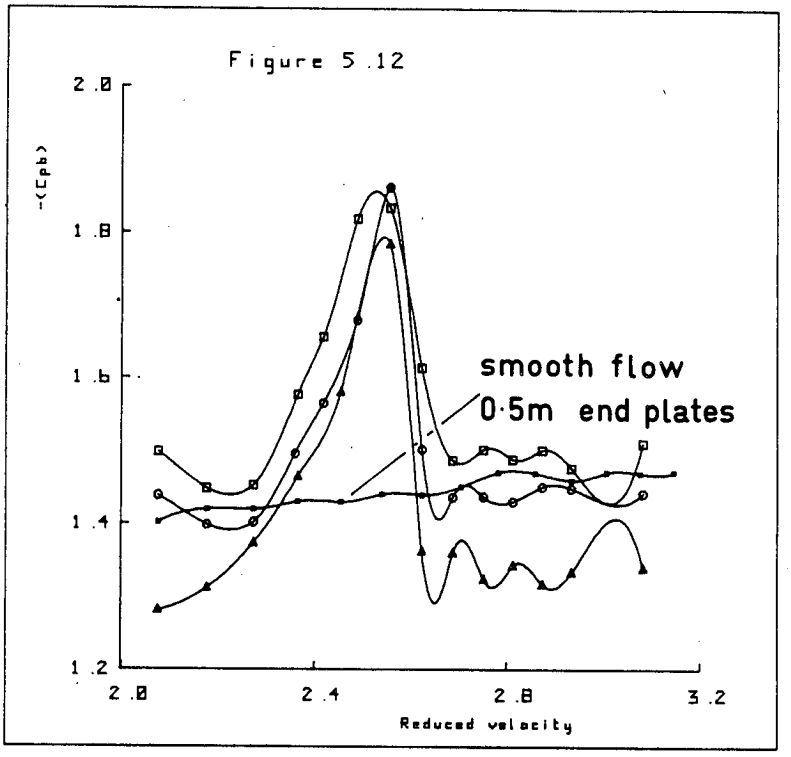

Figure 5.12. The variation of the base pressure coefficient with the reduced velocity for the circular cylinder fitted with each of the end plates in turn. $n_o = 12{\cdot}36$ Hz.
△ *0.3m diameter end plates ;* ○ *0.4m diameter end plates ;*
□ *0.5m diameter end plates.*

0.4m and 0.5m. At lock-in the mean base pressure decreases to approximately the same value, but in steady flow the base pressures are slightly different. The Strouhal number for the circular cylinder was 0.200 for each set of end plates and the lock-in range was unaffected by the change of end plates.

For the flat plate and the D-section Figures 5.13 and 5.14 show that the decrease in the base pressure coefficient is only about half that for the circular cylinder. The decrease in the base pressure found with lock-in is in accord with those results found for a circular cylinder, flat plate and D-section, in forced vibration [Davies (1975) and Stansby (1976)].

Measurements were also made of the base pressure along the span when the shedding frequency was locked-in to the perturbation frequency for both the circular cylinder and the D-section. The results for the base pressure coefficient are shown in Figure 5.3 and for both cylinders the base pressure is uniform along the span.

The surface pressure distribution for the circular cylinder was measured by using the central pressure tapping and rotating the cylinder about its axis. With the perturbation frequency and flow velocity set to produce lock-in, the effect of different perturbation amplitudes was investigated by using all four shutter sets in turn. The results are shown in Figure 5.15. The effect of increasing the perturbation amplitude appears to be limited to reducing the base pressure coefficient at angular positions greater than 60°. The drag coefficient was calculated from the pressure distribution and it increased from 1.28 in steady flow to 1.52 in a perturbed flow produced by shutters D.

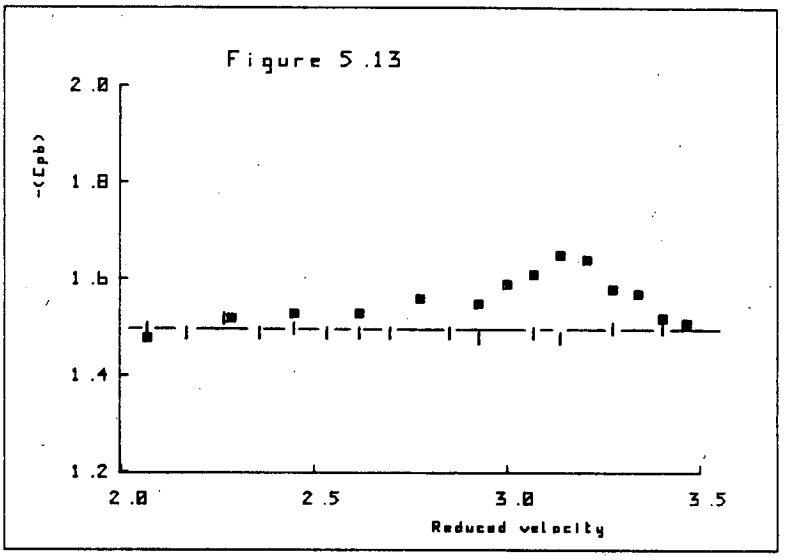

Figure 5.13. The variation of the base pressure coefficient with reduced velocity for the flat plate.
| steady flow ; ■ shutters D, $n_o = 12{\cdot}36$ Hz.

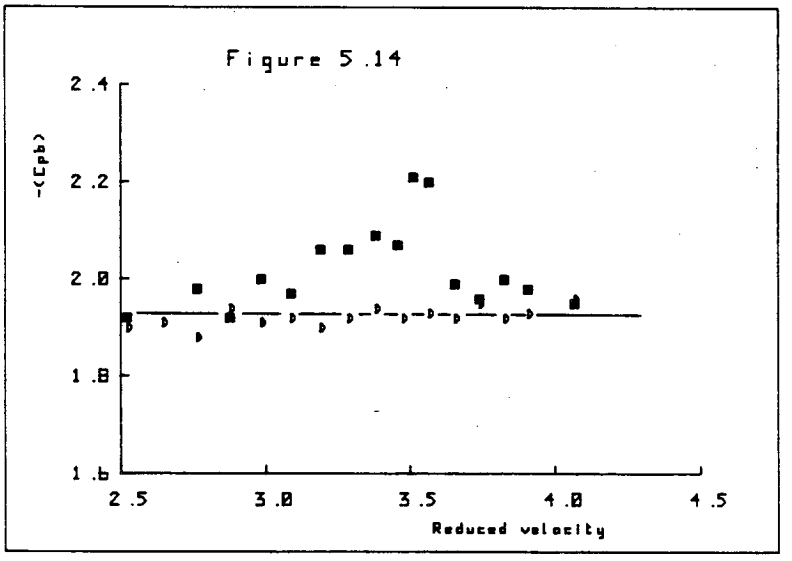

Figure 5.14. The variation of the base pressure coefficient with reduced velocity for the D-section.
D steady flow ; ■ shutters D.

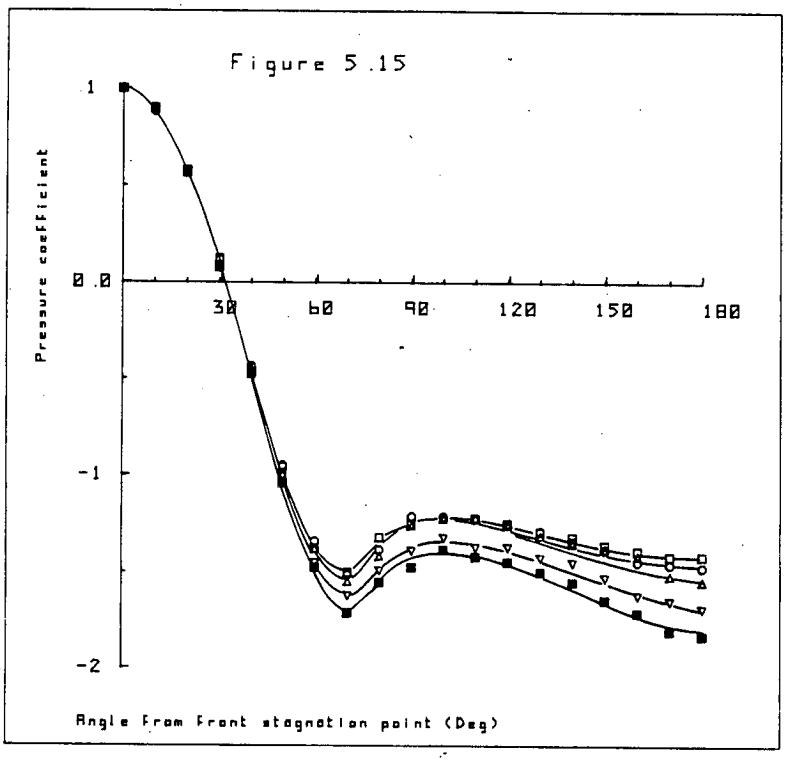

Figure 5.15. The surface pressure distibution around the circular cylinder with $\bar{U}$ = 3.19m/s.
□ *steady flow ;* ○ *shutters A ;* △ *shutters B ;*
▽ *shutters C ;* ■ *shutters D.*

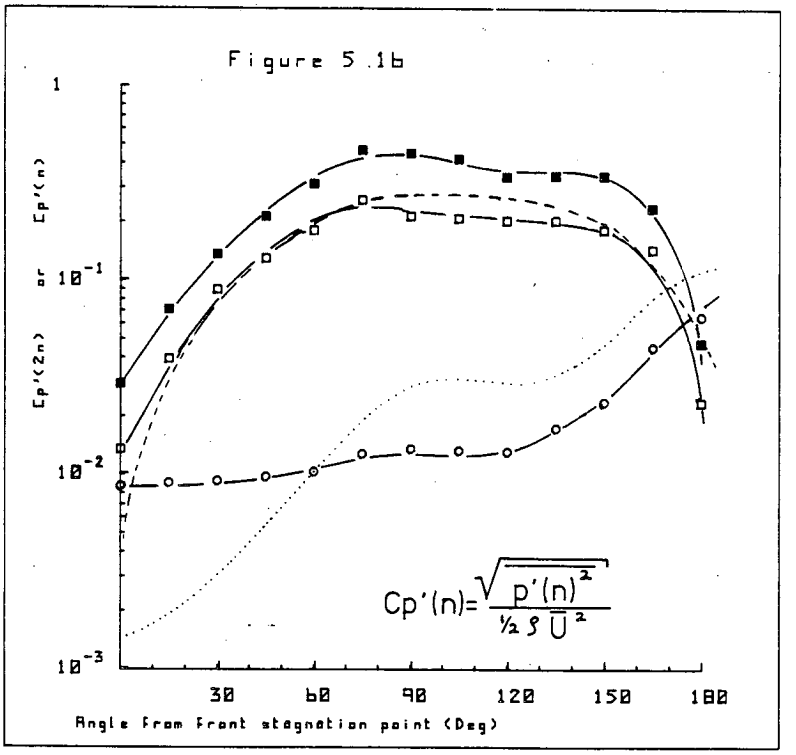

Figure 5.16. The fluctuating surface pressure distribution around the circular cylinder with $\bar{U}$ = 3.19m/s.
□ *Cp'(n) steady flow ;* ■ *Cp'(n), n=12.36Hz, shutters D ;*
○ *Cp'(2n) steady flow.*

iii) The Unsteady Pressure Measurements

A Druck pressure transducer was mounted inside the circular cylinder, as described in Chapter 2, section (f). The total length of the tube between the transducer and the outer surface of the cylinder was 2 cm. The maximum frequency of pressure fluctuation that can be measured with the transducer is reduced as the length of the tube is increased. The frequency response of the transducer with a similar tube of length 3.8 cm was measured by A.J. Baxendale. The frequency response up to about 300 Hz was reasonably constant. The maximum frequency of the fluctuating pressure that was of interest in this investigation. however, was only 25 Hz and, therefore, the frequency response was assumed to be constant over the range of frequencies from OHz to 25Hz. The differential transducer was calibrated with the pressure tapping positioned at the front stagnation point. The reference pressure tapping was connected to the static pressure tapping of the pitot tube. At a number of steady wind speeds, the voltage output of the transducer was recorded. A least squares line was fitted to the plot of the voltage against the pressure $\frac{1}{2}\rho U^2$ and the gradient of this line was the sensitivity of the pressure transducer. When the transducer was used to measure fluctuating pressures the reference pressure tapping was plugged to ensure the reference pressure remained constant. The cylinder tapping connected to the transducer was positioned at 15° intervals from the front stagnation point to the rear stagnation point, and at each position the pressure spectrum was measured. The energy under the spectra over a small band of frequencies around both the vortex shedding frequency and its second harmonic were computed.

The band of frequencies were $n \pm 4\%$ at the vortex shedding frequency and $n_o \pm 2\%$ at the second harmonic of the vortex shedding frequency. The results are presented in Figure 5.16. The dotted lines indicate, approximately, McGregor's (1957) results. The results for $C_p'(2n)$ for the oscillatory flow are not presented as the pressure fluctuations at this frequency are a combination of the pressure fluctuations arising from vortex shedding, and the pressure fluctuations arising from the acoustic radiation of frequency $n_o = 2n$ generated by the operation of the shutters. Figure 5.16 shows that $C_p'(n)$ is increased in oscillatory flow compared to $C_p'(n)$ in steady flow.

An estimate may be made from the results of Figure 5.16 of the fluctuating lift coefficient as

$$C_L' = \sqrt{2} \int_0^{\pi} C_p'(n) \sin\theta \, d\theta$$

[McGregor (1957)].

Using this definition, the estimate of the fluctuating lift coefficient from the steady flow results was $C_L' = 0.48$. McGregor found $C_L' = 0.58$ for a circular cylinder at $Re \sim 4 \times 10^4$. In the oscillatory flow the estimate for C_L' is 0.79. These results suggest that the fluctuating lift coefficient has increased by 65% with lock-in.

(iv) The Correlation Measurements

Measurements were made of the correlation of the vortex shedding along the span of the circular cylinder when the shedding frequency was locked-in to the perturbation frequency. The perturbation frequency was 12.36 Hz and the flow velocity of 3.19 ms^{-1} was chosen, corresponding to the velocity at which the maximum decrease of the base pressure occurred with lock-in. The measurements were made in the same way as the steady flow correlation measurements were made, with one wire fixed at -2.5D from the centre of the cylinder and a second wire traversed in the spanwise direction, in 1D steps to a position of +3.5D. The results for a steady flow and for perturbed flows produced by shutters A, B and C are shown in Figure 5.17. The correlation coefficient for separation lengths greater than 4D increases as the perturbation amplitude increases. However, it is only with the largest perturbation that the coefficient increases substantially. The correlation length for the largest perturbation was estimated to be 5D, whereas that for steady flow was 3D. A uniform perturbation of the flow, therefore, has the effect of improving the synchronisation of vortex shedding along the length of the cylinder.

(v) The Wake Profile Measurements

Measurements were made of the mean velocity and the u component rms turbulence profiles behind each of the cylinders in both steady

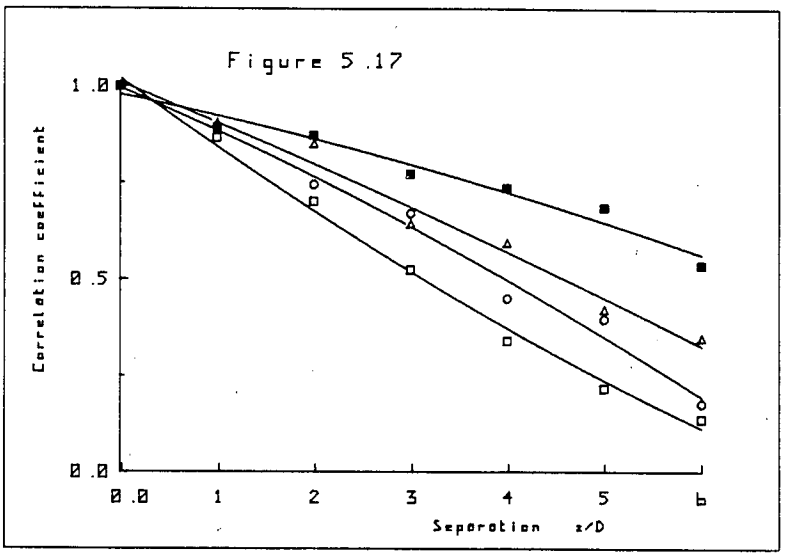

Figure 5.17. The variation of the correlation of vortex shedding from the circular cylinder.
□ *steady flow ;* ○ *shutters A ;* △ *shutters B ;* ■ *shutters D.*

and oscillatory flow. For a given cylinder, the mean velocity was chosen to correspond to the minimum base pressure measured in the cylinder's lock-in range. Therefore, for the circular cylinder, the flat bar and the D-section, the mean velocity chosen was 3.19 ms^{-1}, 3.93 ms^{-1} and 3.59 ms^{-1}, respectively. A hot-wire was positioned 7D downstream of the cylinder position, on the axis of the working section, and was traversed from 3D below the wake centre line to 3D above the wake centre line, in steps of $^{D}/5$. At each measuring position 20K samples of the hot-wire voltage were taken. A cubic least-squares fit to the hot-wire calibration data was used to convert the voltages into velocities from which the mean and rms velocities were calculated. The wake profiles for each of the circular cylinder, the flat bar and the D-section are plotted in Figures 5.18, 5.19 and 5.20, respectively. For the flat bar and the D-section there are no significant changes, within experimental error, in the wake profiles with lock-in. It is possible that the perturbation amplitude is not large enough to cause significant changes in the wake profiles of the flat bar and the D-section. In the case of the circular cylinder, however, the rms of the u fluctuations near the centre line of the wake are increased with lock-in. The mean velocity profile is approximately the same in both steady flow and in oscillatory flow for the circular cylinder. Davies (1975) found that for a D-section cylinder, the mean wake deficit was increased with lock-in compared to the wake deficit of a stationary D-section, whilst the rms turbulence intensity profiles were approximately the same.

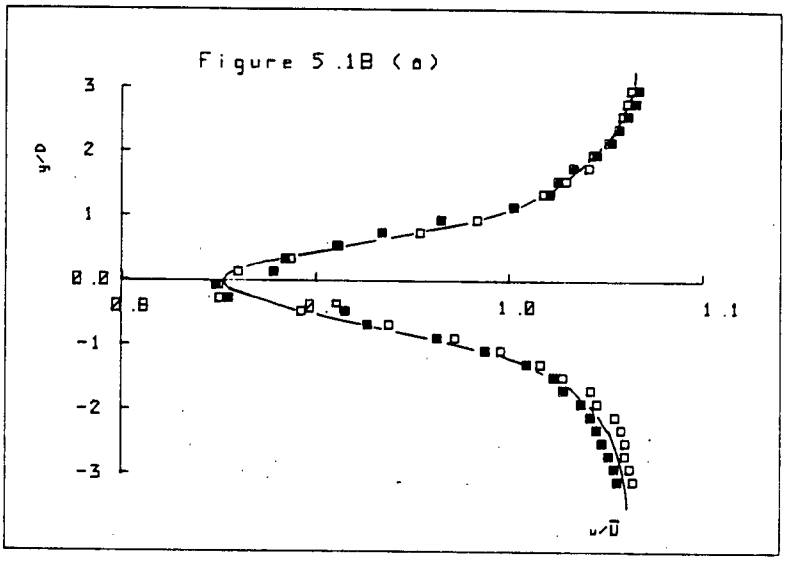

Figure 5.18(a). The mean velocity profile in the wake of the circular cylinder.
☐ *steady flow ;* ■ n_o *=12.36Hz, shutters D.*

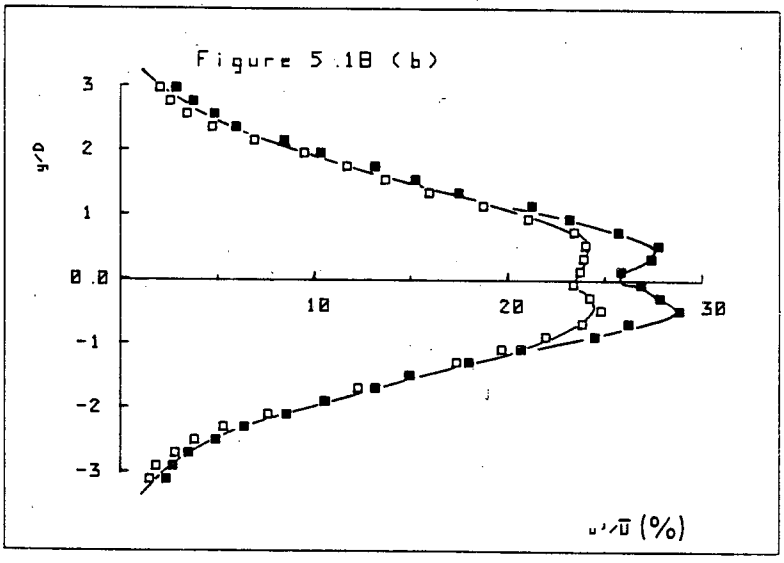

Figure 5.18(b). The variation of the turbulent intensity of the u-component fluctuations in the wake of the circular cylinder.
☐ *steady flow ;* ■ n_o *=12.36Hz, shutters D.*

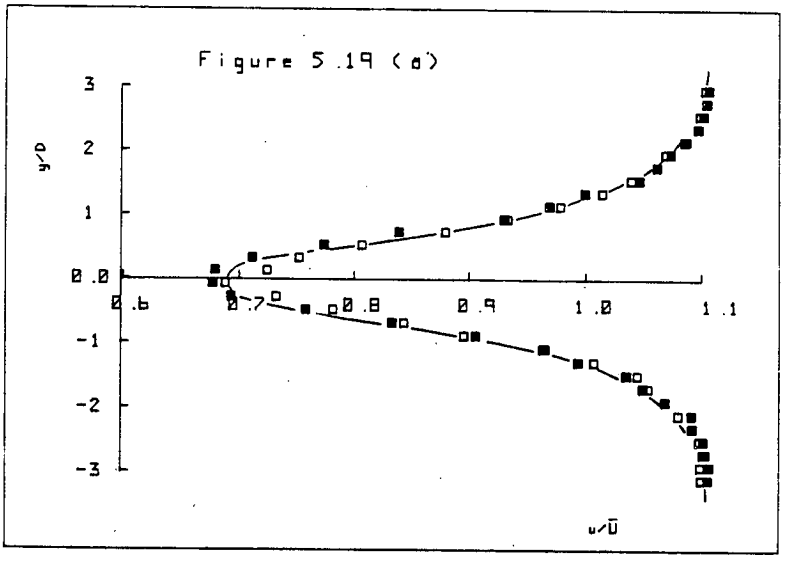

Figure 5.19(a). The mean velocity profile in the wake of the flat plate.
□ steady flow ; ■ n_o=12.36Hz, shutters D.

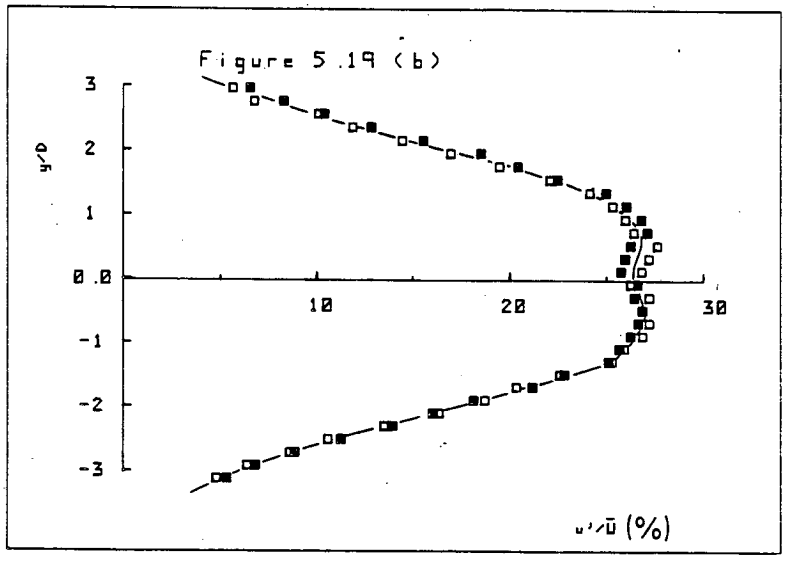

Figure 5.19(b). The variation of the turbulent intensity of the u-component fluctuations in the wake of the flat plate.
□ steady flow ; ■ n_o=12.36Hz, shutters D.

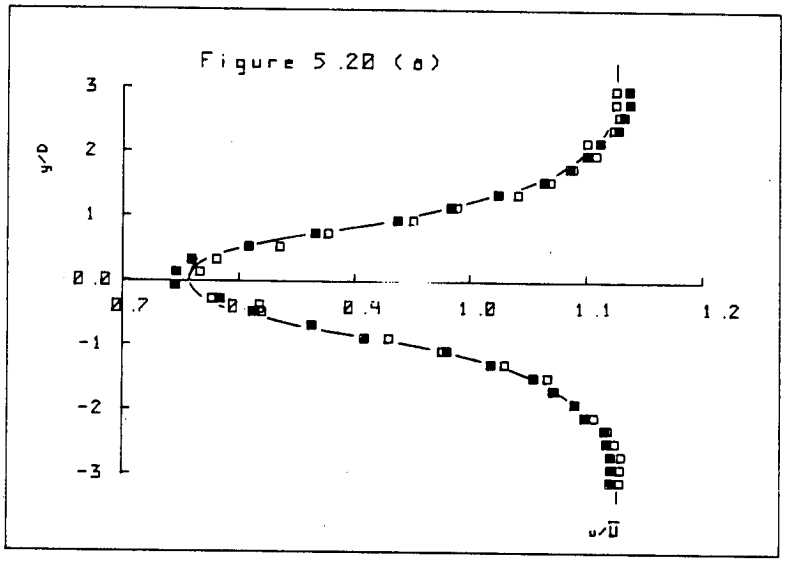

Figure 5.20(a). The mean velocity profile in the wake of the D-section.
□ steady flow ; ■ n_o=9.24Hz, shutters D.

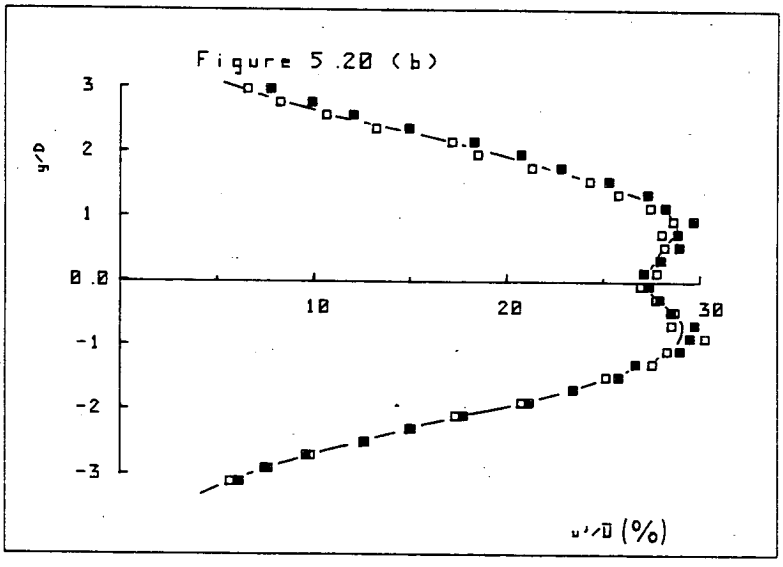

Figure 5.20(b). The variation of the turbulent intensity of the u-component fluctuations in the wake of the D-section.
□ steady flow ; ■ n_o=9.24Hz, shutters D.

(c) Discussion

The purpose of this investigation was to study the vortex shedding from a bluff body in a uniform flow with an oscillatory perturbation. It was stated in the introduction and in Chapter 4 that, for an incompressible fluid, the case in which a stationary body is in a perturbed flow is equivalent to the case in which a body oscillates in-line in a steady flow. For the latter case, if the reference frame is chosen such that the cylinder appears stationary, then a uniform fluctuating inertial force will act through the flow field. The fluctuating inertial force will be exactly balanced, however, by a fluctuating pressure gradient. For incompressible fluids the Navier-Stokes equations for each case are then identical with identical boundary conditions, and, therefore, the resulting flow fields are identical. In reality this cancellation is achieved by sound waves and if the wavelength of the fluctuation is long compared to the length of the body, then the incompressible fluid approximation is valid [Lighthill (1954)]. In Chapter 4 it was remarked that when $\omega\ell/a \ll 1$ the fluid behaves, to a very good approximation, as an incompressible fluid. In the present investigation $\omega D/a \sim 0.002$ and, therefore, the flow field will be very similar to the case of a cylinder vibrating in-line with the flow direction in a steady flow. Therefore, the results of the present investigation are expected to be relevant to the case of a body oscillating in-line with the flow direction.

With regard to the results of section (b), it is interesting to consider the effect of the perturbation amplitude on the amount of circulation which is shed from the cylinder into the wake. A measure

of the rate at which circulation is shed into the detached shear layer downstream of the separation point is given by $\frac{1}{2}U_b^2$, where U_b is the velocity at the edge of the boundary layer at the position of separation. Furthermore, the mean component of U_b^2, $\overline{U}_b^2$, can be related to the mean base pressure C_{pb} as $\overline{U}_b^2 = k^2\overline{U}^2$, where $k^2 = 1 - C_{pb}$. For a bluff body in a flow which far upstream is steady, the fluctuating component of U_b is a result of the unsteadiness of the flow due to the shedding of vortices from the body. Dwyer and McCroskey (1973) found that, for a circular cylinder at a Reynolds' number of 1.06×10^5, the amplitude of the fluctuating component of U_b wa $0.26\overline{U}$, whereas the mean component was $1.42\overline{U}$. Using these results, Davies (1976) showed that the fluctuation contributed approximately 2% only to the total circulation of each sign produced in a vortex shedding cycle and that, therefore, it could be neglected. In the present investigation the contribution to the circulation of the perturbation superimposed on the mean free-stream velocity would appear to be negligible as the amplitude of the fluctuation was less than $0.02\overline{U}$. However, whilst the direct contribution of the perturbation to the shed circulation might be negligible, the perturbation can affect the circulation indirectly by causing lock-in to take place. The base pressure is reduced and the circulation increased. The present results show that for the circular cylinder and a perturbation amplitude of $0.015\overline{U}$ the base pressure is reduced by 29%. Associated with this decrease in the base pressure will be an increase of 17% in the shed circulation.

There is a large amount of cancellation of vorticity in the near wake of the body, where the vortices are formed. Davies (1976) found

found that the fraction of the original circulation that survived into the wake was the same when lock-in took place as when the cylinder was stationary. If it is assumed that the same general behaviour takes place in the present case, then it follows that a 17% increase in the shed circulation produces a 17% increase in the strength of the wake vortices. For such a small perturbation this is a remarkably large increase in the vortex strength, and this result underlines Bearman's remark that interfering with the vortex shedding instability mechanism, may produce large changes in vortex strength, base-pressure, drag and sectional fluctuating lift coefficient. Certainly the present results show that a perturbation of very small amplitude superimposed on a constant mean flow does indeed produce large changes in the base pressure, the fluctuating lift and drag, and also, by inference, a large change in the vortex strength.

The increases in the shed circulation for the flat plate and D-section are 6% and 9%, respectively. These increases are considerably less than the 17% increase found for the circular cylinder. The difference presumably lies in the properties of the separation points - for the flat plate and the D-section they are fixed, whereas for the circular cylinder they are free to move - and also in the effect of the afterbody on the vortex formation process.

The results for the wake profiles for the cylinders are rather unexpected. The mean base pressure measurements suggest that with lock-in a greater amount of circulation is shed into the wake than is shed in steady flow. Therefore, one might expect the strength of the wake vortices to be increased with lock-in. If this is so, and there are no changes in the wake geometry, then an increase in

the mean wake deficit would be expected with lock-in. The mean velocity profiles of the circular cylinder show that no increase in the wake deficit has occurred with lock-in, but the rms profile indicates that larger velocity fluctuations near the wake centre line are present at lock-in. Koopman (1967) and Griffin and Ramberg (1974) found that the lateral spacing of the vortices in the wake of a circular cylinder, was reduced with lock-in. It is possible that the results of the wake profiles of the circular cylinder could be explained on the basis of both a change in the wake geometry and a change in the strength of the wake vortices with lock-in. A more detailed exploration of the wake of the circular cylinder in lock-in and in steady flow is, therefore, required. Such an investigation was carried out and is presented in Chapter 6.

(d) Conclusions

The effects of adding a perturbation of single frequency to a constant velocity flow have been examined for the flow over a bluff cylinder. Three different cylinders, a circular cylinder, a flat plate and a D-section, were used and for each cylinder the frequency of vortex shedding and the base-pressure were measured. It was found that lock-in of the vortex shedding frequency to the perturbation frequency took place such that the shedding frequency remained equal to half the perturbation frequency over a range of reduced velocities. For each of the cylinders the lock-in range included the resonant point.

The lock-in range was found to increase as the perturbation

amplitude was increased. The base pressure decreased with lock-in and measurements made using the circular cylinder showed that the minimum base pressure decreased as the perturbation amplitude was increased. The decrease in the base pressure was smaller for the flat plate and the D-section, both of which have fixed separation points, than it was for the circular cylinder. The surface pressure distribution around the circular cylinder indicated an increase in the steady drag acting on the circular cylinder during lock-in. The distribution of the fluctuating surface pressure indicated a substantial increase in the fluctuating lift acting on the circular cylinder with lock-in.

Measurements were made of the correlation of vortex shedding along the length of the circular cylinder and it was found that the correlation length was increased with lock-in.

Measurements of the mean and fluctuating velocities in the wake of the cylinders showed that, for the D-section and flat plate, no significant changes in the wake profiles occurred with lock-in. For the circular cylinder no change occurred in the mean velocity profile with lock-in, but the turbulent intensity of the velocity fluctuations near the wake centre line increased with lock-in.

Apart from the wake profile measurements, the results described above are consistent with those which have been reported for other cases of lock-in. However, in all those cases lock-in was achieved by vibrating the cylinder in a flow of constant velocity, rather than by perturbing the flow.

CHAPTER 6

THE DETAILED MEASUREMENTS OF THE WAKE OF THE CIRCULAR CYLINDER

INTRODUCTION

In Chapter 5 the effects of adding a single frequency perturbation to a constant velocity flow were examined for the flow over a bluff cylinder. For each cylinder lock-in was found when the perturbation frequency was near to twice the vortex shedding frequency. Measurements of the base pressures, correlation lengths, wake profiles and the range of lock-in were made. In the discussion of Chapter 5 it was remarked that a more detailed exploration of the wake was required to resolve the question of why the mean wake deficit was not changed with lock-in. Measurements of the longitudinal and lateral separation and the strength of the vortices in the wake of the cylinder are required. A number of methods have been used by previous workers to obtain estimates of the vortex strength and spacings.

Bloor and Gerrard (1966) investigated the turbulent wake behind a stationary circular cylinder and at Reynolds numbers of 2000 and 16,000, obtained estimates of the vortex strength and spacings. The longitudinal spacing of the vortices was measured directly from the phase difference between two hot-wires separated longitudinally and positioned just outside the wake. Then, by matching the experimentally measured wake profiles to a viscous vortex model of the wake, they obtained the estimates of the vortex strength and lateral spacing. A brief discussion of viscous vortex models is given in section (d) of this chapter.

Griffin and Ramberg (1974) investigated the wake behind a

circular cylinder oscillating transversely to the flow direction at Reynolds numbers of 144 and 190. They matched the experimentally obtained wake profiles with a viscous vortex model of the wake from which they inferred the vortex strength and lateral spacing. They found that the vortex strength was increased with lock-in and that the lateral separation was reduced.

At a higher Reynolds number of around 2×10^4, Davies (1976) investigated the turbulent wake behind a transversely oscillating D-section. He used a conditional sampling technique to extract the underlying periodic fluctuations in the wake from the turbulent fluctuations in the wake. From these measurements the mean wake was reconstructed so that the vortex strength and lateral separation could be measured directly. The vortex strength was found to increase with lock-in but there were no significant changes in the vortex spacings. Davies also matched his results to a viscous vortex model of the wake, and found that, with the addition of a mean shear to the model, the model gave good agreement with the experimental results.

No measurements appear to have been published on the strength of the vortices in the wake of a cylinder vibrating in-line with the flow direction. Griffin and Ramberg (1976) obtained the vortex spacings in the wake of a circular cylinder vibrating in-line with the flow direction, using a flow visualisation technique. The strength of the vortices, however, could not be measured using this technique. At a Reynolds number of 190 two distinct vortex patterns were observed in the wake. They found many similarities in the characteristics of the wake of an in-line oscillating cylinder with

with those of a transversely oscillating cylinder.

The purpose of the investigation described in this chapter was to examine the structure of the turbulent wake behind a stationary circular cylinder both in steady flow, and in a perturbed flow. In the oscillatory flow the investigation was made when the wake was synchronised with the perturbation, wherein the vortex shedding frequency was exactly half of the perturbation frequency.

Using a conditional sampling technique similar to that used by Davies (1976) direct measurements of the vortex strength and spacings were obtained. Davies appears to be the only previous investigator who has matched conditionally averaged results with a viscous vortex model. In order that a comparison can be made between the results of the present investigation and those of Davies' investigation the present results are also matched with Davies' viscous vortex model. Measurements are also presented of the length of the formation region behind the cylinder.

(a) THE CONDITIONAL SAMPLING TECHNIQUE

At Reynolds numbers of around 2×10^4 the wake behind a bluff body is highly turbulent but contains vortices which are essentially large scale coherent structures of relatively stable and permanent form. The analysis of these structures, in such a wake, is difficult, as the strong influence of the turbulence on the measurements makes interpretation of the hot-wire data difficult. The flow just outside the wake is, however, irrotational and highly periodic, the periodicity arising from the vortices as they sweep past the measuring position.

If a sensor probe and a cross-wire probe are positioned at the same distance downstram of the body, with the sensor probe just outside the wake, the cross-wire signals may be sampled on the basis of the phase of the sensor signal. The phase of the sensor signal may be taken as representing the phase of the vortex cycle. If the cross-wire velocity records, computed from the cross-wire signals, are sampled only when the sensor signal has a particular phase, say ϕ_o, then the mean of these samples represent the mean velocity, at the measuring position, at phase ϕ_o of the vortex cycle. By repeating the sampling process for many different values of ϕ_o, the mean velocity at the measuring position throughout the vortex cycle may be found. The process may be described mathematically by the following.

Suppose that $U(t)$ represents the time varying velocity measured using the cross-wire probe, and has an underlying mean component, $\overline{U}$, an underlying periodic component $\tilde{U}$, and a random component U'. In the following analysis it is assumed that $\langle\tilde{U}\rangle = \langle U'\rangle = \langle\tilde{U}U'\rangle = 0$. If a large number of samples of $U(t)$ are taken then the underlying mean component may be computed as

$$\overline{U} = \langle U_i \rangle = \frac{1}{N_T} \sum_{i=1}^{N_T} U_i \qquad (6.1)$$

where U_i represents the ith sample of $U(t)$ and N_T is the total number of samples of $U(t)$, spanning many cycles of the underlying component $\tilde{U}$. $\tilde{U}$ may be represented by dividing the cycle of $\tilde{U}$ into a number of phase intervals. The value of $\tilde{U}$ within a particular phase interval may be computed by averaging only samples

of U when the reference sensor has a phase within that particular phase interval. The underlying periodic component is, therefore, found, using the sensor signal, by the following method.

$$U + \tilde{U}(\theta_k) = \frac{1}{N_{\theta_k}} \sum_{i=1}^{N_T} U_i \, \mathrm{rect}(\theta_k - \phi_i) \tag{6.3}$$

where $\mathrm{rect}(\theta_k - \phi_i) = 1$ if $-\Delta\theta/2 < \theta_k - \phi_i \leq \Delta\theta/2$

or $-\Delta\theta/2 < \theta_k \pm 2\pi - \phi_i \leq \Delta\theta/2$

$= 0$ otherwise,

where $\Delta\theta = (\frac{2\pi}{N_P})$ and is the phase interval,

N_P = number of phase intervals spanning the vortex cycle of 2π,

θ_k = is the kth phase interval and is centered on $\theta = k\Delta\theta$, where $-N_P \leq k \leq N_P$,

ϕ_i = is the phase of the ith sample of the reference sensor signal mod(2π), (mod$(\theta + 2\pi\ell) = \theta$ for any integer ℓ),

and $N_{\theta_k} = \sum_{i=1}^{N_T} \mathrm{rect}(\theta_k - \phi_i)$, which is the number of samples of U_i in the kth phase interval, θ_k.

$\tilde{U}(\theta_k)$ represents the value of $\tilde{U}$ within the phase interval θ_k.

In (6.3) the rect. function conditionally samples U_i as a particular sample of U, U_i, is included in the computation of $\overline{U} + \tilde{U}(\theta_k)$ only if the phase of the reference sensor, ϕ_i, lies within the kth phase interval θ_k. When ϕ_i lies in the range of the phase interval θ_k, $\mathrm{rect}(\phi_i - \theta_k) = 1$ and the sample U_i is included in

the computation of $\overline{U} + \tilde{U}(\theta_k)$, otherwise it is excluded as $\text{rect}(\phi_i - \theta_k) = 0$. Notice also, that $\tilde{U}$ has been reconstructed over a range of phase from -2π to $+2\pi$. The reason for the extension of $\tilde{U}$ to two cycles is given later.

In this investigation $N_p = 36$, $\Delta\theta = 5°$ and at least 1000 acceptable vortex cycles were analysed. An acceptable vortex cycle is one whose period is $\frac{1}{n} \pm 10\%$, where n is the expected vortex shedding frequency given by $n = \overline{U}St/D$, or in the case of oscillatory flow, $n = \frac{1}{2}n_o$. Thus, $\text{rect}(\theta_k - \phi_i)$ in the above expressions is set to zero if the vortex cycle containing the ith sample of the reference sensor signal is not acceptable. This prevents samples being taken when the sensor signal is not highly periodic. The sensor signal could have been improved by moving the sensor probe further unstream towards the cylinder. However, if the sensor were moved upstream, it would also have to be moved to a position closer to the cylinder centre line, in order to detect the passing vortices. To prevent the wake of the sensor probe support interfering with the cross-wire measurements the sensor probe would also have to be displaced in a spanwise direction. The correlation length of a circular cylinder is, however, much less than the correlation length of sharp edged cylinders, and thus the sensor probe output when placed in such a position, may not be highly related to the flow at the cross-wire position. Therefore, the sensor probe must be positioned as close as possible to the cross-wires. The physical arrangement of the hot-wires, however, prevented their being placed at the same downstream distance from the cylinder and, therefore, the sensor probe was position 6.5D downstream of the cylinder and 3.25D below

the cylinder centre line, on the centre line of the working section. The cross-wire was positioned at 7D downstream of the cylinder position, directly behind the sensor position and traversed through the wake of the circular cylinder from 3D below the cylinder centre line to 3D above the cylinder centre line. The phase difference between the vortex shedding cycle at the sensor position and at the cross-wire position is small and, to a very good approximation, constant. The reconstruction of the vortex cycle will, therefore, be shifted slightly in phase from the phase given by the sensor probe.

The phase of the vortex cycle may be transformed to a position on the x axis by $x = U_c \frac{\theta}{2\pi n}$, where U_c is the vortex convection speed. The assumption used is that the flow field convects past the measuring position without changing appreciably - Taylor's hypothesis. For this investigation Taylor's hypothesis is not strictly applied as the phase is transformed to the x axis, whereas the transformation is actually given by $x = U_c t$, where t is the time axis of the vortex cycle. The method presented here compresses or stretches the time axis, so that all vortices have exactly the same period. The effect on the results will be small as only vortex cycles whose periods are close to the expected period $\frac{1}{n}$ are used in the sampling process. Davies' method, on the other hand, uses the relation $x = U_c t$ to transform the time axis to the x axis, but as a consequence of the variability of the period of the vortex cycle, at the extremes of the vortex cycle the number of samples are fewer than near the zero time lag or zero phase of the vortex cycle. The advantage of the present method is that the number of samples, and hence the statistical accuracy, is the same throughout the vortex

cycle. Since only a small variability in the period of the vortex cycle is accepted, the method is expected to yield very similar results to the results that would be obtained during Davies' method. The reconstruction of the wake has been extended to include two cycles of vortex shedding, or, in terms of the earlier discussion, two cycles of $\tilde{U}$. This means that four vortices appear in the wake reconstruction. The reason for this is so that the measurements of the vortex spacings can be made more easily.

Each reconstructed wake requires 8 hrs of experimental time and approximately 16 hrs of PDP 11 processor time to reduce the data. Approximately 60 Mbytes of data were analysed to produce each wake reconstruction. At least 1000 vortex cycles were used in each of the wake reconstructions. The statistical accuracy of the u or v velocity components may, therefore, be estimated as follows. The 99% confidence interval for the mean, μ, of a normal distribution with known variance, 0.25μ, for a sample size of 1000 is given approximately by $\mu \pm 2\%$. The corresponding 95% confidence interval is approximately given by $\mu \pm 1.5\%$.

The accuracy of the results of the u and v velocity reconstructions is improved by using a Blackman filter, to smooth out the values of u and u velocities over the vortex cycle. The filter is used in a similar fashion to a Hanning function, running in the t or x direction. If a series $S(k)$ is filtered using a Blackman filter, then the filtered series $S'(k)$ is related to the series $S(k)$ by

$$S'(k) = 0.04S(k-2) + 0.25\,S(k-1) + 0.42\,S(k) + 0.25\,S(k+1) + 0.04\,S(k+2)$$

where $0 \leq k \leq 2N_p - 1$.

The series $S(k)$ was, in the case of this investigation, assumed periodic over $2N_p$ samples. The Blackman filter is an example of a non-recursive digital filter with ten degrees of freedom. The accuracy of the smoothed estimates of u and v are estimated to be about 2% of $\overline{U}$ with a 99% confidence level. To improve this accuracy by a factor of 2 would require the conditional averaging of 4 times as many vortex cycles.

Before the conditional sampling technique may be used to reconstruct the vortex structure in the wake of the cylinder, the vortex convection speed must be measured. The speed was measured by placing two hot-wires just outside the wake with one wire 0.45m downstream of the other wire. The upstream wire was placed 6D downstream of the cylinder. The phase difference between the wires was measured and used to compute the longitudinal vortex separation distance. Since the frequency of the vortex shedding was also found from these measurements, the vortex convection speed is easily computed. This method of measuring the vortex convection speed has been used by many workers [Bloor and Gerrard (1966), Davies 1975)]. Davies (1975) points out that errors may occur in the measurement of U_c if the vortices are elliptical and rotating and, therefore, measurements must be made to ensure that U_c is constant. The downstream hot-wire was traversed to various positions further downstream, and the phase difference between the two hot-wire outputs was measured at each of these positions. The phase difference was found to increase linearly with the separation distance of the hot-wires, indicating that the vortices convect downstream with a constant

velocity. In steady flow the vortex convection speed was measured as 0.91 U_o and in oscillatory flow was measured as 0.89 U_o. At a Reynolds number of 16,000 Bloor and Gerrard found that, at a distance of about 6D downstream of a circular cylinder, the vertex convection speed was 0.8 U_o. There is, therefore, a large disagreement between the result for the vortex convection speed obtained in this investigation and the result obtained by Bloor and Gerrard. The blockage in the present investigation, however, was about 10% and, therefore, the mean velocity at the outer wake region was approximately 6% higher than the mean velocity upstream of the cylinder. If the mean outer wake velocity, U_w, is used in the reduction of the vortex convection speed then $U_c/U_w = 0.85$. The high blockage in the present investigation, therefore, appears to have had a considerable effect on the vortex convection speed. This is unfortunate, but as discussed in Chapter 2, the high blockage was unavoidable.

(b) RESULTS

From the records of the conditionally sampled u and v velocity components in the wake of the cylinder, a picture of the whole flow field may be reconstructed. The streamlines were computed using

$$\psi(x, y) = \psi_o + \int udy - vdx \qquad (6.4)$$

and the vorticity in the wake was computed using

$$\omega = -\frac{\partial u}{\partial y} \quad \frac{\partial v}{\partial x} \quad . \qquad (6.5)$$

$\psi_o = 0$ was assumed along $y/D = -3.25$ and $\psi(x,y)$ was computed by integrating upwards from the $\psi = 0$ streamline. The vortex convection speed was subtracted from the u component of the velocities in the wake, so as to make the vortex centres appear stationary. Figure 6.1(a) shows the streamline reconstruction for the case of steady flow, and Figure 6.2(a) shows the reconstruction of the streamlines in the case of the oscillatory flow. The contours of ψ are plotted at 24 equally spaced intervals, ranging from the minimum to the maximum value of ψ occurring in the flow field. The errors in the reconstructions of Figures 6.1(a) and 6.2(a) accumulate as the integration proceeds in the direction of increasing y and this error accumulation is evident in these figures by the greater waviness of the streamlines at the top of the figures compared to the streamlines at the bottom of the figures. In the case of the oscillatory flow reconstruction the errors appear to be worse than in the case of the steady flow reconstruction. This may be a consequence of neglecting the oscillatory perturbation in the free stream velocity, by assuming that U_c has a constant value. This, however, is very unlikely to be the cause of the apparent increase in the errors, as the perturbation amplitude was only 1.15% of $\bar{U}$. It is interesting to note that, in Davies' streamline reconstructions, the apparent errors in the streamline reconstruction of the wake behind the oscillating D-section, were greater than those in the streamline reconstruction of the wake behind the stationary D-section. However, the streamline reconstructions are intended merely as a general impression of the wake and, therefore, the accumulation of the error in the ψ values is not important.

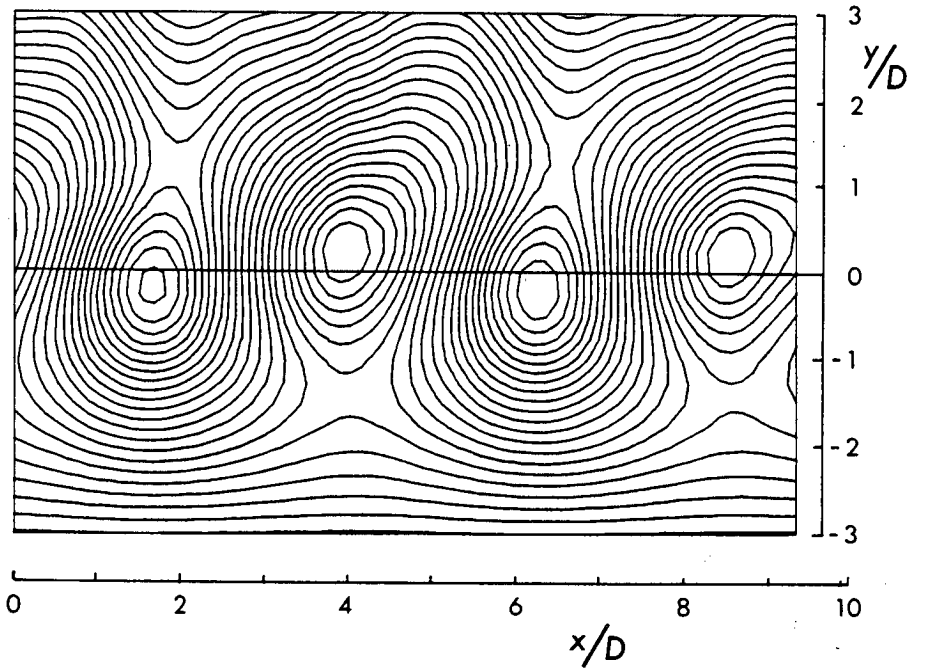

Figure 6.1(a). The reconstruction of the streamlines of the wake of the cylinder in ***steady*** *flow.*

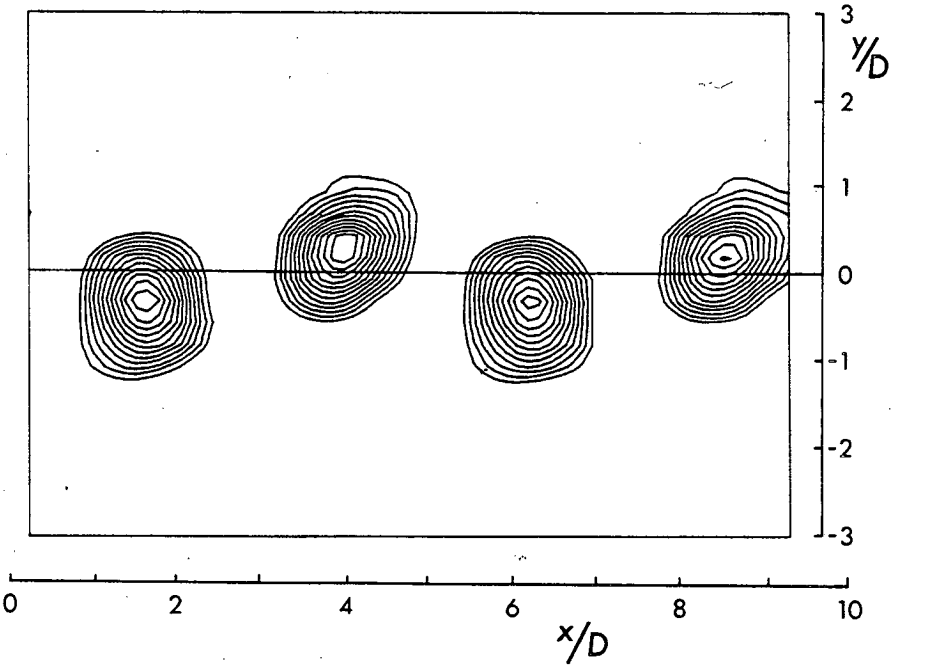

Figure 6.1(b). The contours of vorticity in the wake of the cylinder in ***steady*** *flow with the lowest 30% of the contours removed.*

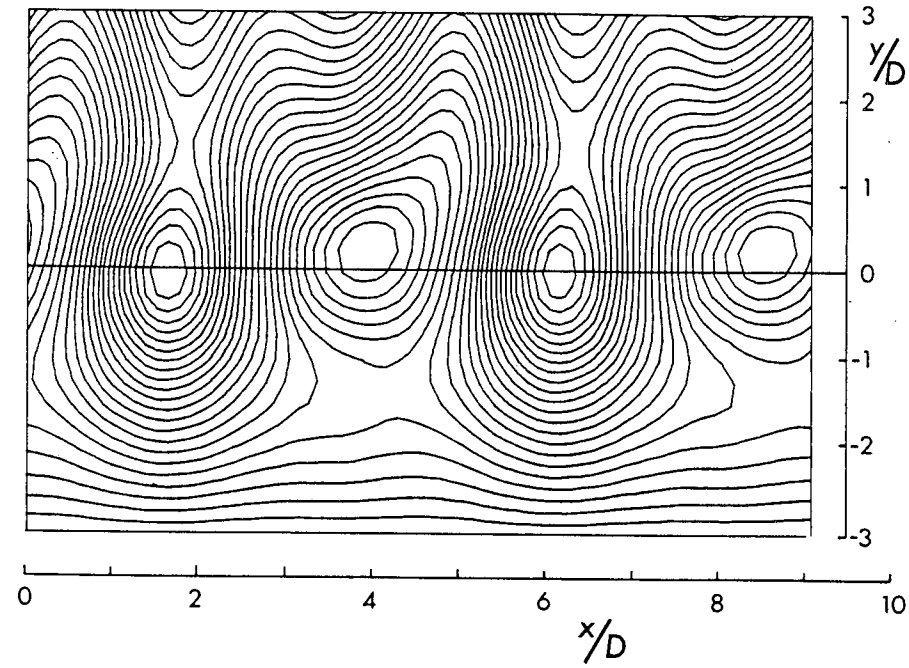

Figure 6.2(a). The reconstruction of the streamlines of the wake of the cylinder in oscillatory flow.

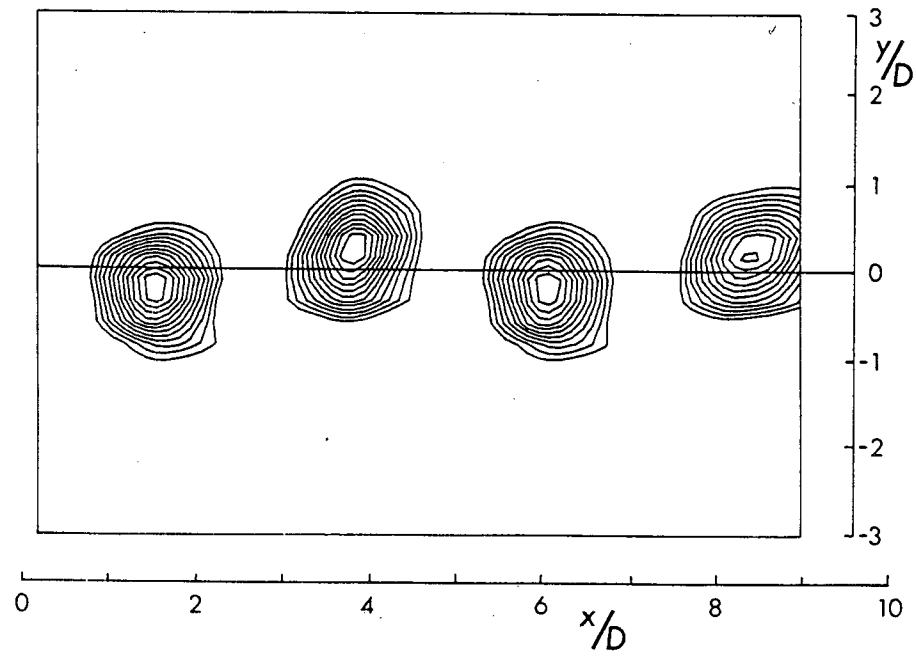

Figure 6.2(b). The contours of vorticity in the wake of the cylinder in oscillatory flow with the lowest 30% of the contours removed.

If the perturbation amplitude were much larger than that of the present investigation, then the vortices might not travel downstream with a constant velocity, and, therefore, the application of Taylor's hypothesis would no longer be valid. Clearly, the present form of conditional sampling is only valid in oscillatory flows where the amplitude of the perturbation is very small.

Figure 6.1(b) shows the contours of the vorticity in the wake of the cylinder in steady flow. The lowest 30% of the vorticity contours have been removed, thereby clearly revealing the vortices in the cylinder wake. The corresponding vorticity contours for the wake in the case of oscillatory flow are shown in Figure 6.2(b). The vorticity contours are plotted at equally spaced intervals. In steady flow the lowest plotted contour is $\left|\omega D/\bar{U}\right| = 0.30$ and the highest plotted contour $\left|\omega D/\bar{U}\right| = 0.95$. In oscillatory flow the lowest plotted contour is $\left|\omega D/\bar{U}\right| = 0.39$ and the highest plotted contour is $\left|\omega D/\bar{U}\right| = 1.25$. In both vorticity contour plots the vortex centres were identified, by eye, allowing the vortex spacings to be measured directly. Having identified the vortex centres, the circulation, or strength, associated with each vortex may be estimated. The circulation around a closed path enclosing a vortex centre is given by

$$\Gamma = \oint_C \underline{U} \cdot \underline{dC} \qquad (6.6)$$

where $\underline{dC}$ is an element of the path C around the vortex centre. The choice of the vortex path is not entirely arbitrary. The paths chosen for the computation of the vortex strength, in this investigation, were rectangular paths centred on the vortex centre. The

length of the horizontal sides of the path were equal to half of the longitudinal separation of the vortices. The estimates of Γ presented in Table 6.1 were obtained when the vertical sides of the path were 3D in length. When the vertical sides of the path were reduced to 2.5D the estimate of Γ decreased by about 6% and the estimate of Γ reduced rapidly with further reductions in the length of the vertical sides. When the length of the vertical side was increased to 3.50D or 4D the estimate of Γ remained constant to within ± 1%. There are four vortices in each reconstruction. For a particular reconstruction, the estimate of Γ for each of the four vortices was constant to within ± 1%.

The estimates of the vortex spacings and vortex strength in steady and oscillatory flow, along with other measured values, are presented in Table 6.1. The vortex strength was found to increase by 29% with lock-in. The lateral separation of the vortices in the street was reduced by about 25% with lock-in, whereas the longitudinal spacing remained almost constant. From the estimates of the vortex strength and the base pressure measurements, it is possible to estimate the fraction of the circulation generated by the cylinder that survives the vortex formation process, and which appears as circulation in the vortices of the wake. The rate of production of circulation by the body, as was discussed in Chapter 5, is given by

$$\frac{d\Gamma}{dt} = \tfrac{1}{2}U_b^2 \,. \qquad (6.7)$$

If all of the produced circulation were to appear within the vortices in the wake, then the vortex strength would be given by

TABLE 6.1 *Various parameters measured for the flow around a circular cylinder in steady and in oscillatory flow.*

Parameter	*Steady flow*	*Oscillatory flow*	*Change with lock-in*
b/D	0.59	0.44	-25 %
l/D	4.61	4.65	+1 %
b/l	0.128	0.095	-26 %
$\Gamma/\bar{U}D$	1.868	2.405	+29 %
R_o/D	0.853	0.858	+0.6 %
$\triangle$	31 %	33 %	+2 %
$\omega_{max}\ D/\bar{U}$	1.03	1.31	+27 %
Cpb	-1.42	-1.84	-30 %
Cd	1.29	1.52	+18 %
St	0.200	0.196	-2 %
Lf/D	1.15	0.92	-20 %

$$\Gamma = U_b^2/2n \quad . \tag{6.8}$$

U_b is related to U by $U_b = kU$ where $k^2 = 1 - C_{pb}$. Thus the fraction Λ of circulation that survives into the wake is given by

$$\Lambda = \frac{2n\Gamma}{U^2(1 - C_{pb})}$$

$$= \frac{2S\,\Gamma/U\,D}{(1 - C_{pb})} \quad . \tag{6.9}$$

Equation (6.9) was used to compute Λ for both steady flow and oscillatory flow, and was approximately 31% in the case of steady flow and approximately 33% in the case of oscillatory flow.

This result is in reasonable agreement with those of Bloor and Gerrard, who found Λ = 20% - 30% for a circular cylinder, at a Reynolds of 2000 and 1.6×10^4. Also, Davies found that Λ = 26% for a D-section, both when the section was held stationary in the flow, and when it was oscillating transversely with the wake synchronised with the body movement.

A brief investigation of the formation region was made by traversing a hot-wire along the wake centre line from x/D = 3.0 to 1.75. The U-wire was algined with the axis of the cylinder and was thus sensitive to the total velocity vector. It was with the U-wire aligned in this manner that Bloor and Gerrard performed their measurements of the formation length. They indicated several criteria which could be used to determine the end of the formation region, one of which was the maximum of the rms velocity fluctuations at the second harmonic of the vortex shedding frequency along the

wake centre line. This was the criterion used in the present investigation. From the spectra of the velocity fluctuations computed from the hot-wire output, the rms fluctuations of velocity over a small band of frequencies centred on the second harmonic of the shedding frequency, were obtained. The results are presented in Figure 6.3, for the cases of steady and oscillatory flow, and the estimates of the length of the formation region are presented in Table 6.1. The formation length is estimated to reduce by about 20% with lock-in. The rms fluctuations near to the base of the cylinder are about 4% larger in the oscillatory flow than in the steady flow, whilst the rms amplitude of the perturbation in oscillatory flow was only about 1%.

(c) DISCUSSION

The measurements of the vortex strength show that with lock-in the vortex strength is increased by about 29%. The fraction of vorticity surviving into the wake is approximately 31% for steady flow and 33% for oscillatory flow with lock-in, supporting the contention in the discussion of Chapter 5, that more vorticity is shed into the wake with lock-in. The increase of 29% in the vortex strength is, however, rather higher than the increase of 17% that was expected on the basis of the base pressure measurements. The discrepancy may be accounted for by the small change in Λ or by a possible inaccuracy in the estimate of the rate of shedding circulation. The increase in Γ with lock-in is consistent with the results of Davies and Griffin and Ramberg (1974), who found an

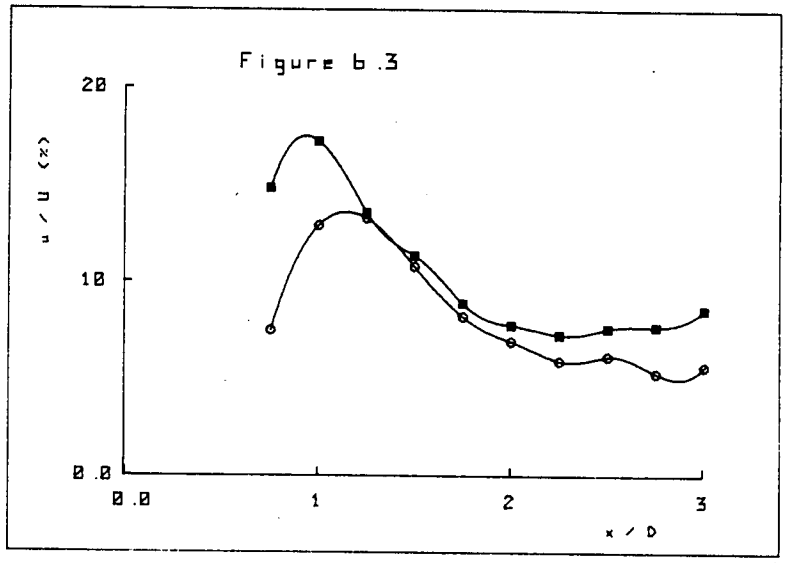

Figure 6.3. The variation of the rms of the 2nd. harmonic of the velocity fluctuations on the wake centre-line with distance from the cylinder.
○ steady flow ; ■ oscillatory flow.

increase in Γ with lock-in for a cylinder oscillating transversely. Davies found an increase in Γ of about 35% with lock-in for a D-section vibrating transversely with an aimpltude of $a = 0.2D$. Griffin and Ramberg found that Γ increased by about 44% with lock-in for a circular cylinder vibrating transversely with an amplitude of $a = 0.2D$, at $Re = 144$. The non-dimensional parameter $\Gamma/\overline{U}D$, for the present investigation is given in Table 6.1. Davies found $\Gamma/\overline{U}D = 2.39$ for the flow behind a stationary D-section and $\Gamma/\overline{U}D = 3.24$ for an oscillating D-section. Bloor and Gerrard found $\Gamma/\overline{U}D \sim 1.4$ at a distance of 6D downstream of a circular cylinder at $Re = 16{,}000$.

The reduction in the lateral spacing of the vortices with lock-in is an interesting result, which casts some light on the mean wake velocity profiles and vortex convection speed measurements. If two vortices are placed a set distance apart, then they will induce a backflow along the wake axis between their centres. If the vortices are Hamel-Oseen viscous vortices whose tangential velocity is given by

$$U_\theta = \frac{\Gamma}{2\pi r}\left(1 - e^{-1.26r^2/R_o{}^2}\right) \qquad (6.10)$$

where r is the radial distance from the vertex centre, $R_o = \sqrt{4\nu t}$ where R_o is the viscous core radius, t is the age of the vortex, and ν is the fluid viscosity, then clearly the backflow will be increased if Γ is increased. If, on the other hand, the separation of the vortex centres is less than $2R_o$, and is reduced, the backflow will be reduced. Therefore, a combination of an increase in the vortex strength and a reduction in the lateral spacing, b, may

leave the backflow unchanged. Such a combination has occurred in the wake of the cylinder during lock-in in the present investigation and, therefore, is a possible explanation of why the mean wake profile was unchanged with lock-in. The reduction in the lateral spacing, b, of the vortices with lock-in was observed at low Reynolds numbers by Koopman (1967) and by Griffin and Ramberg (1976). The investigation of Koopman was of the flow behind a transversely oscillating circular cylinder, and Griffin and Ramberg investigated the flow behind an in-line oscillating circular cylinder. Davies, however, found no such reduction in the lateral spacing with lock-in behind a transversely oscillating D-section. It is interesting to ask whether the reduction of the lateral spacing only occurs with circular cylinders. A circular cylinder has moveable separation points, whereas those of a D-section are fixed. Perhaps the nature of the flow at the separation points plays an important rôle in the determination of the vortex lateral separation.

The longitudinal separation of the vortices was changed by only about 1% and indeed the change may not be significant within the accuracy of the measurement. No significant change in the longitudinal separation was expected as, according to the findings of Griffin and Ramberg (1976), ℓ is dependent on the frequency of the perturbation but not the amplitude. With lock-in the vortex shedding frequency was only shifted very slightly from the steady flow vortex shedding frequency and hence only a small change in the longitudinal separation is to be expected. In the cases of both steady and oscillatory flow the measurement of the longitudinal

separation made from the reconstructed wake was, to within ± 1%, in agreement with the direct measurement of ℓ made during the measurements of the vortex convection speed.

The reduction in the formation length with lock-in is in agreement with the measurements of Griffin and Ramberg (1974). They found that as the perturbation amplitude was increased, the formation length was decreased. Davies (1975) also found, from flow visualisation studies, that with lock-in the vortices appeared to form closer to the base of the D-section with less interference from the opposite shear layer. He also remarked that more intense fluctuations appeared with lock-in, near the base of the D-section. The present results of the rms fluctuations of the velocity at the second harmonic of the vortex shedding frequency certainly show a marked increase near the base of the cylinder with lock-in.

In the present investigation lock-in was obtained for the case of a stationary cylinder in an oscillatory flow. Nevertheless many of the results are similar to those found in the case of lock-in obtained with a circular cylinder vibrating in a steady flow, even if the vibrations are transverse to the flow direction. For example, Griffin and Ramberg (1974) found that with lock-in, for a circular cylinder oscillating transverse to the flow direction, L_f was decreased, the lateral spacing was reduced and Γ was increased. Griffin and Ramberg (1976) found that with lock-in obtained with a circular cylinder oscillating in-line with the flow direction that L_f was reduced, b was reduced and Γ was increased. Davies (1976) found that with lock-in obtained for a D-section

vibrating transverse to the flow direction, Γ was increased but the lateral spacing remained unchanged. Perhaps the lateral spacing reduces with lock-in only in the case of circular cylinders.

The results presented in section (b) of the reconstructed wake behind the cylinder, represent the average wake. The vortices appear closely circular in structure, but they may not necessarily be so in the actual wake. If the vortices were elliptical and arrived at the measuring station with random orientations, then the average of these vortices would be a circular vortex [Davies (1975)]. The use of the equation $x = U_c \theta/2\pi n$ in the reconstruction of the wake is, at best, only first order accurate. However, the conditional sampling technique provides direct measurements of ℓ, b and Γ whereas the methods used by Bloor and Gerrard (1966) and Griffin and Ramberg (1974) provide only a direct measurement of ℓ and indirect measurements of b and Γ. It seems unlikely that this method of wake reconstruction will be improved upon, until laser holographic methods are sufficiently developed to allow measurements of the flow velocities throughout the flow field at any instant in time.

(d) THE VISCOUS VORTEX MODEL

It is useful to try to interpret the results in terms of a viscous vortex model to try to gain a further understanding of the measurements. Many workers have considered such models in the past. Hooker (1936) considered a single axisymmetric viscous vortex in a street of otherwise inviscid vortices. The viscous

vortex that was used in his model was a Hamel-Oseen viscous vortex, whose tangential velocity is given by (6.10). Other workers have improved upon the viscous vortex model used by Hooker, by replacing more than one of the inviscid vortices in the wake with viscous vortices. For example, Schaefer and Eskinazi (1959) matched a viscous vortex model to experimental measurements of the wake behind a circular cylinder at a Reynolds number of 62. The viscous vortices were Hamel-Oseen vortices. Many of the characteristics of the cylinder wake were closely modelled by the viscous vortex model. Also, Bloor and Gerrard (1966) matched their results obtained in the turbulent wake behind a cylinder at Reynolds numbers of 2000 and 16000 to a viscous vortex model. The viscous vortices used in their model were as suggested by Hoffmann and Joubert (1963) from measurements of trailing vortices. Outside a core radius R_c the tangential velocity, U_θ, is the same as that for an inviscid vortex. Between radii of R_c and R_o, U_θ varies logarithmically. Hoffmann and Joubert suggest that the inner core ($r < R_o$) has a velocity distribution similar to solid body rotation where $U_\theta \propto r$. However Bloor and Gerrard found that this representation did not give a good match to the experimental results. They tried three other representations of the inner core and found that a representation very similar to that of (6.10) gave the best fit to the experimental results in the majority of the cases investigated. Griffin and Ramberg (1974) used Hamel-Oseen vortices in a viscous vortex model of the wake and estimated the vortex strength and spacings by matching model wake profiles to experimental wake profiles in a manner similar to that used by Bloor and Gerrard.

The evaluation of these models, however, was indirect as the model was matched to experiment by adjusting all of the parameters Γ, b, and R_o to obtain a least squares fit. A more direct comparison was made by Davies (1976) as direct measurements of Γ and b were made from the reconstruction of the wake. The value of R_o was obtained by matching the vorticity at the centre of a Hamel-Oseen vortex to the vorticity that was measured at the centre of a vortex. The vorticity distribution of the Hamel-Oseen vortex was then found to match closely the measured vorticity distribution. Davies made several comparisons between the predictions of the model and the experimental results. With the addition of a mean shear to the model, good agreement between model and experiment was found. It would seem worthwhile, therefore, to match the experimental results of this investigation with the viscous vortex model proposed by Davies.

The wake is modelled as an infinite street of inviscid vortices with three adjacent vortices replaced by Hamel-Oseen viscous vortices. The coordinate system, and the positions of the three viscous vortices are as shown in diagram 6.1. The complex velocity is given by

$$\nu = u + iv \quad \text{in the} \quad z = x + iy \text{ plane as}$$

$$\bar{\nu} = \frac{i\Gamma}{2\pi}\left\{{}^{\pi}/_{\ell}\cot {}^{\pi}/_{\ell}(Z-Z_A) - {}^{\pi}/_{\ell}\cot {}^{\pi}/_{\ell}(Z-Z_C) - \frac{1}{Z-Z_A} + \frac{1}{Z-Z_B} + \frac{1}{Z-Z_C} + \alpha_A - \alpha_B - \alpha_C\right\} \tag{6.11}$$

where $Z_A = \frac{1}{2}ib$; $r_A^2 = x^2 + (y - {}^{b}/_{2})^2$

$Z_B = -\frac{1}{2}\ell - \frac{1}{2}ib$; $r_B^2 = (x + {}^{\ell}/_{2})^2 + (y + {}^{b}/_{2})^2$

$Z_C = \frac{1}{2}\ell - \frac{1}{2}ib$; $r_C^2 = (x - {}^{\ell}/_{2})^2 + (y + {}^{b}/_{2})^2$

Diagram 6·1 The Viscous Vortex Model

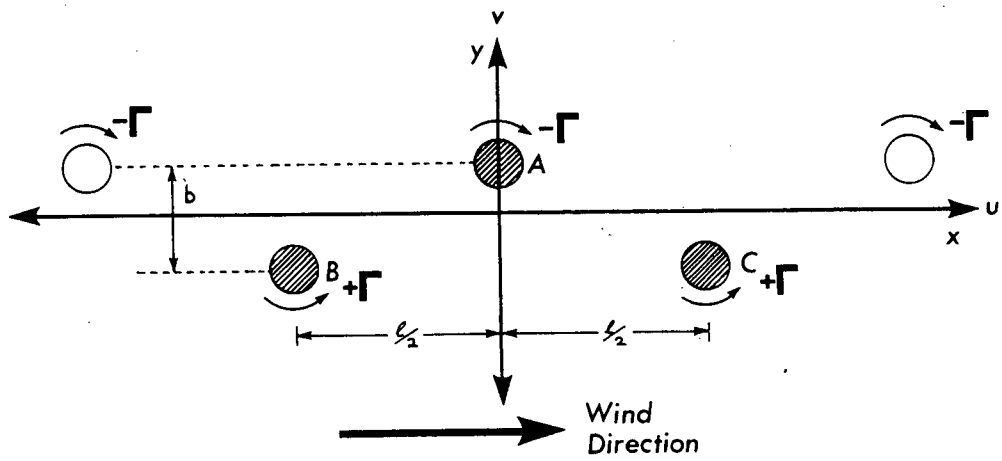

A, B and C are viscous vortices with

$$u_\theta = \frac{\Gamma}{2\pi r}\left|1 - \exp\left(\frac{-1{\cdot}26\,r^2}{R_0^2}\right)\right|.$$

All other vortices are inviscid.

and $\alpha_J = [1 - \exp\{-1.26(r_J/R_o)^2\}(\bar{Z} - Z_J)]/r_J^2$

$\beta_J = \exp\{-1.26(r_J/R_o^2)^2\}/r_J^2$

with $J = A, B, C$ $\bar{Z}$ is the complex conjugate of Z.

Using this model Γ, b and ℓ are known parameters measured directly from the wake reconstruction, and R_o is found by matching the vorticity at the vortex centre as

$$\omega_{max} = 1.26 \frac{\Gamma}{R_o^2} \tag{6.12}$$

For each wake reconstruction there are four vortices and hence four values of ω_{max}. For a particular reconstruction the average value of ω_{max} and the average value of Γ was used in (6.12). In each of the wake reconstructions the value of ω_{max} was constant to within ±3%. For the viscous vortex model a computer program was used to find the u velocity component by computing the real part of the complex velocity as

$$u = \text{Real}(\bar{v}) = \frac{\Gamma}{2\pi}\left[\frac{\pi/\ell \sinh 2\pi/\ell(y - b/2)}{\cosh 2\pi/\ell(y-b/2) - \cos 2\pi x/\ell} - \frac{\pi/\ell \sinh 2\pi/\ell(y+b/2)}{\cosh 2\pi/\ell(y+b/2) + \cos 2\pi x/\ell} - (y-b/2)\beta_A + (y+b/2)\beta_B + (y+b/2)\beta_C\right]. \tag{6.13}$$

From equation (6.13) the u component of velocity at various positions through the flow field of $-\ell/2 \leq x \leq \ell/2$ was calculated. From the model wake reconstruction, mean and rms velocity profiles were calculated. The rms velocity fluctuations were computed by Fourier analysing

the u component of the velocity fluctuations. The procedure will be described in the next section.

(e) COMPARISON OF MODEL AND EXPERIMENT

Figure 6.4(a) shows the variation of the reduced vorticity, $\frac{\omega D}{\bar{U}}$, through the centre of a vortex in the wake of the cylinder in steady flow. Figure 6.4(b) shows the corresponding variation of reduced vorticity in the case of oscillatory flow. The agreement between model and experiment is very good. The Hamel-Oseen viscous vortex representation closely represents the vorticity variation through the centre of the experimentally reconstructed vortex. Figures 6.4(a) and 6.4(b) allow a direct comparison between the model and experiment, unlike the indirect comparisons made by Bloor and Gerrard and by Griffin and Ramberg (1974). The close agreement between the Hamel-Oseen viscous vortex representation and the experimental results was also found by Davies. Clearly the Hoffman-Joubert representation of a viscous vortex, as an inviscid vortex at radii greater than R_o, with an inner solid body of rotation at radii less than R_o, would not fit the experimental results well. Saffman (1973) suggests that a turbulent line vortex has a triple structure, wherein the outer region has a logarithmically increasing circulation, and both the inner regions at radii less than R_o, the motion is closely that of solid body rotation. Saffman suggested this structure in an attempt to explain the observed dependence on Reynolds number of the decay of turbulent line vortices. Clearly, this representation would also be unsuitable as a match to the experimental results.

The mean velocity profiles through the centre of a vortex for

both the experiment and the model are shown for the cases of steady and oscillatory flow in Figure 6.5(a) and 6.5(b), respectively. For the case of steady flow there is a much closer match between model and experiment, than in the case of oscillatory flow. In both cases, however, the match is much poorer than the matches found for the variation of the vorticity through a vortex centre. Davies also found a poor match in the velocity profiles through a vortex centre, in his investigation. A check on the experimental results, the velocity profile through a vortex on the opposite side of the street was compared to the corresponding model profile. Very similar results to those plotted in Figures 6.5(a) and 6.5(b) were found.

Adopting the same approach as taken by Davies, the shear profile, representing the difference between the model and experimental velocity profile was computed for the cases of steady flow and oscillatory flow. Each shear profile was reflected in the x axis and the average of the shear profile and its corresponding reflection were computed. The average mean shear profile computed in this way for the case of steady flow is presented in Figure 6.6(a) and for the case of oscillatory flow is presented in Figure (6.6(b). The dotted lines in Figures 6.6(a) and 6.6(b) are intended merely as a guide to the eye. The mean shear profile in the case of oscillatory flow is much greater in magnitude at the wake centre-line than it is in the case of steady flow.

Figure 6.7(a) shows the experimental and model mean wake velocity profiles for the case of steady flow. The model seriously underestimates the mean wake deficit. With the addition, however, of the mean shear profile of Figure 6.6(a), the agreement between model and

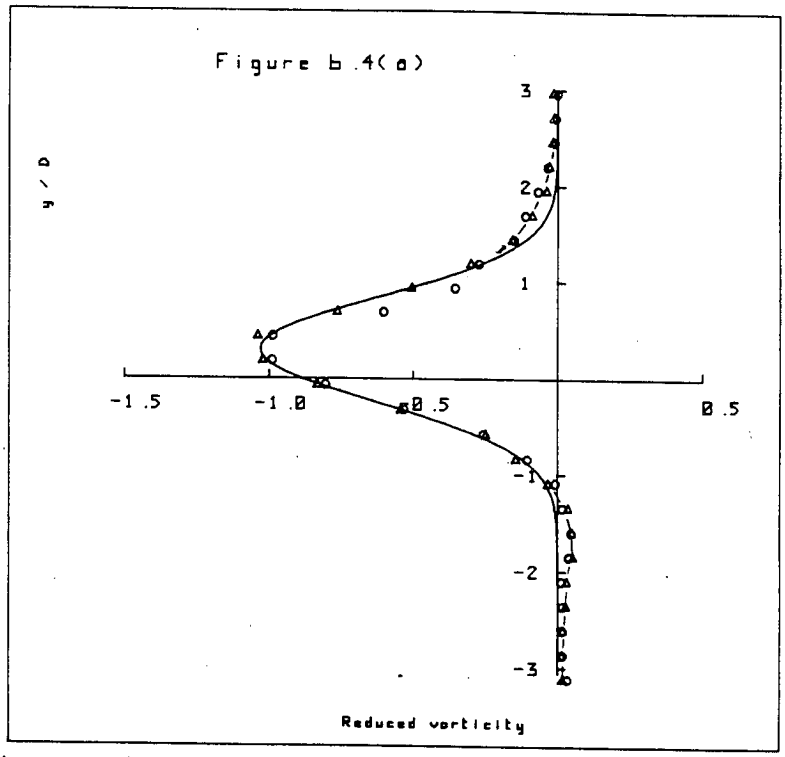

Figure 6.4(a). The variation of the reduced vorticity through a vortex centre in the wake of the cylinder in steady flow.
——model ; ○ experiment ; △ modified model.

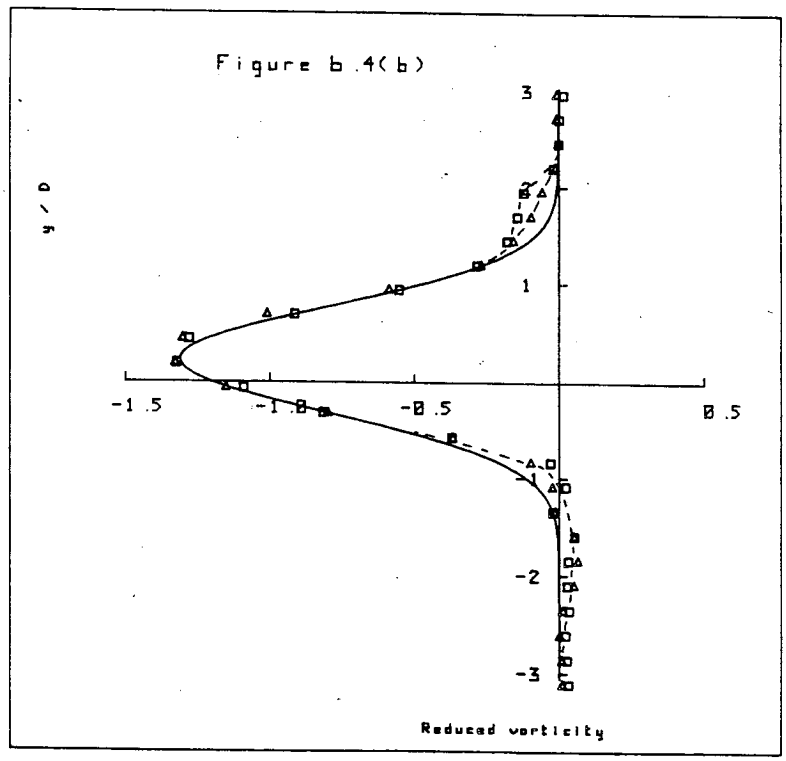

Figure 6.4(b). The variation of the reduced vorticity through a vortex centre in the wake of the cylinder in oscillatory flow.
—— model ; □ experiment ; △ modified model.

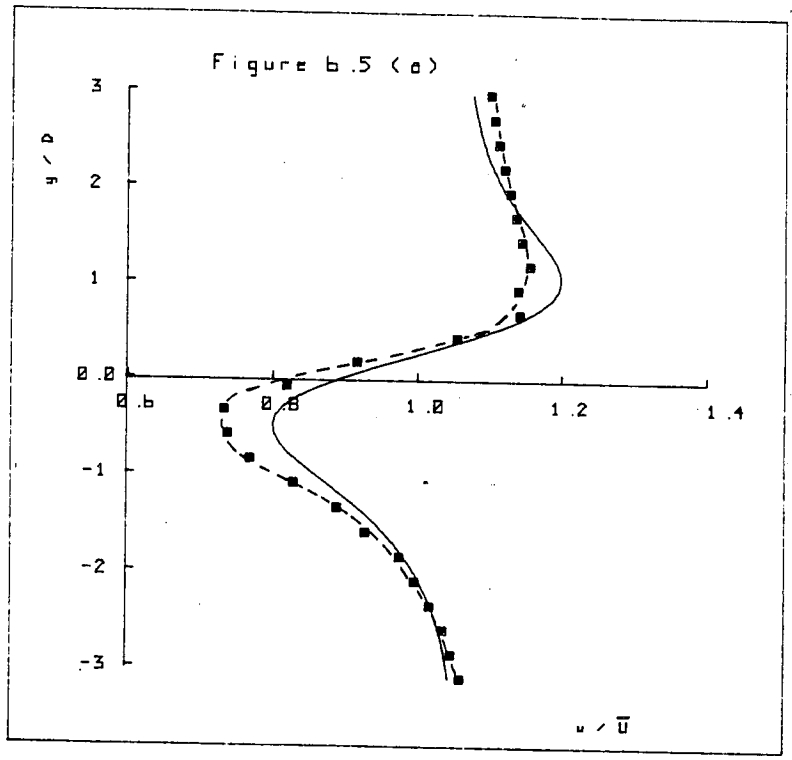

Figure 6.5(a). The variation of the u component of velocity through a vortex centre in the wake of the cylinder in steady flow.
——— model ; ■ experiment.

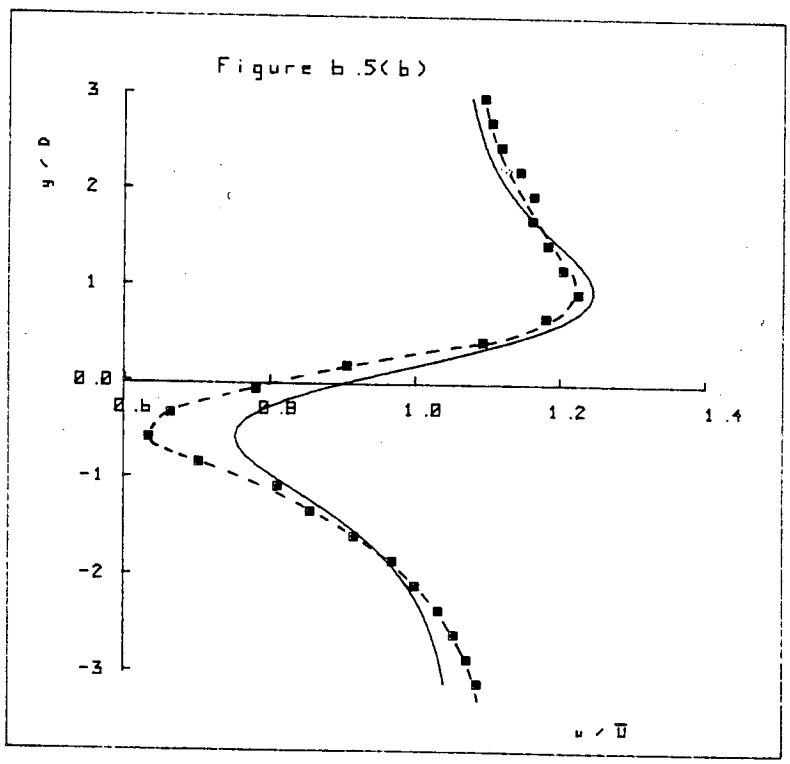

Figure 6.5(b). The variation of the u component of velocity through a vortex centre in the wake of the cylinder in oscillatory flow
——— model ; ■ experiment.

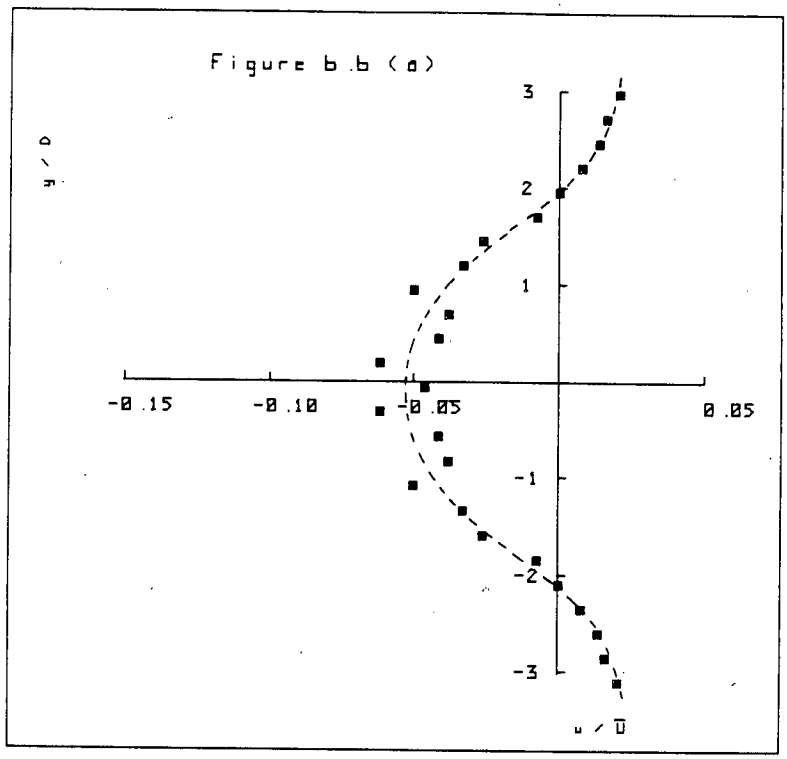

*Figure 6.6(a). The mean shear profile required to match the model wake velocity profile to the experimental wake velocity profile for the case of **steady** flow.*

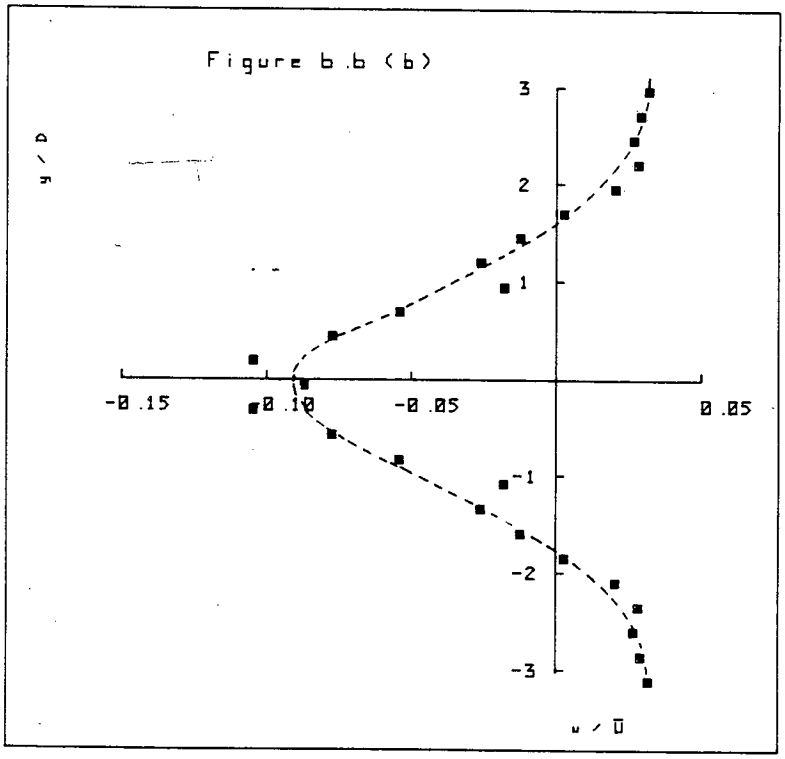

Figure 6.6(b). The mean shear profile required to match the model wake velocity profile to the experimental wake velocity profile for the case of oscillatory flow.

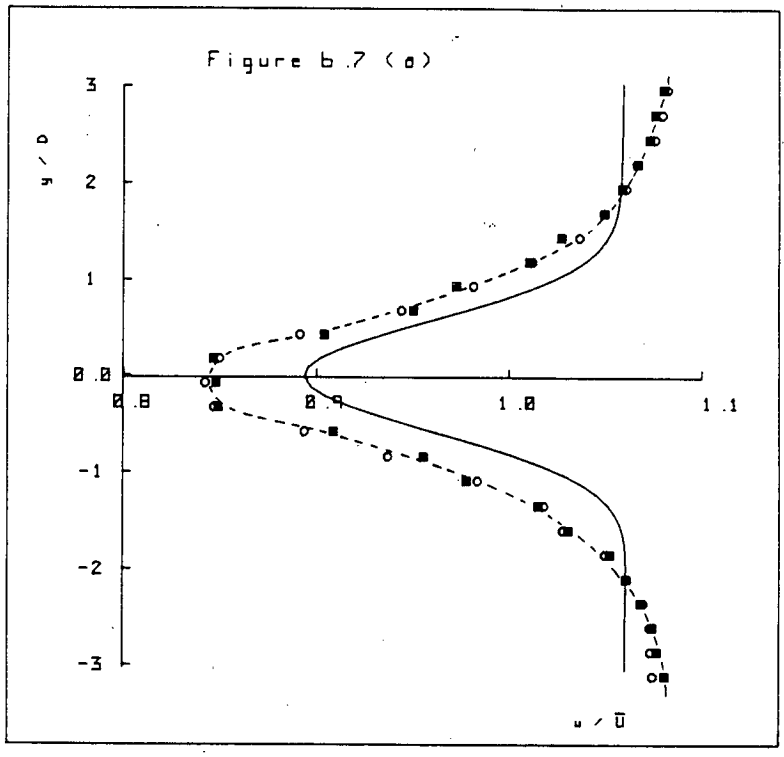

*Figure 6.7(a). The model and experimental wake velocity profiles in the case of **steady** flow.*
—— model ; ○ measured profile ;
■ model with added shear profile.

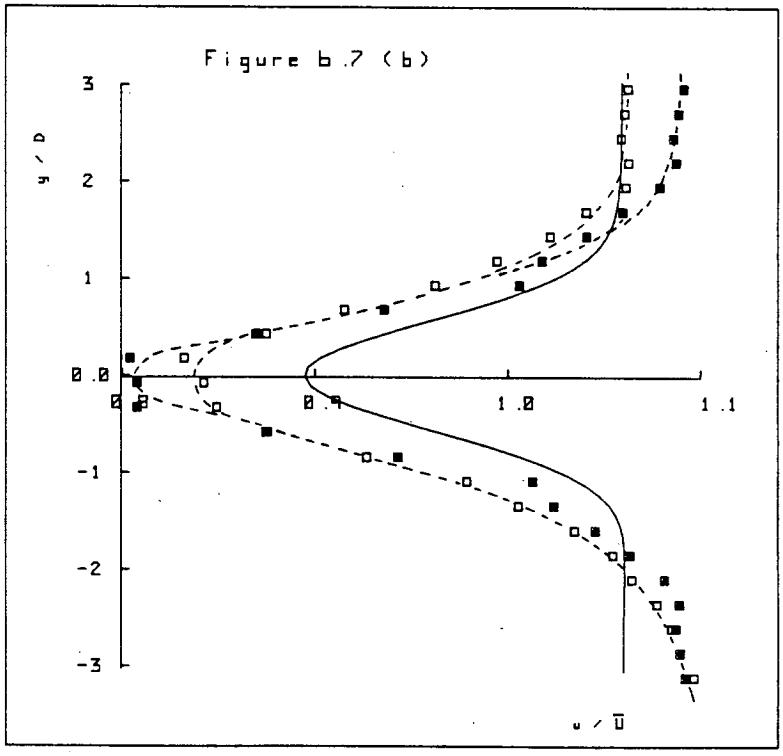

Figure 6.7(b). The model and experimental wake velocity profiles for the case of oscillatory flow.
—— model ; □ measured profile ;
■ model with added shear profile.

experiment is almost perfect. In the case of oscillatory flow, the experimental and model mean wake velocity profiles are shown in Figure 6.7(b). Again the model seriously underestimates the mean wake deficit. With the addition of the mean shear profile of Figure 6.6(b), the agreement between model and experiment is much improved, but the match is not as good as the corresponding match in steady flow.

Neglecting the addition of the mean shear profiles, the mean wake velocity profile predicted by the model in steady flow is almost identical to that predicted by the model for the oscillatory flow. The model, therefore, correctly predicts that no significant change occurs in the mean velocity profile with lock-in, in the case of the present investigation. The experimental mean velocity profiles measured both in steady flow and in oscillatory flow are also almost identical. Thus the changes in the experimental mean wake velocity profiles are correctly modelled.

A comparison may also be made between model and experiment of the variance of the u component of the velocity fluctuations in the wake. The calculation of the variance of the velocity fluctuations at a particular frequency are performed in the following manner. For both model and experiment, the variation of the u component of velocity with x (or t), at a particular position y in the wake, is known. The spectra of the velocity fluctuations may be computed from this information, on the assumption that the variation in u is periodic, with period $T = {}^{1}/n$. At each position y in the wake, the variation of u with t was extended by several periods to improve

the bandwidth of the Fourier analysis. The spectra of the energy of the fluctuations of the u component were computed. The variance of the fluctuations over a small band of frequencies centred at n and 2n were computed, and Figure 6.8(a) shows the comparison of the model and experiment in the case of steady flow. The corresponding results for the case of oscillatory flow can be seen in Figure 6.8(b). In the case of steady flow the model closely predicts the variance of the u velocity fluctuations at the vortex shedding frequency, through the wake of the cylinder. The model overestimates the variance of the u velocity fluctuations at the second harmonic, especially near the wake centre line. The experimental results again show reasonably good symmetry with respect to the wake centre line. The corresponding results for the case of oscillatory flow are plotted in Figure 6.8(b). In this case the model underestimates the variance of the fluctuations of the u velocity at the vortex shedding frequency, but only near the peaks of the variance of the u fluctuations. The model again overestimates the variance of the u fluctuations at the second harmonic of the vortex shedding frequency near the wake centre line.

The results for the variation of the u fluctuations at the second harmonic of the vortex shedding frequency, $u'(2n)$, are somewhat unexpected. They indicate that there are no fluctuations in the u component of velocity at the second harmonic of the vortex shedding frequency on the wake centre line. Other measurements indicate, however, that on the centre line of the wake of a cylinder there are fluctuations at frequency 2n. For example, in the investigation of the formation length behind the cylinder, the rms of

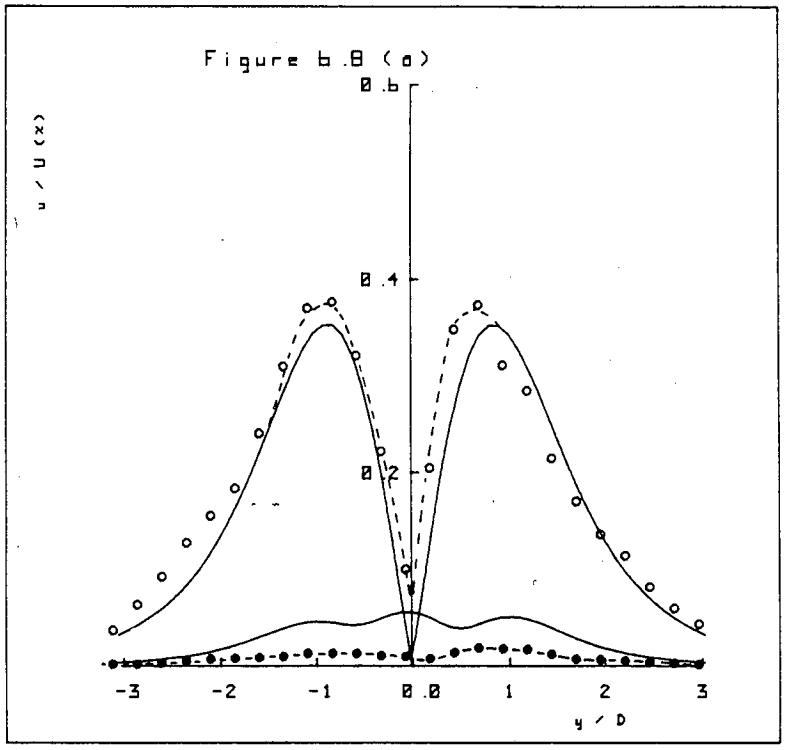

Figure 6.8(a). The variance of the u component velocity fluctuations in the wake of the cylinder in steady flow.
○ fluctuations at frequency n ; ● fluctuations at frequency 2n ;
—— model.

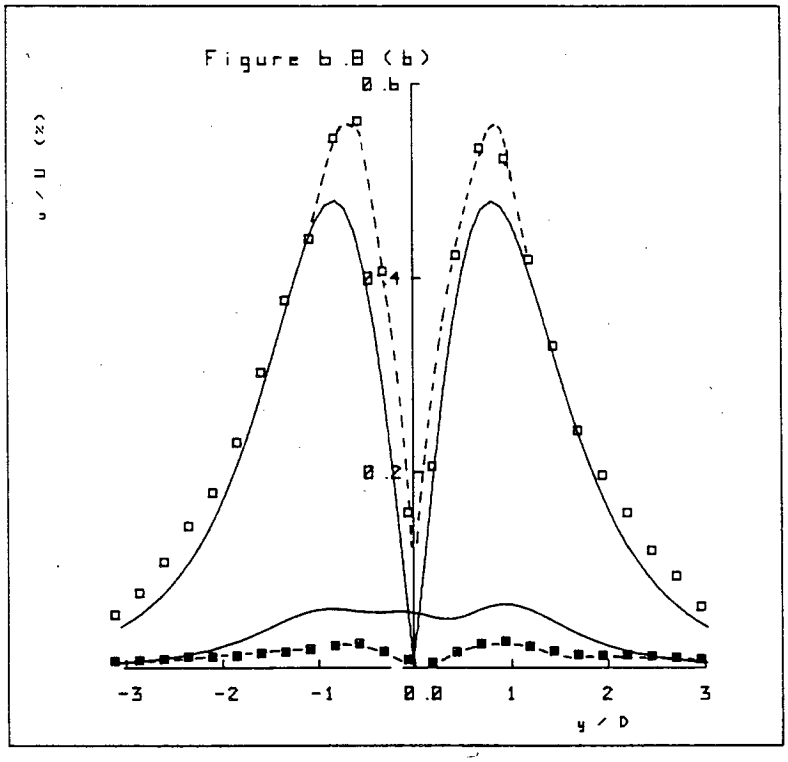

Figure 6.8(b). The variance of the u component velocity fluctuations in the wake of the cylinder in oscillatory flow.
□ fluctuations at frequency n ; ■ fluctuations at frequency 2n ;
—— model

$u'(2n)/\overline{U}$ was 10% at a distance of 3D downstream of the cylinder at the wake centre line. At a distance of 7D downstream, where the conditional sampling measurements were taken, the rms of $u'(2n)/\overline{U}$ would be much less than 10%. Bloor and Gerrard (1966), for example, found that at a distance of 3D downstream of a circular cylinder, the rms of $u'(2n)/\overline{U}$ was about 10%, whereas at a distance of 6D downstream, it was only 5%. The rms fluctuation at the second harmonic of the shedding frequency, associated with the vortices, will be less than 5%, but nevertheless should be clearly revealed by the conditional sampling technique. The present conditional sampling results, however, indicate that there is no energy in the fluctuations of u at the second harmonic of the shedding frequency, at the wake centre line. The reconstructions of the velocity components were filtered by using a Blackman filter. In the case of the present investigation the amplitude of a fluctuation in the u component reconstruction at a frequency of n would have been reduced by about 0.2% and at a frequency of $2n$ would be reduced by about 5%. It is unlikely, therefore, that the filtration could have seriously affected the results. There seems to be no obvious reason as to why the results of the conditional sampling technique have not indicated any energy in $u'(2n)$ near the wake centre line, other than perhaps that the fluctuation of frequency $2n$ is too small in comparison to the statistical accuracy of the u component reconstruction. It is not clear, therefore, as to why there is disagreement between the model and experiment when comparing the variance of the u fluctuations at frequency $2n$. However, Figures 6.8(a) and 6.8(b) show that the agreement between the model and experiment is reasonably good,

when comparing the variance of the u fluctuations at frequency n.

The model is only intended as a first order approximation to the average flow field behind the cylinder. The axisymmetric viscous vortex given by equation (6.10) is a solution of the equation

$$\frac{\partial \omega}{\partial t} = \nu\left(\frac{\partial^2 \omega}{\partial r^2} + \frac{1}{r}\frac{\partial \omega}{\partial r}\right) . \qquad \text{[Davies (1975)]} \qquad (6.14)$$

The vortices in the street, however, exist in the strain field of other viscous vortices, and will distort under the influence of the other vortices in the flow field. The vortices are also highly turbulent, and although relatively permanent and stable structures, the mechanics of the processes that maintain them as such, are not well understood. Turbulent diffusion, entrainment, and stretching all play a rôle in the development of the wake. It is, therefore, unlikely that such a simple model would adequately describe the characteristics of the wake, but nevertheless it does describe the main features of the averaged wake.

(f) SUMMARY AND CONCLUSIONS

Detailed measurements of the turbulent wake behind a circular cylinder at a Reynolds number of 2.15×10^4 have been made, using a conditional sampling technique. The wake in steady flow and the wake in a mean flow with a superimposed oscillatory perturbation were investigated. The oscillatory flow investigation was made when the vortex shedding was locked-on, wherein the vortices were shed at exactly half of the perturbation frequency.

Estimates of the vortex strength and vortex spacings in the

wake were obtained. The vortex strength was increased by 29% with lock-in, with an rms perturbation amplitude of only 1.15%$\overline{U}$. The fraction of vorticity contained in the vortices, of the total vorticity shed by the body, was estimated to be about 31% in the case of steady flow and 33% in the case of oscillatory flow. The longitudinal separation was increased by about 1% with lock-in, whereas the lateral separation was reduced by about 25% with lock-in.

The formation length was reduced by about 20% with lock-in, indicating that with lock-in the vortices are formed closer to the rear of the cylinder.

The results were matched to a viscous vortex model of the wake, using the experimentally obtained parameters Γ, b, ℓ to specify the vortices in the model wake. The model predicts the mean wake velocity profile to be unchanged with lock-in, in agreement with the the experimental results. With the addition of a mean shear to the flow field, a good match is found between experiment and model for the mean wake velocity profiles. The model also predicts, reasonably well, the variance of the u component velocity fluctuations at the vortex shedding frequency, but overestimates the variance fluctuations at twice the vortex shedding frequency.

The results obtained for the flow around a stationary circular cylinder with the vortex shedding locked-in, wherein the lock-in is caused by an oscillatory perturbation superimposed on the steady free-stream flow, show many similarities to corresponding results obtained for a circular cylinder oscillated in a steady flow.

CHAPTER 7

COMPUTER SIMILATIONS

INTRODUCTION

The problem of viscous incompressible fluid flow over bluff bodies has attracted much research interest over the years. As has been mentioned in earlier chapters many experimental investigations have been carried out. In addition, there have been theoretical studies which considered the early stages of viscous flow past an impulsively started circular cylinder. These studies were made using boundary layer theory, and Collins and Dennis (1973) have extended this work to high Reynolds numbers. These studies, however, give results which indicate the structure of the flow only before the appearance of the wake.

Complete time-dependent solutions to the unsteady viscous flow around bluff bodies seem unlikely to be obtained in the near future owing to the difficulty of obtaining analytic solutions to the non-linear Navier-Stokes equation of motion. For this reason many numerical studies have been made of the flow around bluff bodies. The numerical methods may be divided into two distinct categories. The first involves obtaining solutions to the equations of motion of a viscous fluid. This category may be further divided on the basis of the variables used in obtaining these solutions, i.e. 1) the streamfunction and the vorticity (ψ, ω), ii) the primitive variables (u, p), iii) the streamfunction alone (ψ). Various methods have been employed to obtain solutions. Fromm and Harlow (1963) obtained solutions for the unsteady flow around a rectangular obstacle by time-step integration of the transport of vorticity

equation. At each time step the new streamfunction was found. A power series approach was used by Tuann and Olsen (1978), who used a finite-element method to obtain solutions for the steady flow past a circular cylinder. Semi-analytic solutions for the steady viscous flow past a circular cylinder were obtained by Patel (1975), who substituted truncated Fourier series expansions for the stream function and the vorticity into the Navier-Stokes equation of motion.

The second category of numerical method for obtaining solutions to the unsteady flow around bluff bodies is that of the discrete vortex model. This method is quite distinct from the methods mentioned in the first category as the flow is assumed to be inviscid and the shear layers are represented by a discrete vortex approximation. The vortex sheets are represented by an array of line vortices whose axes are aligned with the vorticity of the sheet. Abernathy and Kronauer (1962) used such a representation to compute the interaction of two parallel vortex sheets which were taken to represent the free shear layers generated by a two-dimensional bluff body. The interaction of these vortex sheets led to development of a vortex street similar to the familiar von Kármán street of distinct vortices. Clements (1973) used the discrete vortex model to approximate the time-dependent flow past a rectangular blunt based semi-infinite section. The computations showed that vortex shedding took place and the Strouhal numbers obtained were in agreement with experimental results. Sarpkaya (1975) used the discrete vortex model to obtain an approximation to the time-dependent flow past an inclined flat plate. He found that the model gave results for the Strouhal number in good agreement

with those obtained experimentally by Fage and Johansen (1927), but that the normal force coefficients were 25% - 30% larger than those measured by Fage and Johansen.

Clements (1975) has obtained approximate numerical solutions to the time-dependent flow past a blunt based obstacle where the oncoming uniform flow was given an oscillatory perturbation. The numerical method used was that of the discrete vortex model. The frequency and amplitude of the perturbation was varied. At a perturbation frequency close to twice the vortex shedding frequency lock-in was found with the vortices being shed at exactly half of the perturbation frequency. The shedding was found to remain locked-in over a small range of reduced frequencies. The lock-in range was found to increase with increasing perturbation amplitude. Clements also found lock-in when the frequency of the perturbation was close to four times the vortex shedding frequency. Again, the lock-in range increased with increasing perturbation amplitude.

The advantage of the discrete vortex model is that much less computational time is required to obtain solutions to time-dependent flows, than is required to obtain such solutions using the full Navier-Stokes equations of motion. Also solutions may be obtained at much higher Reynolds numbers than the Reynolds numbers achieved by solutions of the full Navier-Stokes equations as in the latter case the numerical stability is reduced as the Reynolds number is increased. However, solutions obtained using finite-difference approximations to the full Navier-Stokes equations of motion are more representative of the viscous flow around bluff bodies.

The purpose of the investigation described in this chapter was

to obtain approximations to the unsteady viscous flow around a two-dimensional rectangular obstacle. The method used is very similar to that used by Fromm and Harlow (1963). However, the computational grid used is much finer and the simulations were extended to much greater times. An attempt was also made to simulate the flow past the obstacle when a small oscillatory perturbation was superimposed on the mean oncoming flow, where the perturbation frequency was such that lock-in was expected to occur.

(a) THE FROMM AND HARLOW METHOD

The Navier-Stokes equations of motion governing the two-dimensional flow of an incompressible fluid are

$$\begin{aligned} \frac{\partial u}{\partial t} + u\frac{\partial u}{\partial x} + v\frac{\partial u}{\partial y} + \frac{1}{\rho}\frac{\partial p}{\partial x} &= \nu\left(\frac{\partial^2 u}{\partial x^2} + \frac{\partial^2 u}{\partial y^2}\right) \\ \frac{\partial v}{\partial t} + u\frac{\partial v}{\partial x} + v\frac{\partial v}{\partial y} + \frac{1}{\rho}\frac{\partial p}{\partial y} &= \nu\left(\frac{\partial^2 v}{\partial x^2} \quad \frac{\partial^2 v}{\partial y^2}\right) \end{aligned} \tag{7.1}$$

and the equation of continuity is

$$\frac{\partial u}{\partial x} + \frac{\partial v}{\partial y} = 0 \quad . \tag{7.2}$$

Taking the curl of the Navier-Stokes equation gives the transport of vorticity equation,

$$\frac{\partial \omega}{\partial t} + \frac{\partial (u\omega)}{\partial x} + \frac{\partial (v\omega)}{\partial y} = \left(\frac{\partial^2 \omega}{\partial x^2} + \frac{\partial^2 \omega}{\partial y^2}\right) \tag{7.3}$$

where

$$\omega = -\frac{\partial u}{\partial y} + \frac{\partial v}{\partial x} \quad . \tag{7.4}$$

For convenience, the usual streamfunction ψ, is included as a variable such that

$$u = \frac{\partial \psi}{\partial x} \tag{7.5}$$

$$v = -\frac{\partial \psi}{\partial y} \tag{7.6}$$

and

$$\frac{\partial^2 \psi}{\partial x^2} + \frac{\partial^2 \psi}{\partial y^2} = -\omega \, . \tag{7.7}$$

An approximate solution to the equations of motion may be obtained by dividing the spatial region of interest into a mesh of cells and recasting the equations of motion as finite-difference equations governing the flow at discrete points on the mesh. Such a mesh was used for the region close to a rectangular obstacle, the flow around the obstacle being contained between two parallel walls. The mesh is most easily described with reference to diagram 7.1. The spatial region is divided into square cells each of side a. At the corners of each square the values of ψ and ω are defined. The u component of velocity is defined midway along each vertical side of the squares, and the v component is defined midway along each horizontal side of the squares. Having defined the grid the equations of motion are reformulated as finite-difference approximations to the equations of motion, in the following manner.

$$u_{i,jj} = (\psi_{i,j+1} - \psi_{i,j})/a \tag{7.8}$$

$$v_{ii,j} = (\psi_{i+1,j} - \psi_{i,j})/a \tag{7.9}$$

$$\omega_{i,j} = (-u_{i,jj} + u_{i,jj-1} + v_{ii,j} - v_{ii-1})/a \, . \tag{7.10}$$

Poisson's equation, as defined in equation (7.7), may be written as

$$(\psi_{i+1,j} + \phi_{i-1,j} + \phi_{i,j+1} + \phi_{i,j-1} - 4\psi_{i,j}) = -a^2 \omega_{i,j} . \tag{7.11}$$

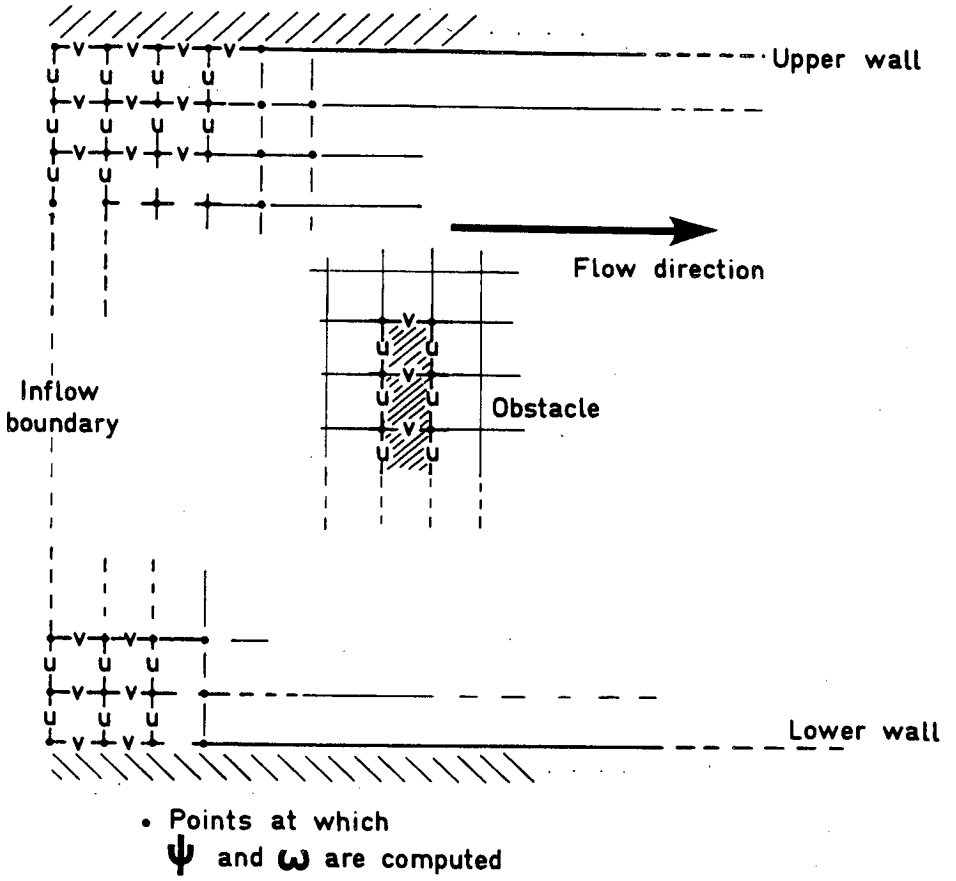

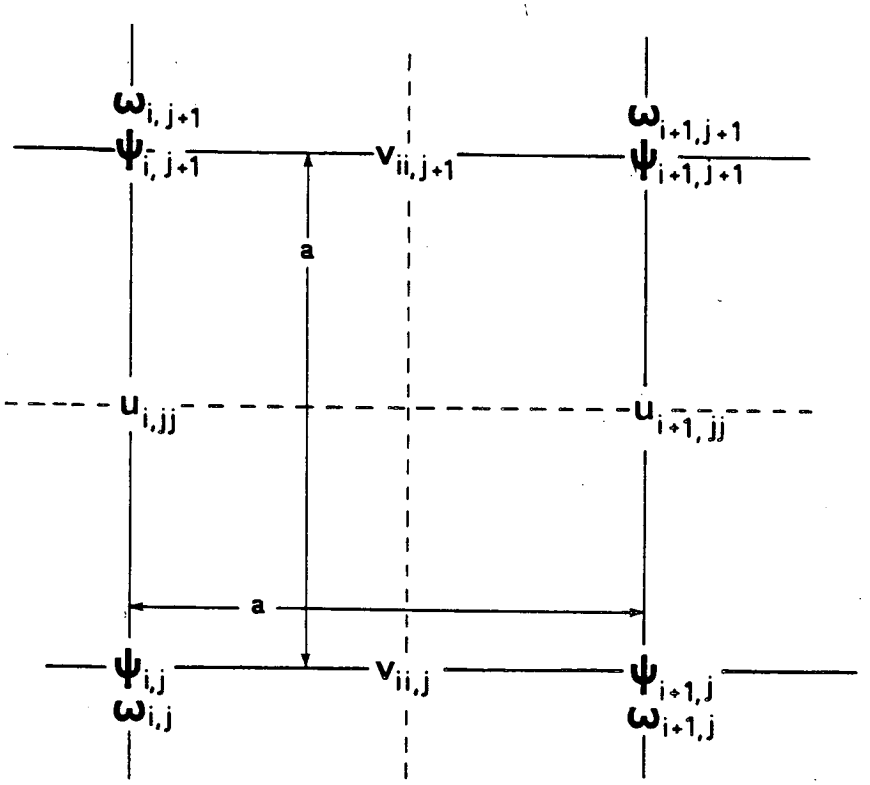

Diagram 7·1 The computational grid

The transport of vorticity equation is used at each time step of the computations and is advanced in time using the Du-fort Frankel Leapfrog method [Roache (1976)] as follows.

$$\omega_{i,j}^{n+1} = \alpha\{\omega_i^{n+1} - \beta[(u\omega)^n_{ii-1,j} - (u\omega)^n_{ii,j} + (v\omega)^n_{i,jj-1} - (v\omega)_{i,jj}]$$

$$+ \gamma(\omega^n_{i+1,j} + \omega^n_{i-1,j} + \omega^n_{i,j-1} + \omega^n_{i,j+1} - 2\omega^{n-1}_{i,j})\} \quad (7.13)$$

where $\alpha = 1/(1 + \frac{4\nu\delta t}{a^2})$ (7.14)

$\beta = 2\delta t/a$ (7.15)

$\gamma = 2\nu\delta t/a^2$ (7.16)

$$u^n_{ii,j} = (u^n_{i+1,jj} + u^n_{i,jj} + u^n_{i+1,jj-1} + u^n_{i,jj-1})/4.0 \quad (7.17)$$

$$v^n_{i,jj} = (v^n_{ii,j+1} + v^n_{ii-1,j+1} + v^n_{ii-1,j} + v^n_{ii,j})/4.0 \quad (7.18)$$

$$\omega^n_{ii,j} = (\omega^n_{i+1,j} + \omega^n_{i,j})/2.0 \quad (7.19)$$

and $\omega^n_{i,jj} = (\omega^n_{i,j+1} + \omega^n_{i,j})/2.0$ (7.20)

where $\omega^n_{i,j}$ is the values of ω at grid point (i,j) at the nth time step, $t = n\delta t$.

The method is second order accurate in space and time. After advancing the vorticity by one time step, using equation (7.13) the new values of ψ_{ij} must be computed at each point in the grid. The new values of ψ are computed by solving Poisson's equation. This is achieved numerically by iterating to a solution using a successive overrelaxation technique. At each point on the grid a residual or "error" may be computed as

$$R^n_{ij} = (\psi^n_{i,j-1} + \psi^n_{i,j+1} + \phi^n_{i-1,j} + \phi^n_{i+1,j} - 4\psi^n_{i,j} + a^2\omega^n_{i,j})/4.0 \quad (7.21)$$

The residual is then used to correct the values of the stream-function by

$$\psi_{i,j}^{n+1} = \psi_{i,j}^{n} + R_{i,j}^{n}\,\omega \tag{7.22}$$

where $\psi_{i,j}$ is the iteration to the correct value of $\psi_{i,j}$, and ω is an acceleration term, where

$$1 \leq \omega < 2 . \tag{7.23}$$

If ω is chosen as 1 and held constant, the iterative scheme is known as Gauss-Seidel (GS) iteration. If ω is a constant greater than 1 but less than 2, the iterative scheme is known as successive overrelaxation, (SOR). However, the GS method is rarely used as convergence to the solution is very slow. The SOR method converges much faster than the GS method and has been used by many workers. The convergence of the SOR method may be greatly improved by the use of Chebychev acceleration [Hockney and Eastwood (1981)]. The iteration proceeds using an odd-even ordering with a two-step calculation. At each half step of the iteration the value of ω is changed as follows.

$$\begin{aligned} \omega^{0} &= 1 \\ \omega^{\frac{1}{2}} &= 1/(1 - \tfrac{1}{2}\rho^{2}) \\ \omega^{n+\frac{1}{2}} &= 1/(1 - \tfrac{1}{4}\rho^{2}\omega^{n}) \\ \omega^{n+1} &= 1/(1 - \tfrac{1}{4}\rho^{2}\omega^{n+\frac{1}{2}}) \end{aligned} \tag{7.24}$$

where $\rho = \cos(\pi/N_G)$ where N_G is the number of grid points along the side of the mesh.

At an even half step the values of $\psi_{i,j}$ with $i+j$ even, are

updated, using equation (7.22), and at odd half steps the values of $\psi_{i,j}$ with $i+j$ odd are updated, again using equation (7.22). The iteration procedure continues until some suitable convergence criterion is reached. The convergence criterion used in the calculations was that

$$|\psi^{n+1}_{i,j} - \psi^{n}_{i,j}| < {}^{a}/1000 \qquad (7.25)$$

for each grid point in the flow field.

Once the new values of ψ were obtained, the new values of the velocity components were computed, using equations (7.8) and (7.9). The vorticity at the surface of the obstacle was then computed using the new velocity components as

$$\omega_{ij} = 2.0(-u_{i,jj} + u_{i,jj-1} + v_{ii,j} - v_{ii-1,j})/a \; . \qquad (7.26)$$

An outline of the numerical procedure for obtaining solutions of the time-dependent flow around the obstacle is shown in diagram 7.2. The steps within the dashed boxes are used only in the oscillatory flow calculations described in section (e). The method, as shown in diagram 7.2, is subject to the boundary conditions imposed on the flow field. At the inflow boundary $u = 1.0\ ms^{-1}$, $v = 0$ and $\omega = 0$. The value of $\psi(1,j)$ was accordingly chosen as $\psi(1,j) = j*a$. $1 \leq j \leq 64$. The grid used was 126×64 points. The value of $a = \frac{1}{7}$, and the obstacle was 7 units high by one unit wide, so that $D = 1$. At the upper and lower horizontal walls the velocity was given a value of $\overline{U} = 1\ ms^{-1}$. Using this boundary condition resulted in their being little vorticity produced at the walls. Fromm and Harlow adjusted the value of ψ at the upper and lower

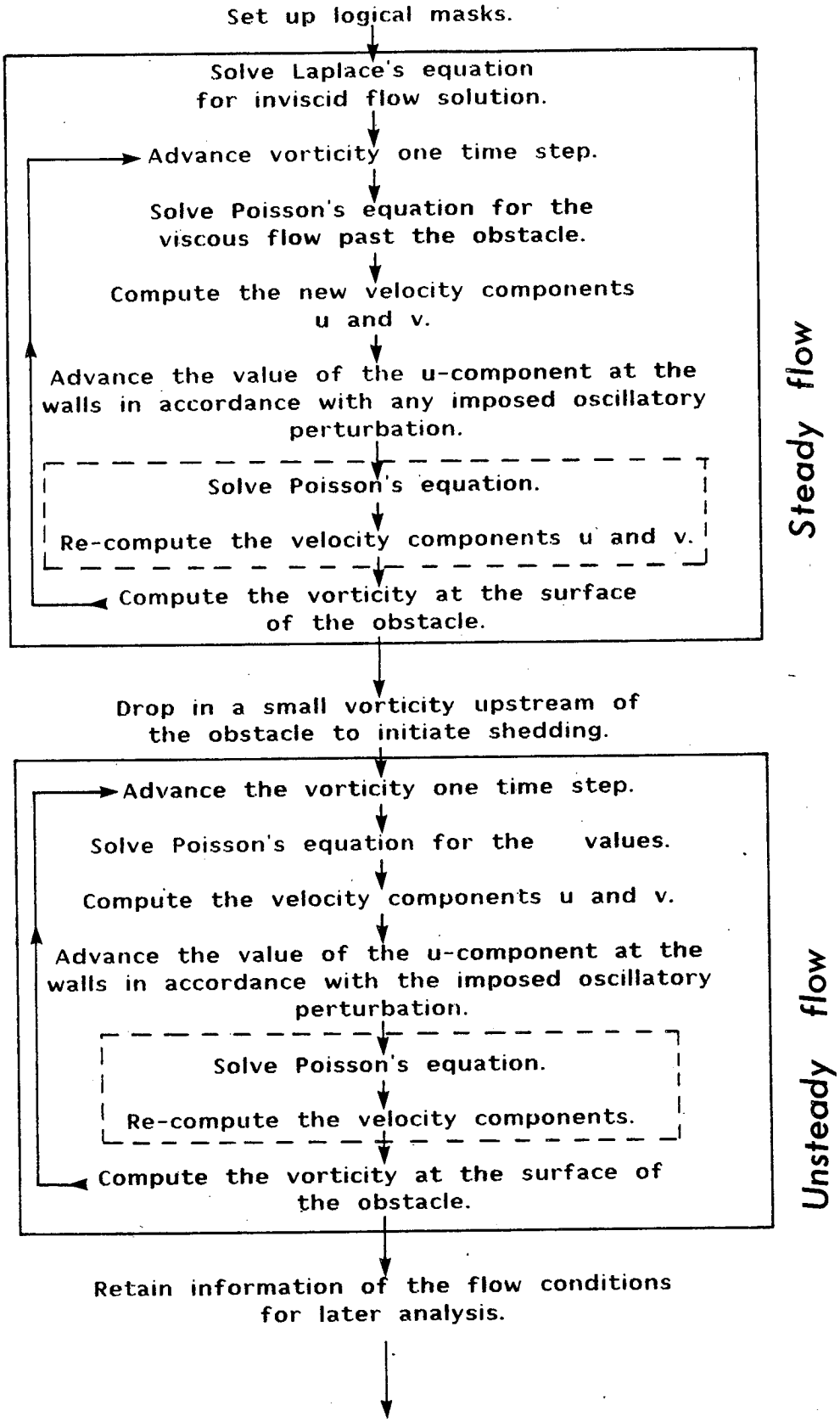

Diagram 7·2 Method of solving the flow equations.

walls using

$$\psi_{i,j_o} = \bar{U}\, a + \frac{1}{i_o} \sum_{i=1}^{i_o} (a^2 \omega_{i,j_o} + \psi_{1,j_o-1}) \tag{7.27}$$

$$\psi_{i,1} = -\bar{U}\, a + \frac{1}{i_o} \sum_{i=1}^{i_o} (a^2 \omega_{i,1} + \psi_{i,2}) \tag{7.28}$$

where j_o is the number of grid points in the vertical direction.

However, since the vorticity production was found to be very small the value of ψ at the walls was held constant at 64a for the upper wall and a for the lower wall.

The value of ψ at the outflow boundary was computed by

$$\psi(i_o,j) = 2\psi(i_o-2, j) - \psi(i_o-1,j) \tag{7.29}$$

where i_o is the number of grid points in the horizontal direction. The outflow vorticity is simply defined as

$$\omega(i_o,j) = \omega(i_o-1,j) \tag{7.30}$$

as given by Roache (1976).

The value of ψ on the obstacle was held fixed at 32.5a throughout the calculations. The value of u on the surface of the obstacle was zero, and the v component on the obstacle surface, or within the obstacle, was also zero.

The stability of the numerical method depends critically on the parameters a, δt, and $\bar{U}$. A brief description of the stability of the scheme is given by Fromm (1963). He suggests that for accuracy and stability of the numerical scheme,

$$\xi = \frac{|u| + |v|}{a} \delta t \leq 1 \tag{7.31}$$

and

$$\eta = \nu \delta t / a^2 \leq \tfrac{1}{4} . \tag{7.32}$$

The value of δt was chosen as 2.5×10^{-2}s in the simulations presented in this chapter, and over the Reynolds number range of 5 to 300 equations (7.31) and (7.32) are easily satisfied.

(b) THE DISTRIBUTED ARRAY PROCESSOR

The DAP is manufactured by ICL and is designed as a memory module for the ICL 2970 series mainframe computers. It can store 2 Mbytes of data for fast access by the mainframe processor. However, it may also be used to process data, stored within the DAP, in a highly parallel manner. It is known as a parallel processor as it can execute a given instruction simultaneously on an array of data.

The DAP may be thought of as an array of 64 × 64 processing elements, each with a local store of 4Ø96 bits. Diagram 7.3 shows how one might think of the layout of the processors and indicates the definition of the axes used in the numerical scheme presented in section (a). Under common control each processor may execute a given instruction on the data in its local store. As each processor must execute the same instruction, the DAP is known as a single instruction multiple data (SIMD) machine. Each processor can transfer data to its nearest neighbour, lying immediately to the North, the South, the East, or the West. These directions are indicated in diagram 7.3. For a given direction these data transfers may be performed simultaneously in one of two modes, namely planar mode or cyclic mode. In cyclic mode if the transfer is, say Northwards, then each processor simultaneously transfers

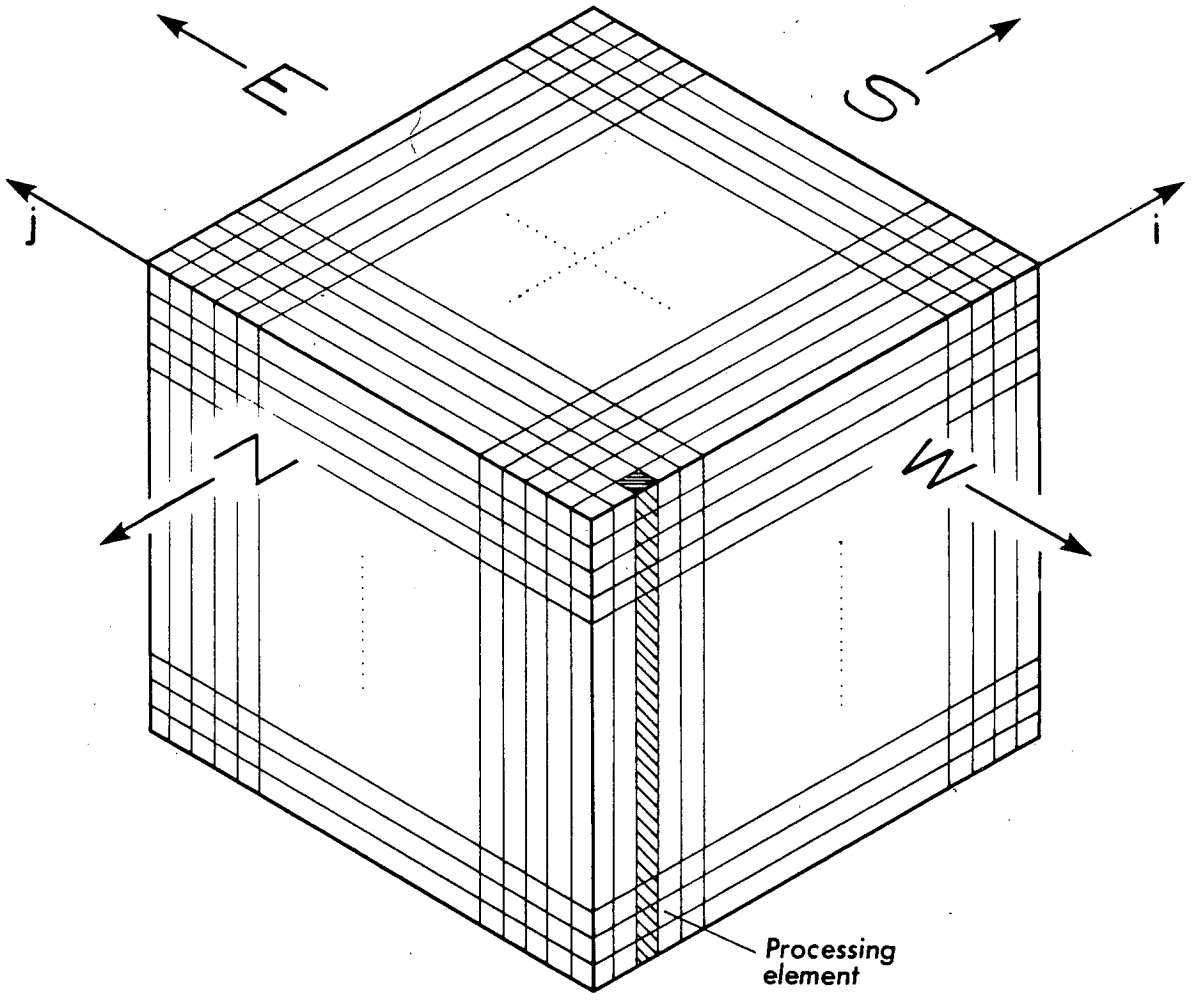

Diagram 7·3 The Distributed Array Processor

data from its local store to the local store of the processor immediately to its North, and the most Northerly processors transfer their local data to the corresponding processor lying at the extreme South of the DAP. In a northerly transfer in planar mode, data is transferred in the same manner as in cyclic mode, but the data transferred off the extreme North of the DAP is lost, and zeros are transferred to the most southerly processors.

A compiler has been written which allows the DAP to be programmed in a language called DAPFORTRAN. This language has many features which allow the parallelism of the DAP to be exploited, and it is worthwhile pointing out some of the more useful features of this language.

An array may be declared implicitly as a 64×64 array, as follows.

```
DIMENSION A( , ), B( , ), C( , ) .
```

Suppose that arrays A and B each contain data. If the arrays were to be added and the results stored in array C, then the following statement is used.

```
C = A + B .
```

The value of $C_{i,j}$ is given by $A_{i,j} + B_{i,j}$ where $C_{i,j}$ denotes C(I,J).

Any commonly used arithmetic operations allowed in FORTRAN may also be used in DAPFORTRAN. For example,

```
C = (A**2)*log(B)
```

where $C_{i,j} = A_{i,j}^2 \log B_{i,j}$.

The above expression requires that every processor performs the calculations. In some applications it is useful to prevent some of the processors from performing a given calculation. Control over which processors are to be excluded from a given calculation is achieved by the use of a logical mask. The logical mask is declared as a one bit logical array. The elements of the mask are set to true only, where the processor is to perform a calculation. For example, the following statements prevent only the most Northerly processors from performing the multiplication of line 5).

```
1)      DIMENSION L( , ), A( , ), B( , ), C( , )
2)      LOGICAL L
3)      L = . TRUE
4)      L(1, )  =  FALSE
           .
           .
           .
           .
5)      A(L)  =  B*C
```

Note in line 4) all the elements of L(I,J) with I = 1 are set to FALSE. The logical masks allow easy implementation of the boundary conditions, as evidenced by the following example of a routine which may be used to solve Laplace's equation by the iterative process

$$\psi_{i,j}^{n+1} = \tfrac{1}{4}(\psi_{i+1,j}^{n} + \psi_{i-1,j}^{n} + \psi_{i,j+1}^{n} + \psi_{i,j-1}^{n}) \cdot \qquad (7.33)$$

Convergence is accepted when

$$|\psi_{i,j}^{n+1} - \psi_{i,j}^{n}| < \text{CONV} \quad \text{for all} \quad i,j$$

```
 1)       SUBROUTINE LAPLAC
 2)       COMMON/CONI/PSI( , ), CONV
 3)       COMMON/LOG/ L( , ),L1( , )
 4)       LOGICAL L, L1
 5)       REAL OLD( , )
 6)       DO 100 IT = 1,1000
 7)           OLD = PS1
 8)           PS1(L) = 0.25*(SHNC(PS1,1)+SHSC(PS1,1)+SHWC(PS1,1)+SHEC(PS1,1))
 9)           L1 = ((OLD-PS1).LT.CONV)
10)           IF(ALL(L1)) GOTO 200
11) 100   CONTINUE
12)       X=SQRT(-1.0)
13) 200   RETURN
14)       END.
```

PS1 is the array holding the values of the streamfunction ψ at each grid intersection point.

L = .TRUE. everywhere except on the boundaries i = 1, i = 64 j = 1, j = 64 and also on the obstacle surface.

L1 is a workspace mask, and where false indicates points at which the value of ψ has not yet converged.

OLD is the array holding the previous iteration values of ψ.

Line 8) indicates the shifting operations performed on the data transferring data in a specified direction. The instruction may be understood as follows.

```
C = SHEC(A,k)
```

requires that the array A be shifted k steps in an Easterly direction

$$C_{i,j} = A_{i,j-k} \quad \text{for} \quad j > k$$

and $$C_{i,j} = A_{i,j-k+64} \quad \text{for} \quad j \leq k.$$

Line 12) is used to ensure that convergence has taken place. If after 10,000 iterations convergence has not been achieved, then line 12) will cause an error and the current values of some of the variables will be listed in the diagnostics of the program failure.

(c) STEADY FLOW SIMULATIONS

Before proceeding to a simulation of the steady flow past the obstacle, the program was first tested by comparing the numerical and analytic solutions for the development of a flow where an exact analytic solution is known. The time dependent viscous flow near an infinite wall started impulsively in its own plane is an example of a simple flow for which an exact analytic solution is known. When a plane wall, which bounds a viscous fluid, is impulsively started, vorticity generated at the surface of the wall diffuses away from the wall. This is known as Rayleigh's problem and the analytic solution for the vorticity is given by

$$\omega(y,t) = \frac{\bar{U}}{\sqrt{\pi\nu t}} e^{-y^2/4\nu t} \qquad (7.34)$$

[Fromm (1963)]

The program was run with no obstacle present on the grid. With the flow everywhere stationary the lower wall was impulsively accelerated to 1 ms^{-1}. For this simulation equations (7.27) and (7.28) were used to update the ψ values at the walls. The boundary condition for the velocity of the upper wall was $u = 0$, $v = 0$. In the case of this simulation the upper wall was far enough away from the lower wall so that the boundary condition for the velocity at the upper wall would have had a negligibly small effect on the

flow near the lower wall. Figure 7.1 shows the vorticity distribution at various stages of the flow development. The theoretical curves have been drawn with the origin at a height, $y = -a/2$, which is the true position of the wall on the grid as indicated by Fromm (1963). The position of the wall is a consequence of using the numerical scheme as described by Fromm (1963). Note that u is not defined on the wall but at a position of $y = a/2$. By using equation (7.10) to compute the vorticity at the wall, the position of the wall is fixed as $y = -a/2$. Fromm does not point out, however, that when using this scheme to simulate the flow near an impulsively started wall, the starting condition is crucial to the development of the flow. The wall is impulsively started at $t = 0$ and $\omega^{o}_{i,1}$ is computed. Before proceeding with the numerical scheme $\omega^{-1}_{i,1}$ must be made equal to $\omega^{o}_{i,1}$, in order that $\omega^{1}_{i,j}$ is correctly computed using equation (7.13). The wall position may, however, be fixed at $y = 0$ if (7.26) is used to compute the wall vorticity and if $\omega^{-1}_{i,1} = 0$. The numerical solutions obtained in this way were in excellent agreement with the analytical solutions for the flow near an impulsively started wall with the wall at a position of $y = 0$. The numerical results obtained using Fromm's method are in excellent agreement with the analytical solutions with the wall at a position of $y = -a/2$, as can be seen in Figure 7.1.

Whilst this type of comparison lends credibility to the numerical method, it does not ensure that the method will accurately simulate the flow around the obstacle. A more crucial test is provided by comparing the numerical and experimental results for the steady flow

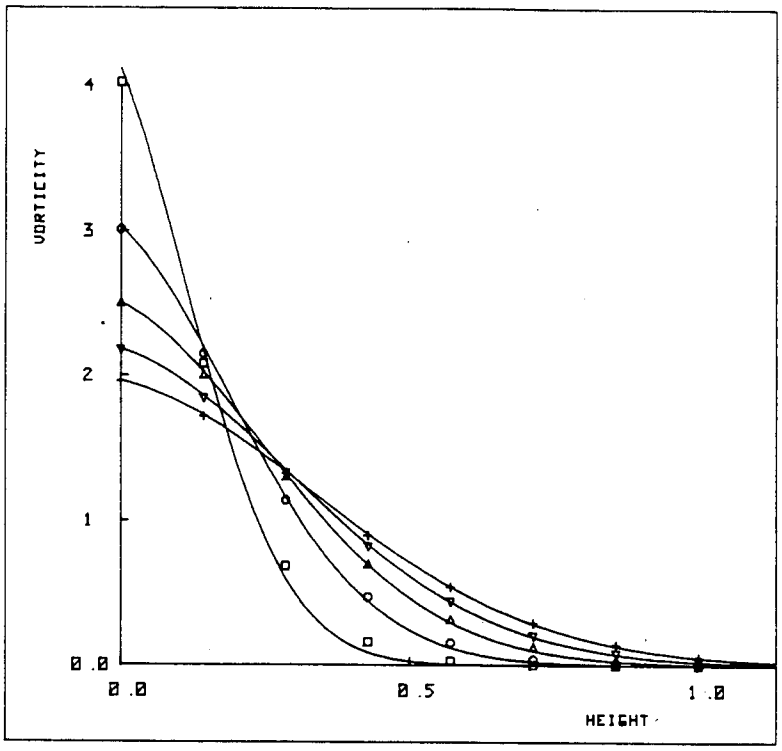

Figure 7.1. The development of the flow with an impulsively started wall at a Reynolds number of 10.
—— Theoretical ; □ t = 0.16s. ; ○ t = 0.32s. ; △ t = 0.48s. ; ▽ t = 0.64s. ; + t = 0.80s.

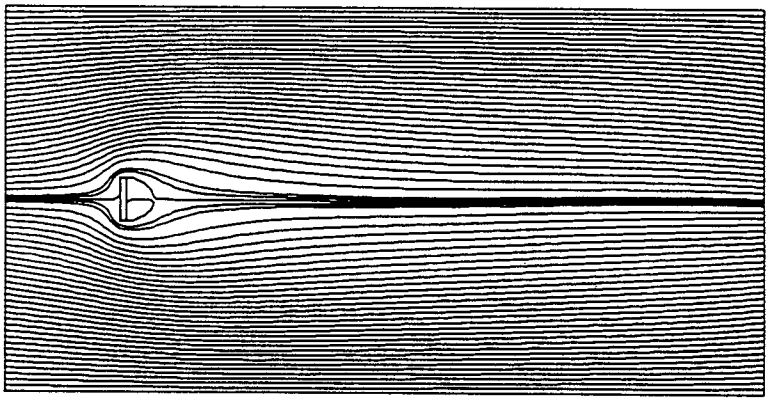

Figure 7.2. The streamline plot for the steady flow past the obstacle at Re = 5, t = 15s.

past the obstacle at a low Reynolds number. There have been many investigations, both numerical and experimental, of the steady flow around a circular cylinder at low Reynolds numbers, but relatively few on the steady flow past a flat plate. The numerical results of the steady flow around the rectangular obstacle must, therefore, be compared with numerical and experimental results for the steady flow around a circular cylinder. At Reynolds numbers of less than around 40 the flow around a circular cylinder is steady and vortex shedding does not normally take place. The wake immediately behind a cylinder is closed and contains a region of re-circulating flow.

The length of the closed wake varies with Reynolds number and this variation has been measured experimentally by Taneda (1956), and by Acrivos, Leal, Snowden and Pan (1968). A number of workers have obtained similar measurements from numerical solutions to the steady viscous flow past a circular cylinder [See Tuann and Olson (1978)]. Much fewer measurements have been made of the length of the closed wake behind a flat plate. However, Prandtl and Tietjens (1934) have presented some flow visualisations of the near wake behind a flat plate. At a Reynolds number of 10 the length of the closed wake was about 1.4D.

With the obstacle present on the grid several runs of the program were made to obtain numerical solutions to the steady viscous flow past the obstacle at various Reynolds numbers. From the numerical solutions, measurements were made of the length of the closed wake region. The closed wake region is most easily identified by inspection of the plots of the stream function. Figure 7.2 shows the streamline plot at $Re = 5$, for the flow behind the obstacle.

The streamlines are plotted at each of 64 values spaced equally, ranging from the ψ value at the lower wall to the ψ value at the upper wall. Three extra streamlines are drawn near the centre of the wake, with one whose value is equal to the value of ψ on the surface of the obstacle. The closed wake region can clearly be seen immediately behind the obstacle. Figures 7.2, 7.3, 7.4 and 7.5 shows the extension of the closed wake with the increase of Reynolds number from 5 to 50. Whereas at $Re = 50$ the closed wake region still appears stable, at $Re = 100$, Figure 7.6, it is obviously not so. In Figure 7.6 the upper vortex appears much larger than the lower vortex and the vortex pair are no longer symmetrically placed directly behind the obstacle. The closed wake region has not developed to the size that might be expected by extrapolating the results for the wake length obtained from Figures 7.2 to 7.5.

Figure 7.6(b) shows the measurements of the closed wake length obtained from the steady flow solutions at $Re = 5$, 10, 20 and 50. The figure also shows the results obtained by other workers for the flow around a circular cylinder. It would appear from the comparison of the results presented in Figure 7.6(b) that the variation of the length of the closed wake behind a rectangular obstacle is very similar to the corresponding variation for a circular cylinder. Very few experimental measurements of the closed wake length appear to have been made for any two-dimensional body other than a circular cylinder. The length of the closed wake behind a flat plate at $Re = 10$, taken from the flow visualisation results of Prandtl and Tietnens (1934), suggest that, at low Reynolds numbers, the flow around a flat plate is similar to the flow around a circular

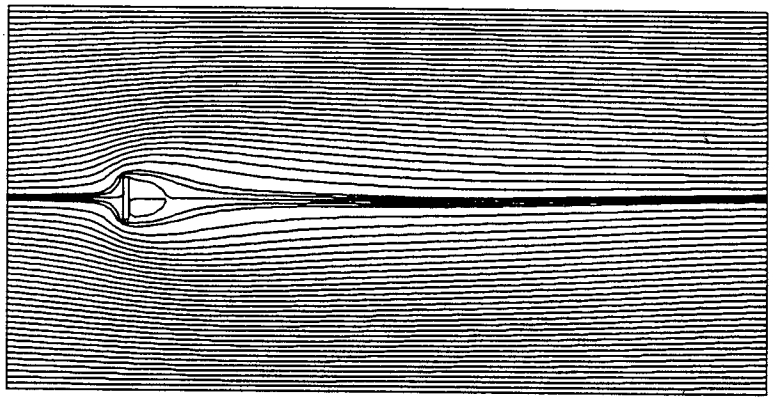

Figure 7.3. The streamline plot for the steady flow past the obstacle at Re = 10, t = 15s.

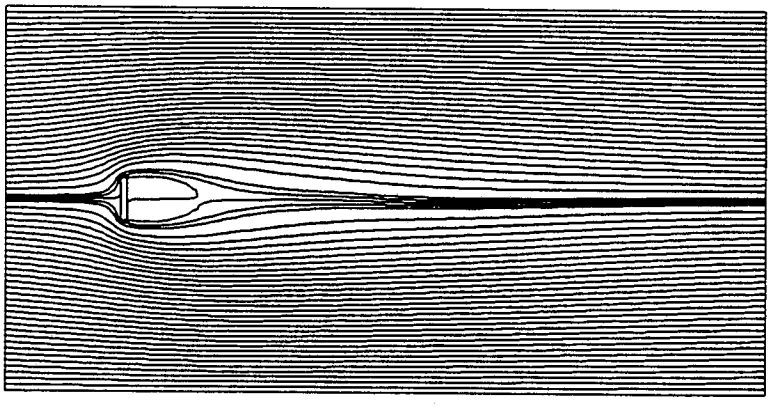

Figure 7.4. The streamline plot for the steady flow past the obstacle at Re = 20, t = 15s.

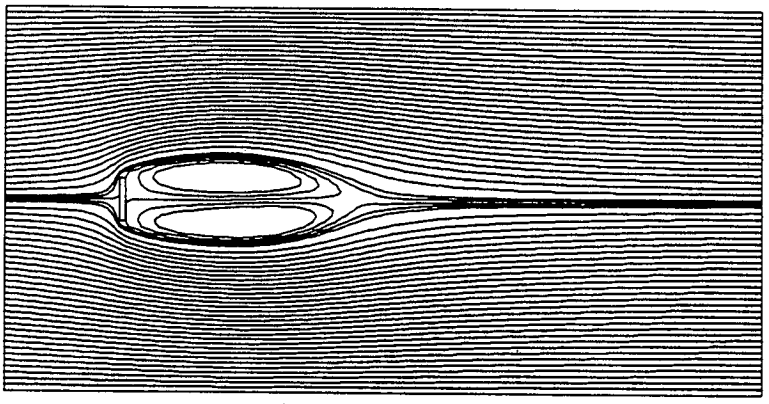

Figure 7.5. The streamline plot for the steady flow past the obstacle at Re = 50, t = 15s.

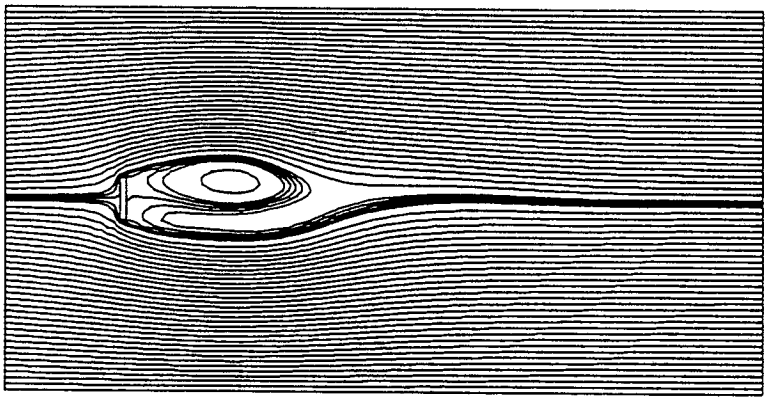

Figure 7.6. The streamline plot for the developing flow past the obstacle at Re = 100, t = 15s.

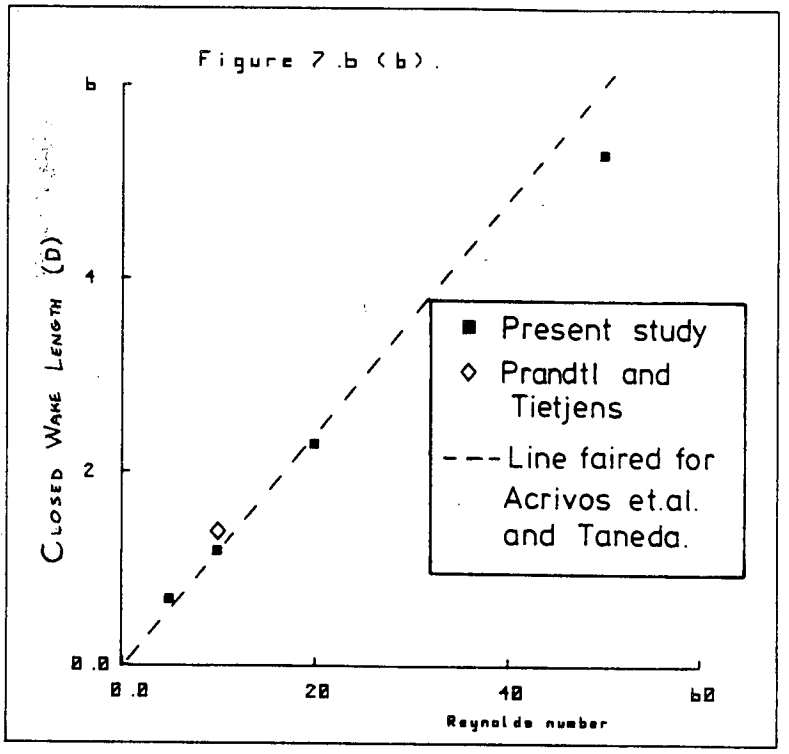

Figure 7.6(b). The variation of the length of the closed wake for the steady flow past the obstacle at low Reynolds number.

cylinder. However, the good agreement between the results presented in Figure 7.6(b) with the corresponding results obtained for the flow around a circular cylinder suggest that the method correctly models some of the main features of the flow around a rectangular obstacle.

The development of the unsteady flow at Re = 200 is presented in Figures 7.7 to 7.10. At t = 15s, the lower vortex appears larger than the upper vortex and has crossed the wake centre line slightly. The upper vortex has, therefore, been displaced slightly outwards away from the wake centre line. At t = 17.5s, Figure 7.8 shows that the lower vortex moves slightly downstream with its long axis directed at an angle to the wake centre line. The upper upper vortex has moved slightly upstream towards the obstacle and has its long axis directed in a similar direction to that of the lower vortex. The wake is no longer closed with a "saddle" point near the downstream end of the eddy pair [Perry & Lim (1978)]. The near wake is clearly in a highly unstable state. At t = 20s the lower eddy has moved to a position approximately 3D downstream of the obstacle. The upper vortex has become much larger and a small lower vortex has appeared very close to the lower edge of the obstacle. At t = 22.5s the first lower vortex no longer has any closed streamlines associated with it, whilst the first upper vortex has grown very large and has moved to a position about 3D downstream of the obstacle, and closer to the wake centre line. The second lower vortex has grown larger and moved much closer to the wake centre line. A very small second upper vortex has just started to form at the upper edge of the obstacle. The flow will thus continue to develop until vortex shedding has

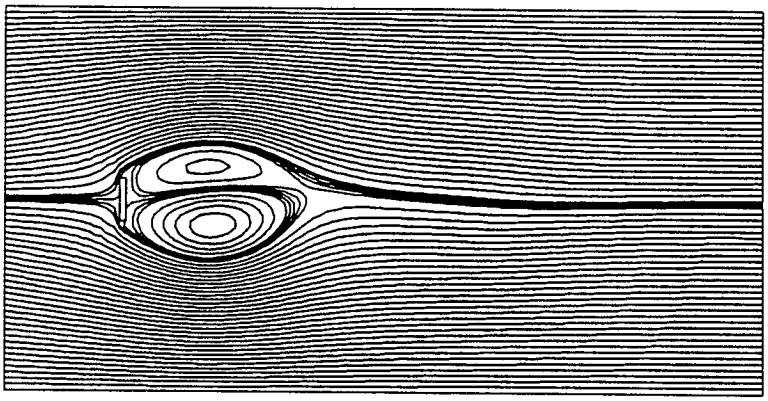

Figure 7.7. The streamline plot for the developing flow past the obstacle at Re = 200, t = 15s.

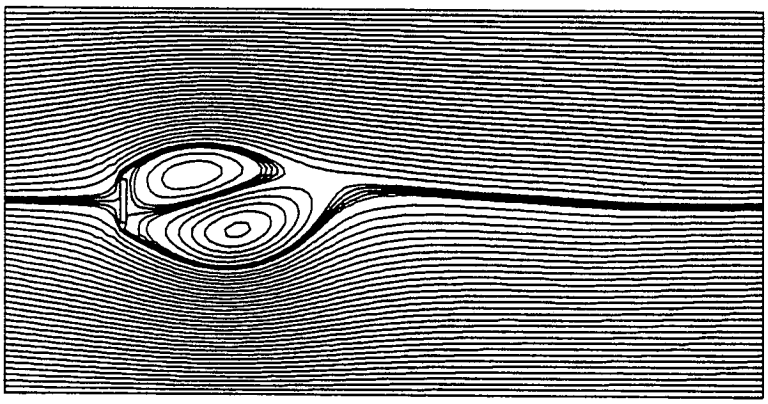

Figure 7.8. The streamline plot for the developing flow past the obstacle at Re = 200, t = 17.5s.

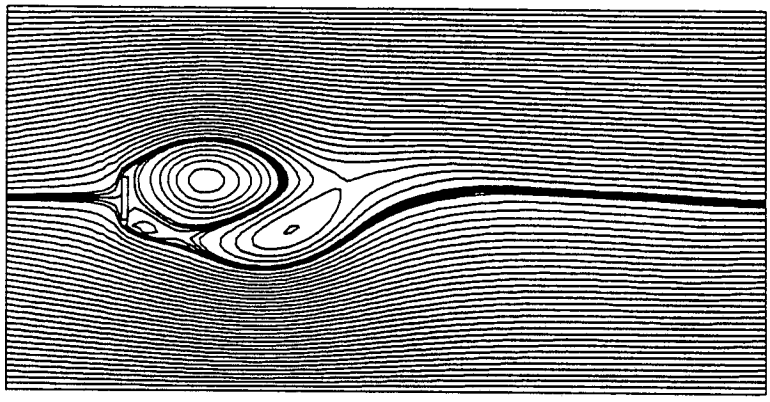

Figure 7.9. The streamline plot for the developing flow past the obstacle at Re = 200, t = 20s.

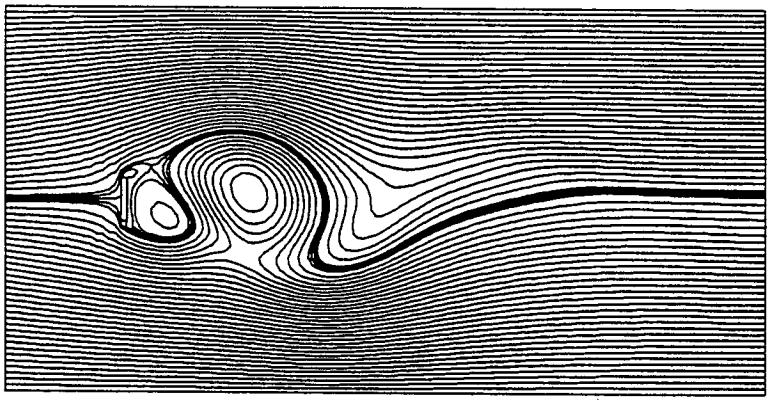

Figure 7.10. The streamline plot for the developing flow past the obstacle at Re = 200, t = 22.5s.

become fully established and vortices are shed with a constant period.

(d) VORTEX SHEDDING SIMULATIONS IN STEADY ONCOMING FLOW

The flow simulations of the previous section show that vortex shedding develops naturally, presumably due to very small instabilities in the numerical scheme. However, long simulation times are required by the numerical scheme before regular vortex shedding is attained. To encourage the onset of vortex shedding a small perturbation is introduced into the flow field. At three positions near the inflow boundary on the stagnation streamline a small vorticity, of about 1% of the vorticity at the upstream corner of the obstacle, is introduced. This vorticity convects towards the obstacle and, as it passes the obstacle, a significant asymmetry is caused in the flow behind the obstacle. Regular vortex shedding develops soon afterwards. Figure 7.11 shows the variation of the v component of velocity at a position about 3D downstream of the obstacle and 1.8D below the wake centre line for Re = 100. At $t > 20s$ the vortex shedding appears highly regular and periodic. By estimating the period of the velocity fluctuation for times $t > 20s$ the Strouhal number may be computed.

Using the above method, several runs of the program were made to obtain the Strouhal numbers for the flow past the obstacle at a number of Reynolds numbers. Figure 7.12 shows the results of these runs, and also shows the experimental results obtained by Roshko (1954), for the flow past a flat plate. The numerical results are in good agreement with the experimental results. Fromm and Harlow

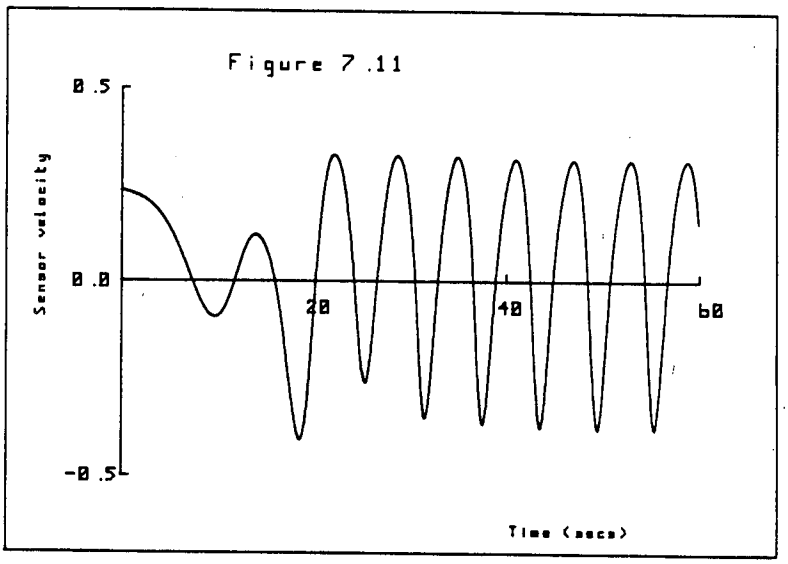

Figure 7.11. The variation of the v-component of velocity at a position 3D downstream of the plate and 1.8D below the wake centre-line. $Re=100.$

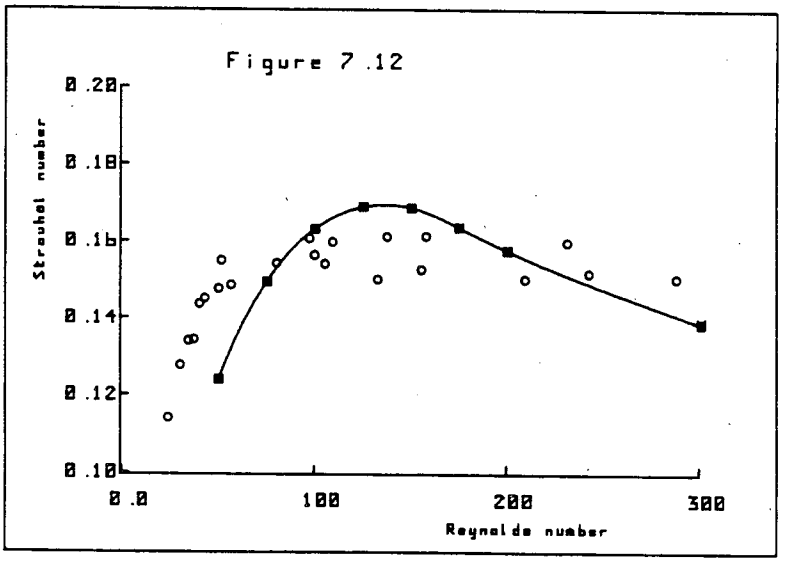

Figure 7.12. The Strouhal numbers computed at various Reynolds numbers for the flow past the obstacle.
○ Experimental values ; ■ DAP simulation values.

(1963) obtained much poorer agreement with the experimental results with a Strouhal number of 0.119 at Re = 100, rising to St = 0.137 at Re = 300. This Strouhal number variation does not closely follow the experimental results of Roshko. It was thought this was perhaps a direct consequence of the fact that they used equation (7.10) to compute the vorticity at the surface of the obstacle, instead of equation (7.26). Some simulations were tried using equation (7.10) and the Strouhal numbers obtained were much higher than those presented in Figure (7.12).

However, the Fromm and Harlow numerical scheme employed periodic boundary conditions at the inflow and outflow boundaries. Thus, when a vortex reached the outflow boundary it would then appear at the inflow boundary. This, of course, limited the length of time of the simulation to the early stages of the development of the wake. A second consequence of the periodic boundary conditions was that the flow was gradually slowed and, therefore, the Reynolds number was gradually reduced. Also, the obstacle in their simulations was only four cells in height and so the accuracy of their numerical results is perhaps less than that of the present investigation. It is interesting to note that the closed wake lengths obtained using equation (7.10) instead of equation (7.26) were almost exactly the same as those presented in Figure 7.6(b). This would appear to indicate that the length of the closed wake behind the obstacle is insensitive to the rate of generation of vorticity at the surface of the obstacle.

The question naturally arises as to which equation, (7.10) or (7.26), should be used to compute the vorticity at the surface of

the obstacle. If equation (7.10) is used, then the "true" surface of the obstacle must be $^{a}/2$ behind the position specified as the surface. Since the object is only one cell thick, then presumably the simulation is that of the flow around a thin plate. If equation (7.26) is used, then the simulation is that of the flow around a rectangular obstacle 1m high and $\frac{1}{7}$m wide. All the flow simulations presented in this thesis used equation (7.26) to compute the vorticity at the surface of the obstacle. The good agreement of the numerical results with Roshko's experimental results provide further justification for the use of equation (7.26) instead of (7.10).

Figure 7.13 shows the streamline plot for the unsteady flow past the obstacle at Re = 200, t = 60s. It would appear from this plot that the wake contains a street of vortices. The appearance of the vortices is not clear, however, and it is more useful to plot the contours of vorticity. Figure 7.14 shows several contours of vorticity plotted at Re = 50, for t = 60s. Vortices can clearly be seen in the wake. Figure 7.14 clearly shows that the concentration of vorticity associated with a vortex reduces with increasing distance downstream of the obstacle, as at this relatively low Reynolds number, the rate of diffusion is significant compared to the rate of convection. The lateral separation of the vortices also increases significantly as the vortices convect downstream.

At Re = 100, t = 60s, Figure 7.15 shows that the diffusion of vorticity associated with the vortices as they travel downstream is not as rapid as in the case of the flow at Re = 50. The lateral

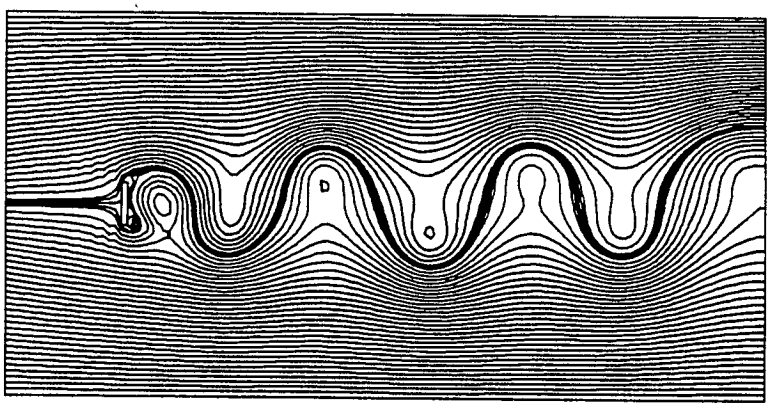

Figure 7.13. The streamline plot for the unsteady flow past the obstacle at at Re = 200, t = 60s.

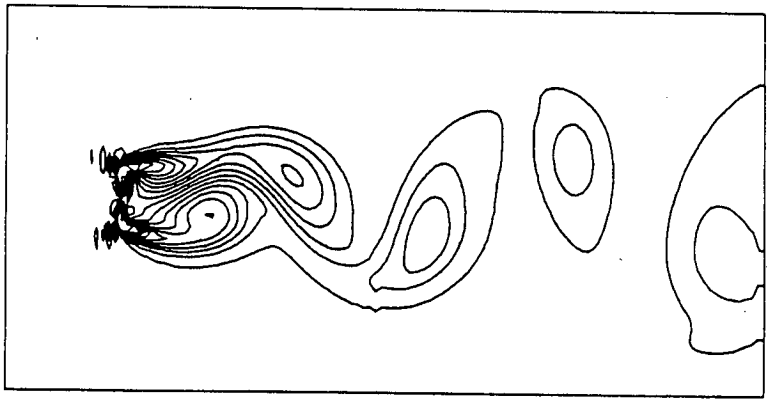

Figure 7.14. Contours of vorticity plotted at Re = 50, t = 60s.

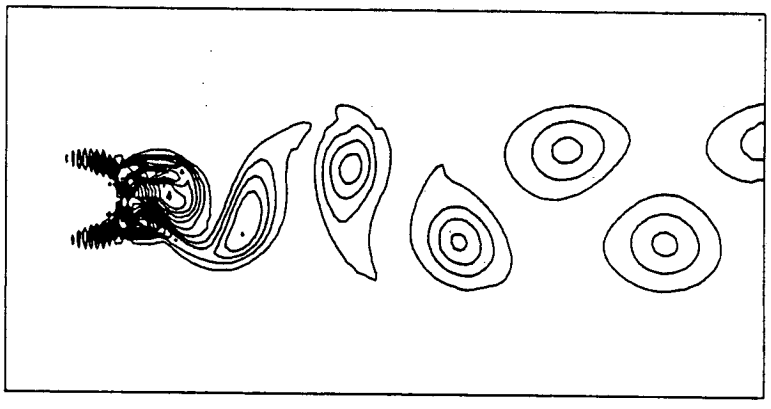

Figure 7.15. Contours of vorticity plotted at Re = 100, t = 60s.

separation of the vortices also increases much more slowly as they convect downstream. The vortices of Figure 7.15 also appear more like the familiar von-Kárman street. Figure 7.16 shows the contours of vorticity plotted for Re = 200, t = 60s, and Figure 7.17 shows the vorticity contours plotted for Re = 300, t = 60s. In both Figures 7.16 and 7.17 the vortex street may be seen. From the plots of the vorticity contours the vortex centres were identified by eye and the longitudinal and lateral separation of the vortices was then measured. The circulation of the vortices may be estimated by using

$$\Gamma = \int_S \omega.da \qquad (7.35)$$

where S is a surface containing the vortex. The surface was a rectangle whose centre was coincident with the centre of the vortex. The length of the horizontal sides was equal to the half of the longitudinal separation of the vortices. The length of the vertical sides of the rectangle was varied and it was found that when their length was greater than 3D, the estimates of Γ for rectangles of different size were constant to within $\pm 1\%$ for $Re \geq 100$. The estimates of the vortex strength and spacings obtained from Figures 7.14 to 7.18 are presented in Table 7.1, along with some experimental results obtained by Griffin and Ramberg (1975). Also presented in Table 7.1 are the vortex convection speeds computed from the longitudinal spacing and the Strouhal number.

Figure 7.18 is presented for completeness and shows the instantaneous streamline plot for an observer moving at 1 ms^{-1} relative to the obstacle. The vortex convection speed at Re = 200 is approximately $0.93\bar{U}$ and hence the vortices in the moving reference frame

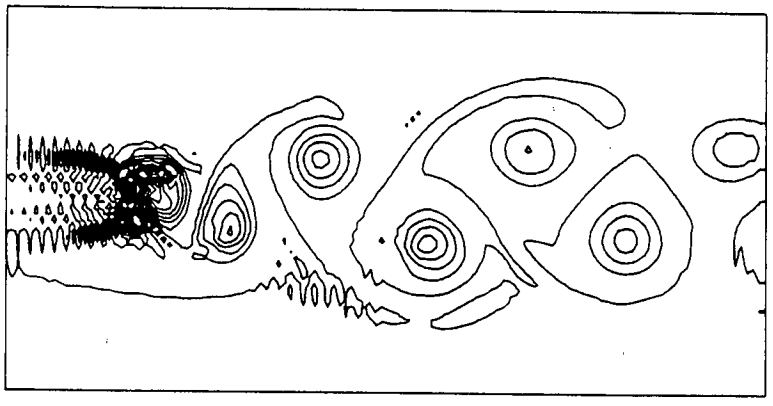

Figure 7.16. Contours of vorticity plotted at Re = 200, t= 60s.

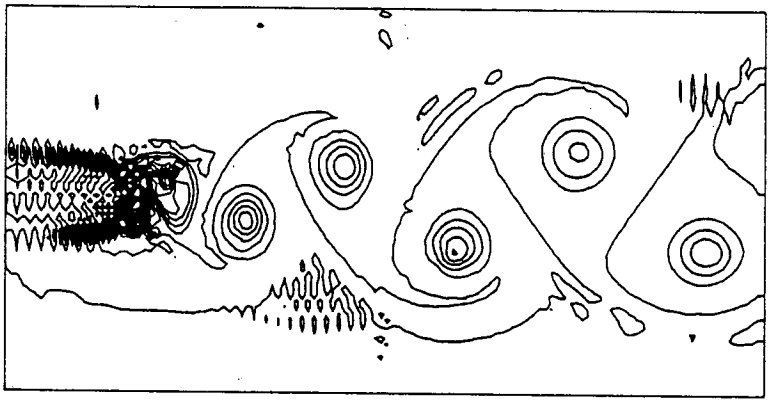

Figure 7.17. Contours of vorticity plotted at Re = 300, t =60s.

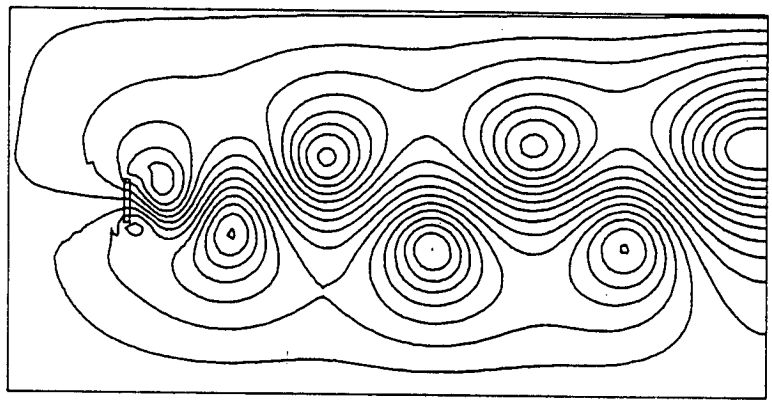

Figure 7.18. The streamline plot for an observer moving at the free-stream speed for the flow past the plate at Re = 200, t=60s.

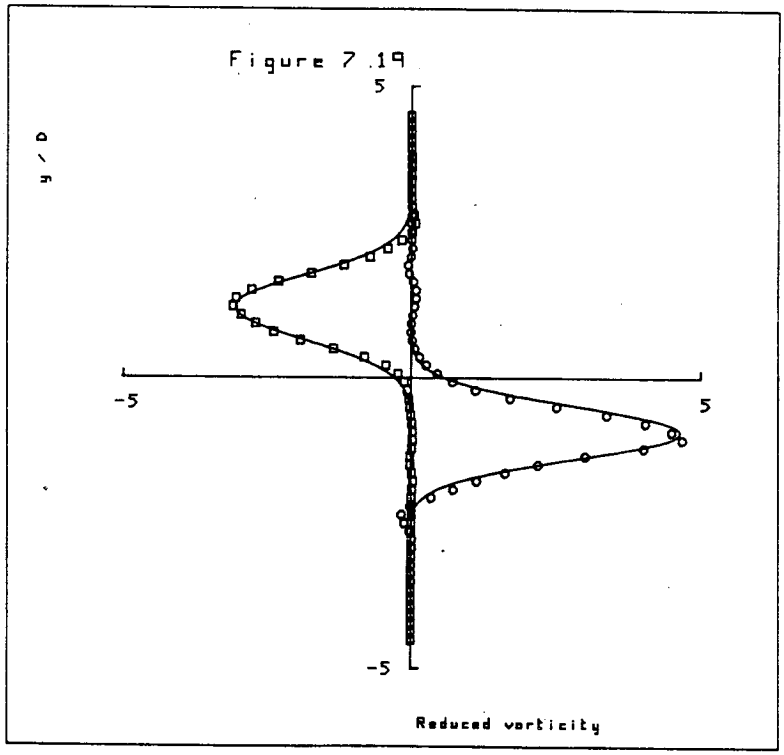

Figure 7.19. The variation of the vorticity through a vortex centre at Re = 200, t = 60s.
—— theoretical fit ; ○ vortex at grid position (70, 25) ;
□ vortex at grid position (87, 41).

TABLE 7.1 Various parameters obtained from numerical simulations of the flow around the obstacle

Re	50	100	200	300	Griffin & Ramberg Re=144	Griffin & Ramberg Re=450
l/D	6.7	4.9	5.8	5.3	5.4	5.0
b/D	1.5	2.4	2.1	2.1	0.97	0.90
b/l	0.22	0.49	0.37	0.40	0.18	0.18
$\Gamma/\bar{U}D$	3.3	4.8	5.9	6.1	2.54	2.01
$U_c/\bar{U}$	0.82	0.80	0.93	0.74	——	——
St	0.123	0.163	0.158	0.139	0.18	0.21

The values of $\Gamma/\bar{U}D$ are for vortices about 12D downstream of the obstacle.

would appear to be almost stationary.

From the measurements of the vortex strength and the vorticity distribution through the vortex centre, a value for the viscous core radius was obtained in the same manner as was described in Chapter 6, section (d). Figure 7.19 shows the comparison between the numerical vorticity distribution through a vortex centre, and a fitted Hamel-Oseen vortex. The match between the numerical and theoretical distributions is excellent. At lower Reynolds numbers the match is much poorer, and at higher Reynolds numbers the match is as satisfactory as that shown in Figure 7.19.

(e) VORTEX SHEDDING SIMULATIONS IN PERTURBED FLOW

Having established the Strouhal numbers for vortex shedding in a steady flow, it is now possible to investigate the effect on the process of vortex shedding of a single frequency perturbation superimposed on the mean free-stream flow. If the frequency of the perturbation is near to twice that of the vortex shedding frequency, then the vortex shedding may become synchronised with the perturbation in the same manner as was found experimentally and which is described in Chapter 5. The Reynolds numbers of the flow simulations are, of course, much lower than the Reynolds numbers used in the experimental investigations described in the previous two chapters. As remarked in those chapters, lock-in has been found experimentally at low Reynolds numbers for the flow around an oscillating circular cylinder and it might be expected to occur for a flat plate in a perturbed flow at low Reynolds numbers. There does not appear to

have been any experimental investigations of lock-in for an oscillating flat plate or rectangular cylinder at low Reynolds numbers, therefore, the numerical results can only be compared with the experimental results for the flow around an oscillating circular cylinder.

The program was run with an oscillatory perturbation superimposed on the free-stream velocity, such that

$$U_{\substack{\text{inflow} \\ \text{Upper Wall.}}} = \bar{U} + p \sin 2\pi ft \qquad (7.36)$$

where p denotes the amplitude of the perturbation and f is the frequency of the superimposed perturbation. Before proceeding to simulate the oscillatory flow past the obstacle, the program was run with no obstacle present and with the flow fully reversing, i.e. with no mean flow. The lower wall was held stationary whilst the upper wall moved with the same velocity as the free-stream. This is an example of a simple time-dependent viscous flow for which an exact analytic solution is known. Shear waves are generated at the wall and move away from the wall with velocity $\sqrt{4\pi\nu f}$ and attenuate in amplitude as $e^{-\sqrt{(\pi f/\nu)}\, y}$. The value of u throughout the flow field is given by

$$u(y,t) = p \sin 2\pi ft. \left[1 - e^{-y\sqrt{(\pi f/\nu)}} \cos(2\pi ft - y\sqrt{(\pi f/\nu)}\right]. \qquad (7.37)$$

[Batchelor (1967)]

Figure 7.20 shows the comparison of the numerical results with the theoretical results for the fully reversing oscillatory flow over the wall. There is a significant discrepancy between the numerical and theoretical results where $\partial^2 U/\partial y^2$ is greatest. This discrepancy is reduced by decreasing the value of δt, as shown on Figure 7.20. The discrepancy was not reduced by extending the simulation to larger

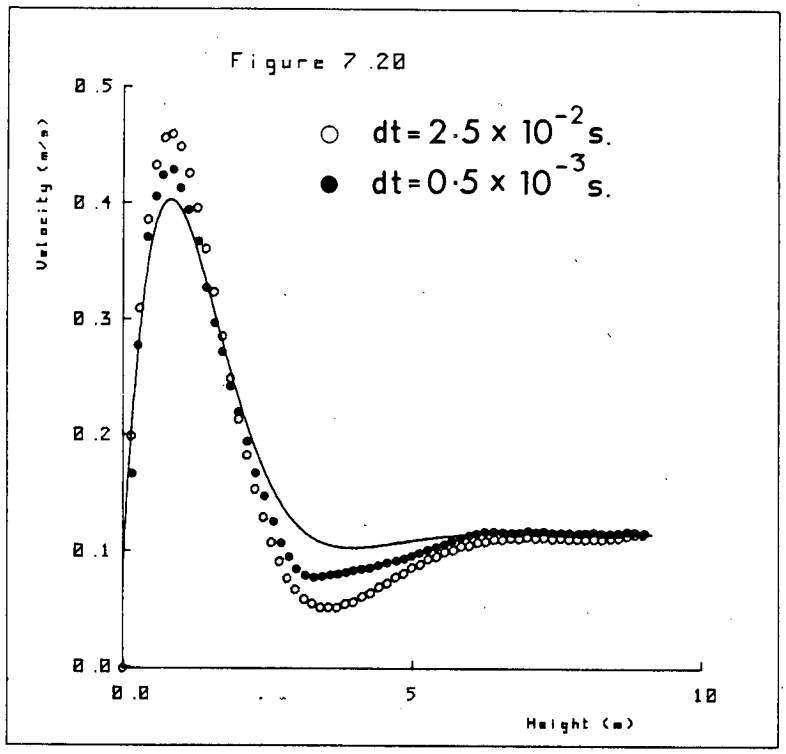

Figure 7.20. The fully oscillatory flow near a stationary wall.
—— Theory ; ●○ DAP simulation, t = 3·2s, p = 0·5ms⁻¹, f = 0.3183Hz.

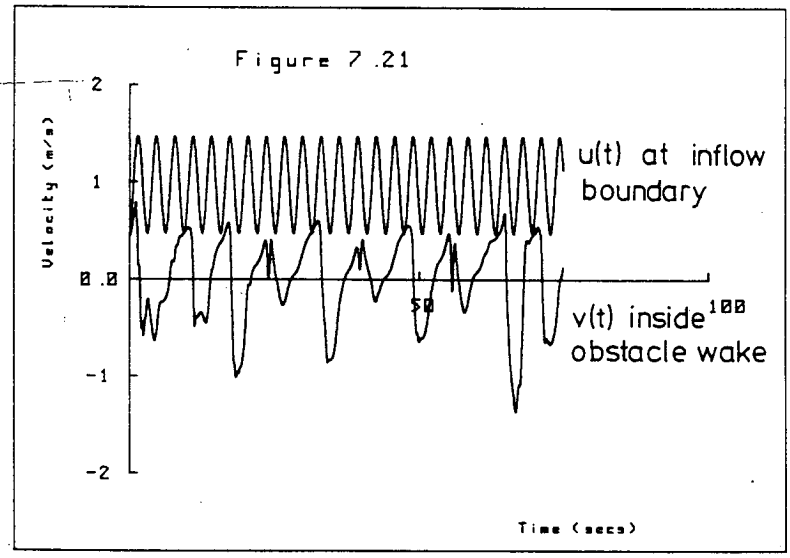

Figure 7.21. Time histories of the variation of certain velocity components in oscillatory flow with p = 0.5ms⁻¹, f = 0.3183Hz, $\bar{u}$ = 1 ms⁻¹.

times. The largest error in the magnitude of the velocity is less than 10% of the amplitude of the oscillation. Since, in the perturbed flow simulations, the oscillatory component is only a perturbation on the mean flow, the magnitude of the error associated with the oscillatory component of velocity will be much less than 10% of the mean inflow velocity. The cost, in terms of computational time, required to reduce the error was not considered worthwhile.

The program was run with the obstacle present in the flow field with a number of perturbations, having different amplitudes and frequencies superimposed upon the mean free-stream flow. The perturbation frequencies were chosen to be over a range which included twice the vortex shedding frequency found for steady flow. The amplitudes were chosen to be from $0.1\overline{U}$ to $0.5\overline{U}$. Lock-in was not found for any of the perturbations that were imposed upon the mean flow. Figure 7.21 shows the time histories of the free-stream velocity and the vortex shedding signal, for a perturbation amplitude of $0.5\overline{U}$ and a perturbation frequdncy of 0.318 Hz. As can be seen by inspection of Figure 7.21, no lock-in has taken place. At a lower amplitude of perturbation the periodicity of the vortex shedding is much better than that shown in Figure 7.21, but was, nevertheless, not locked-in to the perturbation frequency. The results of the simulations of the perturbed flow past the obstacle are rather surprising. One would expect that if lock-in takes place for the in-line oscillation of a circular cylinder at Re = 190 [Griffin and Ramberg (1976)] when the oscillation amplitude is above a threshold value, then lock-in should also take place in the perturbed flow around a rectangular obstacle when the perturbation amplitude is above a threshold value. The threshold amplitude for lock-in for a circular

cylinder oscillating in-line has been measured by Griffin and Ramberg as about $a/D = 0.1$ for frequencies close to twice the natural vortex shedding frequency. The threshold perturbation amplitude for lock-in for the flow around a rectangular obstacle may be higher than that required for lock-in for the flow around a circular cylinder. This might be expected on the basis of the results of Chapter 5 where the lock-in range for the flat plate was about half of the corresponding lock-in range for the circular cylinder. However, the perturbation amplitude of 0.5 is equivalent to an oscillation amplitude of $a/D = 0.53$ at a Strouhal number of 0.15 and this far exceeds the threshold amplitude of 0.1 which was found by Griffin and Ramberg. Also, Clements (1975) has found lock-in for the numerically simulated flow past a blunt based semi-infinite body using the discrete vortex method. At perturbation amplitudes of $p = 0.1$ lock-in was obtained.

In the light of results of other workers the present perturbed flow results seem somewhat unsatisfactory. There are many questions raised by the results and further work is required to establish why lock-in was not found. Unfortunately, the time required to investigate further the problem was simply not available. Program development for programs using the DAP is usually a rather lengthy process. Also, a large number of runs are required even when only minor details in the computational scheme are changed in order to investigate the dependence of the flow simulation on various parameters. Each run usually requires about one hour of DAP time and, due to a rather unacceptable queuing system for jobs awaiting the DAP, these jobs can take as long as three weeks before being run. The queuing

system runs the job in the queue that requires the least time on the DAP. Thus, users running shorter jobs have their jobs run first, no matter how long the longer jobs have been in the queue. The simulations presented in this chapter were run only through the use of a high priority process on EMAS which avoids the queuing system. I wish to thank B. Pendleton for the use of his high priority process.

(f) CONCLUSIONS

A distributed Array Processor (DAP) has been used to obtain solutions to the time-dependent viscous flow around a rectangular obstacle. The solutions were obtained by time-step integration of the transport of vorticity equation. Parallel processors such as the DAP have many applications in the field of Fluid Dynamics, where highly parallel algorithms may be used to solve the governing field equations.

For $Re = 10$ the length of the closed wake was found to be in close agreement with the experimental result obtained by Prandtl and Tietjens. When the numerical results were compared with experimental results for a circular cylinder for the variation of the closed wake length with Reynolds number, there was good agreement for $Re \leq 50$.

The Strouhal frequency variation with Reynolds number was in good agreement with those results obtained experimentally by Roshko. Vortex shedding did not develop for $Re = 20$ but did for $Re = 50$, which is in agreement with the experimental observation that vortex shedding does not occur below $Re \sim 40$.

For Re $\geq$ 50, the vortex street pattern was observed in the wake of the obstacle. The longitudinal spacing of the vortices is close to that obtained experimentally for the flow around a circular cylinder, but the lateral spacing is much larger. The variation of the vorticity through a vortex centre close to that of a Hamel-Oseen viscous vortex at Re $\geq$ 100.

Lock-in was not found when the mean oncoming flow was perturbed. A number of perturbation frequencies and perturbation amplitudes was used, and the frequencies were over a range including twice the vortex shedding frequency that was obtained from the steady flow simulations. This result is in disagreement with the experimental observations described in Chapter 5.

CHAPTER 8

(a) CONCLUSIONS

In all of the investigations presented in this thesis the fluid behaves, to a very good approximation, as an incompressible fluid. The results obtained for the case of a bluff body in an oscillatory flow are, therefore, expected to be relevant to the case of bluff body oscillating in-line with the flow direction.

The forces acting on square flat plates placed normal to the flow direction were measured when the plate was exposed, in turn, to a steady, a turbulent, and an oscillatory flow. These measurements are described in Chapter 4. The results obtained in the steady and the turbulent flow were in agreement with those of other workers. The aerodynamic admittance, relating the velocity spectrum of the approaching flow to the resulting force spectra acting on the plate, was measured in the case of turbulent flow and oscillatory flow. In a turbulent flow the admittance falls off rapidly for reduced frequencies of $^{n\ell}/\overline{U} > 0.1$. The admittances measured for each of the plates in turbulent flow collapses well onto the empirical relation given by Vickery (see equation (4.10). In the case of oscillatory flow, however, the admittance rises rapidly for $^{n\ell}/\overline{U} > 0.1$. With increasing reduced frequency the fluctuating drag coefficient increases whereas the added mass coefficient decreases asymptotically to about 0.6. The results for the variation of the drag coefficient and added mass coefficient are qualitatively similar to those obtained by Davenport for a two-dimensional flat plate oscillating in a steady water current. An approximation to the oscillatory flow

which was investigated may be found in the wake of a bluff body and the results show that great care must be taken in assessing the fluctuating forces likely to be encountered by a structure in the wake of another structure.

Chapter 5 describes a study of the oscillatory flow around each of three bluff cylinders. The cylinders used in the study were a circular cylinder, a flat plate and a D-section. For each cylinder, when the perturbation frequency was close to twice the vortex shedding frequency, the vortex shedding frequency became locked-in to the perturbation frequency over a small range of reduced velocities $\overline{U}/n_o D$. With lock-in the vortices were shed at exactly half of the perturbation frequency. The lock-in range included the resonant point and the range of reduced velocities over which lock-in occurred increased with increasing perturbation amplitude. The base pressure was reduced with lock-in. For the flat plate and the D-section the lock-in ranges, and the changes in the base pressure with lock-in, were about half of those for the circular cylinder. For the circular cylinder, the sectional fluctuating lift coefficient, the mean drag and the correlation length increased with increasing perturbation amplitude.

The base pressure measurements indicated that the rate of shedding of circulation into the wake was increased with lock-in. If it were assumed that the fraction of vorticity surviving the vortex formation process did not change with lock-in, then the strength of the vortices in the wake of the cylinder would be increased with lock-in. If no changes occurred in the wake geometry then this would result in the mean wake deficit being increased. The mean velocity profiles, however, showed that no such change took place with lock-in.

It was then concluded that a more detailed examination of the wake was required.

An investigation of the wake structure was carried out and is described in Chapter 6. The underlying mean wake of the circular cylinder was reconstructed by the conditional sampling of the turbulent wake. This method provides direct measurements of the vortex strength and the spacings of the vortices in the wake. These measurements showed that with lock-in the vortex strength was increased and the lateral separation of the vortices was reduced whilst the longitudinal vortex separation was unchanged. Additional measurements showed that the length of the vortex formation region was decreased with lock-in. An estimate was made of the fraction of the vorticity generated by the cylinder that was found remaining in the developed wake vortices. This fraction was estimated to be about 31% in steady flow and 33% in oscillatory flow.

The conditional sampling measurements were matched to a viscous vortex model of the wake. The vorticity distribution through the centre of a wake vortex was found to be closely matched by a Hamel-Oseen viscous vortex. Without the addition of a mean shear to the model, the model correctly predicted that there would be no change in the mean wake velocity profile with lock-in. With the addition of a mean shear, the model closely matched the experimentally measured mean wake velocity profiles. The model also correctly predicted the variance of the u fluctuations of velocity at the vortex shedding frequency, but overestimated the variance of the u fluctuations at the second harmonic of the shedding frequency.

Chapter 7 describes the use of a distributed array processor (DAP) to obtain approximate solutions to the time-dependent viscous

flow around a rectangular obstacle. At low Reynolds numbers the steady flow results for the length of the closed wake behind the obstacle were in good agreement with the experimentally obtained results for the length of the closed wake behind a circular cylinder. An experimental result for the length of the closed wake behind a flat plate at a Reynolds number of 10, is close to the result obtained for a circular cylinder at the same Reynolds number. When the flow was perturbed at Reynolds numbers greater than, or equal to, 50 vortex shedding developed, but at lower Reynolds numbers vortex shedding did not develop. The Strouhal frequencies of the vortex shedding were in good agreement with those obtained by Roshko for the flow behind a flat plate. The vortices in the wake of the obstacle were closely matched by Hamel-Oseen viscous vortices. The longitudinal spacing of the vortices in the flow behind the obstacle was approximately the same as that measured experimentally for the flow around a circular cylinder, but the lateral spacing was much greater. The lateral spacing of the vortices in the wake of a D-section is much greater than that in the wake of a circular cylinder, but it is still much less than that found in the wake of the obstacle.

An attempt was made to obtain solutions to the time-dependent viscous flow around the obstacle when the oncoming mean flow had a superimposed oscillatory perturbation. A number of frequencies and amplitudes of perturbation were tried but lock-in was not found. The range of perturbation frequencies included frequencies close to twice the frequency of vortex shedding. The failure to find lock-in is in disagreement with the numerical results obtained by other workers.

(b) FUTURE WORK

With the maximum amplitude of perturbation that can be attained using the shutters in the wind tunnel, there would appear to be little further work that might be attempted on an oscillatory flow in the wind tunnel. The conditional sampling of the wake behind the D-section and the flat plate would probably be fruitless as the changes in their wakes with lock-in is much smaller than the changes in the wake of the circular cylinder with lock-in.

An approximation to the perturbation produced by the shutters, but of larger perturbation amplitude, might be obtained by placing a flat plate upstream of the body under investigation. The frequency of the perturbation would be varied by adjusting the angle of the flat plate. The uniformity of the perturbation is, however, much poorer than the uniformity of the perturbation produced by the shutters. A.J. Baxendale is currently investigating the flow around two circular cylinders where the diameter of the upstream cylinder is half of that of the downstream cylinder. Lock-in has been found with the downstream cylinder shedding at exactly half of the shedding frequency of the upstream cylinder. It would be interesting to compare the wake structure of a single cylinder, using the conditional sampling technique, with that of a cylinder whose shedding is locked-in to the shedding of an upstream cylinder. Comparisons of the changes occurring with lock-in in this case with the changes that were found in the present investigation would be useful.

Studies are required on the flow around bodies oscillating in-line with the flow direction with bodies other than a circular cylinder.

It would be interesting to discover whether or not the lateral spacing was reduced with lock-in for sharp edged bodies. It would also be interesting to compare the change in the vortex strength with lock-in for a sharp edged body to that measured for a circular cylinder.

The DAP would appear to be one of the most promising of the research facilities currently available at Edinburgh University. There are a great many Fluid Dynamics problems that may be solved using highly parallel algorithms. The architecture of the DAP is ideally suited for the implementation of such algorithms, particularly those for obtaining solutions to problems using finite-difference approximations to the equations of motion. An obvious extension of the investigation described in Chapter 7 would be to obtain approximate solutions to the time-dependent viscous flow around a circular cylinder. This problem is, however, more complex than that of the flow around a rectangular obstacle. The spatial region around the cylinder must be transformed so that it may be represented on a square grid. Also, more grid points are required near the surface of the cylinder than are required at large distances from the surface. If enough points are used to represent the spatial region near the surface of the cylinder than it may be possible to represent the boundary layer on the surface. This work would, perhaps, require a number of years. Nevertheless, very few numerical solutions have been obtained for the unsteady viscous flow around a circular cylinder by solving the full Navier-Stokes equations.

For the case of the flow around the rectangular obstacle, more work is required to establish the reasons as to why lock-in was not found in the perturbed flow.

REFERENCES

Abernathy, F.H. & Kronauer, R.E. (1962) J. Fluid Mech. 13, 1.

Acrivos, A., Leal, L.G., Snowden, D.D. & Pan, F. (1968.). J. Fluid Mech. 28, 25.

Batchelor, G.K. (1953) The Theory of Homogeneous Turbulence, Cambridge University Press.

Batchelor, G.K. (1967) An Introduction to Fluid Dynamics, Cambridge University Press.

Barnes, F.H. (1966) Ph. D. Thesis, University of Edinburgh.

Bearman, P.W. (1969) "An Investigation of the Forces on Flat Plates in Turbulent Flow", N.P.L. Aero Report 1296.

Bearman, P.W. (1972) J. Fluid Mech. 53, 451.

P.W. Bearman & Currie, I.G. (1979) J. Fluid Mech. 91, 661.

Bearman, P.W. & Obasaju, E.D. (1982) J. Fluid Mech. 119, 297.

Bearman, P.W. (1984) Ann. Rev. Fluid Mech. 16, 195.

Bendat, J.S. & Piersol, A.G. (1966) Random Data: Analysis and Measurement Procedures, Wiley, Interscience.

Berger, E. & Wille, R. (1972) Ann. Rev. Fluid Mech. 4, 313.

Bishop, R.E.D. & Hassan, A.Y. (1964) Proc. Roy. Soc. Lond. A277, 51.

Bloor, M.S. & Gerrard, J.H. (1966) Proc. Roy. Soc. Lond. A294, 319.

Bracewell, R.N. (1978) The Fourier Transform and its Applications, McGraw-Hill Kogakusha Ltd.

Brigham, O.E. (1974) The Fast Fourier Transform and its Applications, Englewood Cliffs.

Chen, C.F. & Ballengee, D.B. (1971) AIAA J. 9, 340.

Clements, R.R. (1973) J. Fluid Mech. 57, 321.

Clements, R.R. (1975) J. Sound Vib. 40, 563.

Collins, W.M. & Dennis, S.C.R. (1973) J. Fluid Mech. 60, 105.

Davenport, A.G. (1961) Ph.D. Thesis, University of Bristol, Dept. of Civil Engineering.

Davies, M.E. (1975) Ph.D. Thesis, University of London.

Davies, M.E. (1976) J. Fluid Mech. 75, 209.

REFERENCES (Contd.)

Dwyer, H.A. & McCroskey, W.J. (1973) J. Fluid Mech. 61, 753.

Fage, A. & Johansen, F.C. (1927) Proc. Roy. Soc. Lond. A116, 170.

Fromm, J. (1963) Los Alamos Scientific Laboratory Report No. LA-2910.

Fromm, J.E. & Harlow, F.H. (1963) Phys. of Fluids 6, 975.

Gerrard, J.H. (1966) J. Fluid Mech. 25, 401.

Griffin, O.M. & Ramberg, S.E. (1974) J. Fluid Mech. 66, 553.

Griffin, O.M. & Ramberg, S.E. (1975) J. Fluid Mech. 69, 721.

Griffin, O.M. & Ramberg, S.E. (1976) J. Fluid Mech. 75, 257.

Hatfield, H.M. & Morkovin, M.V. (1973) Trans. ASME I: J. Fluids Engng 95, 249.

Hockney, R.W. & Eastwood, J.W. (1981) Computer Simulation Using Particles, New York.

Hoffmann, E.R. & P.N. Joubert (1963) J. Fluid Mech. 16, 395.

Hooker, S.G. (1936) Proc. Roy. Soc. Lond. A154, 67.

Hunt, J.C.R. (1973) J. Fluid Mech. 61, 625.

King. R., Prosser, M.J. & Johns, D.J. (1973) J. Sound Vib. 29, 169.

Koopman, G.H. (1967) J. Fluid Mech. 28, 501.

Lighthill, M.J. (1954) Proc. Roy. Soc. Lond. A224, 1.

Maskell, E.C. (1965) R. & M. No. 3400 (1965).

McCroskey, W.J. (1977) Trans. ASME I: J. Fluids Engng 99, 8.

McGregor, D.M. (1957) UTIA Tech. Note No. 14.

Miller, J.A. & Fejer, A.A. (1964) J. Fluid Mech. 18, 438.

Morkovin, M.V., Loehrke, R.I. & Fejer, A.A. (1971) Recent Research on Unsteady Boundary Layers, Vol. 1 IUTAM Symp.

Newland, D.E. (1975) Random Vibration and Spectral Analysis, Longman, London.

Parker, R. (1967) J. Sound Vib. 5, 330.

Patel, V.A. (1976) Computers and Fluids 4, 13.

REFERENCES (Contd.)

Perry, A.E. (1982) Hot-Wire Anemometry, Oxford University Press.

Perry, A.E. & Lim, T.T. (1978) J. Fluid Mech. 88, 451.

Prandtl, L. & Tietjens, O.G. (1934) Applied Hydro- and Aeromechanics, McGraw-Hill.

Pocha, J.J. (1971) Ph.D. Thesis, Queen Mary College, University of London.

Roache, P.J. (1976) Computational Fluid Dynamics, Hermosa Publishers.

Roshko, A. (1954) NACA T.N. 3169.

Saffmann, P.G. (1973) Phys. of Fluids 16, No. 8, 1181.

Sarpkaya, T. (1975) J. Fluid Mech. 68, 109.

Sarpkaya, T. (1979) J. Appl. Mech. 46, 241.

Schaefer, J.W. & Eskinazi, S. (1959) J. Fluid Mech. 6, 241.

Stansby, P.K. (1974) Aero. J. 87, 36.

Stansby, P.K. (1976) J. Eng. Mech. DIV. ASCE 102, 591.

Taneda, S. (1956) J. Phys. Soc. Japan 11, 302.

Tanida, Y., Okajima, A. & Watanabe, Y. (1973) J. Fluid Mech. 61, 769.

Tuann, S. & Olsen, M.D. (1978) Computers and Fluids 6, 219.

Vickery, B.J. (1965) N.P.L. Aero Report 1143.

Wardlaw, R.L. & Davenport, A.G. (1964) NCR (Canada) Aero Report LR416.

West, G.S. & Apelt, C.J. (1982) J. Fluid Mech. 114, 361.

Wooton, L.R., Warner, M.H. & Cooper, D.H. (1974) "Some Aspects of the Oscillation of Full-scale Piles", in Flow Induced Structural Vibrations (ed. E. Naudascher) p. 587, Springer.